frontiers | Research Topics

Imaging techniques to predict outcomes in renal cancers

Edited by
Haibin Shi and Abhishek Mahajan

Published in
Frontiers in Oncology

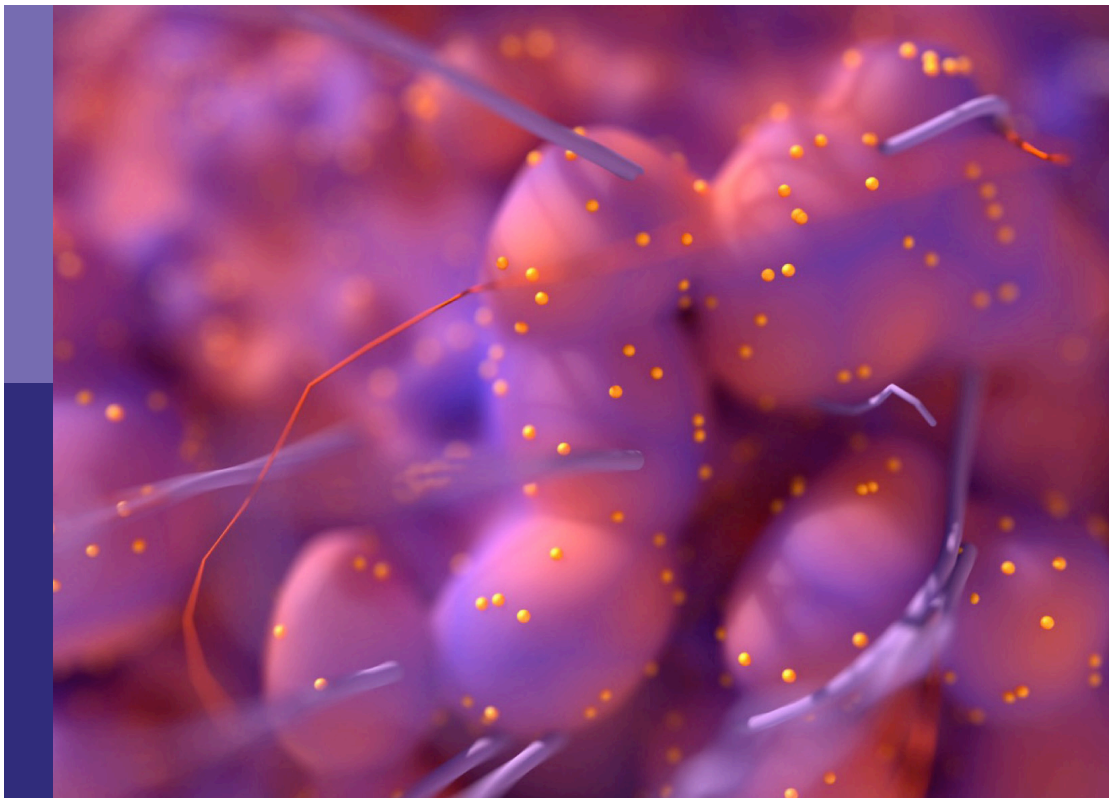

ISSN 1664-8714
ISBN 978-2-8325-4280-4
DOI 10.3389/978-2-8325-4280-4

About Frontiers

Frontiers is more than just an open access publisher of scholarly articles: it is a pioneering approach to the world of academia, radically improving the way scholarly research is managed. The grand vision of Frontiers is a world where all people have an equal opportunity to seek, share and generate knowledge. Frontiers provides immediate and permanent online open access to all its publications, but this alone is not enough to realize our grand goals.

Frontiers journal series

The Frontiers journal series is a multi-tier and interdisciplinary set of open-access, online journals, promising a paradigm shift from the current review, selection and dissemination processes in academic publishing. All Frontiers journals are driven by researchers for researchers; therefore, they constitute a service to the scholarly community. At the same time, the *Frontiers journal series* operates on a revolutionary invention, the tiered publishing system, initially addressing specific communities of scholars, and gradually climbing up to broader public understanding, thus serving the interests of the lay society, too.

Dedication to quality

Each Frontiers article is a landmark of the highest quality, thanks to genuinely collaborative interactions between authors and review editors, who include some of the world's best academicians. Research must be certified by peers before entering a stream of knowledge that may eventually reach the public - and shape society; therefore, Frontiers only applies the most rigorous and unbiased reviews. Frontiers revolutionizes research publishing by freely delivering the most outstanding research, evaluated with no bias from both the academic and social point of view. By applying the most advanced information technologies, Frontiers is catapulting scholarly publishing into a new generation.

What are Frontiers Research Topics?

Frontiers Research Topics are very popular trademarks of the *Frontiers journals series*: they are collections of at least ten articles, all centered on a particular subject. With their unique mix of varied contributions from Original Research to Review Articles, Frontiers Research Topics unify the most influential researchers, the latest key findings and historical advances in a hot research area.

Find out more on how to host your own Frontiers Research Topic or contribute to one as an author by contacting the Frontiers editorial office: frontiersin.org/about/contact

Imaging techniques to predict outcomes in renal cancers

Topic editors

Haibin Shi — Soochow University, China

Abhishek Mahajan — The Clatterbridge Cancer Centre, United Kingdom

Citation

Shi, H., Mahajan, A., eds. (2024). *Imaging techniques to predict outcomes in renal cancers*. Lausanne: Frontiers Media SA. doi: 10.3389/978-2-8325-4280-4

Table of contents

frontiers | Frontiers in Oncology

TYPE Editorial
PUBLISHED 04 January 2024
DOI 10.3389/fonc.2023.1349703

OPEN ACCESS

EDITED AND REVIEWED BY
Zaver Bhujwalla,
Johns Hopkins Medicine, United States

*CORRESPONDENCE
Abhishek Mahajan
drabhishek.mahajan@yahoo.in

RECEIVED 05 December 2023
ACCEPTED 14 December 2023
PUBLISHED 04 January 2024

CITATION
Mahajan A and Shukla S (2024) Editorial: Imaging techniques to predict outcomes in renal cancers.
Front. Oncol. 13:1349703.
doi: 10.3389/fonc.2023.1349703

Editorial: Imaging techniques to predict outcomes in renal cancers

Abhishek Mahajan[1]* and Shreya Shukla[2]

[1]Department of Radiology, The Clatterbridge Cancer Centre NHS Foundation Trust, Liverpool, United Kingdom, [2]Department of Radiology, HBCH and MPMMCC, Tata Memorial Hospital, Varanasi, India

KEYWORDS

editorial, RCC (Renal Cell Carcinoma), renal cancer, MRI, computed tomography

Editorial on the Research Topic
Imaging techniques to predict outcomes in renal cancers

Introduction

In the year 2020, GLOBOCAN data reported a global total of 431,288 new instances of kidney cancer, establishing it as the 14th most prevalent cancer on a worldwide scale. It ranks as the ninth most prevalent cancer in men and the 14th most common among women. Renal cell carcinoma (RCC) makes up the majority (90%) of these cases, with clear cell RCC at 70%, papillary RCC at 10–15%, and chromophobe RCC at 5%. Other subtypes are rare, constituting ≤1% of cases (1). The increased incidence of RCCs can be attributed in part to the rise in cross-sectional imaging in recent decades, leading to more incidentally detected renal masses. Despite rising incidence, kidney cancer has seen a mortality decline of about 2% per year from 2016 to 2020, underlining the impact of improved treatment (2).

Imaging plays a crucial role in the diagnosis and staging of RCC, guiding treatment, and posttreatment evaluation. Computed Tomography (CT) or Magnetic Resonance Imaging (MRI) are ideal imaging tools for the characterization of indeterminate renal lesions. The American Joint Commission on Cancer (AJCC) TNM system is most commonly used system for staging kidney cancer. Clinical staging, which includes physical examination, biopsy, and imaging findings, can pre-surgically determine the T stage, abnormal lymph nodes, venous invasion, and distant metastases. Imaging findings guide management decisions, including intervention choice and surgical approach (3).

Minimally invasive image-guided interventional radiology procedures are applicable in both localized and advanced diseases. Renal mass biopsy is indicated when a kidney lesion is suspected to be hematologic or metastatic. Percutaneous ablation is a potentially curative treatment option for T1a tumors (4). Clear cell RCC's hypervascular nature makes Transarterial Embolization (TAE) a viable adjunctive technique or stand-alone therapy.

The 5-year survival rate among kidney cancer patients has steadily increased due to early tumor detection and more effective systemic therapy for advanced disease.

However, one-third of patients are diagnosed with regional or distant metastases, and approximately one-fourth of those treated surgically with curative intent experience relapse with distant metastases (5). Targeted agents and immunotherapy have improved overall survival and prognosis, but responses vary among patients. Imaging biomarkers and response evaluation criteria have been developed to predict their efficacy.

This Research Topic, led by Dr. Mahajan and team, explores novel imaging techniques for predicting outcomes in renal cancers. The Research Topic includes nine manuscripts, comprising seven original research articles, one meta-analysis, and one review article. The following is a summary of each manuscript:

Diffusion Weighted Imaging (DWI) based diffusion kurtosis imaging (DKI) and Intravoxel incoherent motion (IVIM) models have evolved over recent years. In their original research, Cheng et al. studied the ability of DKI and IVIM to differentiate histologic grades and clinical stages of clear cell RCC.

The field of modern imaging has taken a giant leap with radiomics, now widely utilized in the diagnosis, prognostication, and post-treatment follow-up in tumor imaging. Radiomics involves extracting quantitative features from radiographic images, analyzing the heterogeneity of tumors throughout their volume, and developing predictive models that link imaging features with genomic patterns and clinical outcomes. This Research Topic includes four manuscripts specifically focused on the application of radiomics in renal cell carcinoma (RCC).

Xing et al. have applied contrast-enhanced CT-based radiomics to predict overall survival (OS) in RCC patients. Yin et al. have used radiomics features based on the differential network feature selection (FS) method to determine the feasibility of predicting WHO/ISUP grade and progression-free survival (PFS) of clear cell RCC. There is considerable overlap in the imaging appearance of Renal angiomyolipoma without visible fat and clear cell RCC which poses a challenge to radiologists. In their radiomics-based study, Wang et al. have created a scoring system to distinguish the two using CT imaging by establishing a model using logistic regression and weighted to be a scoring system.

In their original research, Huang et al. established an integrative nomogram model using contrast-enhanced CT features and underlying genomics patterns to predict the overall survival (OS) of clear cell RCC patients.

Liu et al. have explored the feasibility of utilizing urine metabolites for early clinical diagnosis of RCC by demonstrating different urine metabolic profiles in RCC patients, healthy and benign controls.

Kode et al. retrospectively analysed standard uptake values (SUVs) in patients with and without renal failure, finding that renal failure patients do not require a protocol adjustment for 2-deoxy-2-[18F]fluoro-d-glucose Positron Emission Tomography/Computed Tomography (PET/CT).

Pan et al. conducted a meta-analysis exploring the value of contrast-enhanced ultrasound (CEUS) in the diagnosis of renal cancer.

Liu has reviewed the usefulness of 18F-fluorodeoxyglucose FDG PET/CT in RCC, emphasizing its efficacy in postoperative surveillance and restaging when conventional imaging is inconclusive.

In conclusion, the editors express gratitude to all the contributors for their valuable input in this Research Topic, which aims to inspire future and novel research approaches in the field of imaging in renal cancers.

Author contributions

AM: Conceptualization, Supervision, Writing – original draft, Writing – review & editing. SS: Conceptualization, Writing – original draft, Writing – review & editing.

Conflict of interest

The authors declare that the research was conducted in the absence of any commercial or financial relationships that could be construed as a potential conflict of interest.

Publisher's note

References

1. Bukavina L, Bensalah K, Bray F, Carlo M, Challacombe B, Karam JA, et al. Epidemiology of renal cell carcinoma: 2022 update. *Eur Urol* (2022) 82(5):529–42. doi: 10.1016/j.eururo.2022.08.019

2. Clancy E. ACS report shows prostate cancer on the rise, cervical cancer on the decline. *Renal Urol News* (2023).

3. Heilbrun ME, Remer EM, Casalino DD, Beland MD, Bishoff JT, Blaufox MD, et al. ACR Appropriateness Criteria indeterminate renal mass. *J Am Coll Radiol* (2015) 12 (4):333–41. doi: 10.1016/j.jacr.2014.12.012

4. Campbell S, Uzzo RG, Allaf ME, Bass EB, Cadeddu JA, Chang A, et al. Renal mass and localized renal cancer: AUA guideline. *J Urol* (2017) 198(3):520–9. doi: 10.1016/j.juro.2017.04.100

5. Siegel RL, Miller KD, Jemal A. Cancer statistics, 2019. *CA: Cancer J Clin* (2019) 69 (1):7–34. doi: 10.3322/caac.21551

frontiers in Oncology

REVIEW
published: 06 September 2016
doi: 10.3389/fonc.2016.00201

The Place of FDG PET/CT in Renal Cell Carcinoma: Value and Limitations

*Yiyan Liu**

Nuclear Medicine Service, Department of Radiology, New Jersey Medical School, Rutgers University, Newark, NJ, USA

Unlike for most other malignancies, application of FDG PET/CT is limited for renal cell carcinoma (RCC), mainly due to physiological excretion of 18F-fluoro-2-deoxy-2-D-glucose (FDG) from the kidneys, which decreases contrast between renal lesions and normal tissue, and may obscure or mask the lesions of the kidneys. Published clinical observations were discordant regarding the role of FDG PET/CT in diagnosing and staging RCC, and FDG PET/CT is not recommended for this purpose based on current national and international guidelines. However, quantitative FDG PET/CT imaging may facilitate the prediction of the degree of tumor differentiation and allows for prognosis of the disease. FDG PET/CT has potency as an imaging biomarker to provide useful information about patient's survival. FDG PET/CT can be effectively used for postoperative surveillance and restaging with high sensitivity, specificity, and accuracy, as early diagnosis of recurrent/metastatic disease can drastically affect therapeutic decision and alter outcome of patients. FDG uptake is helpful for differentiating benign or bland emboli from tumor thrombosis in RCC patients. FDG PET/CT also has higher sensitivity and accuracy when compared with bone scan to detect RCC metastasis to the bone. FDG PET/CT can play a strong clinical role in the management of recurrent and metastatic RCC. In monitoring the efficacy of new target therapy such as tyrosine kinase inhibitors (TKIs) treatment for advanced RCC, FDG PET/CT has been increasingly used to assess the therapeutic efficacy, and change in FDG uptake is a strong indicator of biological response to TKI.

Keywords: renal cell carcinoma, FDG PET/CT, staging, restaging, tyrosine kinase inhibitors

OPEN ACCESS

Edited by:
Georgios S. Limouris, National and Kapodistrian University of Athens, Greece

Reviewed by:
Nghi Co Nguyen, University of Pittsburgh, USA
Cigdem Soydal, Ankara University, Turkey

***Correspondence:**
Yiyan Liu
liuyl@njms.rutgers.edu

Specialty section:
This article was submitted to Cancer Imaging and Diagnosis, a section of the journal Frontiers in Oncology

Received: *29 February 2016*
Accepted: *26 August 2016*
Published: *06 September 2016*

Citation:
Liu Y (2016) The Place of FDG PET/CT in Renal Cell Carcinoma: Value and Limitations. Front. Oncol. 6:201. doi: 10.3389/fonc.2016.00201

INTRODUCTION

Renal cell carcinoma (RCC) is the most common solid tumor of the kidneys, accounting for 3% of all malignancies and representing the seventh leading cause of cancer. The most common histological subtype of RCC is clear cell RCC, followed by papillary carcinoma. Standard imaging evaluation for the characterization of primary renal tumor includes ultrasound, CT, and MRI. Cross-sectional imaging, especially contrast CT, is a primary imaging modality for tumor detection and diagnosis, and its increasing use has led to an increased diagnosis of RCC. Surgical resection through either partial or radical nephrectomy remains the mainstay of treatment for the localized disease.

Positron emission tomography (PET) has emerged as one of the most important imaging modality in staging, restaging, detecting recurrence and/or metastasis, and monitoring therapeutic response in most malignant diseases (1, 2). In PET, a trace amount of a radioactive compound is administered, and the resultant images are obtained from three-dimensional spatial reconstructions. The intensity of the imaging signal is proportional to the amount of tracer and, therefore, is potentially

semiquantitative (3). Whereas conventional imaging techniques can provide information on anatomic abnormalities, PET imaging relies on both molecular biology and *in vivo* imaging to provide information about the preceding changes in metabolism and function, including glucose metabolism, cell proliferation, cell membrane metabolism, or receptor expression. Furthermore, integrated PET/CT units allow correct co-registration and fused imaging of anatomical and functional data. The integration of CT imaging with PET has been demonstrated to significantly decrease false positive results and improve accuracy of the PET study (4–6).

18F-fluoro-2-deoxy-2-D-glucose (FDG), a non-physiological radiotracer with a chemical structure similar to that of naturally occurring glucose, is most commonly used in PET imaging. FDG enters cells through the same membrane glucose transporter proteins utilized by glucose, which are commonly overexpressed in cancer cells (7, 8). FDG imaging relies upon Warburg's observation that increased glycolysis generated adenosine triphosphate is required to meet the metabolic demands of rapidly dividing tumor cells. Membrane glucose transporters, mainly GLUT-1, actively transport FDG into the cell, where hexokinase then converts it into FDG-6-phosphate. As FDG-6-phosphate is not a substrate for further steps in glycolysis, it is trapped in the cell and accumulates correspondingly to the cell's glucose metabolic activity. FDG accumulation rate is semiquantitatively measured by the standardized uptake value (SUV). Malignant cells exhibit increased FDG accumulation due to increased membrane transporters, increased intracellular hexokinase, and low glucose-6-phosphatase (8).

Unlike for most other malignancies, application of FDG PET/CT is limited for RCC, mainly due to physiological excretion of FDG from the kidneys, which decreases contrast between renal lesions and normal tissue, and may obscure or mask the lesions of the kidneys. However, published clinical observations were discordant. In the era of PET/CT in oncology, clarification and validation of FDG PET/CT for RCC is of great significance for urologists, oncologists, and radiologists. This review presents the studies regarding the FDG PET/CT for RCC. The role of FDG PET/CT is discussed based on the critical, non-structured review of the literature.

FDG PET/CT FOR PRIMARY RCC

Many early clinical observations showed unfavorable results about the role of FDG PET/CT for detection and characterization of lesions of the kidney, with pooled sensitivity of 50–60% (9). Even forced diuresis coupled with parenteral hydration could not improve the sensitivity (10). In Miyakita's study (11), 19 consecutive patients with RCC were imaged using FDG PET preoperatively, the results of which were then compared with the histology obtained after radical surgery. Increased FDG uptake was found in only in 6 out of the 19 patients (31.5%) while immunohistochemistry of GLUT-1 in RCC produced varying results; there was no correlation of GLUT-1 immunoreactivity and FDG PET positivity. Aide et al. prospectively compared the efficiency of FDG PET with diagnostic CT in the characterization and primary staging of 35 suspicious renal masses (12). A high rate of false negative results was reported with FDG PET, leading to 47% sensitivity, 80% specificity, and 51% accuracy; all lower than those of CT. The author concluded that, in the characterization of renal masses, FDG PET imaging does not offer any additional advantages compared with CT. In another retrospective study of 66 patients with known RCC by Kang et al. (13), the accuracies of FDG PET and conventional imaging modalities were also compared. FDG PET exhibited a sensitivity of 60% and specificity of 100% for primary RCC tumors, while abdominal CT demonstrated 91.7% sensitivity and 100% specificity. Ozulker et al. evaluated the efficacy of FDG PET/CT in the detection of RCC in patients with indeterminate renal masses detected by conventional imaging from 18 patients (14). All patients underwent nephrectomy or surgical resection of the renal mass, and the final diagnoses were based on histopathology. Fifteen patients had RCC, and three renal tumors were benign. FDG PET/CT accurately detected seven malignant lesions and false negative results in eight patients. FDG PET/CT yielded true negatives in two cases of renal cortical cyst and false positive in one case with oncocytoma. For primary RCC tumors, PET showed 46.6% sensitivity, 66.6% specificity, and 50% accuracy. The median size of visualized tumors was greater than that of non-visualized tumors, and the average Fuhrman grade of the patients with FDG-positive malignant lesions were higher than that of the patients with FDG-negative lesions. There was no significant change in average and maximum SUVs between early and delayed imaging for malignant tumors.

However, some clinical observations demonstrated favorable results regarding the role FDG PET/CT in RCC and showed high FDG avidity in the majority of RCC lesions. In a study by Kumar et al. (15), FDG PET was performed in 28 solid renal masses visualized by CT/MRI. Of the lesions, FDG PET was accurately able to depict 23 out of 27 (85%) malignant renal masses. Of the 10 primary renal tumors (9 malignant, 1 benign), FDG PET yielded 8 out of 9 true positive results (89%), 1 true negative, and 1 false negative. In addition to characterization of the lesions, FDG PET also contributed to primary staging, altering management in 3 out of 10 patients (30%). Of metastatic renal tumors, FDG PET was positive in 15 out of 18 (83%). There was no significant difference in SUVs between primary and metastatic renal masses. Nakhoda et al. evaluated the sensitivity of FDG PET/CT to detect different renal lesions (16). Fifteen out of 18 RCC were detectable by PET, whereas all renal lymphomas and metastases were detectable. None of the metabolic parameters were statistically significant between RCC and renal lymphoma. However, all metabolic parameters were statistically and significantly greater for renal metastases compared with RCC and renal lymphoma, and for clear cell RCC compared with papillary RCC. In addition to a sensitivity of 88% for detection of solid malignant renal lesions in patients with known renal malignancy, FDG PET/CT also reveals differences in metabolic activity based on histopathological type.

Recently, Takahashi et al. retrospectively analyzed FDG PET/CT findings in 98 lesions from 93 patients who had partial or radical nephrectomy after imaging (17). The SUVs of high-grade clear cell RCC were significantly higher when compared with that of the control benign lesions and low-grade tumors. An optimal SUV cutoff value of 3.0 had 89% sensitivity and 87% specificity

in differentiating between high-grade and low-grade clear cell RCCs. Multiple regression analysis demonstrated that a high-grade clear cell RCC was the most significant predictor of SUV.

Overall, the results were heterogeneous. Although FDG PET/CT may be helpful in the characterization and detection of primary renal tumors, it has low negative predictive value. In addition, it seems that FDG PET/CT does not have significant advantage in diagnosis and staging of RCC compared with the diagnostic CT.

PREDICTIVE ROLE OF FDG PET/CT IN PROGNOSIS

Metabolic quantitation by SUV measurement on FDG PET/CT may play a role in the evaluation of biological behavior of lesion and prediction of patient's prognosis. Namura et al. evaluated the impact of the maximum SUV (SUV_{max}) from FDG PET/CT on survival in 26 patients with advanced RCC (18). High SUV_{max} in patients with RCC correlated with poor prognosis, as there was a statistically significant difference in the survival between patients with SUV_{max} equal or greater than the mean of SUV_{max}, 8.8 and patients with SUV_{max} less than 8.8. The authors revealed that the SUV_{max} might have a role as a novel biomarker in prognosticating the survival time of patients with advanced RCC by multivariate analyses with standard risk factors or risk classifications. In another study by Ferda et al. (19), 60 RCC patients had follow-ups for development of the disease 12 months after FDG PET/CT. The highest FDG accumulation was seen in the tumor of the highest grade, and the highest mortality was found for tumors exceeding SUV_{max} of 10. Lee et al. investigated the relationship between the SUV_{max} of primary RCC with and without metastatic lesions in 23 patients (20). The median SUV_{max} of primary RCC of the 16 patients without metastasis was 2.6 (range of 1.1–5.6) while that of the patients with metastasis was 5.0 (range of 2.9–7.6). The SUV_{max} of the primary RCC with metastasis (5.3 ± 1.7) was significantly higher than those without metastasis (2.9 ± 1.0). Thus, one of the roles of FDG PET/CT in the initial evaluation of a patient with RCC may be in predicting extrarenal disease, as patients who have primary RCC with high SUV_{max} are suggested to have a likelihood of metastasis.

Based on the limited data, quantitative FDG PET/CT imaging may facilitate the prediction of the degree of tumor differentiation and allow for prognosis of the disease. FDG PET/CT may be an effective imaging biomarker to provide useful information about patient's survival. However, more studies are needed to justify these preliminary findings.

FDG PET/CT FOR RESTAGING RCC

Metastatic RCC is one of the most lethal urologic cancers. Up to one-third of patients with newly diagnosed RCC have metastatic diseases (21). Even after nephrectomy of a locally confined disease, more than 30% of the patients develop metastases, most commonly to the lung, bone, skin, liver, and brain (21). Effective staging of RCC, therefore, is crucial for the management of patients.

Although the role of FDG PET/CT in diagnosing RCC is conflicting, it has been more effective in the detection of metastatic disease, thus affecting therapeutic decisions. Obviously, size of the lesions has been shown to be a significant factor affecting sensitivity of PET/CT. Majhail et al. evaluated the performance of FDG PET in detecting metastatic lesions in 24 patients with histologically proven RCC and suspected distant metastases based on conventional anatomic imaging (22). Histologically documented distant metastases were present in 33 sites. Overall sensitivity, specificity, and positive predictive value of FDG PET for the detection of distant metastases from RCC was 63.6% (21 out of 33), 100% (3 out of 3), and 100% (21 out of 21), respectively. The mean size of distant metastases in patients with true positive FDG PET was 2.2 cm (95% CI, 1.7–2.6 cm) compared with 1.0 cm in patients with false negative FDG PET.

18F-fluoro-2-deoxy-2-D-glucose (FDG) PET seems useful for postoperative surveillance in patients with RCC. It can detect recurrence in the surgical site. Nakatani et al. evaluated the surveillance role of FDG PET in 23 postoperative patients with RCC (23). Histological final diagnosis of at least 6 months clinical follow-up was used to confirm diagnostic accuracy of visually interpreted PET. FDG PET was demonstrated to have 81% sensitivity, 71% specificity, and 79% diagnostic accuracy. PET was able to accurately detect local recurrence and metastases to the peritoneum, bone, muscle, and adrenal gland in all cases. In six cases (21%), additional information was obtained from scans, ultimately affecting the course of therapeutic management in three cases (11%). The cumulative survival rate over 5 years in the PET-positive was 46%, whereas that of the PET-negative group was 83%. Kumar et al. assessed 103 FDG PET/CT scans of 63 patients with suspected recurrent RCC after nephrectomy, confirmed with histological examination and/or clinical follow-up and conventional imaging modalities (24). The results of the 103 FDG PET/CT scans were 63 true positive studies, 30 true negative studies, 7 false negative studies, and 3 false positive studies. 109 lesions were detected by FDG PET/CT in the 63 true positive scans. FDG PET/CT was demonstrated to have 90% sensitivity, 91% specificity, and 90% accuracy in the study. Bertagna et al. retrospectively evaluated 68 patients with renal carcinoma who had postoperative FDG PET/CT following partial or radical nephrectomy (25). FDG PET/CT was reported to have 82% sensitivity, 100% specificity, 100% positive predictive value, 66.7% negative predictive value, and 86.6% accuracy. In another study reported by Fuccio et al., the usefulness of FDG PET/CT was assessed in the restaging of 69 RCC patients with clinical or radiological suspicion of metastases after nephrectomy (26). Validation of FDG PET/CT results was established by biopsy, other imaging modalities, and/or clinical and radiological follow-up of 12 months. Forty patients had true positive, 2 patients false positive, 23 patients true negative, and 4 patients false negative. Sensitivity, specificity, accuracy, positive predictive value, and negative predictive value were 90, 92, 91, 95, and 85%, respectively. On a lesion basis, FDG PET/CT detected 114 areas of abnormal uptake in 42 positive patients of which 112 resulted to be true positive.

In another large series study, Win and Aparici retrospectively reviewed the FDG PET/CT studies in 315 RCC patients with biopsy results (27). FDG PET/CT studies exhibited 100%

sensitivity and 100% specificity in detecting all metastatic lesions of RCC, the smallest of which detected was a 7 mm lymph node. Therefore, the authors recommended the use of FDG PET/CT in routine standard protocols for RCC.

18F-fluoro-2-deoxy-2-D-glucose (FDG) PET/CT is a valuable tool both in guiding management and treatment in patients with RCC, as well as in predicting survival and progression. A more recent study confirmed the clinical role of FDG PET/CT in the restaging of RCC in a large group of patients (28). For recurrent and/or metastatic lesions in 104 patients, FDG PET/CT demonstrated sensitivity and specificity of 74 and 80%, respectively. FDG PET/CT findings affected management therapies in 45/104 cases (43%). In looking at overall survival (OS), positive FDG PET/CT associated with lower cumulative survival rates cover a 5-year period compared with that of negative FDG PET/CT. Likewise, a positive FDG PET/CT was associated with a lower 3-year progression-free survival (PFS) rate and was associated with high risk of progression, alone or in combination with disease stage or nuclear grading.

In patients with underlying primary malignancy, there is a high incidence of thrombosis, which can develop from venous thromboembolism (VTE) or more rarely, tumor thrombus. VTE is a common occurrence in cancer, managed with anticoagulant therapy, while tumor thrombosis requires aggressive multimodality therapeutics. Tumor thrombosis most commonly develops in solid tumors, such as RCC and hepatocellular carcinoma, adjacent to large veins as an extension of the malignancy and/or tumor infiltration (29). Sharma et al. conducted a retrospective review of FDG PET/CT scans in patients who had FDG-avid thrombosis (30). FDG PET/CT results were confirmed with clinical follow-up, structural imaging, and histopathology when available. On the basis of structural imaging and clinical follow-up, 10 patients had benign and 14 patients had tumor thrombosis. The most common site of thrombosis was the inferior vena cava. The mean SUV_{max} was 3.2 in the benign thrombosis group and 6.0 in the tumor thrombosis group. The difference in SUV_{max} was significant. In Ravina's series (31), out of 21 tumor thrombosis cases incidentally detected by FDG PET/CT, 6 were from RCCs. Ferda et al. also reported that FDG PET/CT successfully detected all 7 cases with tumor invasion into the inferior vena cava of 60 patients with RCC (19). The results showed that SUV and the pattern of FDG uptake are helpful for differentiating benign or bland emboli from tumor thrombosis in RCC patients, which is essential for management of patients (**Figure 1**).

Bone lesions associated with RCC are typically osteolytic. Traditional bone scintigraphy with Tc-99m methylene diphosphonate has limited sensitivity compared with FDG PET/CT, which has a higher sensitivity and a better accuracy in detecting bone metastases in patients with RCC. Wu et al. compared FDG PET with bone scan in 18 patients with biopsy-proven RCC and suspected bone metastases confirmed by histopathology or clinical follow-up of at least 1 year and conventional imaging or FDG PET/bone scans (32). Fifty-two bone lesions, 40 metastatic, and 12 benign, were found on either FDG-PET or bone scan. FDG PET accurately diagnosed all 40 metastatic and 12 benign bone lesions. In comparison, only 31 metastatic bone lesions were accurately detected by bone scan. FDG PET had 100% diagnostic sensitivity and 100% accuracy while that of bone scan were 77.5 and 59.6%, respectively.

18F-fluoro-2-deoxy-2-D-glucose (FDG) PET/CT can provide useful information and has a strong clinical role in the management of recurrent and metastatic RCC (**Figures 2–4**). In a 58-patient series reported by Rodriguez Martinez de Llano et al. (33), FDG PET/CT had the clinical impact in 25 cases (43%) and no impact in only 10 studies (17.2%). In more recently reported

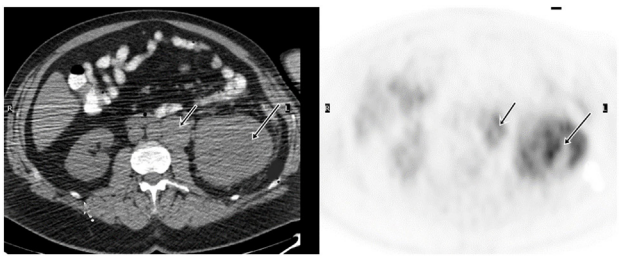

FIGURE 1 | Demonstration of primary RCC and tumor thrombosis on FDG PET/CT. A 53-year-old man had a large left renal mass seen on the CT. FDG PET/CT showed increased, heterogeneous uptake of the mass in the left kidney. There was also tumor thrombosis in the renal vein, evidenced by FDG avid intraluminal lesion.

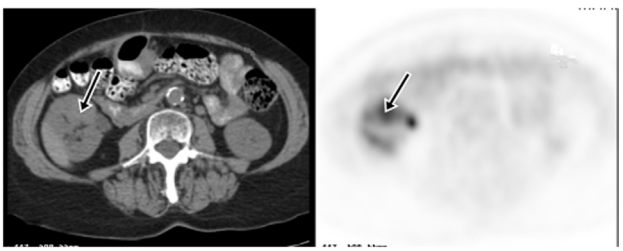

FIGURE 2 | Demonstration of RCC recurrence on FDG PET/CT. A 66-year-old woman had right partial nephrectomy for RCC. Two years later, a diagnostic CT showed a new mass in the anterior midpole of the right kidney, which was FDG avid on PET imaging. Subsequent nephrectomy confirmed recurrence of RCC.

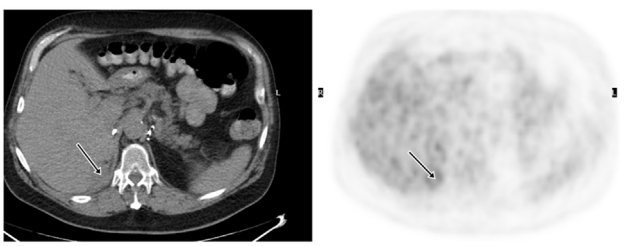

FIGURE 3 | Demonstration of RCC recurrence on FDG PET/CT. A 68-year-old man had right radical nephrectomy for RCC. FDG PET/CT was obtained for surveillance 5 years later, which showed a 2.0 cm density with moderate uptake in the surgical bed and was suspicious for recurrence. Surgical pathology revealed recurrent malignancy.

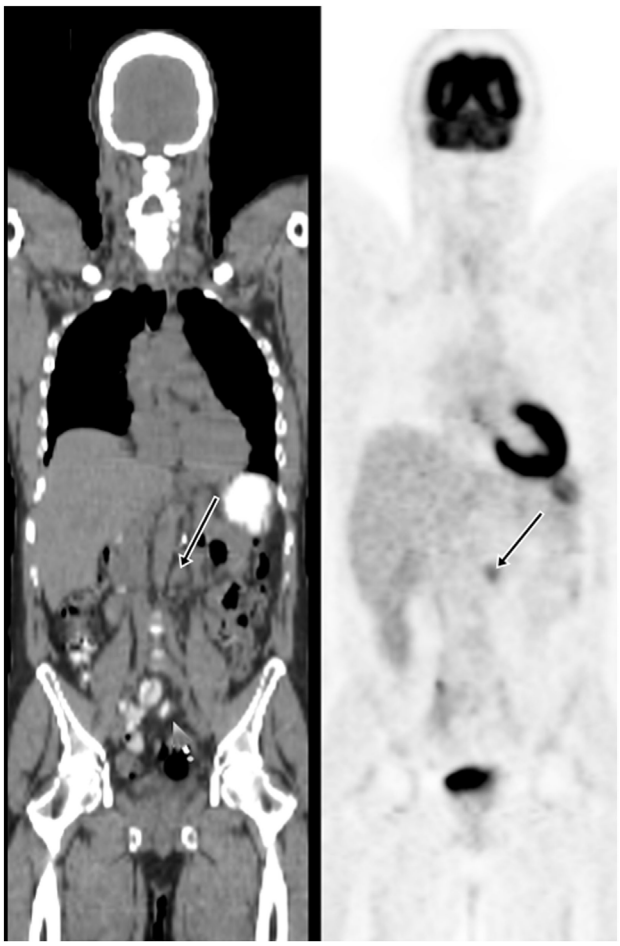

FIGURE 4 | Demonstration of metastatic lymph node on FDG PET/CT. A 57-year-old man had the left nephrectomy for RCC 5 years ago. A restaging FDG PET/CT showed a 1.5 cm left para-aortic node with moderate uptake. Subsequent node dissection confirmed metastasis.

large series by Alongi et al. (28), FDG PET/CT findings influenced therapeutic management in 45/104 cases (43%), treatment was switched from palliative to salvage in 12 patients, and new chemotherapy or immunotherapy was initiated in 24 patients.

Compared to conventional imaging modalities, FDG PET/CT has the advantage in detection of early metastatic disease and identification of musculoskeletal metastases, which are difficult to assess on CT and MRI. Bertagna et al. reported that histologically confirmed bone metastases were revealed at FDG PET/CT in the presence of negative diagnostic CT in 3 out of 27 cases (25). Park et al. compared FDG PET/CT to conventional imaging modalities for restaging 63 patients with RCC who have a high risk of local recurrence or distant metastasis (34). FDG PET/CT accurately classified the presence of a recurrence or metastasis in 56 (89%) patients. FDG PET/CT had 89.5% sensitivity, 83.3% specificity, 77.3% positive predictive value, 92.6% negative predictive value, and 85.7% accuracy in detecting recurrence or metastasis, which were similar to the results with conventional methods. Since FDG PET/CT is versatile and examines all organ systems with high accuracy in one procedure, and with no need for contrast agents, it might replace conventional methods for restaging RCC. Additionally, FDG PET/CT has a unique value in the prediction of survival and risk of progression in patients with recurrent or metastatic RCC (28).

However, FDG is not specific for malignant neoplasm. Increased uptake can be seen in many benign tumors and non-neoplastic processes. On FDG PET/CT for RCC, the false positive results are often due to concomitant inflammatory/infectious disease (9, 28), postoperative scar (26), postradiation inflammation, etc. The most common reason of a false negative FDG PET/CT finding is the small size of lesion and limited spatial resolution of PET scanner (26, 28). In RCC, another potential source of false negative result may be due to close proximity of the lesion to the urinary tract where there is physiologic urine activity (26).

FDG PET/CT FOR MONITORING THERAPEUTIC RESPONSE TO TYROSINE KINASE INHIBITOR

Adjuvant therapy remains a poor treatment alternative for advanced RCC. RCC is resistant to both conventional cytotoxic chemotherapy and radiation therapy, which carry a significant toxicity burden. However, a variety of targeted therapies including tyrosine kinase inhibitors (TKIs) have showed promising efficacy in advanced or metastatic RCC, with satisfactory results on PFS and quality of life (35, 36). TKIs, such as sunitinib and sorafenib, are antiangiogenic and can effectively inhibit tumor proliferation.

Although tumor size measurements with the response evaluation criteria in solid tumors (RECIST) criteria have been used for monitoring response to chemotherapy, there is often little change in size of the lesions, and some metastases even increase in size while the drug is prolonging survival (37). In the recent years, FDG PET/CT has been increasingly used to assess the therapeutic efficacy of TKIs in patients with metastatic RCC. According to Caldarella's systematic review of seven published studies, a good correlation was found between partial metabolic response and PFS and/or OS, with the highest survival rates in patients showing the greatest post-therapeutic reduction in SUV_{max} (38). In contrary, increase on FDG uptake was associated with lower OS (39). Pooled studies showed that FDG PET/CT had a high predictive value in the evaluation of response to SKI treatment in both skeletal and soft tissue lesions of metastatic RCC although there was heterogeneity of available data (38).

Some studies compared the values of FDG PET/CT and RECIST in predicting PFS and OS of patients treated with SKIs for metastatic RCC. Lyrdal et al. reported that FDG PET/CT was more useful than RECIST criteria, especially for the evaluation of skeletal lesions (40), as RECIST is limited to soft tissue lesions.

Kakizoe et al. reported that the decreased ratio of FDG accumulation of RCC lesions, as assessed 1 month following initiation of TKI treatment by FDG PET/CT, was not influenced by the site of RCC metastasis (41). The study suggests that TKIs can be used in the treatment of advanced RCC regardless of the metastatic site, and that FDG PET/CT is a useful method of surveillance to monitor therapeutic response in all lesions.

CONCLUSION

Although the usefulness of FDG PET/CT in primary RCC remains unclear, and FDG PET/CT is not currently recommended for the diagnosis and staging of RCC based on updated national and international guidelines (42–44), it can effectively be used for postoperative surveillance and restaging as an adjunct when conventional imaging is not conclusive, as early diagnosis of recurrent/metastatic disease can drastically affect therapeutic decision and alter outcomes of patients (45). FDG uptake is helpful for differentiating benign or bland emboli from tumor thrombosis in RCC patients. FDG PET/CT has a higher sensitivity and accuracy in detecting bone metastases in patients with RCC than that of bone scan. Pretreatment SUV_{max} assessed by FDG PET/CT can provide helpful information for clinical decision-making as it can serve as a useful prognostic marker for patients with advanced RCC. High SUV_{max} in patients with primary RCC is suggested with correlate with a high likelihood of metastasis, and FDG accumulation may be useful in estimating patient's survival. In monitoring the efficacy of TKI treatment for advanced RCC, FDG PET/CT has been increasingly used to assess the therapeutic efficacy, and change of FDG uptake is a powerful index for evaluating the biological response to TKI.

AUTHOR CONTRIBUTIONS

The author confirms being the sole contributor of this work and approved it for publication.

REFERENCES

1. Fletcher JW, Djulbegovic B, Soares H, Siegel BA, Lowe VJ, Lyman GH, et al. Recommendations on the use of 18F-FDG PET in oncology. *J Nucl Med* (2008) 49:480–508. doi:10.2967/jnumed.107.047787
2. Rohren EM, Turkington TG, Coleman RE. Clinical applications of PET in oncology. *Radiology* (2004) 231:302–32. doi:10.1148/radiol.2312021185
3. Kapoor V, McCook BM, Torok FS. An introduction to PET-CT imaging. *Radiographics* (2004) 24:523–43. doi:10.1148/rg.242025724
4. Antoch G, Saoudi N, Kuehl H, Dahmen G, Mueller SP, Beyer T, et al. Accuracy of whole-body dual-modality fluorine-18-2-fluoro-2-deoxy-D-glucose positron emission tomography and computed tomography (FDG-PET/CT) for tumor staging in solid tumors: comparison with CT and PET. *J Clin Oncol* (2004) 22:4357–68. doi:10.1200/JCO.2004.08.120
5. Pelosi E, Messa C, Sironi S. Value of integrated PET/CT for lesion localization in cancer patients: a comparative study. *Eur J Nucl Med Mol Imaging* (2004) 31:932–9. doi:10.1007/s00259-004-1483-3
6. Reinartz P, Wieres FJ, Schneider W, Schur A, Buell U. Side-by-side reading of PET and CT scans in oncology: which patients might profit from integrated PET/CT? *Eur J Nucl Med Mol Imaging* (2004) 31:1456–61. doi:10.1007/s00259-004-1593-y
7. Delbeke D, Martin WH. Positron emission tomography imaging in oncology. *Radiol Clin North Am* (2001) 39:883–917. doi:10.1016/S0033-8389(05)70319-5
8. Liu Y, Ghesani NV, Zuckier LS. Physiology and pathophysiology of incidental findings detected on FDG-PET scintigraphy. *Semin Nucl Med* (2010) 40:294–315. doi:10.1053/j.semnuclmed.2010.02.002
9. Wang HY, Ding HJ, Chen JH, Chao CH, Lu YY, Lin WY, et al. Meta-analysis of the diagnostic performance of [18F] FDG-PET and PET/CT in renal cell carcinoma. *Cancer Imaging* (2012) 12:464–74. doi:10.1102/1470-7330.2012.0042
10. Kamel EM, Jichlinski P, Prior JO, Meuwly JY, Delaloye JF, Vaucher L, et al. Forced diuresis improves the diagnostic accuracy of 18F-FDG PET in abdominopelvic malignancies. *J Nucl Med* (2006) 47:1803–7.
11. Miyakita H, Tokunaga M, Onda H, Usui Y, Kinoshita H, Kawamura N, et al. Significance of 18F-fluorodeoxyglucose positron emission tomography (FDG-PET) for detection of renal cell carcinoma and immunohistochemical glucose transporter 1 (GLUT-1) expression in the cancer. *Int J Urol* (2002) 9:15–8. doi:10.1046/j.1442-2042.2002.00416.x
12. Aide N, Cappele O, Bottet P, Bensadoun H, Regeasse A, Comoz F, et al. Efficiency of [(18)F]FDG PET in characterizing renal cancer and detecting distant metastases: a comparison with CT. *Eur J Nucl Med Mol Imaging* (2003) 30:1236–45. doi:10.1007/s00259-003-1211-4
13. Kang DE, White RL Jr, Zuger JH, Sasser HC, Teigland CM. Clinical use of fluorodeoxyglucose F 18 positron emission tomography for detection of renal cell carcinoma. *J Urol* (2004) 171:1806–9. doi:10.1097/01.ju.0000120241.50061.e4
14. Ozulker T, Ozulker F, Ozbek E, Ozpacaci T. A prospective diagnostic accuracy study of F-18 fluorodeoxyglucose-positron emission tomography/computed tomography in the evaluation of indeterminate renal masses. *Nucl Med Commun* (2011) 32:265–72. doi:10.1097/MNM.0b013e3283442e3b
15. Kumar R, Chauhan A, Lakhani P, Xiu Y, Zhuang H, Alavi A. 2-Deoxy-2-[F-18] fluoro-D-glucose-positron emission tomography in characterization of solid renal masses. *Mol Imaging Biol* (2005) 7:431–9. doi:10.1007/s11307-005-0026-z
16. Nakhoda Z, Torigian DA, Saboury B, Hofheinz F, Alavi A. Assessment of the diagnostic performance of (18)F-FDG-PET/CT for detection and characterization of solid renal malignancies. *Hell J Nucl Med* (2013) 16:19–24. doi:10.1967/s002449910067
17. Takahashi M, Kume H, Koyama K, Nakagawa T, Fujimura T, Morikawa T, et al. Preoperative evaluation of renal cell carcinoma by using 18F-FDG PET/CT. *Clin Nucl Med* (2015) 40:936–40. doi:10.1097/RLU.0000000000000875
18. Namura K, Minamimoto R, Yao M, Makiyama K, Murakami T, Sano F, et al. Impact of maximum standardized uptake value (SUVmax) evaluated by 18-Fluoro-2-deoxy-D-glucose positron emission tomography/computed tomography (18F-FDG-PET/CT) on survival for patients with advanced renal cell carcinoma: a preliminary report. *BMC Cancer* (2010) 10:667. doi:10.1186/1471-2407-10-667
19. Ferda J, Ferdova E, Hora M, Hes O, Finek J, Topolcan O, et al. 18F-FDG-PET/CT in potentially advanced renal cell carcinoma: a role in treatment decisions and prognosis estimation. *Anticancer Res* (2013) 33:2665–72.
20. Lee H, Hwang KH, Kim SG, Koh G, Kim JH. Can initial (18)F-FDG PET-CT imaging give information on metastasis in patients with primary renal cell carcinoma? *Nucl Med Mol Imaging* (2014) 48:144–52. doi:10.1007/s13139-013-0245-1
21. Figlin RA. Renal cell carcinoma: management of advanced disease. *J Urol* (1999) 161:381–6. doi:10.1016/S0022-5347(01)61897-4
22. Majhail NS, Urbain JL, Albani JM, Kanvinde MH, Rice TW, Novick AC, et al. F-18 fluorodeoxyglucose positron emission tomography in the evaluation of distant metastases from renal cell carcinoma. *J Clin Oncol* (2003) 21:3995–4000. doi:10.1200/JCO.2003.04.073
23. Nakatani K, Nakamoto Y, Saga T, Higashi T, Togashi K. The potential clinical value of FDG-PET for recurrent renal cell carcinoma. *Eur J Radiol* (2011) 79:29–35. doi:10.1016/j.ejrad.2009.11.019
24. Kumar R, Shandal V, Shamim SA, Jeph S, Singh H, Malhotra A. Role of FDG PET-CT in recurrent renal cell carcinoma. *Nucl Med Commun* (2010) 31:844–50. doi:10.1097/MNM.0b013e32833d6882
25. Bertagna F, Motta F, Bertoli M, Bosio G, Fisogni S, Tardanico R, et al. Role of F18-FDG-PET/CT in restaging patients affected by renal carcinoma. *Nucl Med Rev Cent East Eur* (2013) 16:3–8. doi:10.5603/NMR.2013.0002
26. Fuccio C, Ceci F, Castellucci P, Spinapolice EG, Palumbo R, D'Ambrosio D, et al. Restaging clear cell renal carcinoma with 18F-FDG PET/CT. *Clin Nucl Med* (2014) 39:e320–4. doi:10.1097/RLU.0000000000000382
27. Win AZ, Aparici CM. Clinical effectiveness of (18)f-fluorodeoxyglucose positron emission tomography/computed tomography in management of renal cell carcinoma: a single institution experience. *World J Nucl Med* (2015) 14:36–40. doi:10.4103/1450-1147.150535
28. Alongi P, Picchio M, Zattoni F, Spallino M, Gianolli L, Saladini G, et al. Recurrent renal cell carcinoma: clinical and prognostic value of FDG PET/CT. *Eur J Nucl Med Mol Imaging* (2016) 43:464–73. doi:10.1007/s00259-015-3159-6

29. Sharma P, Kumar R, Singh H, Jeph S, Patnecha M, Reddy RM, et al. Imaging thrombus in cancer patients with FDG PET-CT. *Jpn J Radiol* (2012) 30:95–104. doi:10.1007/s11604-011-0016-9
30. Sharma P, Kumar R, Jeph S, Karunanithi S, Naswa N, Gupta A, et al. 18F-FDG PET-CT in the diagnosis of tumor thrombus: can it be differentiated from benign thrombus? *Nucl Med Commun* (2011) 32:782–8. doi:10.1097/MNM.0b013e32834774c8
31. Ravina M, Hess S, Chauhan MS, Jacob MJ, Alavi A. Tumor thrombus: ancillary findings on FDG PET/CT in an oncologic population. *Clin Nucl Med* (2014) 39:767–71. doi:10.1097/RLU.0000000000000451
32. Wu HC, Yen RF, Shen YY, Kao CH, Lin CC, Lee CC. Comparing whole body 18F-2-deoxyglucose positron emission tomography and technetium-99m methylene diphosphate bone scan to detect bone metastases in patients with renal cell carcinomas – a preliminary report. *J Cancer Res Clin Oncol* (2002) 128:503–6. doi:10.1007/s00432-002-0370-1
33. Rodriguez Martinez de Llano S, Jimenez-Vicioso A, Mahmood S, Carreras-Delgado JL. Clinical impact of (18)F-FDG PET in management of patients with renal cell carcinoma. *Rev Esp Med Nucl* (2010) 29:12–9. doi:10.1016/j.remn.2009.11.008
34. Park JW, Jo MK, Lee HM. Significance of 18F-fluorodeoxyglucose positron-emission tomography/computed tomography for the postoperative surveillance of advanced renal cell carcinoma. *BJU Int* (2009) 103:615–9. doi:10.1111/j.1464-410X.2008.08150.x
35. Jonasch E, Corn P, Pagliaro LC, Warneke CL, Johnson MM, Tamboli P, et al. Upfront, randomized, phase 2 trial of sorafenib versus sorafenib and low-dose interferon alfa in patients with advanced renal cell carcinoma: clinical and biomarker analysis. *Cancer* (2010) 116:57–65. doi:10.1002/cncr.24685
36. Procopio G, Verzoni E, Bracarda S, Ricci S, Sacco C, Ridolfi L, et al. Sorafenib with interleukin-2 vs sorafenib alone in metastatic renal cell carcinoma: the ROSORC trial. *Br J Cancer* (2011) 104:1256–61. doi:10.1038/bjc.2011.103
37. Chen JL, Appelbaum DE, Kocherginsky M, Cowey CL, Rathmell WK, McDermott DF, et al. FDG-PET as a predictive biomarker for therapy with everolimus in metastatic renal cell cancer. *Cancer Med* (2013) 2:545–52. doi:10.1002/cam4.102
38. Caldarella C, Muoio B, Isgro MA, Porfiri E, Treglia G, Giovanella L. The role of fluorine-18-fluorodeoxyglucose positron emission tomography in evaluating the response to tyrosine-kinase inhibitors in patients with metastatic primary renal cell carcinoma. *Radiol Oncol* (2014) 48:219–27. doi:10.2478/raon-2013-0067
39. Kayani I, Avril N, Bomanji J, Chowdhury S, Rockall A, Sahdev A, et al. Sequential FDG-PET/CT as a biomarker of response to Sunitinib in metastatic clear cell renal cancer. *Clin Cancer Res* (2011) 17:6021–8. doi:10.1158/1078-0432.CCR-10-3309
40. Lyrdal D, Boijsen M, Suurkula M, Lundstam S, Stierner U. Evaluation of sorafenib treatment in metastatic renal cell carcinoma with 2-fluoro-2-deoxy-glucose positron emission tomography and computed tomography. *Nucl Med Commun* (2009) 30:519–24. doi:10.1097/MNM.0b013e32832cc220
41. Kakizoe M, Yao M, Tateishi U, Minamimoto R, Ueno D, Namura K, et al. The early response of renal cell carcinoma to tyrosine kinase inhibitors evaluated by FDG PET/CT was not influenced by metastatic organ. *BMC Cancer* (2014) 14:390. doi:10.1186/1471-2407-14-390
42. Ljungberg B, Hanbury DC, Kuczyk MA, Merseburger AS, Mulders PF, Patard JJ, et al. Renal cell carcinoma guideline. *Eur Urol* (2007) 51:1502–10. doi:10.1016/j.eururo.2007.03.035
43. Boellaard R, Delgado-Bolton R, Oyen WJ, Giammarile F, Tatsch K, Eschner W, et al. FDG PET/CT: EANM procedure guidelines for tumour imaging: version 2.0. *Eur J Nucl Med Mol Imaging* (2015) 42:328–54. doi:10.1007/s00259-014-2961-x
44. Escudier B, Porta C, Schmidinger M, Algaba F, Patard JJ, Khoo V, et al. Renal cell carcinoma: ESMO Clinical Practice Guidelines for diagnosis, treatment and follow-up. *Ann Oncol* (2014) 25(Suppl 3):iii49–56. doi:10.1093/annonc/mdu259
45. Bouchelouche K, Choyke PL. PET/computed tomography in renal, bladder, and testicular cancer. *PET Clin* (2015) 10:361–74. doi:10.1016/j.cpet.2015.03.002

Conflict of Interest Statement: The author declares that the research was conducted in the absence of any commercial or financial relationships that could be construed as a potential conflict of interest.

frontiers in Oncology

ORIGINAL RESEARCH
published: 21 July 2017
doi: 10.3389/fonc.2017.00155

Impact of Renal Failure on F18-FDG PET/CT Scans

*Vishwajit Kode[1], Holly Karsch[2], Medhat M. Osman[3] and Razi Muzaffar[3]**

[1] Saint Louis University School of Medicine, Saint Louis, MO, United States, [2] Division of Nuclear Medicine Technology, Saint Louis University Hospital, Saint Louis, MO, United States, [3] Division of Nuclear Medicine, Department of Radiology, Saint Louis University, Saint Louis, MO, United States

Objective: The current guidelines for 2-deoxy-2-[18F]fluoro-D-glucose PET/CT scanning do not address potential inaccuracies that may arise due to patients with renal failure. We report a retrospective analysis of standard uptake values (SUVs) in patients with and without renal failure in order to warrant a protocol adjustment.

Methods: Patients were matched based on age, gender, and BMI all of which are potential effectors on observed SUV. Thirty patients were selected with clinically diagnosed renal failure, of which 12 were on dialysis. All 30 patients had age, gender, and BMI control matches. Blood urea nitrogen and creatinine levels were measured within 1 month of the scan to assess renal failure. PET/CT scans for both the renal failure patients and controls were performed 60 min after FDG injection. SUVs were measured by placing circular regions of interest in the right hepatic lobe (LSUV) and left psoas muscle (PSUV).

Results: For the 30 renal failure patients, the mean LSUV was 2.77 (SD = 0.57) and PSUV was 1.43 (SD = 0.30) while the controls had mean LSUV 2.74 (SD = 0.50) and PSUV 1.42 (SD = 0.37). The SUVs from both the liver and psoas muscle were not significantly different between the renal failure patients and the normal controls with p values >0.05. In addition, dialysis and gender also had no effect on SUVs.

Conclusion: Our data suggest that renal failure patients do not require an adjustment in protocol and the standard protocol times should remain.

Keywords: PET/CT, renal failure, ESRD, FDG, PET

OPEN ACCESS

Edited by:
Georgios S. Limouris, National and Kapodistrian University of Athens, Greece

Reviewed by:
Cigdem Soydal, Ankara University, Turkey
Elgin Ozkan, Ankara University Medical School, Turkey

****Correspondence:***
Razi Muzaffar
rmuzaffa@slu.edu

Specialty section:
This article was submitted to Cancer Imaging and Diagnosis, a section of the journal Frontiers in Oncology

Received: *15 February 2017*
Accepted: *30 June 2017*
Published: *21 July 2017*

Citation:
Kode V, Karsch H, Osman MM and Muzaffar R (2017) Impact of Renal Failure on F18-FDG PET/CT Scans. Front. Oncol. 7:155. doi: 10.3389/fonc.2017.00155

INTRODUCTION

According to the Center for Disease Control, the ninth leading cause of death in the United States is kidney disease with more than 47,000 deaths each year (1). Kidney disease is a prevalent and growing problem in the United States with over 26 million American adults afflicted (2). The two leading causes of kidney disease are high blood pressure and diabetes, both of which are rising (3). In addition to kidney disease, many of these patients have various other co-morbidities such as cancer. Consequently, there is a large overlap in these patient populations. In 2015, an estimated 1.7 million FDG PET/CT scans were performed while over 1.6 million cancer cases were newly diagnosed (4, 5). Therefore, it is important to evaluate the effects of renal failure on the biodistribution of FDG in FDG PET/CT scans.

Renal failure is defined as an 85–90% loss of kidney function with a glomerular filtration rate less than 15 ml/min/1.73m^2. Treatments for renal failure include kidney transplants, hemodialysis, and peritoneal dialysis (6). It is hypothesized that patients with renal failure may require a greater uptake time during an FDG PET/CT exam than patients with normal kidney function due to the impaired distribution and clearance of FDG. Other nuclear medicine studies such as bone scanning have addressed the altered biodistribution caused by renal failure and recommend additional delayed imaging to allow for an improved target to background ratio (7). However, neither the US nor the European guidelines addresses the impact of kidney disease on PET/CT scanning and whether there should be an adjustment to the protocol (8, 9). The standard uptake time for most malignancies is 60 min after the injection of FDG (10). While this is standard for a patient with normal kidney function, it is believed that a patient with renal failure may need a longer uptake time to improve the target to background ratio as in bone scanning.

Currently, information regarding FDG clearance time in patients with renal failure is limited. However, it has been hypothesized that a patient with renal failure might need a greater uptake time to improve diagnostic accuracy (11). Currently, the only exceptions to the 60-min uptake time are breast, hepatocellular, prostate, and pancreatic cancers, which require a 90 min uptake. However, a study has been performed on patients with high creatinine and found that the FDG accumulated in the blood of these patients (12).

In this study, we hypothesized higher standard uptake values (SUVs) in the internal reference points in patients with renal failure compared to the age and gender matched controls which could imply a need for a change in protocol.

MATERIALS AND METHODS

Patient Selection

Our Institutional Review Board approved this single institution, retrospective study, and the requirement to obtain informed consent was waived. We retrospectively reviewed 1,095 [18F] fluoro-D-glucose PET/CT scans of known cancer patients. The majority of patients were scanned from the vertex of the skull to the toes, as it is the standard of care in our institution. A log was kept for patients with clinically diagnosed renal failure. Exclusion criteria included patients with renal transplant, patients with primary liver or metastatic cancer in the liver, patients who did not have blood urea nitrogen or creatinine levels within 1 month of the scan and patients who were given a 90 min uptake time instead of the standard 60 min uptake. Thirty patients were selected with 12 of these patients on dialysis. However, this was not considered as a parameter for exclusion.

In order to minimize variance between a control group and the renal failure patients, we selected 30 controls with normal kidney function that matched each renal failure patient in BMI, age, and gender. In addition, BUN and creatinine levels were measured within 1 month of the scan. The BUN levels for the control group fell within the acceptable 7–26 mL/dL limit and the creatinine levels fell within the acceptable 0.6–1.2 mL/dL limit.

PET/CT Scan

FDG PET/CT scans were acquired using PET/CT scanner (Gemini TF; Philips Medical Systems) with an axial co-scan range of 193 cm. Per institutional protocol, all patients were instructed to fast at least 4 h prior to receiving the radiopharmaceutical injection. Blood glucose level was <200 mg/dL in all patients. On the day of the exam, intravenous injection of 5.18 MBq/kg (0.14 mCi/kg) of FDG was administrated. Patients sat in a quiet room without talking for 60 min during the uptake phase prior to imaging.

CT Scanning

The CT component of the PET/CT scanner has 64 multidetector helical CT with a gantry port of 70 cm. The parameters of CT detectors were set as follow for 20–21 bed acquisitions: 120–140 kV and 33–100 mAs (based on body mass index), 0.5 s per CT rotation, pitch of 0.9 and 512 × 512 matrix data were used for image fusion and the generation of the CT transmission map. The CT images were obtained without oral or IV contrast administration according to the standard PET/CT protocol at our institution.

PET Scanning and Image Processing

The PET component of the PET/CT scanner is composed of lutetium-yttrium oxyorthosilicate-based crystal. Emission scans were acquired at 1–2 min per bed position. The FOV was from the top-of-head to the bottom of feet in the vast majority of patients. The three-dimensional (3D) whole-body (WB) acquisition parameters were 128 × 128 matrix and 18 cm FOV with a 50% overlap. Processing used the 3D Row Action Maximum Likelihood Algorithm method. Total scan time per patient was approximately 20–45 min.

Data Analysis

PET/CT images were retrospectively evaluated on the Gemini TF extended brilliance workstation by board certified nuclear medicine physicians. Quantitative analysis of the data was done using SUV, standardized maximum uptake values. A 30 mm circular region of interest was used to record the liver SUV (LSUV) from the right hepatic lobe and psoas SUV (pSUV) from the left psoas muscle.

The median SUVs for both the control group and the renal failure group were compared using a Mann–Whitney *U* test. In addition, Mann–Whitney *U* test comparison was also done for the dialysis and non-dialysis patients using the same methodology. Statistics were completed using IBM SPSS Statistics, version 23. Statistical significance was set at $p < 0.05$.

RESULTS

The participant characteristics are presented in **Table 1**. For the 30 renal failure patients, the median LSUV 2.90 (min–max = 1.60–3.90) and PSUV 1.30 (min–max = 1.10–2.50) while the controls had median LSUV was 2.60 (min–max = 1.80–3.90) and PSUV was 1.35 (min–max = 0.90–2.80). The median SUVs from both the liver ($p = 0.62$) and psoas muscle ($p = 0.57$) were not significantly different between the renal failure patients and

TABLE 1 | Patient characteristics.

	Overall ($n = 60$)	Renal failure ($n = 30$)	Matched controls ($n = 30$)	p-Value
Age, mean (SD)	68.93 (12.63)	68.17 (12.66)	69.14 (12.81)	0.90
Gender, *n* (%)				1.00
Male	42 (70.0)	21 (70.0)	21 (70.0)	
Female	18 (30.0)	9 (30.0)	9 (30.0)	
BMI, mean (SD)	26.66 (5.86)	26.82 (5.55)	26.50 (6.24)	0.84

TABLE 2 | Median (min–max) liver and psoas muscle standard uptake values (SUVs) for renal failure and control patients.

	Renal failure ($n = 30$)	Matched controls ($n = 30$)	p-Value
Liver SUVmax	2.90 (1.60–3.90)	2.60 (1.80–3.90)	0.62
Psoas muscle SUVmax	1.30 (1.10–2.50)	1.35 (0.90–2.80)	0.57

TABLE 3 | Median (min–max) liver and psoas muscle standard uptake values (SUVs) for renal failure patients on dialysis and control patients.

	Dialysis ($n = 12$)	Non-dialysis ($n = 18$)	p-Value
Liver SUVmax	2.95 (2.00–3.80)	2.75 (1.60–3.90)	0.20
Psoas muscle SUVmax	1.30 (1.10–3.50)	1.30 (1.10–2.50)	0.54

the normal controls (**Table 2**). In addition, the dialysis patients demonstrated median LSUV was 2.95 (min–max = 2.00–3.80) and mean PSUV was 1.30 (min–max = 1.01–1.90) and the non-dialysis patients had LSUV 2.75 (min–max = 1.60–3.90) and PSUV 1.30 (min–max = 1.10–2.50), differences between them were not significant (**Table 3**). **Figure 1** illustrates the FDG distribution in a typical renal failure patient and control. **Figure 2** demonstrates the circular region of interest on the liver and left psoas muscle.

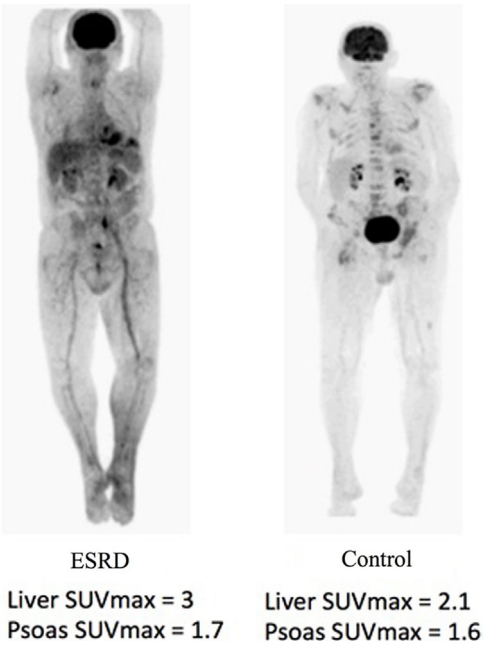

FIGURE 1 | In a typical patient, the PET/CT will show an accumulation of the F18-FDG marker in areas that consume the most glucose, as well as the renal system in the body. As a result, areas of accumulation appear in the brain, kidneys, and bladder. The brain consumes much of the glucose and the kidneys filter the marker to the bladder. In the patient with renal failure, due to the slower filtration rate of blood, the areas of uptake seem to be increased within the soft tissue.

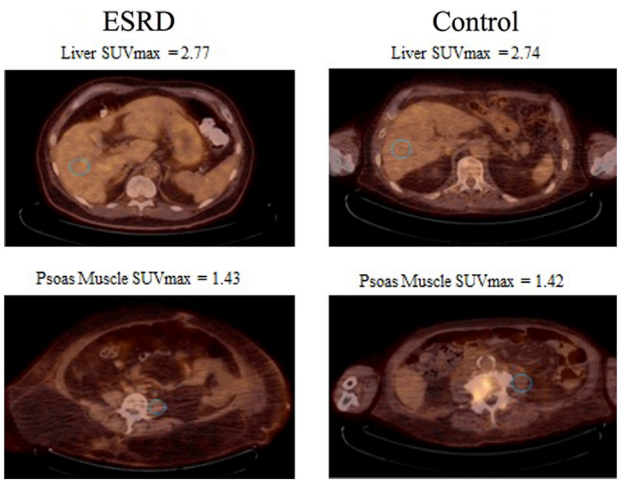

FIGURE 2 | 30 mm circular regions of interest (blue) were placed. The first in the right hepatic lobe and second in the left psoas muscle. In addition, the figure shows the mean standard uptake values (SUVs) between the controls and the renal failure patients.

DISCUSSION

The basics of pharmacokinetics state that drugs which are cleared primarily by the kidneys will have altered biodistribution and will require dose adjustment with compromised renal function (13). It has been established that renal clearance is integral for FDG metabolism and with the increased rates of renal failure in America, it is essential the effects of renal failure on FDG uptake are studied. However, there is limited information in the US and European guidelines as well as the literature to assess impaired renal function on FDG PET/CT scans. We hypothesized that patients with renal failure would have slower clearance of FDG and would require a longer time for the tracer to be metabolized. Consequently, patients with renal failure and in need of an FDG PET/CT scan could require an altered uptake time that may be different from the uptake times of patients without renal failure.

In this study, we compared the SUVs of internal reference points of patients with renal failure to age, gender, and BMI-matched controls. We found the SUVs for these patients are not statistically different from the non-renal failure patients. The data to support this come from the p-value for renal failure patients and the control group for both liver and psoas muscle were >0.05. In addition, we also compared renal failure patients on dialysis to normal controls who were not on dialysis and they too had no

significant difference in their SUVs. This was also indicated by a p-value >0.05. Therefore, we can conclude that the uptake time in patients with renal failure does not need to change to compensate for any altered biodistribution.

Our study is not without limitations. The retrospective nature of the study is a potential limitation. Also, imaging at different time intervals could give further verification if an increased uptake time would be statistically significant. A study of this nature was performed by Akers et al. (14) who investigated the effects of various degrees of compromised renal function on FDG uptake and clearance at multiple time points in normal tissues. They too concluded that compromised renal function did not affect clearance of background activity. However, some limitations of their study were their lack of controls, which were present in our study. Nevertheless, they also concluded that there is no need to alter standard uptake times for patients with renal failure.

The sample size of our study was relatively small with only 30 renal failure patients. Some models have shown an association between the severity of the renal failure and the inaccuracy of the SUVs (15). A larger sample size would allow for various stages and severities of renal failure. The severity could be an important factor due to the urine excretion rate. Since urine production has such a drastic impact on the amount of dosage excreted, it can be associated with the rates of delayed urine production between severe and mild renal failure. Lastly, there was no standardization for hydration status in our study before the PET/CT scanning.

With the limited information on the topic of renal failure affecting the uptake time for FDG, it is important that further studies are done to fully comprehend any affects that it may have on PET/CT scans. As the rates of renal failure increase and the increased utility of PET/CT, it is imperative that any factor affecting image quality be addressed to avoid inaccurate interpretations.

CONCLUSION

Renal disease has not been found to have a significant impact on the FDG biodistribution in FDG PET/CT studies. Therefore, patients with renal failure do not require an adjustment to the protocol.

AUTHOR CONTRIBUTIONS

VK is the first author and wrote the major portion of the manuscript. HK performed the data collection and helped writing the manuscript as well as capturing figures. MO assisted in editing and writing the manuscript. RM assisted in writing, editing, and optimizing figures for the manuscript.

REFERENCES

1. Center for Disease Control. *National Vital Statistics Reports* (Vol. 64), Issue No. 2. Available from: http://www.cdc.gov/nchs/data/nvsr/nvsr64/nvsr64_02.pdf
2. Coresh J, Selvin E, Stevens LA, Manzi J, Kusek JW, Eggers P, et al. Prevalence of chronic kidney disease in the United States. *JAMA* (2007) 298:2038–47. doi:10.1001/jama.298.17.2038
3. USRDS. *United States Renal Data System. 2015 USRDS Annual Report Volume2: ESRD in the United States* (2015). Available from: https://www.usrds.org/2015/download/vol2_USRDS_ESRD_15.pdf
4. Siegel R, Miller KD, Ahmedin J. Cancer statistics, 2015. *CA Cancer J Clin* (2015) 65(1):5–29. doi:10.3322/caac.21254
5. IMV PET Products. *2015 PET Imaging Market Summary Report*. Des Planes, IL: IMV (2015).
6. National Kidney Foundation. *What is Kidney Failure?* New York, NY: Natl kidney foundation (2016).
7. Donohoe KJ, Brown ML, Collier BD. Society of nuclear medicine procedure guideline for bone scintigrapy. Society of nuclear medicine procedure guidelines manual. *Bone Scintigr* (2003) 205:209.
8. Delbeke D, Coleman RE, Guiberteau MJ, Brown ML, Royal HD, Siegel BA, et al. Procedure guideline for tumor imaging with 18F-FDG PET/CT 1.0. *J Nucl Med* (2006) 47(5):885–95.
9. Boellaard R, O'Doherty MJ, Weber WA, Mottaghy FM, Lonsdale MN, Stroobants SG, et al. FDG PET and PET/CT: EANM procedure guidelines for tumour PET imaging: version 1.0. *Eur J Nucl Med Mol Imaging* (2010) 37(1):181–200. doi:10.1007/s00259-009-1297-4
10. Kinahan PE, Fletcher JW. PET/CT standardized uptake values (SUVs) in clinical practice and assessing response to therapy. *Semin Ultrasound CT MR* (2010) 31(6):496–505. doi:10.1053/j.sult.2010.10.001
11. Cheng G, Torigian DA, Zhuang H, Alavi A. When should we recommend use of dual time-point imaging techniques in FDG PET? *Eur J Nucl Med Mol Imaging* (2013) 40:779–87. doi:10.1007/s00259-013-2343-9
12. Minamimoto R, Takahashi N, Inoue T. FDG-PET of patients with suspected renal failure: standardized uptake values in normal tissues. *Ann Nucl Med* (2007) 21(4):217–22. doi:10.1007/s12149-007-0012-4
13. Dreisbach AW, Lertora JJ. The effect of chronic renal failure on drug metabolism and transport. *Expert Opin Drug Metab Toxicol* (2008) 4(8):1065–74. doi:10.1517/17425255.4.8.1065
14. Akers SR, Werner TJ, Rubello D, Alavi A, Cheng G. 18F-FDG uptake and clearance in patients with compromised renal function. *Nucl Med Commun* (2016) 37(8):825–32. doi:10.1097/MNM.0000000000000513
15. Yasuda S, Ide M, Takagi S, Shohtsu A. Elevated F-18 FDG uptake in skeletal muscle. *Clin Nucl Med* (1998) 23:111. doi:10.1097/00003072-199802000-00014

Conflict of Interest Statement: The authors declare that the research was conducted in the absence of any commercial or financial relationships that could be construed as a potential conflict of interest.

frontiers in Oncology

ORIGINAL RESEARCH
published: 17 July 2019
doi: 10.3389/fonc.2019.00663

Urine Metabolomics for Renal Cell Carcinoma (RCC) Prediction: Tryptophan Metabolism as an Important Pathway in RCC

Xiaoyan Liu[1†], Mingxin Zhang[2,3†], Xiang Liu[1†], Haidan Sun[1], Zhengguang Guo[1], Xiaoyue Tang[1], Zhan Wang[2], Jing Li[1], Hanzhong Li[2], Wei Sun[1] and Yushi Zhang[2*]*

[1] School of Basic Medicine, Institute of Basic Medical Sciences, Peking Union Medical College, Chinese Academy of Medical Sciences, Beijing, China, [2] Department of Urology, Peking Union Medical College Hospital, Chinese Academy of Medical Science, Beijing, China, [3] Department of Urology, The Affiliated Hospital of Qingdao University, Qingdao, China

OPEN ACCESS

Edited by:
Marie-France Penet,
Johns Hopkins University,
United States

Reviewed by:
Paloma V. Ballesteros,
Universidad Nacional de Educación a Distancia, Spain
Tone Frost Bathen,
Norwegian University of Science and Technology, Norway

***Correspondence:**
Wei Sun
sunwei1018@sina.com
Yushi Zhang
zhangyushi2014@126.com

[†]These authors have contributed equally to this work

Specialty section:
This article was submitted to Cancer Imaging and Image-directed Interventions, a section of the journal Frontiers in Oncology

Received: 12 October 2018
Accepted: 05 July 2019
Published: 17 July 2019

Citation:
Liu X, Zhang M, Liu X, Sun H, Guo Z, Tang X, Wang Z, Li J, Li H, Sun W and Zhang Y (2019) Urine Metabolomics for Renal Cell Carcinoma (RCC) Prediction: Tryptophan Metabolism as an Important Pathway in RCC. Front. Oncol. 9:663. doi: 10.3389/fonc.2019.00663

Renal cell carcinoma (RCC) is the second most lethal urinary cancer. RCC is frequently asymptomatic and it is already metastatic at diagnosis. There is an urgent necessity for RCC specific biomarkers selection for diagnostic and prognostic purposes. In present study, we applied liquid chromatography—mass spectrometry (LC-MS) based metabolomics to analyze urine samples of 100 RCC, 34 benign kidney tumors and 129 healthy controls. Differential metabolites were analyzed to investigate if urine metabolites could differentiate RCC from non-RCC. A panel consisting of 9 metabolites showed the best predictive ability for RCC from the health controls with an area under the curve (AUC) values of 0.905 for the training dataset and 0.885 for the validation dataset. Separation was observed between the RCC and benign samples with an AUC of 0.816. RCC clinical stages (T1 and T2 vs. T3 and T4) could be separated using a panel of urine metabolites with an AUC of 0.813. One metabolite, N-formylkynurenine, was discovered to have potential value for RCC diagnosis from non-RCC subjects with an AUC of 0.808. Pathway enrichment analysis indicated that tryptophan metabolism was an important pathway in RCC. Our data concluded that urine metabolomics could be used for RCC diagnosis and would provide candidates for further targeted metabolomics analysis of RCC.

Keywords: renal cell carcinoma, metabolomics, benign tumors, biomarker, tryptophan metabolism

INTRODUCTION

Renal cell carcinoma (RCC) is the second most lethal urinary cancer and accounts for 5% of all adult malignancies (1). Clinically, dynamic contrast-enhanced computed tomography (CT) provides an accurate diagnosis of RCC in most cases. However, some small carcinomas are difficult to confirm. Furthermore, differentiating benign kidney tumors from RCC still remains a clinical challenge, even when images are re-examined by experienced radiologists. Final confirmation of RCC requires pathological examination of puncture or surgical resection. Approximately 20–30% of small renal masses that are surgically removed are found to be benign (2). Thus, the development of new, accurate, non-invasive diagnostic methods will have an important impact in RCC clinical management in its earliest stage and could reduce unnecessary treatment for benign tumors and increase the chance of nephron-sparing treatment.

RCC as a metabolic disease is well-suited to metabolomic analysis. Understanding and measuring metabolic status variations accompanying disease progression would be a useful strategy for potential new diagnostic biomarker discovery. Metabolomic analysis of urine, which is obviously closely related to RCC status, is an ideal non-invasive means to explore RCC (3). In 2011, Kim et al. performed a metabolomic analysis of urine from 29 RCC patients using LC-MS and GC-MS and found that quinolinate, 4-hydroxybenzoate, and gentisate are differentially expressed (4). In 2012, Ganti et al. utilized metabolomics to evaluate compounds appearing in the urine of kidney cancer patients (29 subjects) and control patients (33 subjects). Several acylcarnitines were discovered as a function of both cancer status and kidney cancer grade, with most of the acylcarnitine levels showing an increase in the urine of cancer patients (5). In 2016, Monteiro et al. analyzed the urine metabolome of RCC patients ($n = 42$) and controls ($n = 49$) using nuclear magnetic resonance (NMR) spectroscopy. A 32-metabolite/resonance signature, including 2-KG, N-methyl-2-pyridone-5-carboxamide (2-Py), bile acids, galactose, hypoxanthine, isoleucine, pyruvate, and succinate, could successfully distinguish RCC patients from controls (6).

The research described above applied urine metabolomics for RCC diagnosis from healthy controls based on a small sample size, and more samples are necessary to discover and validate RCC biomarkers. In addition, to our knowledge, there are still no studies that present urine metabolome differences between RCC and benign tumors. In the present work, we applied LC-MS-based metabolomics to analyse 263 urine samples from Chinese subjects, including 100 RCCs, 34 benign controls and 129 healthy controls, to investigate whether metabolic profiles could differentiate RCC from non-RCC samples (including healthy and benign controls). Furthermore, a study was also performed to distinguish RCC stages (T1 and T2 vs. T3 and T4) using urine metabolomics. This study will provide new insights into the diagnosis of RCC and possible clues for a metabolic mechanism.

MATERIALS AND METHODS

Sample Collection

First morning urine (midstream) samples were collected from ∼07:00 to 09:00 a.m. on an empty stomach from two cohorts: the training set includes 67 RCC patients, 34 benign tumor patients and 96 healthy human adults, while the test set includes 33 RCC patients, 7 benign tumor patients and 33 healthy controls. All cases were from Beijing Union Hospital. These groups did not include subjects suffering from any acute conditions or taking any medications in the latest 3 months. The glomerular filtration rate (GFR) and urine protein content of RCC patients were within normal ranges. The healthy control subjects were enrolled with matched genders and ages with the RCC patients to reduce interference from physiological factors. Both informed verbal and written consent were obtained from the subjects before participating in this study. RCC was diagnosed by a pathological investigation and graded according to the Union for International Cancer Control (UICC) tumor node-metastasis (TNM) staging system. RCC without metastases (T1–2, limited to the kidney) was categorized as early stage and RCC with metastases (T3–4) as late stage. The detailed demographics are shown in **Table 1** and **Table S1**.

Sample Preparation

Urine sample preparation was performed based on previous methods (7). In brief, acetonitrile (200 μl) was added to each urine sample (200 μl), then the mixture was vortexed for 30 s and centrifuged at 14,000 × g for 10 min. The supernatant was dried under vacuum and then reconstituted with 200 μl of 2% acetonitrile. Urinary metabolites were further separated from larger molecules using 10 kDa molecular weight cut-off ultracentrifugation filters (Millipore Amicon Ultra, MA) before being transferred to the autosamplers. The quality control (QC) sample was a pooled urine sample prepared by mixing aliquots of fifty representative samples across different groups to be analyzed and was therefore globally representative of the whole sample set. The QC samples were injected every 10 samples throughout the analytical run to provide a set of data from which method stability and repeatability can be assessed.

LC-MS Analysis

Ultra-performance LC-MS analyses of samples were conducted using a Waters ACQUITY H-class LC system coupled with an LTQ-Orbitrap Velos pro mass spectrometer (Thermo Fisher Scientific, MA. USA). Detailed parameters are listed in the **Supplementary Methods**.

TABLE 1 | Subjects information.

	Cohort 1 (training set)		
	RCC (F/M)	**Healthy control (F/M)**	**Benign (F/M)**
# of subjects	67 (19/48)	96 (35/61)	34 (20/14)
Age	53.5 ± 14.7	54.8 ± 11.5	46.4 ± 11.5
BMI	24.7 ± 3.7	22.7 ± 1.8	24.8 ± 3.6
eGFR (ml/min/1.7312)	98.2 ± 13.8	102.9 ± 10.5	98.1 ± 12.3
	Cohort 2 (validation set)		
# of subjects	33 (4/29)	33 (6/27)	7 (2/5)
Age	50.0 ± 14.3	51.5 ± 16.4	49.1 ± 8.7
BMI	25.6 ± 3.2	22.8 ± 2.4	24.5 ± 1.8
eGFR (ml/min/1.7312)	102.4 ± 10.3	105.6 ± 10.4	99.8 ± 11.7
	RCC Staging (Combination of cohort 1 and 2)		
Early (T1 and T2)	86 (18/68)		
Late (T3 and T4)	14 (5/9)		

Abbreviations: AUC, area under the curve; BMI, body mass index; CT, computed tomography; IDO, indoleamine-2,3-dioxygenase; KP, kynurenine pathway; LC-MS, liquid chromatography—mass spectrometry; NMR, nuclear magnetic resonance; OPLS-DA, orthogonal partial least squares discriminant analysis; PCA, principal component analysis; QC, quality control; RCC, renal cell carcinoma.

Statistical Data Analysis

Raw data files were processed by Progenesis QI (Version 2.0, Nonlinear Dynamics) software. The detailed processing parameters are provided in the **Supplementary Methods** file. The raw data file exported from QI was further processed by MetaboAnalyst 3.0 (http://www.metaboanalyst.ca), including missing value estimation, log2 transformation and Pareto scaling. Variables missed in 50% or greater of all samples were removed from further statistical analysis. Pattern recognition analysis (principal component analysis, PCA; orthogonal partial least squares discriminant analysis, OPLS-DA) was performed based on a training set using SIMCA 14.0 (Umetrics, Sweden) software. One hundred permutation validations were performed to evaluate the fitting of the OPLS-DA model. Variable importance for the projection (VIP) values obtained from the OPLS-DA were used for differential metabolite selection. Non-parametric tests (Wilcoxon rank-sum test) were used to evaluate the significance of the variables. False discovery rate (FDR) correction was used to estimate the chance of false positives and correct for multiple hypothesis testing. Differential metabolites were selected from the training set according to the criteria: (1) VIP value above 1; and (2) adjusted p-value below 0.05. These metabolites were further validated in the validation set. Features showing significant differences in both training and validation sets were considered as disease-related. An ROC curve was constructed based on differential metabolites selected from the training set using logistic regression algorithm. For RCC vs. healthy controls and RCC vs. non-RCCs, an external validation set was used to validate the accuracy of the potential biomarker panels. However, for RCC vs. benign and RCC early stage vs. late stage, 10-fold cross-validation was performed in the training set. These model constructions and validation were carried out based on MetaboAnalyst 3.0 platforms.

Metabolite Annotation and Pathway Analysis

Metabolic pathways and predicted metabolites in the pathways were analyzed using the "Mummichog" algorithm based on the MetaboAnalyst 3.0 platform. The detailed parameters for the Mummichog analysis were provided in the **Supplementary Methods**. Metabolite annotation was further determined from the exact mass composition, from the goodness of isotopic fit for the predicted molecular formula and from MS/MS fragmentation comparing hits with databases (HMDB http://www.hmdb.ca/), thus qualifying for annotation at MSI level II using Progenesis QI. For endogenous metabolites lacking a chemical formula, the accurate molecular mass was given based on the calculated isotopic features and ion adducts. Detailed methods were listed in the **Supplementary Methods**.

RESULTS

The major objective of our study was to discover potential biomarkers to distinguish RCC not only from healthy controls but also from subjects with benign tumors. The experimental strategy is shown in **Figure 1**. Metabolite variation and pathway regulation associated with RCC were explored based on analysis of metabolic profile differences between RCC and healthy and benign controls. Potential biomarkers for RCC were further explored based on differential metabolites and were validated using 10-fold cross validation or external validation.

Quality Control

This cohort of samples was analyzed randomly, which took almost a week. Tight clustering of QC samples (**Figure S1**) demonstrated the quality of the QC data and essential repeatability and stability throughout the analytical run.

Distinguishing RCC From Healthy Controls by Urine Metabolomics

LC-MS-based urine samples from RCC and controls yielded 2,500 spectral features after QC filtering. Apparent differences between the metabolic profiles of RCC and the healthy controls were observed from the PCA score plot (**Figure 2A**). Furthermore, the OPLS-DA model achieved better separation (**Figure 2B**). Permutation tests were performed to confirm the stability and robustness of the supervised models presented in this study (**Figure S2**). In total, 455 differential metabolites were assigned, contributing to group separation, among which, 145 metabolites were also significantly changed in the validation set. These metabolites were further submitted for pathway analysis and prediction model construction.

Pathway enrichment analysis using the Mummichog algorithm showed significant enrichment ($p < 0.05$) of several pathways in the RCC group compared with those in healthy controls, including galactose metabolism, linoleate metabolism, leukotriene metabolism, tryptophan metabolism, etc. (**Figure 2C**; **Table S2**). The predicted activity network is shown in **Figure S3**. Mutual regulation of these disturbed pathways contributes to metabolic disorder in RCC.

Annotation of the top discriminatory features followed by MS/MS evaluation showed 65 metabolites were significantly differentially detected between RCC and healthy control samples (**Table S3**). Metabolites with higher levels in RCC included steroids such as androstenedione, alpha-CEHC, and 19-nor-5-androstenediol, dipeptides such as aspartyl-phenylalanine and glutamyl-threonine, bile acid metabolites such as 7-alpha-hydroxy-3-oxochol-4-en-24-oic acid and lithocholyltaurine, and exogenous sulfate metabolites. On the other hand, metabolites with lower levels included steroid glucuronidation metabolites such as tetrahydroaldosterone-3-glucuronide and cortolone-3-glucuronide, indicating a potential roles for glucuronidation in RCC development. Moreover, a caffeine metabolite (methylxanthine) was found to be decreased in RCC patients, which pinpoints aberrations in xenobiotic metabolism. A free fatty acid (11-dodecenoic acid) showed higher levels in RCC, and the oxidation intermediate 2,6-dimethylheptanoyl carnitine showed lower levels, indicating a high energy requirement in RCC.

The diagnostic accuracy of the identified differential metabolites for RCC vs. healthy controls was further evaluated. A total of 45 metabolites had a potentially useful diagnostic value, with an AUC above 0.7, and 10 metabolites had a good diagnostic

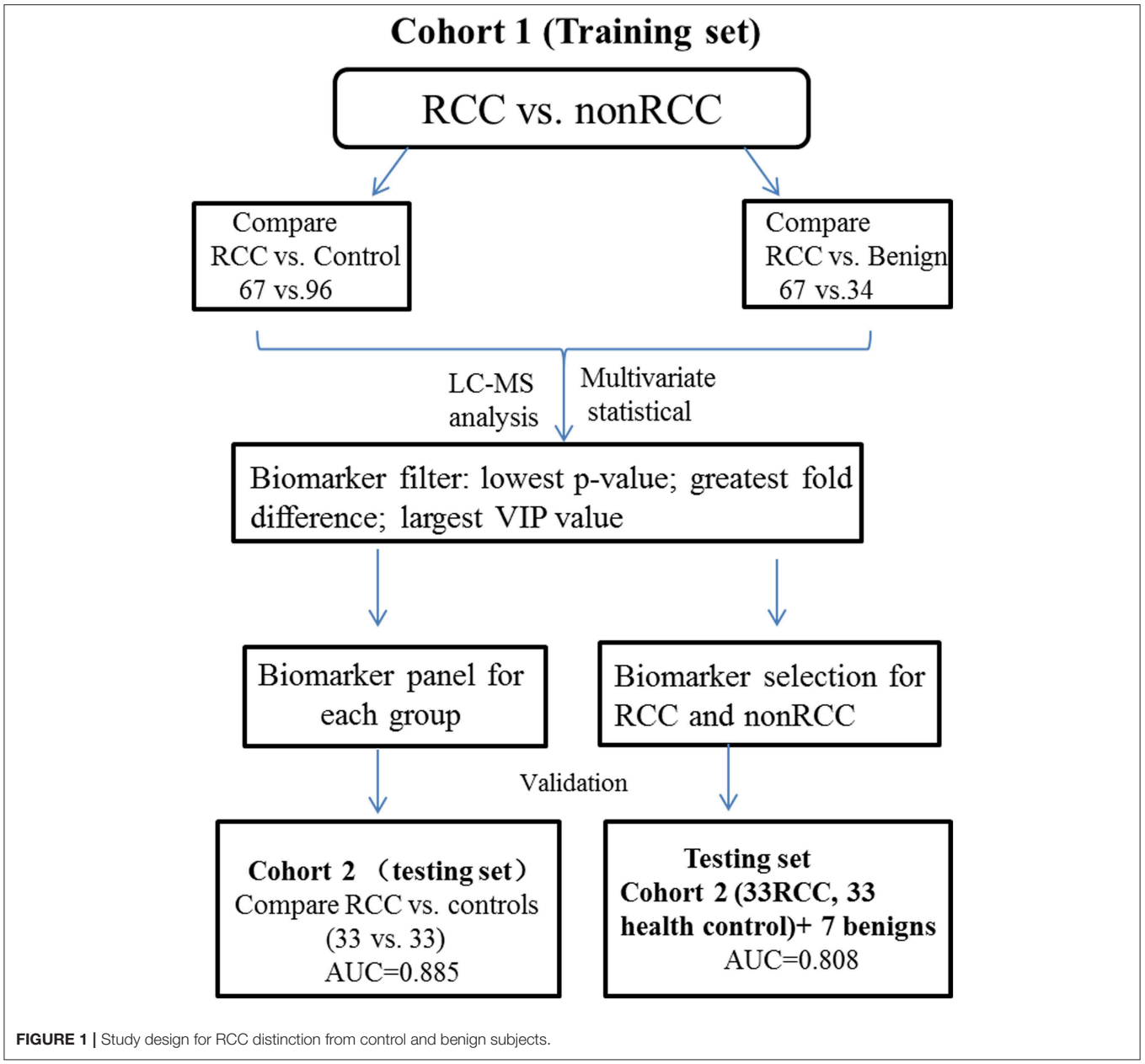

FIGURE 1 | Study design for RCC distinction from control and benign subjects.

value, with an AUC above 0.8 (**Table S4**). A multivariate ROC curve-based exploratory analysis was performed to achieve a better predictive model (http://www.metaboanalyst.ca/faces/Secure/upload/RocUploadView.xhtml) using a logistic regression algorithm. As a result, a metabolite panel consisting of 9 metabolites as shown in **Table S5** showed the best predictive ability. The 10-fold cross validation for the training set achieved an AUC of 0.905 (**Figure 2D**). The sensitivity and specificity were 0.871 and 0.902, respectively. Further external validation using an independent sample set was performed and achieved good performance with values for AUC, sensitivity and specificity of 0.885, 0.851 and 0.875, respectively, correctly predicting 26 out of 33 RCC patients in the validation set (**Figure 2E**).

Distinguishing RCC From Benign Kidney Tumors by Urine Metabolomics

Distinguishing RCC from benign kidney tumors was further performed to explore metabolic differences between the two groups. PCA analysis showed slight discrimination of RCC from benign tumors (**Figure S4**). Furthermore, an OPLS-DA model achieved significant separation ($p < 0.05$) (**Figure 3A**), with 694 features contributing to group separation (VIP value > 1). However, only 39 features showed a significant p-value below 0.05, indicating larger inter-individual variations. Differential features were submitted to perform pathway enrichment analysis using the Mummichog algorithm. Several pathways, including folate metabolism, tryptophan metabolism

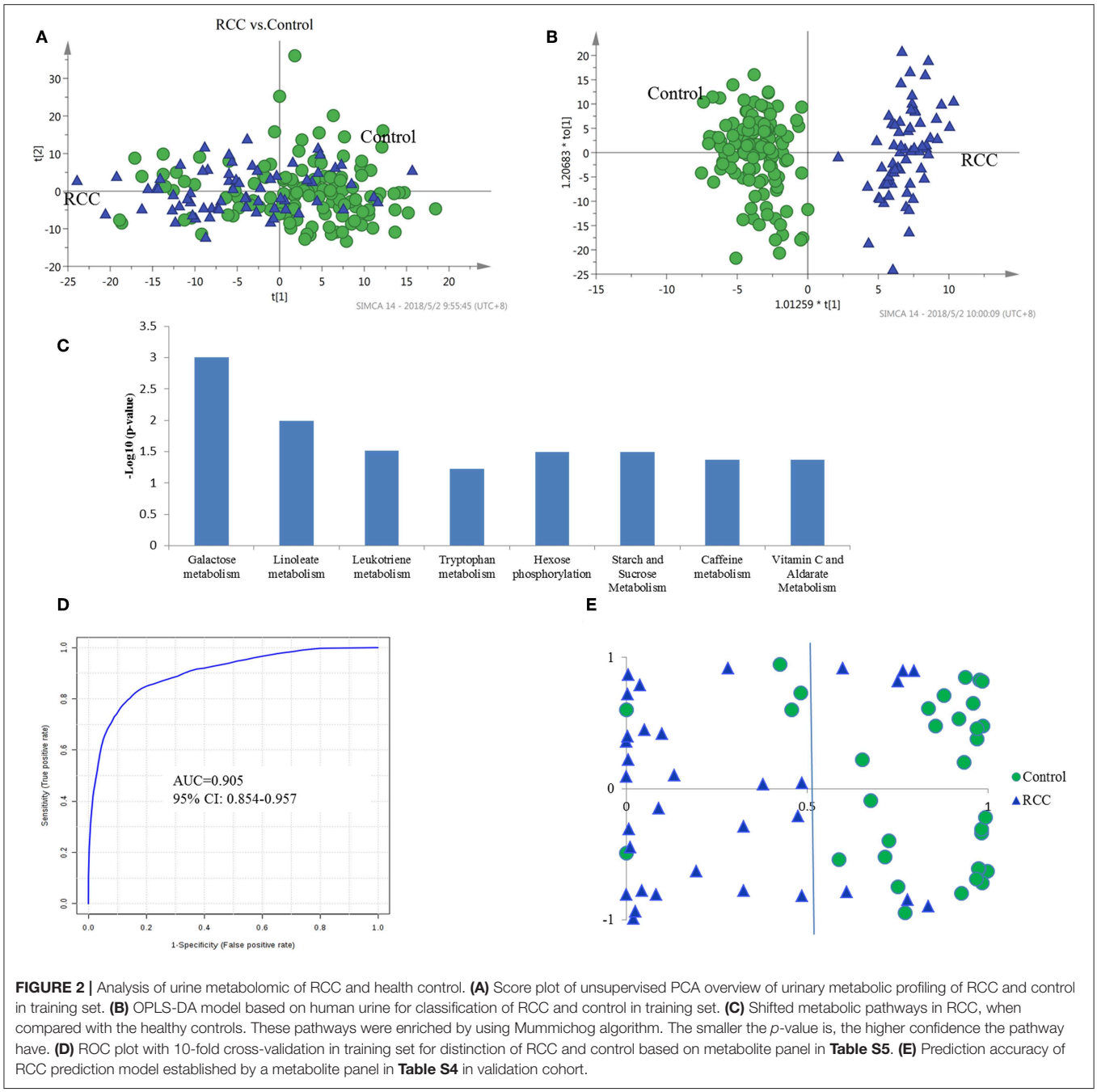

FIGURE 2 | Analysis of urine metabolomic of RCC and health control. **(A)** Score plot of unsupervised PCA overview of urinary metabolic profiling of RCC and control in training set. **(B)** OPLS-DA model based on human urine for classification of RCC and control in training set. **(C)** Shifted metabolic pathways in RCC, when compared with the healthy controls. These pathways were enriched by using Mummichog algorithm. The smaller the *p*-value is, the higher confidence the pathway have. **(D)** ROC plot with 10-fold cross-validation in training set for distinction of RCC and control based on metabolite panel in **Table S5**. **(E)** Prediction accuracy of RCC prediction model established by a metabolite panel in **Table S4** in validation cohort.

and biopterin metabolism, were significantly enriched in RCC compared to the benign group (**Figure 3B**; **Table S6**).

Further annotation of the top discriminatory features determined by MS/MS evaluation identified 22 significantly differentially detected metabolites (**Table S7**). ROC analysis showed that all 22 metabolites have a good diagnostic value for RCC and benign controls with AUC values above 0.70 (**Table S8**). Using a logistic regression algorithm, a metabolite panel consisting of L-3-hydroxykynurenine, 1,7-dimethylguanosine, and tetrahydroaldosterone-3-glucuronide was used to establish a robust model for distinguishing between RCC and benign samples. The AUC was 0.834 for the training dataset and 0.816 for 10-fold cross-validation (**Figure 3C**). The sensitivity and specificity were 0.741 and 0.794, respectively, for the training set and 0.746 and 0.800, respectively, for cross-validation.

N-formylkynurenine as a Potential Biomarker for the Differential Diagnosis of RCC vs. Non-RCC

According to the above analysis, urine metabolites could distinguish RCC from healthy and benign controls with

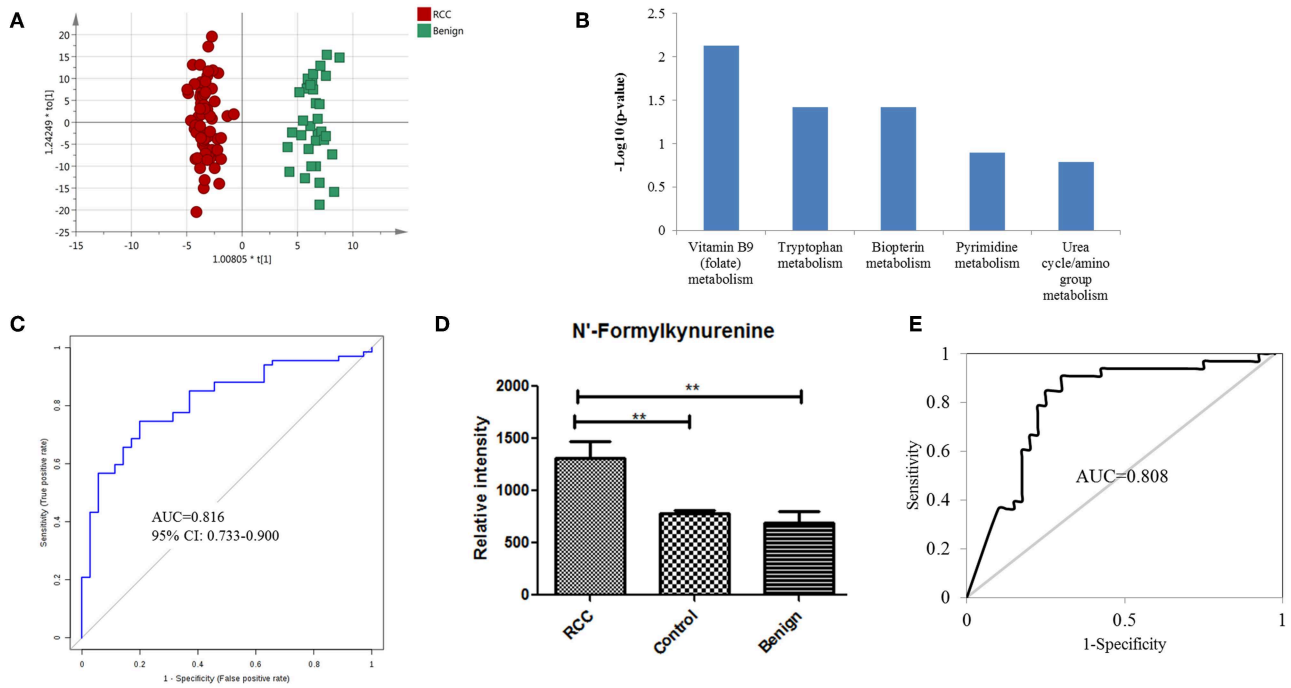

FIGURE 3 | Analysis of urine metabolomic variation between RCC and benign. **(A)** OPLS-DA model based on human urine for classification of RCC and benign in the training set. **(B)** Top five shifted metabolic pathways in RCC compared with benign group. **(C)** ROC plot with 10-fold cross-validation in the training set for distinction of RCC and benign based on metabolites panel of L-3-Hydroxykynurenine, 1,7-Dimethylguanosine, and Tetrahydroaldosterone-3-glucuronide. **(D)** Relative intensity of N-formylkynurenine in RCC, benign and control groups in the training set. **(E)** ROC plot of N-Formylkynurenine for distinction of RCC and non-RCC in the validation group.

high accuracy. Perhaps the common differential metabolites of the two comparisons could be used to diagnose RCC from both healthy and benign controls (non-RCCs). The present results found one common differential metabolite, N'-formylkynurenine, which could discriminate RCC not only from healthy controls but also from benign controls. The relative content of N-formylkynurenine in the RCC group and non-RCC group was plotted in **Figure 3D**, showing higher levels of N-formylkynurenine in the RCC group compared with the non-RCC group. The relative content of N-formylkynurenine showed a 1.67-fold increase compared to the healthy control group and showed a 2.07-fold increase compared to the benign control group. These results suggest that accumulation of N-formylkynurenine in RCC patients' urine may be used as a potential biomarker for RCC diagnosis.

As a potential biomarker for RCC diagnosis compared to non-RCC cases, we further validated the predictive ability of N-formylkynurenine using the validation group consisting of 33 RCC subjects, 33 healthy controls, and 7 benign controls. The AUC value of the ROC curve was 0.808 (**Figure 3E**). The sensitivity and specificity were 0.848 and 0.838, respectively. These results suggest that N-formylkynurenine could be significant as a potentially useful metabolite for RCC distinction from healthy controls and benign controls.

Distinguishing RCC Stages by Urine Metabolomics

Due to RCC sample size limitations, we combined RCC samples of the training set and the validation set. Overall, 84 patients were diagnosed as the pT1 stage, 2 as the pT2 stage, 10 as the pT3 stage, and 4 as the pT4 stage according to pathologic evaluation. T1 and T2 are designated as early stage RCC because the tumor lesion is inside the kidney. T3 and T4 are designated as late stage RCC because the tumor has spread to other organs. Herein, the samples from pT3 and pT4 were relatively few in number, and we performed a pilot comparison of metabolic profiling between early stage and late stage RCC. A PCA score plot showed overlap between early and late stages (**Figure S5A**). Furthermore, OPLS-DA showed improved separation with R2Y = 0.71 and Q2 = 0.33 (**Figure S5B**), with 156 features contributing to stage separation. A total of 24 differential metabolites were identified (**Table S9**), and 12 of them have potential diagnostic value with an AUC above 0.70 (**Table S10**). A panel consisting of thymidine, cholic acid glucuronide, alanyl-proline, isoleucyl-hydroxyproline, and myristic acid was used for predictive model construction using logistic regression. The AUC value was 0.881 for the testing dataset and 0.813 for the 10-fold cross-validation (**Figure S5C**). The sensitivity and specificity were 0.921 and 0.756, respectively, for the testing set and 0.857 and 0.721, respectively, for the cross-validation. These results indicate acceptable performance of RCC staging using urine metabolomics.

DISCUSSION

Our results suggest that the urine metabolome could differentiate RCC patients from healthy controls and from benign kidney tumor patients. Potential biomarkers for RCC and RCC stages were explored and discovered tentatively, which provide new insights into RCC diagnosis. This is the first attempt at applying urine metabolomics for differential diagnosis of RCC vs. benign kidney tumors.

Metabolite Regulation in RCC Compared With Healthy Controls

Androstenedione, 7-alpha-hydroxy-3-oxochol-4-en-24-oic acid and lithocholyltaurine are the most significantly differentially detected metabolites that have good prediction accuracy between RCC and healthy controls, likely playing important roles during RCC occurrence. Androstendione occurs naturally in the body and is a direct precursor to the hormone testosterone. The conversion of androstendione to testosterone via 17-beta-hydroxysteroid dehydrogenase occurs in the kidney (8). Androstendione levels could be affected by the kidney function status, showing inverse linear associations with renal function (9). Increased secretion levels of androstenedione could result from glomerular filtration function disorder in RCC patients. Lithocholyltaurine and 7-alpha-hydroxy-3-oxochol-4-en-24-oic acid are bile acid conjugation molecules. It has been reported that renal bile acid excretion is a cause of neoplastic lesions (10) and could cause partially reversible renal tubular damage (11). We also noted increases in some dipeptides that may be produced through protein degradation/reutilization processes, such as lysosomal degradation, phagocytosis, endocytosis, pinocytosis, and autophagy (12).

Metabolite Regulation in RCC Compared With That in Benign Controls

In the clinic, some small renal carcinomas are still difficult to distinguish from benign kidney tumors, and some benign tumors, such as angiomyolipoma, are easily misdiagnosed as malignant tumors. Early and accurate distinction of benign tumors from RCC could reduce the unnecessary treatment for benign tumors. Biopterin metabolism and tryptophan metabolism were found to be disturbed in RCC compared with benign tumors. Disorders of biopterin metabolism in RCC may be accompanied with impaired functioning of tyrosine and tryptophan hydroxylases and the resultant deficiency of tyrosine- and tryptophan-derived monoamine neurotransmitters (13), which is supported by the disturbed tryptophan metabolism suggested by our results. N-formylkynurenine, an intermediate in tryptophan catabolism, was found to be increased in RCC compared with that in benign controls. Accumulation of serum N-formylkynurenine has been reported in patients and experimental animals with renal diseases (14–17). Moreover, patients with chronic kidney disease are permanently exposed to uremic toxins from the kynurenine pathway, which could be mediated by activation of transcription factor aryl hydrocarbon receptor (AhR) (18). These previous results were consistent with

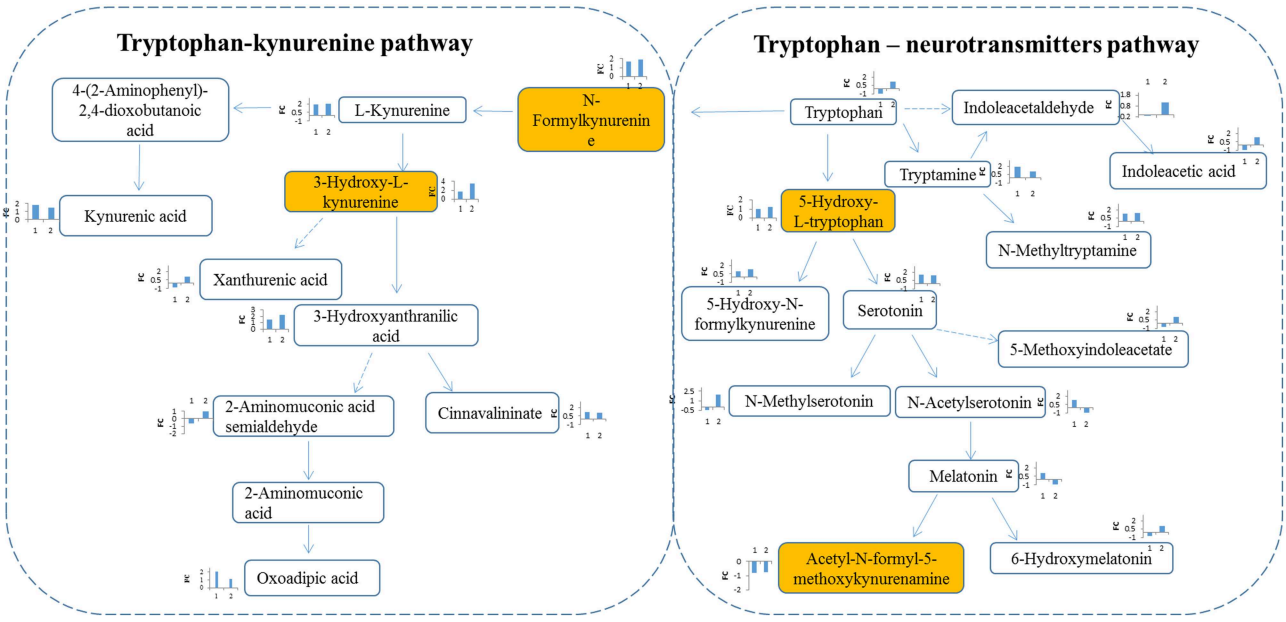

FIGURE 4 | Metabolites interaction in tryptophan metabolism. Tryptophan pathway was significantly changed in RCC. Tryptophan is metabolized through two pathways: tryptophan-kynurenine pathway and tryptophan—neurotransmitters pathway. Metabolites annotation with Mummichog and MS/MS validation are located in colored boxes; Metabolites annotation only with "Mummichog" algorithm are located in blank boxes. The bar figures around each metabolite represents the fold change of metabolite in RCC compared with health control (x-coordinate:1) and the benigns (x-coordinate: 2). Direction of bars represent up-regulated (above X-aixs) or down-regulated (below X-axis).

our results in the present work, which suggest a significant accumulation of N-formylkynurenine in RCC urine.

Distinguishing RCC From Non-RCC: Tryptophan Metabolism as a Target Pathway

Tryptophan-kynurenine pathway (KP) metabolites, N-formylkynurenine, kynurenine and 3-hydroxy-L-kynurenine were found to be disturbed in RCC (**Figure 4**), indicating a potential role of tryptophan metabolism during RCC development. Tryptophan-KP metabolism in cancer has increasingly been recognized as an important microenvironmental factor that suppresses antitumor immune responses (19–21). Depletion of tryptophan induces signaling events in T cells, leading to anergy, apoptosis, and active immunomodulation by accumulating tryptophan-KP metabolites (22). During RCC development, tryptophan-KP metabolism has been found to be highly represented in tissues, which is associated with immune suppression (23). Indoleamine-2,3-dioxygenase (IDO) can possibly catalyze an early step in tryptophan metabolism, regulating the conversion of tryptophan to immunosuppressive metabolites that could work to the tumor's advantage (24). The same has occurred in RCC patient serum and urine (3, 25), which is consistent with our results.

In humans, >95% of tryptophan is metabolized through the kynurenine pathway, and other tryptophan is converted into the key neurotransmitters serotonin and tryptamine (26). Herein, apart from tryptophan-KP metabolite variations, we also observed increase of tryptophan-neurotransmitter metabolites, such as 5-hydroxy-L-tryptophan, serotonin, and tryptamine, in RCC (**Figure 4**), indicating neuroendocrine involvement of tryptophan metabolism in human RCC (27). Neuroendocrine markers have been reported in RCC serum, including chromogranin (Cg) A and B, pancreastatin and serotonin (28). These results indicate the potential value of tryptophan metabolism for designing new targets of RCC.

CONCLUSIONS

In conclusion, we have applied urine metabolomic approach to dissect metabolic features of RCC not only compared with healthy controls but also compared with benign controls. These results showed markedly different metabolic profiles between RCC and healthy controls or benign controls, which suggests the feasibility of utilizing urine metabolites for early clinical diagnosis. Potential biomarkers for RCC were tentatively explored. The changes in tryptophan metabolism have profound implications for designing new targets for RCC. Moreover, N-formylkynurenine was discovered to have potential value for RCC distinction from healthy and benign controls. However, in our present study, the influence of diet on urine metabolomics might not be completely eliminated, though all subjects were from the same region. For future validation analysis, the influence of diet would be systematically analyzed and evaluated using a diet standardization design.

ETHICS STATEMENT

This study was approved by the Institutional Review Board of the Institute of Basic Medical Sciences, Chinese Academy of Medical Sciences. All human subjects provided informed consent before participating in this study.

AUTHOR CONTRIBUTIONS

XoL, MZ, XnL, WS, and YZ conceived and designed the study, helped to interpret the data, wrote the first draft of the manuscript, and contributed to the final version of the manuscript. MZ, HL, and ZW collected the urine samples. HS and XT helped to interpret the data, performed the statistical analysis, and contributed to the final version of the manuscript. ZG and JL helped the data analysis. WS is the guarantor of this work and, as such, had full access to all the data in the study and takes responsibility for the integrity of the data and the accuracy of the data analysis.

FUNDING

This work was supported by National Key Research and Development Program of China (No. 2016 YFC 1306300, 2018YFC0910202), National Natural Science Foundation of China (No. 30970650, 31200614, 31400669, 81371515, 81170665, 81560121), Beijing Natural Science Foundation (No. 7173264, 7172076), Beijing cooperative construction project (No. 110651103), Beijing Science Program for the Top Young (No. 2015000021223TD04), Beijing Normal University (No. 11100704), Peking Union Medical College Hospital (No. 2016-2.27), CAMS Innovation Fund for Medical Sciences (2017-I2M-1-009, 2018-I2M-1-001), and Biologic Medicine Information Center of China, National Scientific Data Sharing Platform for Population and Health.

ACKNOWLEDGMENTS

The authors thank all participants in this study.

SUPPLEMENTARY MATERIAL

The Supplementary Material for this article can be found online at: https://www.frontiersin.org/articles/10.3389/fonc.2019.00663/full#supplementary-material

REFERENCES

1. Linehan WM, Srinivasan R, Schmidt LS. The genetic basis of kidney cancer: a metabolic disease. *Nat Rev Urol.* (2010) 7:277–85. doi: 10.1038/nrurol.2010.47

2. Johnson DC, Vukina J, Smith AB, Meyer AM, Wheeler SB, Kuo TM, et al. Preoperatively misclassified, surgically removed benign renal masses: a systematic review of surgical series and United States population level burden estimate. *J Urol.* (2015) 193:30–5. doi: 10.1016/j.juro.2014.07.102

3. Ganti S, Taylor SL, Abu Aboud O, Yang J, Evans C, Osier MV, et al. Kidney tumor biomarkers revealed by simultaneous multiple matrix metabolomics analysis. *Cancer Res*. (2012) 72:3471–9. doi: 10.1158/0008-5472.can-11-3105
4. Kim K, Taylor SL, Ganti S, Guo L, Osier MV, Weiss RH. Urine metabolomic analysis identifies potential biomarkers and pathogenic pathways in kidney cancer. *OMICS*. (2011) 15:293–303. doi: 10.1089/omi.2010.0094
5. Ganti S, Taylor SL, Kim K, Hoppel CL, Guo L, Yang J, et al. Urinary acylcarnitines are altered in human kidney cancer. *Int J Cancer*. (2012) 130:2791–800. doi: 10.1002/ijc.26274
6. Monteiro MS, Barros AS, Pinto J, Carvalho M, Pires-Luis AS, Henrique R, et al. Nuclear Magnetic Resonance metabolomics reveals an excretory metabolic signature of renal cell carcinoma. *Sci Rep*. (2016) 6:37275. doi: 10.1038/srep37275
7. Liu X, Cheng X, Liu X, He L, Zhang W, Wang Y, et al. Investigation of the urinary metabolic variations and the application in bladder cancer biomarker discovery. *Int J Cancer*. (2018) 143:408–18. doi: 10.1002/ijc.31323
8. Benghuzzi H, Mohamed A. The effects of androstenedione on renal tubule epithelial cells. *Biomed Sci Instrum*. (2007) 43:63–8.
9. Tomaszewski M, Charchar FJ, Maric C, Kuzniewicz R, Gola M, Grzeszczak W, et al. Inverse associations between androgens and renal function: the Young Men Cardiovascular Association (YMCA) study. *Am J Hypertens*. (2009) 22:100–5. doi: 10.1038/ajh.2008.307
10. Grun M, Richter E, Heine WD. Renal bile acid excretion as a cause of neoplastic lesions in the urinary tract after total portacaval shunt in the normal rat? *Hepatogastroenterology*. (1982) 29:232–5.
11. Bairaktari E, Liamis G, Tsolas O, Elisaf M. Partially reversible renal tubular damage in patients with obstructive jaundice. *Hepatology*. (2001) 33:1365–9. doi: 10.1053/jhep.2001.25089
12. Hakimi AA, Reznik E, Lee CH, Creighton CJ, Brannon AR, Luna A, et al. An integrated metabolic atlas of clear cell renal cell carcinoma. *Cancer Cell*. (2016) 29:104–16. doi: 10.1016/j.ccell.2015.12.004
13. Longo N. Disorders of biopterin metabolism. *J Inherit Metab Dis*. (2009) 32:333–42. doi: 10.1007/s10545-009-1067-2
14. Pawlak D, Tankiewicz A, Buczko W. Kynurenine and its metabolites in the rat with experimental renal insufficiency. *J Physiol Pharmacol*. (2001) 52(Pt 2):755–66.
15. Pawlak D, Tankiewicz A, Matys T, Buczko W. Peripheral distribution of kynurenine metabolites and activity of kynurenine pathway enzymes in renal failure. *J Physiol Pharmacol*. (2003) 54:175–89.
16. Schefold JC, Zeden J-P, Fotopoulou C, von Haehling S, Pschowski R, Hasper D, et al. Increased indoleamine 2,3-dioxygenase (IDO) activity and elevated serum levels of tryptophan catabolites in patients with chronic kidney disease: a possible link between chronic inflammation and uraemic symptoms. *Nephrol Dial Transplant*. (2009) 24:1901–8. doi: 10.1093/ndt/gfn739
17. Zhao J. Plasma kynurenic acid/tryptophan ratio: a sensitive and reliable biomarker for the assessment of renal function. *Ren Fail*. (2013) 35:648–53. doi: 10.3109/0886022x.2013.790301
18. Sallee M, Dou L, Cerini C, Poitevin S, Brunet P, Burtey S. The aryl hydrocarbon receptor-activating effect of uremic toxins from tryptophan metabolism: a new concept to understand cardiovascular complications of chronic kidney disease. *Toxins*. (2014) 6:934–49. doi: 10.3390/toxins6030934
19. Juhasz C, Nahleh Z, Zitron I, Chugani DC, Janabi MZ, Bandyopadhyay S, et al. Tryptophan metabolism in breast cancers: molecular imaging and immunohistochemistry studies. *Nucl Med Biol*. (2012) 39:926–32. doi: 10.1016/j.nucmedbio.2012.01.010
20. Platten M, Wick W, Van den Eynde BJ. Tryptophan catabolism in cancer: beyond IDO and tryptophan depletion. *Cancer Res*. (2012) 72:5435–40. doi: 10.1158/0008-5472.CAN-12-0569
21. Santhanam S, Alvarado DM, Ciorba MA. Therapeutic targeting of inflammation and tryptophan metabolism in colon and gastrointestinal cancer. *Transl Res*. (2016) 167:67–79. doi: 10.1016/j.trsl.2015.07.003
22. Opitz CA, Wick W, Steinman L, Platten M. Tryptophan degradation in autoimmune diseases. *Cell Mol Life Sci*. (2007) 64:2542–63. doi: 10.1007/s00018-007-7140-9
23. Wettersten HI, Hakimi AA, Morin D, Bianchi C, Johnstone ME, Donohoe DR, et al. Grade-dependent metabolic reprogramming in kidney cancer revealed by combined proteomics and metabolomics analysis. *Cancer Res*. (2015) 75:2541–52. doi: 10.1158/0008-5472.can-14-1703
24. Balachandran VP, Cavnar MJ, Zeng S, Bamboat ZM, Ocuin LM, Obaid H, et al. Imatinib potentiates antitumor T cell responses in gastrointestinal stromal tumor through the inhibition of Ido. *Nat Med*. (2011) 17:1094–100. doi: 10.1038/nm.2438
25. Lin L, Huang Z, Gao Y, Yan X, Xing J, Hang W. LC-MS based serum metabonomic analysis for renal cell carcinoma diagnosis, staging, and biomarker discovery. *J Proteome Res*. (2011) 10:1396–405. doi: 10.1021/pr101161u
26. Maddison DC, Giorgini F. The kynurenine pathway and neurodegenerative disease. *Semin Cell Dev Biol*. (2015) 40:134–41. doi: 10.1016/j.semcdb.2015.03.002
27. Ronkainen H, Soini Y, Vaarala MH, Kauppila S, Hirvikoski P. Evaluation of neuroendocrine markers in renal cell carcinoma. *Diagn Pathol*. (2010) 5:28. doi: 10.1186/1746-1596-5-28
28. Edgren M, Stridsberg M, Kalknar KM, Nilsson S. Neuroendocrine markers; chromogranin, pancreastatin and serotonin in the management of patients with advanced renal cell carcinoma. *Anticancer Res*. (1996) 16:3871–4.

Conflict of Interest Statement: The authors declare that the research was conducted in the absence of any commercial or financial relationships that could be construed as a potential conflict of interest.

frontiers in Oncology

SYSTEMATIC REVIEW
published: 18 November 2020
doi: 10.3389/fonc.2020.586949

Diagnostic Performance of Contrast-Enhanced Ultrasound in Renal Cancer: A Meta-Analysis

Ke-Hao Pan[1†], Li Jian[2†], Wei-Jun Chen[3†], Abdul Aziz Nikzad[4], Fang Q. Kong[5], Xu Bin[1], Ya-Li Wang[1*] and Ming Chen[1*]*

[1] Affiliated Zhongda Hospital of Southeast University, Southeast University, Nanjing, China, [2] Department of Urology, Jinhu People's Hospital, Jinghua, China, [3] Department of Urology, JinTan People's Hospital, Changzhou, China, [4] Department of Urology, Affiliated Zhongda Hospital of Southeast University, Nanjing, China, [5] Department of Nosocomial Infection, Affiliated Zhongda Hospital of Southeast University, Nanjing, China

OPEN ACCESS

Edited by:
Po-Hsiang Tsui, Chang Gung University, Taiwan

Reviewed by:
Christoph Dietrich, Hirslanden Private Hospital Group, Switzerland
Kun Zheng, Peking Union Medical College Hospital (CAMS), China

***Correspondence:**
Xu Bin
xb15896450810@126.com
Ya-Li Wang
15150666260@163.com
Ming Chen
mingchenseu@126.com

[†]These authors have contributed equally to this work and share first authorship

Specialty section:
This article was submitted to Cancer Imaging and Image-directed Interventions, a section of the journal Frontiers in Oncology

Received: *24 July 2020*
Accepted: *20 October 2020*
Published: *18 November 2020*

Citation:
Pan K-H, Jian L, Chen W-J, Nikzad AA, Kong FQ, Bin X, Wang Y-L and Chen M (2020) Diagnostic Performance of Contrast-Enhanced Ultrasound in Renal Cancer: A Meta-Analysis. Front. Oncol. 10:586949. doi: 10.3389/fonc.2020.586949

Background: Contrast-enhanced ultrasound (CEUS) is an examination mode for detecting blood vessels in tissues, and it has been gradually used in the diagnosis of kidney cancer in recent years. This study explores the value of contrast-enhanced ultrasound in the clinical diagnosis of renal cancer, and provides an accurate and effective method for clinical diagnosis of renal cancer.

Methods: CEUS and RCC were selected as the keywords. Searching the PubMed and Embase from 2007 to 2020, the original data were abstracted and performed heterogeneity test with the Meta-Disc software. The weighted sensitivity, specificity, positive likelihood ratio and negative likelihood ratio were calculated, as well as the summary receiver operating characteristic (SROC) curve. Further estimated the diagnostic value of CEUS in the research of renal cancer by calculating the area under the curve (AUC). The quality of evidence in researches was evaluated by QUADAS items. Meta-disc, Review Manager 5.3, and STATA 13 were used.

Results: A total of 20 studies were adopted for Meta-analysis. The weighted sensitivity, specificity, positive likelihood ratio, negative likelihood ratio, and diagnostic odds ratio were 0.97, 0.86, 6.8, 0.04 and 171, respectively; and AUC was 0.97. The results showed that there was high heterogeneity.

Conclusion: CEUS technology has a good diagnostic value for RCC.

Keywords: renal cancer, contrast-enhanced ultrasound, diagnosis, meta-analysis, tumor imaging

INTRODUCTION

Renal cancer (RCC) is the most common primary malignant tumor of the kidney, accounting for 80% to 90% of primary malignant tumors of the kidney (1). In recent years, the incidence of kidney cancer and the number of deaths has increased significantly (2). Most patients with kidney cancer lack typical clinical symptoms and signs at an early stage (3). One third of RCC cases were reported

Abbreviations: RCC, renal cell carcioma; CEUS, contrast-enhanced ultrasound; AUC, area under the curve.

with metastasis by the time of diagnosis (4). Therefore, there is still a need for an effective kidney cancer imaging diagnosis method.

RCC usually presents as a large mass on CT, mostly with soft tissue density; papillary RCC is less malignant than RCC and has less blood supply than its blood supply. Therefore, enhanced CT scan show either uneven or relatively uniform mild to moderate enhancement. CT examination is considered to be a gold standard for the diagnosis of kidney tumors, but CT can easily confuse cystic kidney cancer with renal abscess and hydronephrosis. MRI is usually used as a diagnostic tool for kidney tumors that cannot be characterized by CT, and is mainly used for typical lesions in CT. MRI is also often used in patients who cannot undergo CT enhancement due to impaired renal function. The limitation of MRI is that the acquisition time is long and people with metal implants such as pacemakers cannot be examined. Its availability and timeliness are not as good as CT.

The current clinical diagnosis methods for RCC are mainly imaging examinations such as ultrasound, contrast-enhanced CT, contrast-enhanced MR, non-contrast CT, non-contrast MR among which ultrasound has become the main method due to its simplicity and non-invasiveness, but the accuracy of conventional ultrasound for qualitative diagnosis of tumors is limited. Non-contrast CT/MR can only observe a specific section at a specific time, and the display rate of necrotic lesions is not as good as that of contrast enhanced ultrasound (CEUS), and it may be misdiagnosed due to missing the peak period of tumor enhancement and making the contrast enhancement characteristics unclear.

Contrast-enhanced CT and MR contrast agents can cause certain damage to the physiological functions of the liver and kidneys, and can also cause allergic reactions.

Contrast-enhanced ultrasound is a new detection method developed in ultrasound contrast agent and contrast imaging technology. It can observe blood perfusion in tumor in real time, continuously and dynamically, which further improves the accuracy of clinical diagnosis (5–7). CEUS can effectively display the low blood perfusion state and ischemic necrosis of tumor lesions with a diameter of less than 1 cm, thereby providing more information for the diagnosis of renal cancer, and at the same time eliminates the disadvantages of enhanced CT and MRI examinations (8, 9). CT/MR can only observe a specific section at a specific time. In addition, CEUS can display small blood vessels more sensitively than CT/MR, so as to more accurately observe blood perfusion of new tumors, which can evaluate the angiogenesis of renal cancer before surgery. CEUS cannot observe the surrounding and distant metastasis of the tumor, and cannot provide information on the clinical staging of renal cancer.

This study explores the value of contrast-enhanced ultrasound in the clinical diagnosis of renal cancer. The contrast-enhanced ultrasound examination method has high efficiency in diagnosing kidney cancer, nonradioactive and has very few contrast agents to cause allergic reactions. Compared with MRI, the examination time is short, therefore, it has higher clinical promotion value. With improvement of functions and performance of Doppler ultrasound equipment, the development of safer, cheaper, and better imaging performance contrast agents, contrast-enhanced ultrasound may become the first choice for renal cancer in the near future.

METHODS

Search Strategy

Computer searches include PubMed, Embase to collect relevant literature on the diagnosis of kidney cancer by contrast-enhanced ultrasound. Search period: 2007 to 2020. Subject terms include contrast-enhanced ultrasound, kidney tumor, kidney cancer, renal cancer and renal tumor, and the search method is adjusted according to the specific database, and the search strategy is determined after multiple pre-searches. Using a combination of database retrieval and manual retrieval, two evaluators independently retrieve and re-search the references of the included literature. Another reviewer Xu Bin and Ke-Hao Pan are both medically-trained urologists in China with certain clinical and imaging experience. Xu Bin is the deputy chief physician of Chinese Urology. The deviation between the two reviewers is relatively small. The language is limited to Chinese or English.

Study Selection

The exclusion criteria for the systematic review were: (a) articles not within the field of interest; (b) editorials or letters, review articles, comments, conference proceedings; and (c) case reports.

Literature Screening

Literature was independently screened by 2 reviewers based on the inclusion criteria, first reading the title and abstract. Then read the full text of the documents that may meet the inclusion criteria. After cross-checking the results, data were extracted from cohort studies. The basic characteristics of the included literature are shown in **Table 1**.

Quality Assessment

Two reviewers individually evaluated the quality of the included literature, and discussed when they disagree. This meta-analysis was carried out according to the QUADAS (Quality Assessment of Diagnostic Accuracy Studies) standard, which can be divided into three situations: "yes," "no," and "unclear." "Yes" means that the criteria for this item are met, "no" means that the criteria are not met, and "unclear" means that the standards are partially met or sufficient information cannot be obtained from the document (30).

Statistical Analysis

The weighted sensitivity, specificity, positive likelihood ratio and negative likelihood ratio were calculated, as well as the summary receiver operating characteristic (SROC) curve. The larger the area under the curve and the closer the SROC curve is to the upper left corner, the higher the value of the diagnostic test. Between-study statistical heterogeneity was assessed using I^2 and the Cochrane Q test. The meta-regression and subgroup analysis of CEUS are shown in **Figure 1**, divided into five sub-groups

TABLE 1 | Study and patient characteristics.

Studies	Year	Size Age	Lesions	Study Type	Lesion size	TP	FP	FN	TN
Li et al. (10)	2008	71 53.6	72	Prospective	1.3–5	26	18	0	28
Xu et al. (11)	2010	119 42.9	126	Retrospective	1.5–11.7	82	11	1	32
Lgnee et al. (12)	2010	135 66	127	Prospective	NA	114	11	3	9
Zhou et al. (13)	2011	51 37	51	Prospective	1.5–6	20	14	2	15
Lu et al. (14)	2012	122 41.3	123	Retrospective	1–11.5	105	0	3	15
Li et al. (15)	2013	91 62.0	100	Retrospective	0.9–9.7	83	1	2	14
Oh et al. (16)	2014	49 61	49	Retrospective	<4	33	4	5	7
Barr et al. (17)	2014	721 70	306	Retrospective	0.2–16.1	139	8	0	159
Nicolau et al. (18)	2015	72 64.9	83	Prospective	5–6.5	31	2	2	48
Lu et al. (19)	2015	174 40.3	174	Retrospective	1.0–7.5	136	10	6	22
Chen et al. (20)	2015	99 56.6	102	Prospective	1–3	73	4	17	17
Rubnthaler et al. (21)	2016	36 NA	36	Retrospective	NA	27	0	1	8
Yong et al. (22)	2016	63 48.7	76	Retrospective	0.4–7.9	21	3	1	49
Wei et al. (23)	2017	128 53.6	118	Retrospective	1–3.9	87	8	6	17
Zarzour et al. (24)	2017	41 NA	41	Retrospective	NA	20	3	0	18
Clevert et al. (25)	2008	32 56	37	Retrospective	NA	12	5	0	20
Ascenti et al. (26)	2007	40 48	44	Retrospective	NA	5	0	6	33
Quaia et al. (27)	2008	40 62	40	Retrospective	2–8	18	4	3	15
Guillaume et al. (28)	2017	47 64.7	19	Prospective	1.8–5.8	14	1	0	32
Sanz et al. (29)	2016	66 67.8	67	Prospective	3.8	66	12	0	54

according to whether the article publication year is beyond 2015, whether the case was greater than 100, whether lesion was greater than 100, whether the study was retrospective or prospective, and whether the age of patients above 60. The number of articles published before and after 2015 is close.

RESULTS

Literature Search

279 documents were first detected. 79 duplicated publications were excluded through literature manager software. And after the abstracts were screened, 140 records were excluded. 40 publications were excluded due to inadequate outcome because they lack information about the true positive rate, true negative rate, false negative rate and false positive rate of CEUS diagnosis. Finally, a total of 20 articles were included (10–29). The flow chart is shown in **Figure 2**.

Twenty studies including 2197 patients and 1791 lesions were selected for the meta-analysis. The basic characteristics of the included literature are shown in **Table 1**.

Inclusion criteria: 1 Pathological diagnosis should be adopted as "gold standard" for all adopted literature; 2 The research object is the literature using contrast-enhanced ultrasound to diagnose RCC; 3 The interval between ultrasound examination and pathological examination should not exceed 1 month; 4 Each study can be successfully extracted to TP, FP, TN, and FN.

Exclusion criteria: 1 Excluded documents that did not use contrast enhancement technology. 2 Excluded secondary literature and conference papers such as experience exchange, abstracts, lectures and reviews.

Histopathological Results

The histopathological results of included studies are shown in **Table 2**. Most of the included articles are RCC, Papillary RCC and so on. CEUS is effective in diagnosing these kidney cancers.

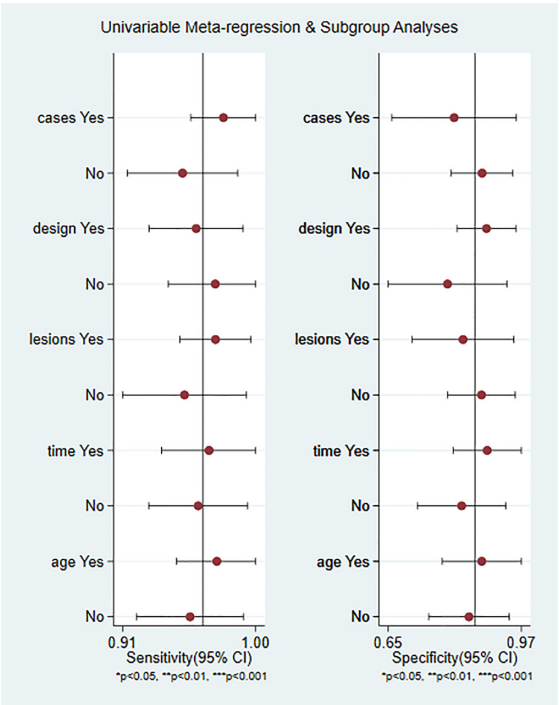

FIGURE 1 | Meta-regression and subgroup analyses of studies.

Qualitative Analysis

The quality of the articles included was satisfactory. The research quality evaluation is shown in **Figure 3**. In patient selection, one article is high risk. On Index Test, there is no high risk, however,

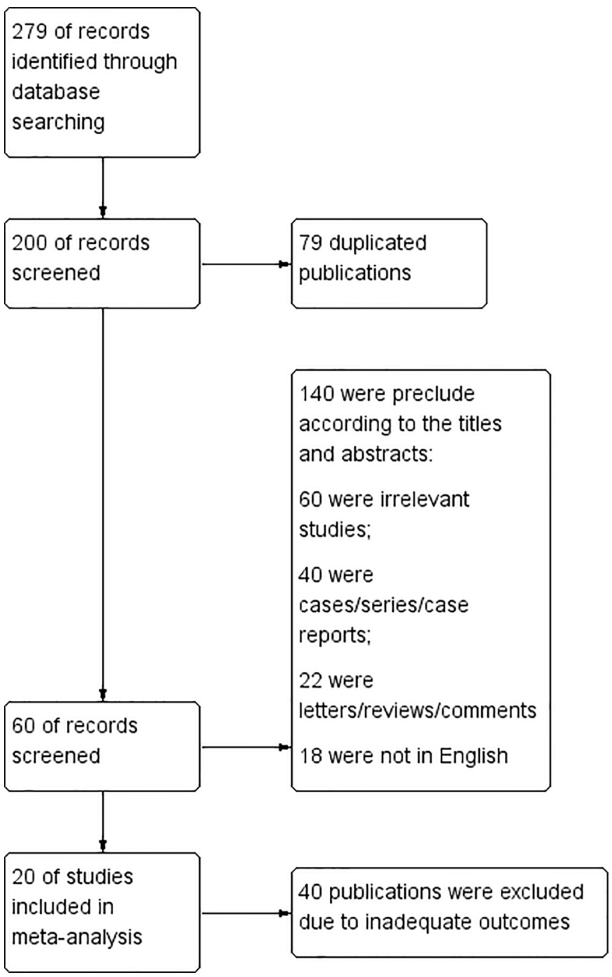

FIGURE 2 | Flowchart.

TABLE 2 | Histopathological results of the included studies.

Author	Histopathological results
Li et al. (10)	RCC
Xu et al. (11)	RCC+Papillary RCC
Lgnee et al. (12)	ccRCC
Zhou et al. (13)	Small Papillary RCC
Lu et al. (14)	RCC
Li et al. (15)	Small Cystic RCC
Oh et al. (16)	Small RCC
Barr et al. (17)	Cystic RCC
Nicolau et al. (18)	RCC+Papillary RCC
Lu et al. (19)	RCC
Chen et al. (20)	RCC
Rubnthaler et al. (21)	Cystic RCC
Yong et al. (22)	RCC
Wei et al. (23)	Papillary RCC
Zarzour et al. (24)	Cystic RCC
Clevert et al. (25)	Small RCC
Ascenti et al. (26)	Papillary RCC
Quaia et al. (27)	RCC+Papillary RCC
Guillaume et al. (28)	Cystic RCC
Sanz et al. (29)	RCC

one article on Reference Standard is high risk. The overall quality of the article is high.

Meta Analysis

Twenty studies including 2197 patients and 1791 lesions were selected for the meta-analysis. Results of the meta-analysis are presented in **Figure 4**. The SROC curve and the forest map of CEUS are shown in **Figures 5** and **6**, respectively. Pooled Sen, Spe, LR+, LR-, DOR were 0.97, 0.86, 6.8, 0.04, and 171, respectively. In **Figure 5**, the areas under the SROC curve are 0.97 (95% CI, 0.96–0.98).

Heterogeneity Analysis

As shown in **Figure 6**, CEUS has heterogeneity in the sensitivity and specificity of the diagnosis of kidney cancer (Q value, P value, I^2 value are 134.94, < 0.01, 85.92% and 115.84, <0.01, 83.60%, respectively). A randomed-effects model was used. The Spearman correlation coefficients of the sensitivity logarithm and (1-specificity) logarithm of CEUS diagnosis of renal cancer were −0.190 (P>0.05), indicating that there is no threshold effect. To further explore the potential sources of heterogeneity, a subgroup analysis and meta-regression was performed. It showed that no definite variable was the source of heterogeneity in the current meta-analysis (**Figure 1**).

Sensitivity Analysis

Sensitivity analysis is shown in **Figure 7**. The results showed that the meta-analysis results are stable.

Clinical Application Analysis

Fagan diagram was constructed for clinical application analysis as shown in **Figure 8**. The post-test probability of CEUS was 87% and is higher than the pre-test probability (50%), indicating that CEUS is effective in the diagnosis of renal cancer. As can be seen from **Figure 9**, the combined negative likelihood ratios for the diagnosis of renal cancer were >0.1 and the positive likelihood ratio was <10.

Publication Bias

The Deeks' funnel chart shows asymmetry in scattered points, suggesting that there is publication bias (P<0.05). It is shown in **Figure 10**. However, the sensitivity analysis showed that our results are stable. Despite there is publication bias, our sensitivity test found that the article is stable, indicating that our results are reliable.

DISCUSSION

CEUS is a new type of ultrasound diagnosis technology that uses contrast enhancers and corresponding analysis software to display the state of tissue blood perfusion on the basis of conventional ultrasound. CEUS uses high-intensity nonlinear harmonic signals generated by contrast agents to increase the contrast between normal tissues and lesions. Kidney cancer has the characteristics of infinite growth of microvessels in malignant

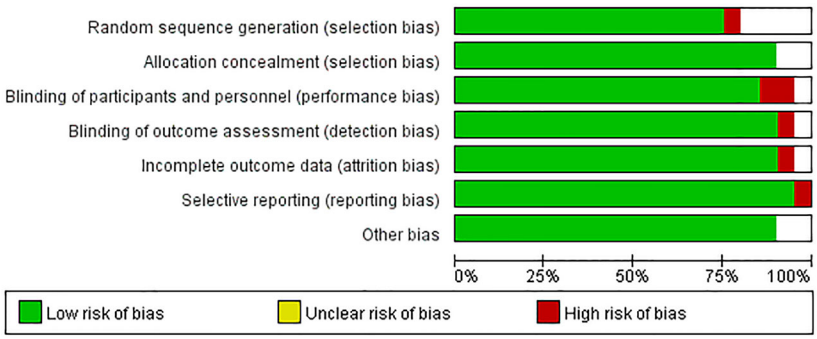

FIGURE 3 | Summary of risk of bias and applicability concerns.

SUMMARY PERFORMANCE ESTIMATES

Parameter	Estimate	95% CI
Sensitivity	0.97 [	0.93, 0.98]
Specificity	0.86 [	0.77, 0.92]
Positive Likelihood Ratio	6.8 [	4.1, 11.2]
Negative Likelihood Ratio	0.04 [	0.02, 0.08]
Diagnostic Odds Ratio	171 [	70, 418]

FIGURE 4 | The combined statistics.

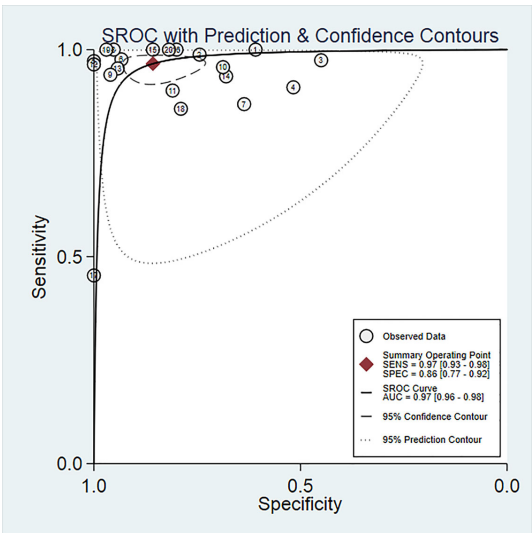

FIGURE 5 | SROC curves of CEUS for diagnosis of renal cancer.

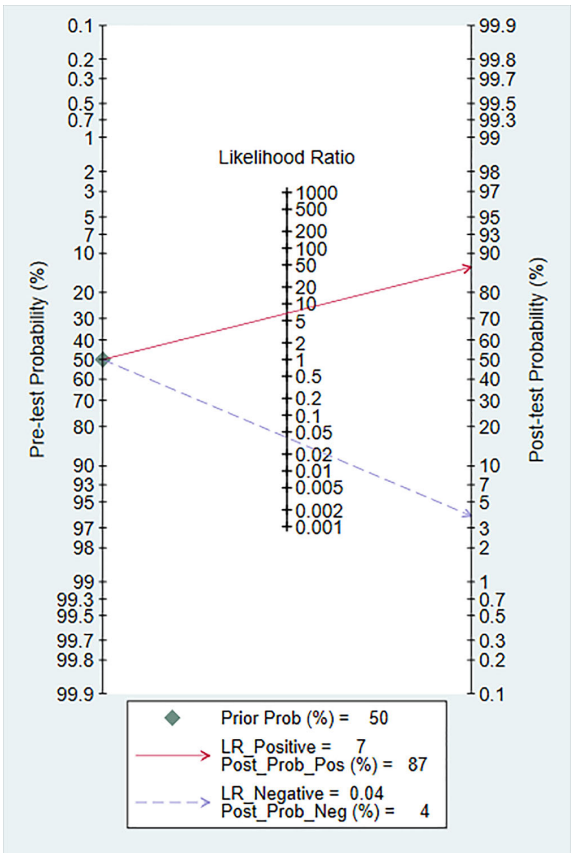

FIGURE 8 | The Fagan map.

tumors. Most malignant tumors have a large number of aggressive capillary formations around and inside the tumor. CEUS can enhance the display of blood perfusion of kidney and tumor microvessels. During the examination, the contrast agent is injected into the blood circulation through the peripheral vein, and the microbubbles are in full contact with the red blood cells

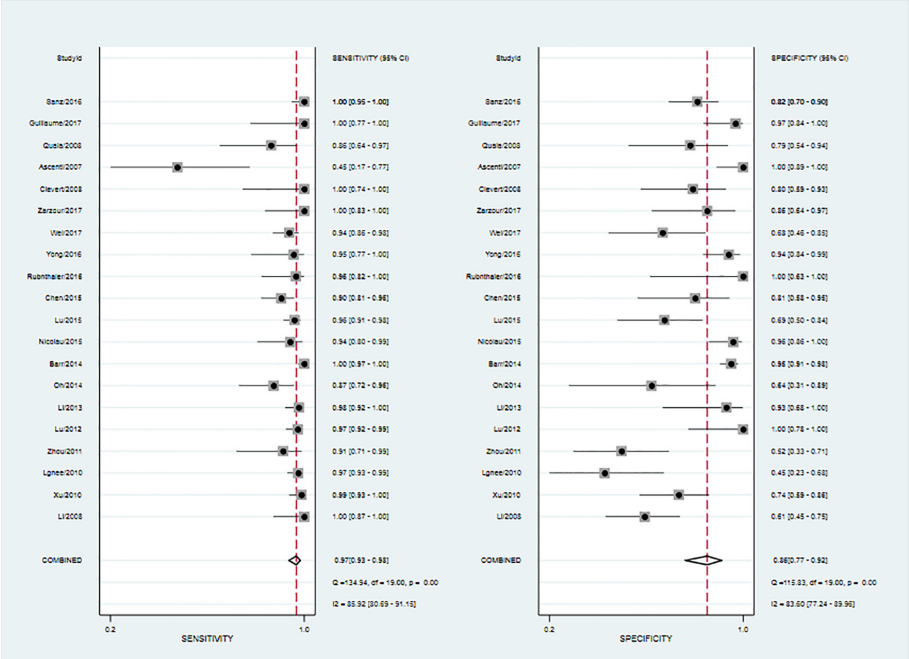

FIGURE 6 | Forest map of CEUS for diagnosis of renal cancer.

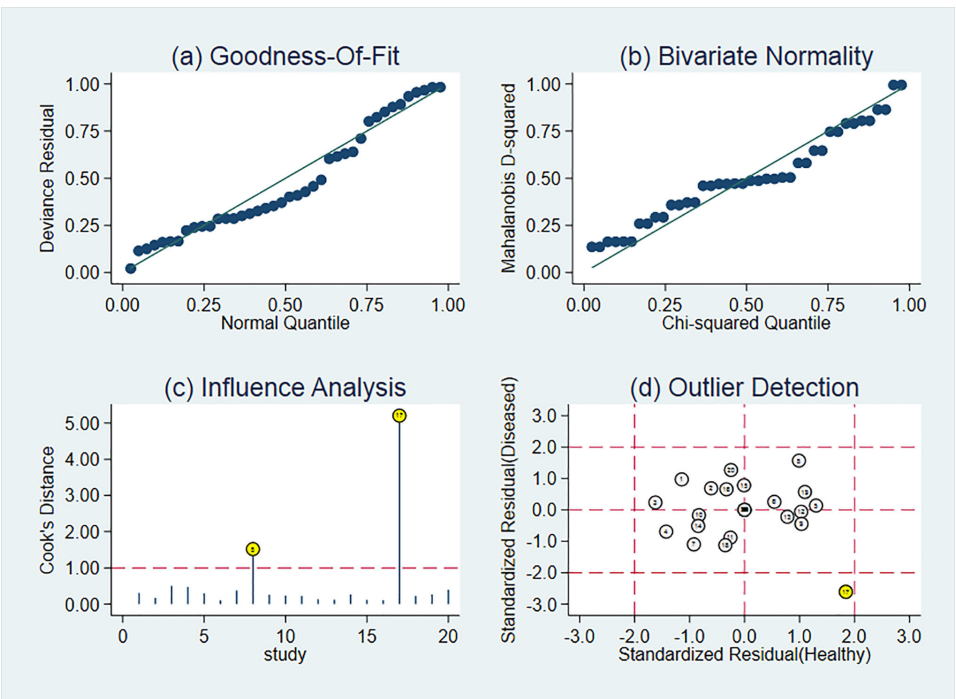

FIGURE 7 | Sensitivity analysis of studies.

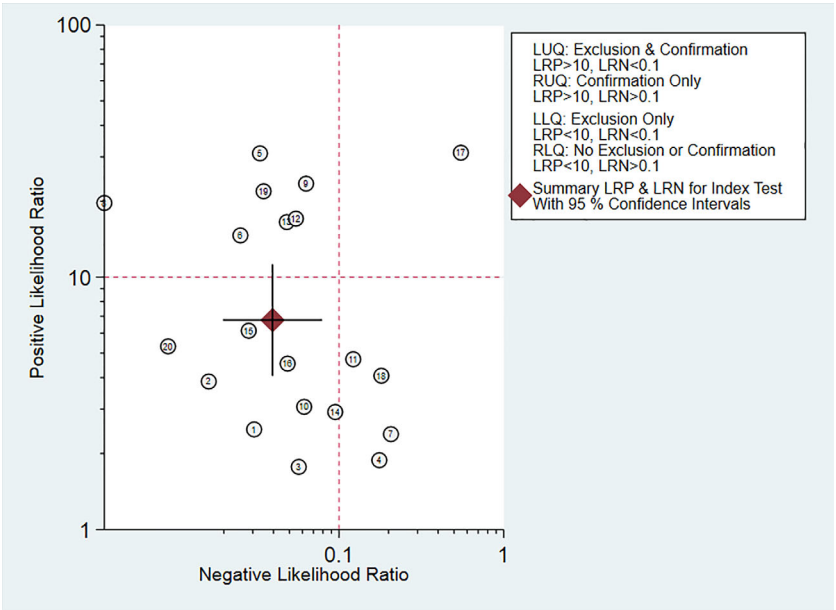

FIGURE 9 | Likelihood ratio dot plot.

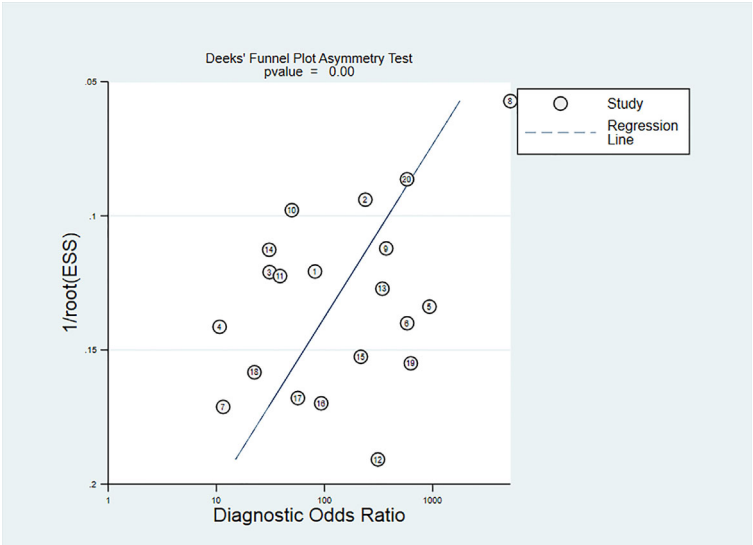

FIGURE 10 | Deeks' test.

in the capillaries, forming many blood bubble interfaces, thereby changing the basic function between the ultrasound and the basic tissues, enhancing the ultrasound signal of the whole body blood pool, and improving the signal-to-noise ratio of echo, thereby improving the display of tumors. In addition, CEUS can also improve the sensitivity of detecting small tumors or slow blood vessels. The results of this study show that the weighted sensitivity, specificity, positive likelihood ratio, negative likelihood ratio, and diagnostic odds ratio were 0.97, 0.86, 6.8, 0.04 and 171, respectively; and AUC is 0.97. This suggests that CEUS could be used as a diagnostic tool for RCC.

CEUS features of renal cancers are that the cortical phase contrast agent can quickly fill the lesion tissue, and the enhancement degree of CEUS is equal to or significantly higher

than that of the renal parenchyma, and in the late medulla and delayed phase, the contrast agent quickly exits the lesion organization, mainly manifested as low enhanced performance. CEUS shows the enhancement feature of fast forward and fast out.

CEUS provides a new method for diagnosing kidney tumors. The application of TIC can make the diagnosis of RCC more objective by analyzing the AT, TP, and DPI values of the tumor and surrounding renal cortex. Most renal cancers have pseudo-capsules. The display rate of pseudo-capsules after contrast is higher than that of conventional ultrasound, and the enhancement time is long and obvious. In CEUS, the hemorrhagic and necrotic foci in the tumor are in sharp contrast with the enhanced foci, and the display rate of the necrotic foci is higher than that of conventional ultrasound. Although CT and MRI have high diagnostic rates, contrast agents can cause certain damage to the physiological functions of the liver and kidneys. At the same time, the patient's body can also be damaged by radiation. CT/MR can only observe a specific section at a specific time, and the display rate of necrotic lesions is not as good as that of CEUS, and it may be misdiagnosed by missing the peak period of tumor enhancement and making the contrast enhancement characteristics unclear. In addition, CEUS can display small blood vessels more sensitively than CT/MR, so more accurate to observe the blood perfusion of new tumors, which can used to evaluate the angiogenesis of renal cancer before surgery. CEUS cannot observe the surrounding and distant metastasis of the tumor, and it has no guidance on the clinical staging of renal cancer.

The heterogeneity of this study is high. According to the results of the subgroup and meta-regression analysis, the five subgroups are not sources of heterogeneity and a comprehensive analysis requires more subgroup data. First, the characteristics of ultrasonography determine that factors such as the experience and skills of the diagnostician, as well as the subjective evaluation of the imaging results, have a great influence on the diagnosis. In Rubnthaler (21) article, all CEUS examinations were performed and interpreted by a single radiologist with more than 15 years of experience in CEUS. In Lu (19) article, a sonologist with 10 years' experience with CEUS did diagnosis. Obviously, different experiences of the two sonologists will lead to different diagnosis of kidney cancer. Then, although each study uses the same contrast agent, the ultrasound equipment and probe models used are different, and even the same study uses different ultrasound equipment and probes. In Wei (23) article, CEUS examinations were performed using a Sequoia 512ultrasound system (Siemens, Mountain View, CA, USA). In Quaia (27) article, CEUS examinations were performed using Sequoia, Acuson-Siemens. These factors may affect the diagnosis rate and cause heterogeneity. These may be the reason for the heterogeneity.

This research still has some limitations. First, the number of documents is limited and retrospective studies account for a large amount, so can cause selection bias; second, due to the different publication time of the literature, the CEUS diagnostic standards in some literatures have certain differences, which may affect the results; third, There are poor quality research in these documents, which leads to the bias of the publication of this article.

CONCLUSION

Contrast enhanced ultrasound technology has a good diagnostic clinical value for RCC.

DATA AVAILABILITY STATEMENT

The original contributions presented in the study are included in the article/supplementary material. Further inquiries can be directed to the corresponding authors.

AUTHOR CONTRIBUTIONS

AN and W-JC revised the manuscript. K-HP, LJ and W-JC contributed equally to this work and should be considered co-first authors. AN and FK contributed equally to this work and should be considered second authors. XB, Y-LW and MC contributed equally to this work and should be considered corresponding authors. All authors contributed to the article and approved the submitted version.

FUNDING

Foundations: This study was funded by The National Natural Science Foundation of China (No. 81872089, 81370849, 81672551, 81300472, 81070592, 81202268, 81202034), Natural Science Foundation of Jiangsu Province (BK20161434, BL2013032, BK20150642 and BK2012336), Six talent peaks project in Jiangsu Province, Jiangsu Provincial Medical Innovation Team (CXTDA2017025), The National Key Research and Development Program of China (SQ2017YFSF090096), Jiangsu Provincial Key Research and Development Program (BE2019751), Innovative Team of Jiangsu Provincial (2017ZXKJQWO7), Jiangsu Provincial Medical Talent (ZDRCA2016080).

REFERENCES

1. Udea N, Nagira H, Sannomiya N, Ikunishi S, Hattori Y, Kamida A, et al. Contrast-enhanced ultrasonography in evaluation of therapeutic effect of chemotherapy for patients with liver metastases. *Yonago Acts Med* (2016) 59 (4):255–61.
2. Siegel RL, Miller KD, Jemal A. Cancer statistics, 2017. *CA Cancer J Clin* (2017) 67:177–93. doi: 10.3322/caac.21395
3. Skinner DG, Vermillion CD, Pfister RC, Leadbetter WF. Renal cell carcinoma. *Am Fam Physician* (1971) 4:89–94.
4. Gore ME, Larkin JM. Challenges and opportunities for converting renal cell carcinoma into a chronic disease with targeted therapies. *Br J Cancer* (2011) 104:399–406. doi: 10.1038/sj.bjc.6606084
5. Zarzour JG, Porter KK, Tchelepi H, Robbin ML. Contrast-enhanced ultrasound of benign liver lesions. *Abdom Radiol (NY)* (2018) 43:848–60. doi: 10.1007/s00261-017-1402-2

6. Nakata N, Ohta T, Nishioka M, Takeyama H, Toriumi Y, Kato K, et al. Optimization of region of interest drawing for quantitative analysis: differentiation between benign and malignant breast lesions on contrast-enhanced sonography. *J Ultrasound Med* (2015) 34:1969–76. doi: 10.7863/ultra.14.10042
7. Kasoji SK, Chang EH, Mullin LB, Chong WK, Rathmell WK. Dayton PA. A pilot clinical study in characterization of malignant renal-cell carcinoma subtype with contrast-enhanced ultrasound. *Ultrason Imaging* (2017) 39:126–36. doi: 10.1177/0161734616666383
8. Kabakci N, Igci E, Secil M, Yorukoglu K, Mungan U, Celebi I, et al. Echo contrast-enhanced power Doppler ultrasonography for assessment of angiogenesis in renal cell carcinoma. *J Ultrasound Med* (2005) 24:747–53. doi: 10.7863/jum.2005.24.6.747
9. Matsumoto S, Minami T, Yamamoto Y, Nishioka T, Akiyama T, Onoue A. Efficacy of contrast-enhanced color Doppler ultrasonography for the diagnosis of renal mass lesions. *Hinyokika Kiyo* (2001) 47:299–302.
10. Li F, Du LF, Xing JF, Su YJ, Wu Y. Diagnostic efficacy of contrast-enhanced ultrasonography in solid renal parenchymal lesions with maximum diameters of 5 cm. *J Ultrasound Med* (2008) 27:875–85. doi: 10.7863/jum.2008.27.6.875
11. Xu ZF, Xu HX, Xie XY, Liu GL, Zheng YL, Lu MD. Renal cell carcinoma and renal angiomyolipoma: differential diagnosis with real-time contrast-enhanced ultrasonography. *J Ultrasound Med* (2010) 29:709–17. doi: 10.7863/jum.2010.29.5.709
12. Ignee A, Straub B, Brix D, Schuessler G, Ott M, Dietrich CF. The value of contrast enhanced ultrasound (CEUS) in the characterisation of patients with renal masses. *Clin Hemorheol Microcirc* (2010) 46:275–90. doi: 10.3233/CH-2010-1352
13. Zhou X, Yan F, Luo Y, Peng Y-L, Parajuly SS, Wen X-R, et al. Characterization and diagnostic confidence of contrast-enhanced ultrasound for solid renal tumors. *Ultrasound Med Biol* (2011) 37:845–53. doi: 10.1016/j.ultrasmedbio.2011.02.015
14. Lu Q, Wang W, Huang B, Li C, Li C. Minimal fat renal angiomyolipoma: the initial study with contrast-enhanced ultrasonography. *Ultrasound Med Biol* (2012) 38:1896–901. doi: 10.1016/j.ultrasmedbio.2012.07.014
15. Li X, Liang P, Guo M, Yu J, Yu X, Cheng Z, et al. Real-time contrast-enhanced ultrasound in diagnosis of solid renal lesions. *Discovery Med* (2013) 16:15–25.
16. Oh TH, Lee YH, Seo IY. Diagnostic efficacy of contrast-enhanced ultrasound for small renal masses. *Korean J Urol* (2014) 55:587–92. doi: 10.4111/kju.2014.55.9.587
17. Barr RG, Peterson C, Hindi A. Evaluation of indeterminate renal masses with contrast-enhanced US: a diagnostic performance study. *Radiology* (2014) 271:133–42. doi: 10.1148/radiol.13130161
18. Nicolau C, Buñesch L, Paño B, Salvador R, Ribal MJ, Mallofré C, et al. Prospective evaluation of CT indeterminate renal masses using US and contrast-enhanced ultrasound. *Abdom Imaging* (2015) 40:542–51. doi: 10.1007/s00261-014-0237-3
19. Lu Q, Huang BJ, Wang WP, Li CX, Xue LY. Qualitative and quantitative analysis with contrast-enhanced ultrasonography: diagnosis value in hypoechoic renal angiomyolipoma. *Korean J Urol* (2015) 16:334–41. doi: 10.3348/kjr.2015.16.2.334
20. Chen L, Wang L, Diao X, Qian W, Fang L, Pang Y, et al. The diagnostic value of contrast-enhanced ultrasound in differentiating small renal carcinoma and angiomyolipoma. *Biosci Trends* (2015) 9:252–8. doi: 10.5582/bst.2015.01080
21. Rubenthaler J, Paprottka K, Marcon J, Hameister E, Hoffmann K, Joiko N, et al. Comparison of magnetic resonance imaging (MRI) and contrast-enhanced ultrasound(CEUS) in the evaluation of unclear solid renal lesions. *ClinHemorheol Microcirc* (2016) 64:757–63. doi: 10.3233/CH-168034
22. Yong C, Teo YM, Jeevesh K. Diagnostic performance of contrast-enhanced ultrasound in the evaluation of renal masses inpatients with renal impairment. *Med J Malaysia* (2016) 71:193–8.
23. Wei SP, Xu CL, Zhang QR, Zhang Q-R, Zhao Y-E, Huang P-F, et al. Contrast-enhanced ultrasound for differentiating benign from malignant solid small renal masses: comparison with contrast-enhanced CT. *Abdom Radiol (NY)* (2017) 42:2135–45. doi: 10.1007/s00261-017-1111-x
24. Zarzour JG, Lockhart ME, West J, Turner E, Jackson BE, Thomas JV, et al. Contrast-enhanced ultrasound classification of previously indeterminate renal lesions. *J Ultrasound Med* (2017) 36:1819–27. doi: 10.1002/jum.14208
25. Clevert DA, Minaifar N, Weckbach S, Jung EM, Stock K, Reiser M, et al. Multislice computed tomography versus contrast-enhanced ultrasound in evaluation of complex cystic renal masses using the Bosniak classification system. *Clin Hemorheol Microcirc* (2008) 39(1-4):171–8. doi: 10.3233/CH-2008-1083
26. Ascenti G, Mazziotti S, Zimbaro G, Settineri N, Magno C, Melloni D, et al. Complex cystic renal masses: characterization with contrast-enhanced US. *Radiology* (2007) 243(1):158–65. doi: 10.1148/radiol.2431051924
27. Quaia E, Bertolotto M, Cioffi V, Rossi A, Baratella E, Pizzolato R, et al. Comparison of contrast -enhanced sonography with unenhanced sonography and contrast -enhanced CT in the diagnosis of malignancy in complex cystic renal masses. *AJR* (2008) 191(4):1239–49. doi: 10.2214/AJR.07.3546
28. Defortescu G, Cornu J-N, Béjar S, Giwerc A, Gobet F, Werquin C, et al. Diagnostic performance of contrast-enhanced ultrasonography and magnetic resonance imaging for the assessment of complex renal cysts: A prospective study. *Int J Urol* (2017) 24:184–9. doi: 10.1111/iju.13289
29. Sanz E, Hevia V, Gómez V, Álvarez S, Fabuel JJ, Martínez L, et al. Renal Complex Cystic Masses: Usefulness of Contrast-Enhanced Ultrasound (CEUS) in Their Assessment and Its Agreement with Computed Tomography. *Curr Urol Rep* (2016) 17:89. doi: 10.1007/s11934-016-0646-7
30. Yoshida K. Levels of free prostate specific antigen (PSA) can be selectively measured by heat treatment of serum: Free/total-PSA ratios improve detection of prostate carcinoma. *Clin Chim Acta* (1999) 280(1-2):195–203. doi: 10.1016/S0009-8981(98)00189-2

Conflict of Interest: The authors declare that the research was conducted in the absence of any commercial or financial relationships that could be construed as a potential conflict of interest.

frontiers in Oncology

ORIGINAL RESEARCH
published: 08 March 2021
doi: 10.3389/fonc.2021.640881

Exploration of an Integrative Prognostic Model of Radiogenomics Features With Underlying Gene Expression Patterns in Clear Cell Renal Cell Carcinoma

Yeqian Huang[1,2], *Hao Zeng*[1,3], *Linyan Chen*[1,3], *Yuling Luo*[1,3], *Xuelei Ma*[1,3*] *and Ye Zhao*[4*]

[1] Department of Biotherapy, Cancer Center, West China Hospital, Sichuan University, Chengdu, China, [2] West China School of Medicine, West China Hospital, Sichuan University, Chengdu, China, [3] State Key Laboratory of Biotherapy and Cancer Center, Collaborative Innovation Center for Biotherapy, West China Hospital, Sichuan University, Chengdu, China, [4] School of Bioscience and Technology, Chengdu Medical College, Chengdu, China

OPEN ACCESS

Edited by:
Haibin Shi,
Soochow University, China

Reviewed by:
Guolin Ma,
China-Japan Friendship Hospital, China
Zhi-Cheng Li,
Chinese Academy of Sciences (CAS), China

***Correspondence:**
Xuelei Ma
drmaxuelei@gmail.com
Ye Zhao
zhaoye525@cmc.edu.cn

Specialty section:
This article was submitted to Cancer Imaging and Image-directed Interventions, a section of the journal Frontiers in Oncology

Received: 12 December 2020
Accepted: 26 January 2021
Published: 08 March 2021

Citation:
Huang Y, Zeng H, Chen L, Luo Y, Ma X and Zhao Y (2021) Exploration of an Integrative Prognostic Model of Radiogenomics Features With Underlying Gene Expression Patterns in Clear Cell Renal Cell Carcinoma. Front. Oncol. 11:640881. doi: 10.3389/fonc.2021.640881

Background: Clear cell renal cell carcinoma (ccRCC) is one of the most common malignancies in urinary system, and radiomics has been adopted in tumor staging and prognostic evaluation in renal carcinomas. This study aimed to integrate image features of contrast-enhanced CT and underlying genomics features to predict the overall survival (OS) of ccRCC patients.

Method: We extracted 107 radiomics features out of 205 patients with available CT images obtained from TCIA database and corresponding clinical and genetic information from TCGA database. LASSO-COX and SVM-RFE were employed independently as machine-learning algorithms to select prognosis-related imaging features (PRIF). Afterwards, we identified prognosis-related gene signature through WGCNA. The random forest (RF) algorithm was then applied to integrate PRIF and the genes into a combined imaging-genomics prognostic factors (IGPF) model. Furthermore, we constructed a nomogram incorporating IGPF and clinical predictors as the integrative prognostic model for ccRCC patients.

Results: A total of four PRIF and four genes were identified as IGPF and were represented by corresponding risk score in RF model. The integrative IGPF model presented a better prediction performance than the PRIF model alone (average AUCs for 1-, 3-, and 5-year were 0.814 *vs.* 0.837, 0.74 *vs.* 0.806, and 0.689 *vs.* 0.751 in test set). Clinical characteristics including gender, TNM stage and IGPF were independent risk factors. The nomogram integrating clinical predictors and IGPF provided the best net benefit among the three models.

Conclusion: In this study we established an integrative prognosis-related nomogram model incorporating imaging-genomic features and clinical indicators. The results

indicated that IGPF may contribute to a comprehensive prognosis assessment for ccRCC patients.

Keywords: clear cell renal cell carcinoma, radiomics, genomics, machine learning, prognosis

INTRODUCTION

Renal cell carcinoma (RCC) is a common heterogeneous malignancy originated from renal tubular epithelial cells, with clear cell renal cell carcinoma (ccRCC) comprising about 80% of RCC cases (1, 2). Owing to the insufficient clinical symptoms and reliable diagnostic biomarkers at the early stage, about 30% of ccRCC patients had metastasis at the time of diagnosis, and about one-fifth of patients may experience metastasis or recurrence after radical treatment (3, 4). Imageological examinations such as conventional ultrasound, contrast-enhanced ultrasound, CT, contrast-enhanced CT and MRI have been applied to assess the overall profile of the tumor as noninvasive methods. However, there are limitations in these conventional imaging tests for differential diagnosis, preoperative pathological grading and prognosis of ccRCC, which also lack quantitative criteria.

Radiomics was first proposed by Lambin et al. (5) in 2012, which exploits high-throughput feature extraction algorithms to extract quantitative image features from standard medical images. Radiomics managed to perform the conversion from images into mineable data, which could then be applied to clinical decision support systems to achieve precise prediction, diagnosis, and prognostic evaluation of cancers (6, 7). A number of studies have reported that radiomics has been successfully applied in renal tumors researches, including Fuhrman staging of ccRCC (8–10), assessment of cancer phenotype and tumor microenvironment (11), differentiation of RCC and benign renal tumors (12, 13) and efficacy and prognosis evaluation (14, 15).

However, most studies regarding radiomics were primarily focused on the selection of image features and the quantitative analysis of tumors at the macroscopic level, and there has been little research into the mechanisms of deeper molecular biology. Combined with machine learning algorithms, we can further correlate the imaging data that reflects the quantitative phenotype of the disease with the genotype feature data which reveals the molecular activity. Correlation analysis between gene mutation, expression and imaging characteristics has been proved effective in the research of liver cancer (16), lung cancer (16–18), glioblastoma (19, 20) and Alzheimer's disease (21). Therefore, it is of vital importance to analyze the correlation and integration between imaging and genomic features of ccRCC, so as to understand the biological mechanism and furthermore obtain biomarkers for prognosis prediction, which will be more rewarding in personalized precision therapy.

Previous studies have proven that certain molecules and the activation of a series of signaling pathways are in close relation with the tumorigenesis and progression in ccRCC. For instance, the overexpression of vascular endothelial growth factor (VEGF) and platelet derived growth factor (PDGF) receptor tyrosine kinases are of great significance in promoting tumor angiogenesis and cell division. In addition, PI3K/AKT/mTOR pathway also results in affecting tumor cell growth and metabolism. Nevertheless, the associated gene expression profiles have not been thoroughly studied.

Standard treatments for ccRCC patients encompass surgery, radiotherapy and chemotherapy, and specific treatments including targeted therapy in combination with immune checkpoint inhibitors have shown efficacy in improving the overall survival (OS) of ccRCC patients (22, 23). However, the response of personalized therapy does vary and the prognosis is not as satisfactory. So far no routine genetic tests have been conducted, and these molecules concerning the mechanism of ccRCC development may provide opportunities to investigate potential biomarkers for diagnosis and prognosis. Therefore, it's essential to establish an effective model that conduce to risk stratification, treatment strategy support and prognostic prediction for patients with ccRCC.

In this study we concentrate on analyzing the radiomics features of contrast-enhanced CT and their association with genomics profiles of ccRCC samples, which has not been extensively researched. In order to select the imaging features significantly correlated to the prognosis of ccRCC, we applied several machine learning algorithms. Through machine-learning algorithms, we further estimated the correlation between prognosis-related image features (PRIF) and expressed genes profiles. Furthermore, the integration of radiomics and gene features was conducted to enhance the accuracy of prognostic evaluation. Eventually, we conducted validation of the imaging-genomic prognostic factors (IGPF) model, and the results suggested that these features may be of help in the prediction of prognosis in ccRCC patients. The potential connection and integration of macroscopic radiomics and genetic characteristics at the microscopic level needs further exploration.

MATERIALS AND METHODS

Data Source and Processing

The overall structure of our study was demonstrated in **Figure 1**. The detailed information of each section will be interpreted as follows. We downloaded the available enhanced CT images from the Cancer Imaging Archive (TCIA) portal (http://www.cancerimagingarchive.net/) and the information containing clinical features and mRNA sequencing data of corresponding ccRCC samples from the Cancer Genome Atlas (TCGA) database (https://portal.gdc.cancer.gov). In total 205 available samples were gathered. For data normalization, we firstly acquired the raw count data of the ccRCC patients from the

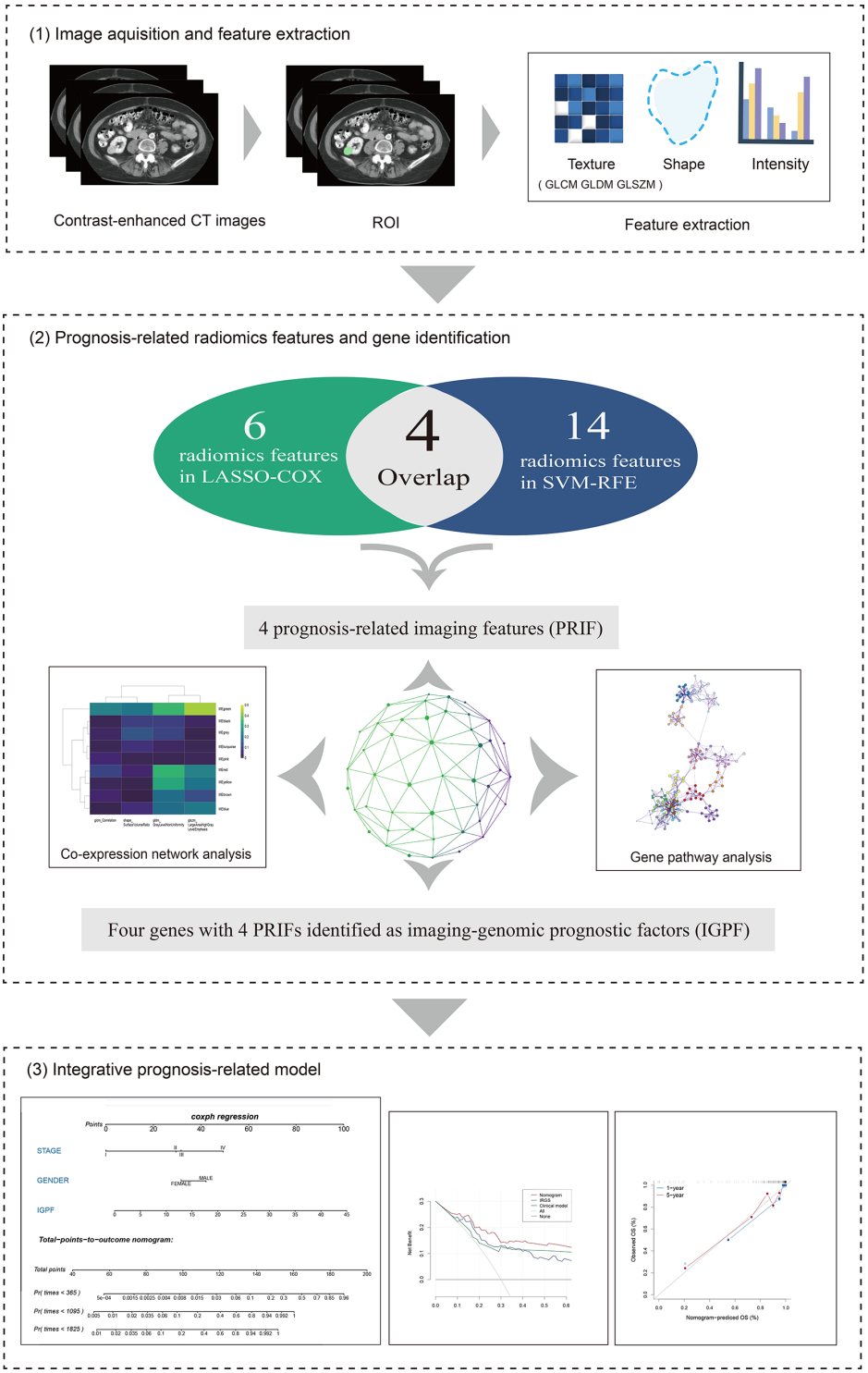

FIGURE 1 | The overall framework of data analysis and model integration. 1) The segmentation of tumor region of interest (ROI) of contrast-enhanced CT images was performed by 3D slicer. Radiomics features of the ROIs were then extracted. 2) The selection of prognosis -related radiomics features was implemented by LASSO-COX Regression and SVM-RFE machine learning methods. The identification of prognostic gene modules was carried out by co-expression gene network analysis through WGCNA, and gene pathway analysis was subsequently performed. 3) The integration and assessment of prognosis-related radiomics features and gene signature was conducted by random forest (RF). Finally, the nomogram incorporating clinical predictors and imaging-genomic prognostic factors (IGPF) of ccRCC patients was constructed *via* R package rms.

TCGA-KIRC project. Then we normalized the raw count data using variance stabilizing transformation through the vst function of DESeq2 package.

Extraction of CT Image Features

Tumor segmentation and feature extraction were performed using 3D slicer (Version 4.7) software. 3D slicer is an open source software platform which functions in medical image processing, analysis (including registration and interactive segmentation) and versatile visualization for image-guided therapy (24). We loaded deidentified transverse CT images (DICOM) of ccRCC into the software and conducted segmentation of area for each lesion with a paint function. The delineation of the region of interest (ROI) was firstly conducted by Xuelei Ma, an oncologist with experience in CT interpretation. To access the intra- and inter-rater feature stability against ROI delineation variations caused by human factors, Xuelei Ma and another experienced oncologist Ye Zhao conducted the delineation of the ROI again. Through the icc function of R package irr, we calculated the intraclass correlation coefficient and accessed the repeatability and stability of the radiomics features based on the ROI conducted by Xuelei Ma twice and that conducted by Ye Zhao (used for accessing the inter-rater stability of radiomics features).

Next we performed feature extraction calculations of ccRCC patients *via* pyradiomics package (https://pyradiomics.readthedocs.io/en/latest/), an extension *via* the 3D Slicer ExtensionManager. The pyradiomics is an open-source python package for the extraction of radiomics features from medical imaging, and most features are in compliance with feature definitions as described by the Imaging Biomarker Standardization Initiative (IBSI). Notes are added to specify the differences where the features vary in the website (25). Eventually, we obtained a total of 107 features in various classes. For instance, first order statistics describe the distribution of voxel intensities within the image region, including skewness, maximum, minimum, mean, range, and entropy etc. Shape-based category depicts shape eigenvalue of ROI and in 3-dimentional size. Gray Level Cooccurrence Matrix (GLCM) features and Gray Level Run Length Matrix (GLRLM) represent the eigenvalue of high-order texture characteristics. Other features extracted were contained in Gray Level Size Zone Matrix (GLSZM), Neighboring Gray Tone Difference Matrix (NGTDM) and Gray Level Dependence Matrix (GLDM).

Selection of Prognosis-Related Radiomics Features

All the ccRCC samples were randomly assigned to training and test cohorts on a scale of 1:1. Based on the training set, we applied the least absolute shrinkage and selection operator COX (LASSO-COX) and support vector machines-recursive feature elimination (SVM-RFE) algorithm in R package "glmnet" and "e1071" respectively using 5-fold cross-validation approach to filtrate prognosis-related imaging features (PRIF). LASSO-COX reduces feature space dimension and filters variables by performing a penalized function that compresses insignificant coefficients to zero, and therefore contracts subsets and processes data with complex collinearity. The cv.glmnet function of glmnet package provides an argument for K-fold cross validation called "nfolds", and this argument was set at 0.04396 for 5-fold cross validation.

SVM arranges the extracted image features in descending order according to the variable importance and inputs them to the training model in sequence in each iteration of the cross-validation calculation, thus measuring the overall accuracy of the training sets during the accumulation course. SVM-RFE is a sequence backward selection algorithm based on the maximum interval principle of SVM. We applied the 5-fold cross validation algorithm as the resampling method for SVM-RFE. The final importance of features was based on the average importance of each feature in each iteration. Afterwards, we compared the features displayed in the outcome of two methods and selected those within the intersection of two subsets as PRIF for subsequent analyses.

Gene Co-Expression Network Analysis

To further explore the molecular biological mechanisms of the prognostic-related CT image features and obtain gene expression modules, we conducted weighted gene co-expression network analysis (WGCNA) based on training dataset. WGCNA is a systematic analytical tool which describes the correlation patterns among genes across microarray samples and clusters genes into modules, hence investigating the association between gene sets and clinical traits. The main workflow started with measuring adjacency coefficient which computes the joint strength between two nodes. Next we reduced the co-expression similarity to ensure a scale-free network. The topological overlap measure (TOM) was performed to eliminate false correlation, and then we conducted average linkage hierarchical clustering and classified functional gene modules in the co-expressed network. The module eigengenes (ME) was the first principal component of the expression matrix which represented the gene expression profile of the entire module. Afterwards we assessed the correlation between MEs and previously screened image features to identify the most relevant clinically significant module. Then to assess the preservation of the connectivity and density between each couple of modules (from the train and test networks), we carried out a permutation test through the function modulePreservation from the WGCNA package. This function provides a summary preservation Z-score for each module. Furthermore we applied Gene ontology (GO) enrichment analysis *via* Metascape (http://metascape.org) to evaluate the interlinkage between key modules.

Construction of Integrative Imaging-Genomic Prognostic Model

We utilized random forest (RF) algorithm with 1,000 decision trees (DTs) through "randomForestSRC" (rfsrc) in R to obtain optimal prognostic factors. RF algorithm constructs and assembles multiple decision trees based on data samples to attain a more precise prediction, which can reduce the over-

fitting by averaging the result. The default arguments of the rfsrc function contained a resampling method argument "bootstrap". The default value of the "bootstrap" argument was "by.root", which bootstraps the data by sampling with replacement at the root node before growing the tree. Based on training set we firstly constructed two prognostic models, one of which incorporated prognosis-related imaging features (PRIF) and the other integrated PRIF and the expressed genes profiles. The latter was defined as imaging-genomic prognostic factor (IGPF) model. Meanwhile we evaluated the prediction performance of the two models with test set using 5-fold cross-validation. Subsequently, we performed the discrimination of the signature by plotting the receiver operating curve (ROC) and calculating the corresponding area under curve (AUC) based on average accuracy of 5 iterations. ROC curve analysis obtained generalization abilities based on the means computed by all cross validation sets and the average 1-, 3-, and 5-year AUCs were then assessed. Furthermore, we calculated the risk scores for all ccRCC patients using RF, and patients were then separated into high-risk group and low-risk group based on the median cut-off value of risk scores. The overall survival (OS) of the two groups was acquired and displayed *via* Kaplan-Meier survival curve analysis and then compared by log rank test.

Univariate and multivariate Cox regression analyses were performed to further identify the predictive factors of survival outcome. Variables with $p < 0.05$ in univariate Cox regression analysis were considered statistically significant and selected for multivariate analysis. On the grounds of the results of Cox regression analysis we established a nomogram based on the training dataset, which comprised the IGPF and certain clinical factors including stage and gender through R package rms. Calibration plots were then applied based on training set to evaluate the predictive performance of the nomogram by illustrating the consistency between predicted OS and observed OS and model discrimination was estimated by the concordance index (C-index). Moreover we employed the decision curve analysis (DCA) based on training set to assess the clinical availability of the nomogram by calculating the net benefit under a range of threshold probabilities.

TABLE 1 | Demographic and clinical characteristics of patients.

Characteristics	Total (n=205)	Train (n=103)	Test (n=102)	P value
	NO.	NO. (%)	NO. (%)	
Age at diagnosis (years)				0.081
Mean ± SD	59.7 ± 12.2	58.4 ± 12.7	61.0 ± 11.7	
Gender				0.433
Male	134	70(68.0)	64(62.7)	
Female	71	33(32.0)	38(37.3)	
T classification				0.179
T1	109	56(54.4)	53(52.0)	
T2	22	15(14.6)	7(6.9)	
T3	70	31(30.1)	39(38.2)	
T4	4	1(0.9)	3(2.9)	
N classification				0.856
N0	83	43(41.7)	40(39.2)	
N1	5	2(1.9)	3(2.9)	
Unknown	117	58(56.4)	59(57.9)	
M classification				0.146
M0	176	93(90.3)	83(81.4)	
M1	28	10(9.7)	18(17.6)	
Unknown	1	0(0.0)	1(1.0)	
TMN stage				0.200
I	106	56(54.4)	50(49.0)	
II	18	12(11.6)	6(5.9)	
III	51	24(23.3)	27(26.5)	
IV	30	11(10.7)	19(18.6)	
Grade				0.227
G1	1	1(1.0)	0(0.0)	
G2	80	40(38.8)	40(39.2)	
G3	91	50(48.5)	41(40.2)	
G4	33	12(11.7)	21(20.6)	
OS (days)				0.090
Mean ± SD	1371.0 ± 925.1	1493.5 ± 996.7	1247.2 ± 833.5	

RESULTS

Acquisition of Prognosis-Related Radiomics Features

We initially obtained the patient data containing clinical features and mRNA sequencing data of 537 ccRCC samples from TCGA database and the matched CT images of 237 ccRCC patients from TCIA portal, among which 205 samples with available and complete data were enrolled for subsequent analyses. The patient clinical characteristics are listed in **Table 1**. The results of the repeatability and stability assessment showed that most of the radiomics features (104 of 107) were stable against ROI delineation variations caused by human factors (icc > 0.75 and $p < 0.05$). The raw data of the ROI delineation by two oncologists were presented in **Supplementary Material 1**. A total of 107 features of six categories were firstly extracted from original CT images from the ROIs using pyradiomics package, and the results adhered to the IBSI recommendations (**Supplementary Material 1**, icc data). To acquire a reliable and robust model, we randomly divided the ccRCC samples into a training set (n=103) and a test set (n=102) in a 1:1 ratio and proceeded to the further selection based on the training dataset. In an attempt to diminish the possibility of module overfitting by too many radiomics features and select the ones with higher prediction accuracy for OS, two machine-learning approaches including LASSO-Cox regression and SVM-RFE were employed for mutual authentication. The tuning parameter λ was settled at an optimal value of 0.04396 with the minimum criteria in LASSO regression, and 6 prognostic features were identified with nonzero coefficients out of 107 radiomics features (**Figure 2A**). As the extracted features ranked and excluded sequentially in SVM classifier during each iteration by contribution value, we found that the best prediction performance appeared when the first 14 radiomics features were included during the 5-fold cross validation (**Figure 2B**).

Therefore, the top 14 features in contribution value were filtrated as prognosis-related features for further module construction, covering six in GLCM, three in GLSZM, one in GLDM, two in shape, one in NGTDM and one in first order.

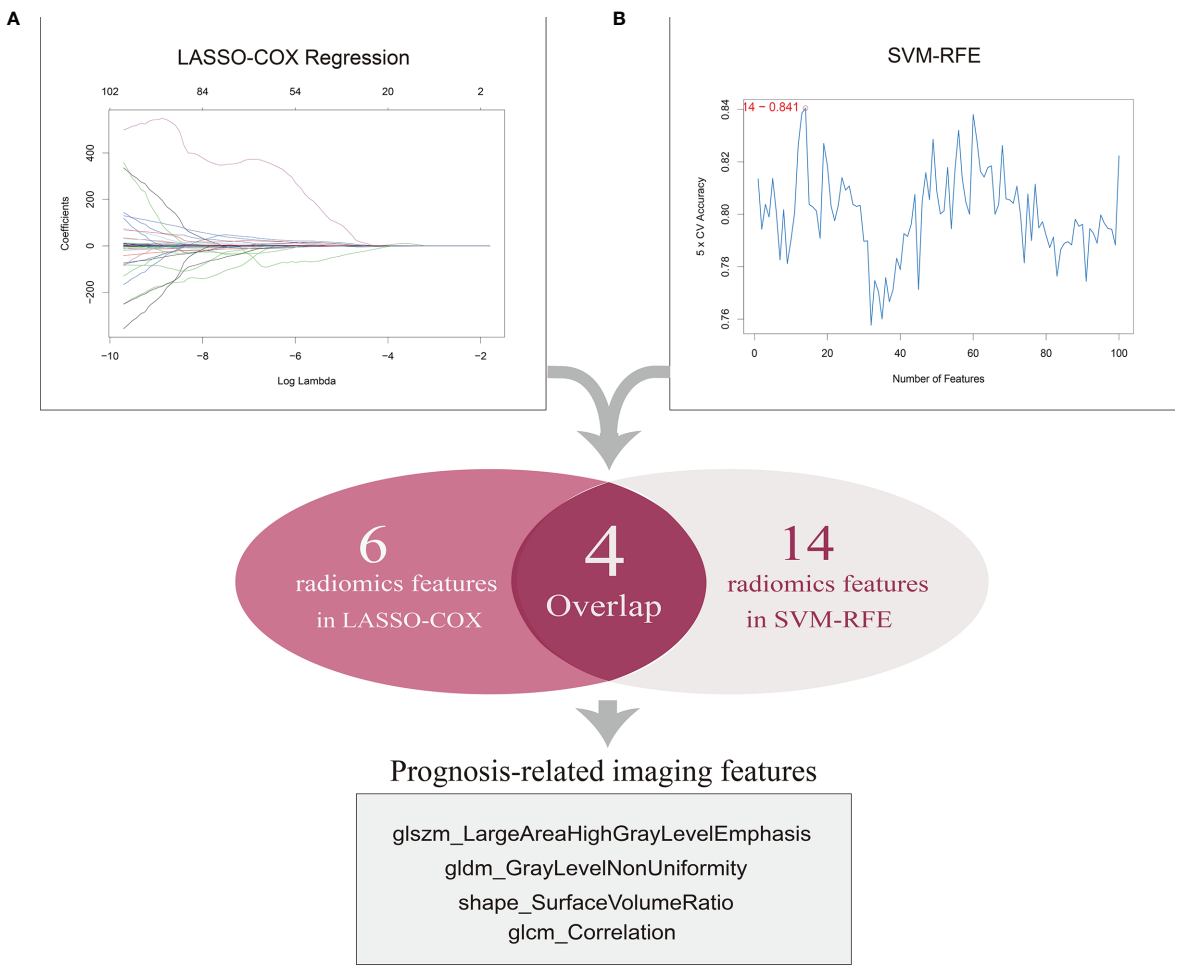

FIGURE 2 | Selection of prognosis-related imaging features (PRIF). **(A)** A total of six features were identified by LASSO-COX regression analysis. The horizontal axis represents the lambda value and vertical axis represents independent variable coefficient. **(B)** A total of 14 features selected by SVM-RFE. And four imaging features within in the overlap were defined as PRIF.

Eventually four features with predictive efficiency (glszm_LargeAreaHighGrayLevelEmphasis, gldm_GrayLevelNonUniformity, shape_SurfaceVolumeRatio, glcm_Correlation) within the overlap of the results produced by the two methods were identified as prognosis-related imaging features (PRIF) (**Figure 2**).

Identification of Co-Expressed Gene Modules Related to Prognostic Image Features

To identify the gene modules highly correlated to PRIF in the ccRCC samples, we performed WGCNA to build a gene co-expression network based on training dataset. Threshold powers were set from 1 to 20 to choose an applicable soft-thresholding power, and the top 25% most variant genes (4,936 genes) ranked in descending order of SD sequence were included for subsequent analyses. A total of nine co-expressed gene modules were identified *via* the hierarchical clustering dendrogram (**Figures 3A, B**). Relationships of the modules were illustrated in a heatmap drawn by adjacencies (**Figure 3C**). Afterwards, we conducted correlation analysis to estimate the association between nine MEs and image traits (**Figure 3D**). The correlation coefficients and FDR values between each of the nine gene modules and PRIF were displayed in **Supplementary Material 2**. Of all the nine gene co-expression modules, the green module (625 genes) displayed the most significant correlation with the prognosis-related image features of ccRCC, including glszm_LargeAreaHighGrayLevelEmphasis, gldm_GrayLevelNonUniformity, shape_SurfaceVolumeRatio and glcm_Correlation. The module preservation analysis presented by the summary preservation Z-score showed that all the modules were rather stable and the green module was the most robust between training and test sets (**Figure 3E**). Thus we identified the green module as the key module of significant prognostic importance for continuous research.

Furthermore we carried out enrichment analysis to describe the biological interpretations of the genes in green module (**Supplementary Material 3**). As illustrated in **Figure 4**, the

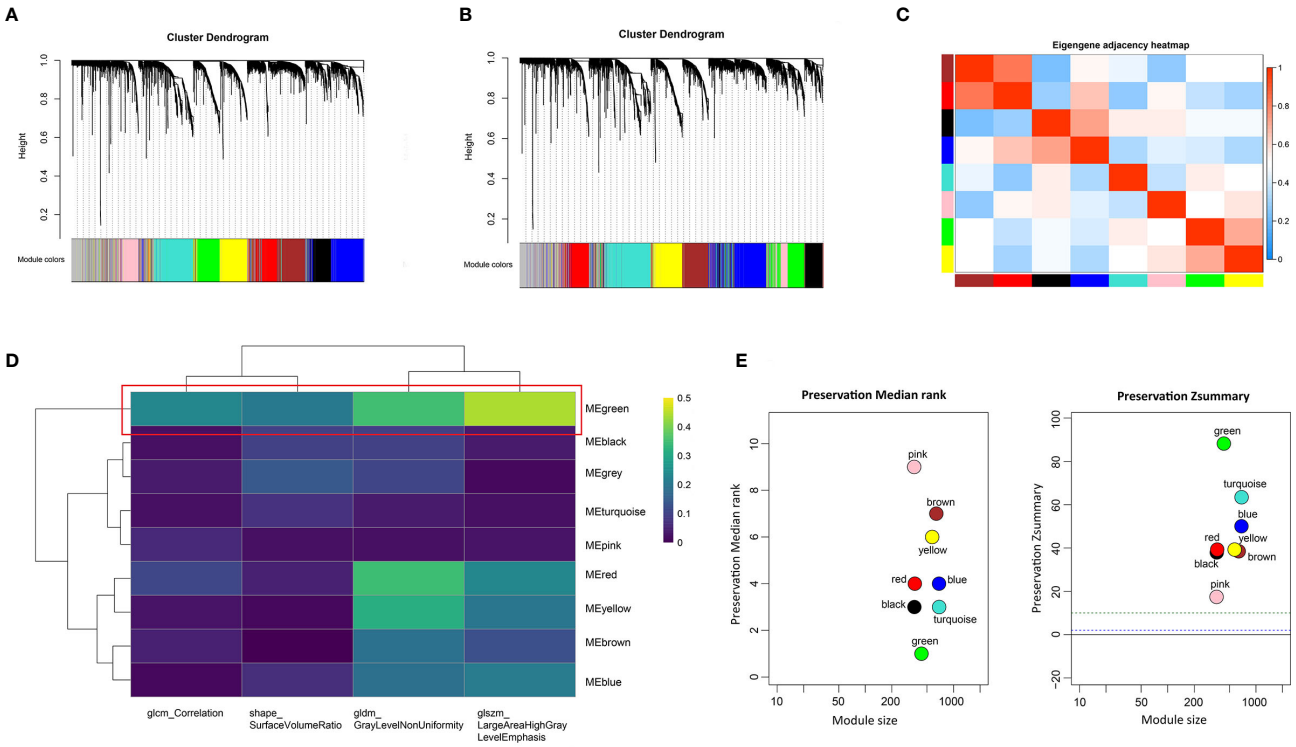

FIGURE 3 | Identification of prognosis-related co-expressed gene module. **(A)** The cluster dendrogram of genes in training dataset. **(B)** The cluster dendrogram of genes in test dataset. Each branch represents one gene and each color below denotes one co-expression gene module. **(C)** Heatmap plot of relationship analysis between co-expression gene modules. **(D)** Heatmap of the correlation analysis between module eigengenes and PRIF. The green module showed the most significant correlation. **(E)** The summary preservation Z-score for each module. The higher the Z-score is, the higher the module preservation will be, whereas values below 10 indicate a moderate-to-low preservation.

genes were significantly related to certain biological processes such as blood vessel development, circulatory system process, cell morphogenesis involved in differentiation, cell-substrate adhesion, and extracellular structure organization. The results suggested that these genes may be involved in tumor angiogenesis and cell adhesion, which have been proved to be associated with tumorigenesis and progression.

Construction and Validation of Integrated Imaging-Genomic Prognostic Model

In order to establish an integrative model of PRIF and prognostic co-expressed gene profile, we applied RF algorithm based on training dataset, and furthermore performed model verification with the test dataset. Initially we presented PRIF as an independent variable to analyze its impact on prognosis and found a significant correlation. Then to explore the combined effect of genomics and imaging features, we assessed gene expression profiles in the prognostic-related green module and selected the top four genes with the highest module membership (MM) value (RPS6KA2, CYYR1, KDR, GIMAP6) (**Supplementary Material 4**, **Figure S1**).

Furthermore, we integrated the four genes with PRIF which were identified as imaging-genomic prognostic factors (IGPF) and calculated the risk score of each ccRCC patient. The patients were divided into high-risk and low-risk groups in light of the median value of risk scores and then estimated with time-dependent ROC. To evaluate the statistical differences between different models, we applied the compare function of timeROC package in both training and test sets. The result showed that there were statistically significant differences between RPIF and IGPF models in 1-, 3-, and 5-year OS ($P<0.05$) (**Table 2**). The outcome illustrated a more satisfactory predictive performance of IGPF model compared to the RPIF model alone (**Table 3**). In the training set, the average AUCs for 1-, 3-, and 5-year OS were 0.845, 0.772, and 0.737 in PRIF model compared to 0.898, 0.849 and 0.808 in IGPF model respectively (**Figures 5C**, **6C**). In the test set, the average AUCs for 1-, 3-, and 5-year OS were 0.814, 0.74 and 0.689 of PRIF model compared to 0.837, 0.806 and 0.751 of the combined IGPF module (**Figures 5D**, **6D**).

Establishment and Evaluation of Nomogram Model

According to Kaplan-Meier survival curves, a distinctly significant difference of $p < 0.0001$ can be seen between the two groups in both test and train cohorts, and patients in the low-risk group showed a more promising OS than the high-risk group (**Figures 5A, B**, **6A, B**). In consideration of the relationship of IGPF and certain clinical predictors, we

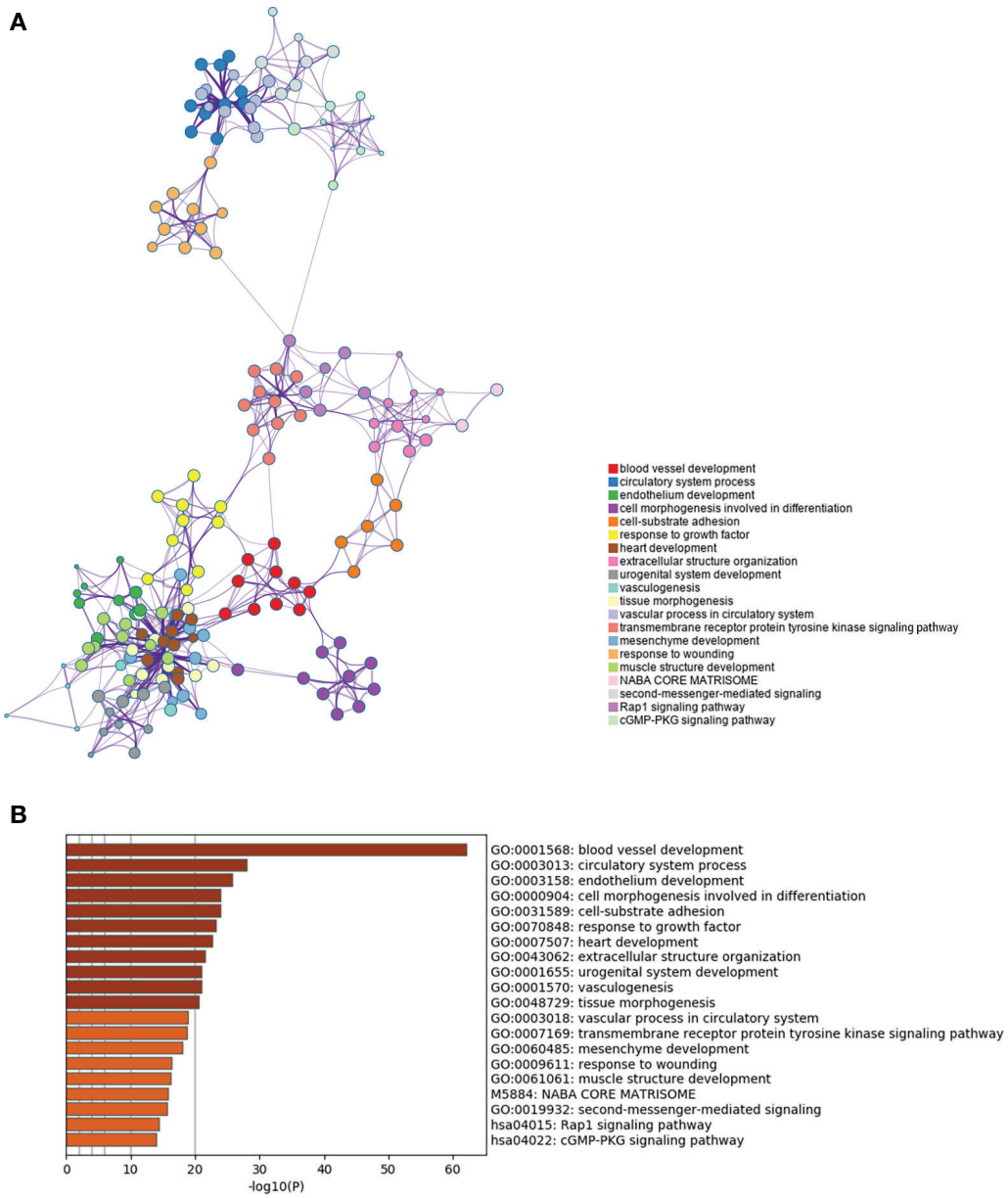

FIGURE 4 | Enrichment analysis of the prognosis-related gene co-expression green module. **(A)** Metascape enrichment network visualization cluster of genes in green module. Each circle node denotes one term and the color of node indicates its cluster identity, representing the intra-cluster and inter-cluster similarities of enriched terms. Cluster annotations and the most significantly enriched terms are shown in color code. **(B)** GO enrichment analysis of the co-expressed genes in green module.

TABLE 2 | Comparison of PRIF and IGPF models in training set and test set.

Dataset	Time (d)	P value
Train	t=365	0.294493777
(n=103)	t=1095	0.012522423
	t=1825	0.006498863
Test	t=365	0.048720526
(n=102)	t=1095	0.02381105
	t=1825	0.007957811

PRIF, prognosis-related imaging features; IGPF, imaging-genomic prognostic factors.

performed univariate and multivariate Cox analysis. The results indicated that clinical characteristics including gender, TNM stage and IGPF were independent risk factors for OS of ccRCC patients. In order to acquire a quantitative prediction method for disease progression and survival probability of ccRCC, we established a nomogram on the basis of the independent predictors of OS (gender, TNM stage, and IGPF) identified earlier (**Figure 7A**). Calibration plots were then applied to assess the consistency between the nomogram-predicted values and actual values, and the calibration curves in **Figure 7B**

TABLE 3 | Survival models based on PRIF and IGPF in training set and test set.

Model		HR	z	P value	lower	upper	c-index	se(C-index)
Train	IGPF	9.555645221	3.663583845	0.000248711	2.856506317	31.96574608	0.7435393	0.0303249
(n=103)	PRIF	5.890757826	3.171763552	0.001215163	2.833927216	14.04278158	0.68764045	0.04130209
Test	IGPF	7.624785255	4.189170631	0.000027998	2.947573776	19.72379815	0.74161074	0.02908009
(n=102)	PRIF	4.461795265	3.522355167	0.000427731	1.941329799	10.25462907	0.68504314	0.03922711

PRIF, prognosis-related imaging features; IGPF, imaging-genomic prognostic factors.

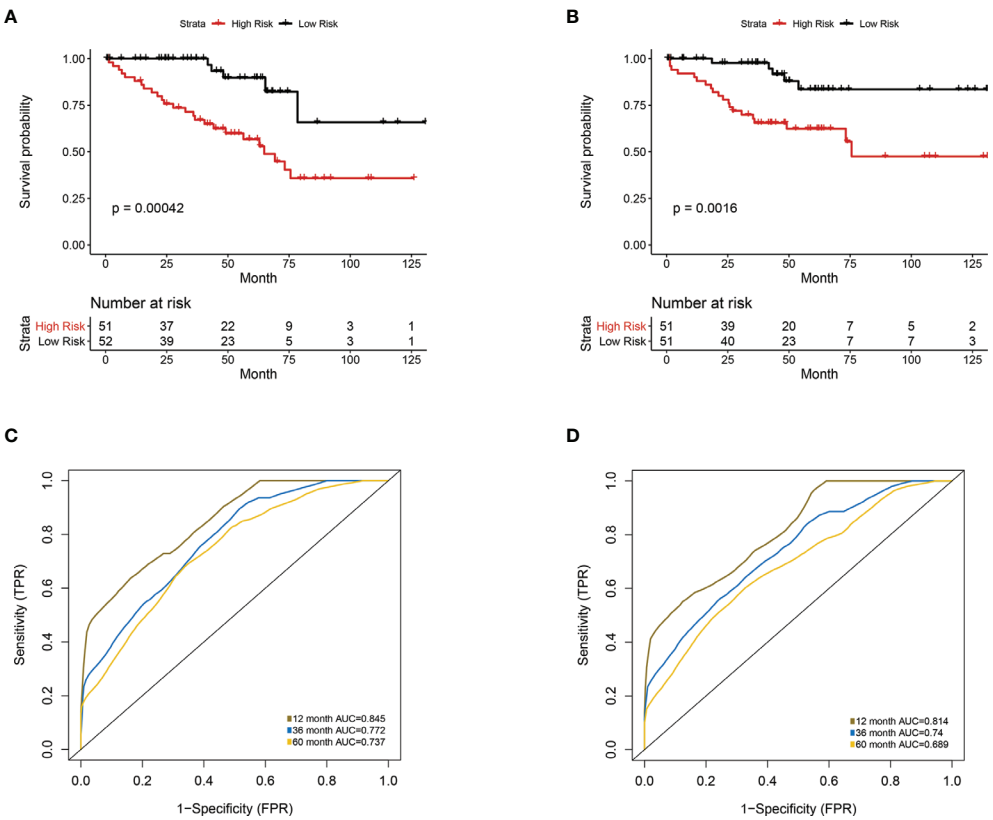

FIGURE 5 | Univariate analysis of prognosis-related radiomics features model. Patients were divided into high-risk group and low-risk group according to the median value of IGPF risk score. **(A, B)** Kaplan-Meier curves demonstrating overall survival (OS) of patients in high-risk group and low-risk group in **(A)** training set and **(B)** test set. **(C, D)** The 1-, 3-, and 5-year area under curve (AUC) of receiver operating curve (ROC) in **(C)** training set and **(D)** validation test set.

denoted good performance of 1- and 5-year nomogram model which showed a closer tendency to the 45-degree standard line. Meanwhile, the decision curves analysis evaluated the clinical utility of IGPF model containing radiomics and gene features, clinical model that involved TNM stage and gender and nomogram which integrated the former two models **(Figure 7C)**. As depicted in the results, nomogram provided the best net benefit among most of the threshold probabilities range.

DISCUSSION

In this study, we extracted radiomics features from contrast-enhanced CT images of ccRCC, and subsequently selected prognosis-related image features (PRIF) with significant prognostic value *via* several machine-learning algorithms. Furthermore we identified gene modules that are most relevant to PRIF through co-expression network. Based on the PRIF (screened by LASSO and SVM-RFE) and genes (screened by WGCNA and MM value), we constructed a robust imaging-genomic prognostic factors (IGPF) model incorporating prediction features in the two categories through random survival forest algorithm. The random survival forest algorithm acts as a bootstrap algorithm and can predict the overall survival. The OS prediction analysis demonstrated a notable performance of the integrative prognostic model, and thus the IGPF based risk score was considered as an independent prognostic factor. Afterwards, through nomogram we integrated the IGPF model

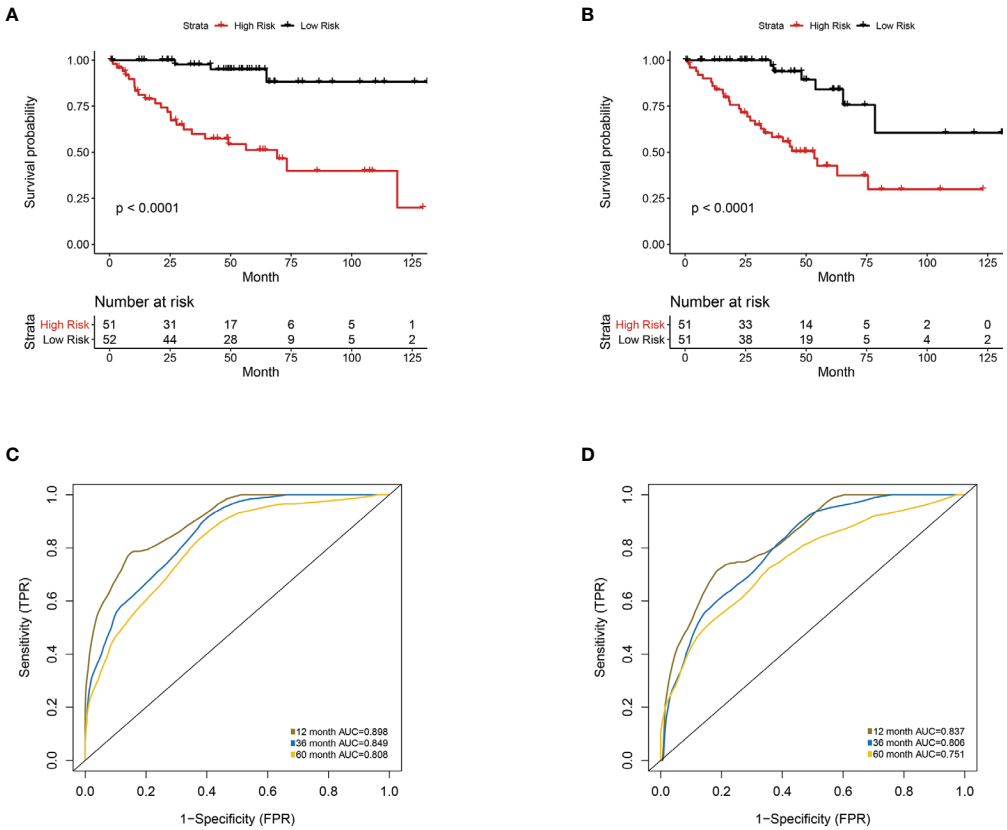

FIGURE 6 | Multivariate analysis of the integrative prognostic model incorporating radiomics and genomics features. Patients were divided into high-risk group and low-risk group according to the median value of IGPF risk score. **(A, B)** Kaplan-Meier curves demonstrating OS of patients in high-risk group and low-risk group in **(A)** training set and **(B)** test set. **(C, D).** The 1-, 3-, and 5-year area under curve (AUC) of receiver operating curve (ROC) in **(C)** training set and **(D)** validation test set.

and clinical predictor model, and then made comparisons of the three prognostic models. Ultimately, the prediction capability of the nomogram model outweighed the other two.

On the basis of the initially obtained 107 imaging features, we employed two machine-learning methods LASSO-Cox and SVM-RFE in combination aiming to achieve a group of prognostic radiomics features with more robust and accurate prediction abilities. Four conspicuous prognosis-related image features in our study were included in Gray Level Size Zone Matrix (GLSZM), Gray Level Dependence Matrix (GLDM), shape and Gray Level Cooccurrence Matrix (GLCM) respectively. As illustrated in the results, features based on intensity discretization were not screened out in the end. The results suggested that under these two unsupervised feature selection algorithms, the gray level-based features and shape-based features had a better prognostic performance than intensity discretization-based features in this cohort. However, considering the differences and limitations among multiple algorithms and cohorts, we cannot completely deny the importance of intensity discretization-based features.

A gray level zone is described as the number of connected voxels which show the same intensity. The texture feature Large Area High Gray Level Emphasis from GLSZM quantifies the proportion in the image of the joint distribution of smaller size zones with higher gray-level values, which has been formerly adopted in the assessment of the robustness or patient response in different imageological examinations (26, 27). The GLDM-based textural feature Gray Level Non Uniformity (GLN) calculates the similarity of gray-level intensity values, where a lower GLN refers to a higher intensity value in the image (28). Surface Area to Volume Ratio is a shape feature that is not dimensionless and is partly dependent on the volume of the ROI. It has been utilized in differentiating the benign and malignant tumors based on shape and margin of the lesions (29, 30). GLCM conduces to reflecting the comprehensive information about pixel distribution containing direction, distance, gray value, and the pattern of gray level arrangement (28), and Correlation represents the linear dependency of gray level values to their respective voxels in the GLCM textural features. It has been applied previously in the evaluation of breast cancer, osteosarcoma, lung cancer and gliomas in imaging modalities such as CT, MRI, and PECT (31–35).

In our study, the predictive efficacy of the elected prognostic related radiomics features based on training set were found to be in accordance with some of the reference research above (30, 33,

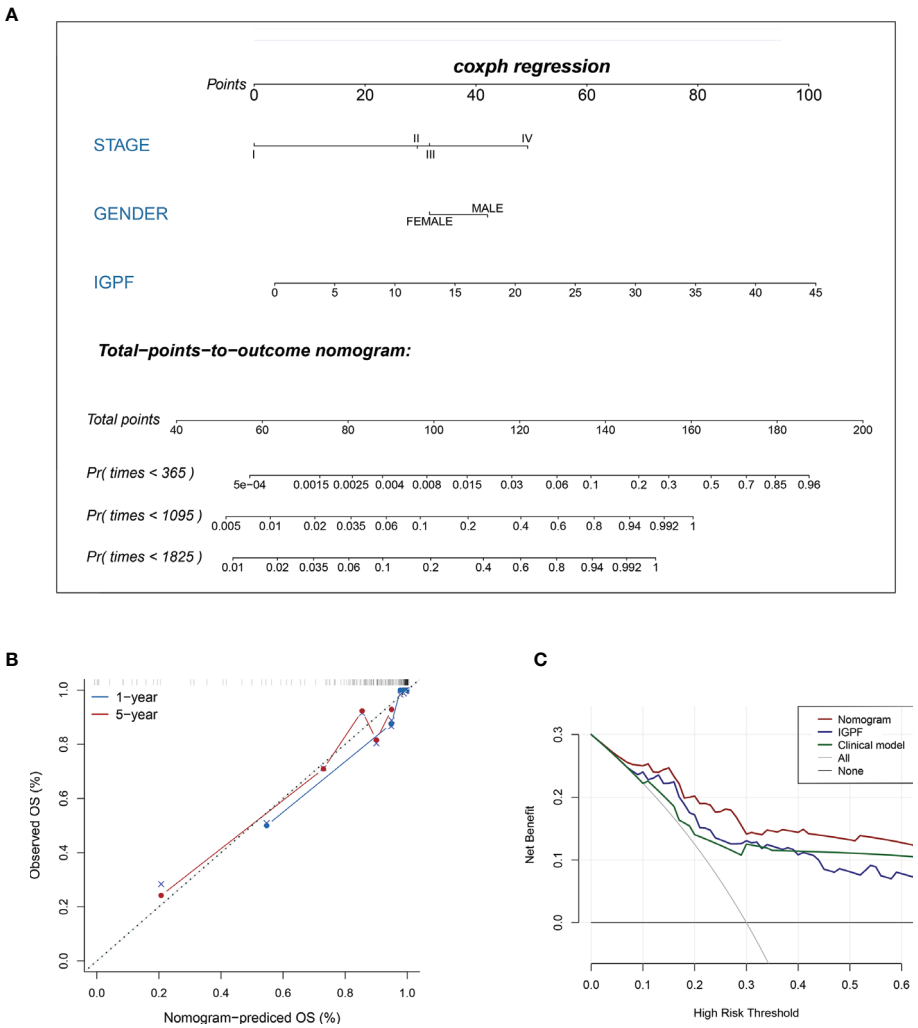

FIGURE 7 | Construction and validation of prognostic nomogram model. **(A)** The nomogram prediction of the 1-, 3-, and 5-year OS of ccRCC patients. **(B)** Calibration plots of the nomogram for 1- and 5-year OS prediction. The horizontal axis represents nomogram-predicted survival probability and the vertical axis represents actual survival. **(C)** Decision curve analyses of IGPF, clinical and nomogram model. The gray oblique line represents the net benefit of all intervening patients, and the horizontal gray line indicates the net benefit of no intervening patients. The nomogram model showed the best net benefits in the vast majority of the threshold probability range.

34, 36). However, a lot of former studies have concentrated on the performance of textural features of radiographic images, which may lack a comprehensive explanation of the biological mechanism and potential biomolecular features of the disease. While in our study, we conducted the identification of the prognostic gene co-expression module and then evaluated the association between the imaging phenotype and genomic characteristics. The results demonstrated that the green module was most related to all the PRIF, and gldm_gray level non uniformity feature could be mostly affected by gene expression pattern. In addition, the red and yellow modules also had a relatively high correlation with the gldm_gray level non uniformity feature. This may be related to the objective attributes of this feature, and further studies are still needed to explain the potential relevance and biological mechanism between gene modules and radiomics features. Moreover, we implemented enrichment analysis in order to elaborate the latent molecular pathways relevant to the prognostic significant green gene module.

The results indicated that the most prominent enrichment leans towards pathways involved in tumor angiogenesis, cell adhesion and extracellular structure organization. Formation of new vascular networks is a pivotal step in tumor progression and also expedites the metastasis of cancer cells (37). At present, tumor microvessel density (MVD) and VEGF are important immunohistochemical indicators for tumor angiogenesis, and studies have reported that three-phase dynamic enhanced CT and MRI can be utilized as auxiliary evaluation methods for tumor angiogenesis, malignancy and prognosis in ccRCC (38–40). Cell-substrate adhesion has been widely demonstrated as an

indispensable process of metastasis *in vivo* (41). The modification of cell adhesion status has significant impact on biophysical patterns of tumor microenvironment (TME) and structure of extracellular matrix (ECM), which has been reported to be related to the prognosis of colorectal cancer, lung cancer and gastric cancer (42–45). In accordance with previous researches, the results may provide a chance to understand the upstream biological mechanisms of tumor development in ccRCC (46–48). RPS6KA2, CYYR1, KDR, and GIMAP6 were discovered to be most correlated with the prognostic-related module eigengene, which was also found relevant to blood vessel development and cell proliferation in existing researches. For instance, KDR has been reported to acts as an important mediator of VEGF-induced endothelial proliferation, tubular morphogenesis and sprouting and associate with signaling by GPCR pathway (49, 50). RPS6KA2 has been found to act downstream of EGFR, RAS, and ERK signaling, which mediates mitogenic and stress-induced activation of transcription factors and thus regulate the proliferation and differentiation of cells (51, 52).

Subsequently, we integrated the prognosis-related image features and gene profiles into an IGPF model and obtained corresponding risk scores. The clinical model took in gender and TNM stage as the common tumor assessment indicators for prognosis, but the predictive accuracy is still limited. The nomogram which integrated IGPF and clinical predictors was validated to outperform all the models with the best prediction performance.

There were several limitations to this study. First of all, the sample size was comparatively small because patients with available identified transverse CT images and gene expression profiles were limited. Secondly, the data of patients we enrolled may be incomplete, which might create discrepancies and lead to potential bias. To better promote the conclusions and understand the underlying biology molecular mechanism, a larger scale of multi-center data verification is necessarily needed. Thirdly, since we used random survival forest algorithm to build survival prognosis model in this study, the bootstrap step was a built-in process and the bootstrap corrected results could not be reported. Fourthly, more clinical trials and experimental researches are needed to assess the prove the adaptability of the imaging-genomic prognostic model, and the molecular mechanisms remain to be further explored.

In conclusion, in this study we constructed an integrative prognosis-related model incorporating radiomics features, genomic profile and clinical indicators. The results illustrated that IGPF may improve the prognostic modalities on the basis of conventional clinical indexes, and the nomogram prediction model can serve as an advantageous measurement tool which may be conducive to personalized treatment and prognosis for ccRCC patients.

DATA AVAILABILITY STATEMENT

Publicly available datasets were analyzed in this study. This data can be found here: http://www.cancerimagingarchive.net/; https://portal.gdc.cancer.gov.

AUTHOR CONTRIBUTIONS

YH: data curation, writing – original draft and submission. HZ: conceptualization, methodology, and software. LC: validation, writing – reviewing and editing. YL: writing – reviewing and editing. XM: conceptualization and supervision. YZ: conceptualization and supervision. All authors contributed to the article and approved the submitted version.

FUNDING

The study was funded by the National Natural Science Foundation of China, grant no. 31701212.

SUPPLEMENTARY MATERIAL

The Supplementary Material for this article can be found online at: https://www.frontiersin.org/articles/10.3389/fonc.2021.640881/full#supplementary-material

REFERENCES

1. Hsieh JJ, Purdue MP, Signoretti S, Swanton C, Albiges L, Schmidinger M, et al. Renal cell carcinoma. *Nat Rev Dis Primers* (2017) 3:17009–9. doi: 10.1038/nrdp.2017.9
2. Jiang Y, Li W, Huang C, Tian C, Chen Q, Zeng X, et al. Preoperative CT Radiomics Predicting the SSIGN Risk Groups in Patients With Clear Cell Renal Cell Carcinoma: Development and Multicenter Validation. *Front Oncol* (2020) 10:909. doi: 10.3389/fonc.2020.00909
3. Siegel R, Miller K, Jemal A. Cancer statistics, 2019. *CA: Cancer J Clin* (2019) 69(1):7–34. doi: 10.3322/caac.21551
4. Cairns P. Renal cell carcinoma. *Cancer Biomarkers Section A Dis Markers* (2010) 9:461–73. doi: 10.3233/CBM-2011-0176
5. Lambin P, Rios-Velazquez E, Leijenaar R, Carvalho S, van Stiphout RG, Granton P, et al. Radiomics: extracting more information from medical images using advanced feature analysis. *Eur J Cancer* (2012) 48(4):441–6. doi: 10.1016/j.ejca.2011.11.036
6. Lambin P, Leijenaar RTH, Deist TM, Peerlings J, de Jong EEC, van Timmeren J, et al. Radiomics: the bridge between medical imaging and personalized medicine. *Nat Rev Clin Oncol* (2017) 14(12):749–62. doi: 10.1038/nrclinonc.2017.141
7. Balagurunathan Y, Gu Y, Wang H, Kumar V, Grove O, Hawkins S, et al. Reproducibility and Prognosis of Quantitative Features Extracted from CT Images. *Trans Oncol* (2014) 7(1):72–87. doi: 10.1593/tlo.13844
8. Cui E, Li Z, Ma C, Li Q, Lei Y, Lan Y, et al. Predicting the ISUP grade of clear cell renal cell carcinoma with multiparametric MR and multiphase CT radiomics. *Eur Radiol* (2020) 30(5):2912–21. doi: 10.1007/s00330-019-06601-1
9. Shu J, Wen D, Xi Y, Xia Y, Cai Z, Xu W, et al. Clear cell renal cell carcinoma: Machine learning-based computed tomography radiomics analysis for the

prediction of WHO/ISUP grade. *Eur J Radiol* (2019) 121:108738. doi: 10.1016/j.ejrad.2019.108738
10. Goyal A, Razik A, Kandasamy D, Seth A, Das P, Ganeshan B, et al. Role of MR texture analysis in histological subtyping and grading of renal cell carcinoma: a preliminary study. *Abdom Radiol (NY)* (2019) 44(10):3336–49. doi: 10.1007/s00261-019-02122-z
11. Coy H, Young JR, Pantuck AJ, Douek ML, Sisk A, Magyar C, et al. Association of tumor grade, enhancement on multiphasic CT and microvessel density in patients with clear cell renal cell carcinoma. *Abdom Radiol (NY)* (2020) 45 (10):3184–92. doi: 10.1007/s00261-019-02271-1
12. Ma Y, Cao F, Xu X, Ma W. Can whole-tumor radiomics-based CT analysis better differentiate fat-poor angiomyolipoma from clear cell renal cell caricinoma: compared with conventional CT analysis? *Abdom Radiol (NY)* (2020) 45(8):2500–7. doi: 10.1007/s00261-020-02414-9
13. Nie P, Yang G, Wang Z, Yan L, Miao W, Hao D, et al. A CT-based radiomics nomogram for differentiation of renal angiomyolipoma without visible fat from homogeneous clear cell renal cell carcinoma. *Eur Radiol* (2020) 30 (2):1274–84. doi: 10.1007/s00330-019-06427-x
14. Goh V, Ganeshan B, Nathan P, Juttla JK, Vinayan A, Miles KA. Assessment of response to tyrosine kinase inhibitors in metastatic renal cell cancer: CT texture as a predictive biomarker. *Radiology* (2011) 261(1):165–71. doi: 10.1148/radiol.11110264
15. Schieda N, Thornhill RE, Al-Subhi M, McInnes MD, Shabana WM, van der Pol CB, et al. Diagnosis of Sarcomatoid Renal Cell Carcinoma With CT: Evaluation by Qualitative Imaging Features and Texture Analysis. *AJR Am J Roentgenol* (2015) 204(5):1013–23. doi: 10.2214/AJR.14.13279
16. Peng J, Zhang J, Zhang Q, Xu Y, Zhou J, Liu L. A radiomics nomogram for preoperative prediction of microvascular invasion risk in hepatitis B virus-related hepatocellular carcinoma. *Diagn Interv Radiol* (2018) 24(3):121–7. doi: 10.5152/dir.2018.17467
17. Aerts HJ, Velazquez ER, Leijenaar RT, Parmar C, Grossmann P, Carvalho S, et al. Decoding tumour phenotype by noninvasive imaging using a quantitative radiomics approach. *Nat Commun* (2014) 5:4006. doi: 10.1038/ncomms5644
18. Lv J, Zhang H, Ma J, Ma Y, Gao G, Song Z, et al. Comparison of CT radiogenomic and clinical characteristics between EGFR and KRAS mutations in lung adenocarcinomas. *Clin Radiol* (2018) 73(6):590.e1–8. doi: 10.1016/j.crad.2018.01.009
19. Itakura H, Achrol AS, Mitchell LA, Loya JJ, Liu T, Westbroek EM, et al. Magnetic resonance image features identify glioblastoma phenotypic subtypes with distinct molecular pathway activities. *Sci Transl Med* (2015) 7 (303):303ra138. doi: 10.1126/scitranslmed.aaa7582
20. Seow P, Wong JHD, Ahmad-Annuar A, Mahajan A, Abdullah NA, Ramli N. Quantitative magnetic resonance imaging and radiogenomic biomarkers for glioma characterisation: a systematic review. *Br J Radiol* (2018) 91 (1092):20170930. doi: 10.1259/bjr.20170930
21. Kohannim O, Hibar DP, Jahanshad N, Stein JL, Hua X, Toga AW, et al. Predicting Temporal Lobe Volume On Mri From Genotypes Using L(1)-L(2) Regularized Regression. *Proc IEEE Int Symp BioMed Imaging* (2012) 1160–3. doi: 10.1109/ISBI.2012.6235766
22. Gill D, Hahn A, Hale P, Maughan B. Overview of Current and Future First-Line Systemic Therapy for Metastatic Clear Cell Renal Cell Carcinoma. *Curr Treat Options Oncol* (2018) 19(1):6. doi: 10.1007/s11864-018-0517-1
23. Allen E, Jabouille A, Rivera L, Lodewijckx I, Missiaen R, Steri V, et al. Combined antiangiogenic and anti-PD-L1 therapy stimulates tumor immunity through HEV formation. *Sci Trans Med* (2017) 9(385):eaak9679. doi: 10.1126/scitranslmed.aak9679
24. Fedorov A, Beichel R, Kalpathy-Cramer J, Finet J, Fillion-Robin J-C, Pujol S, et al. 3D Slicer as an image computing platform for the Quantitative Imaging Network. *Magn Reson Imaging* (2012) 30(9):1323–41. doi: 10.1016/j.mri.2012.05.001
25. van Griethuysen J, Fedorov A, Parmar C, Hosny A, Aucoin N, Narayan V, et al. Computational Radiomics System to Decode the Radiographic Phenotype. *Cancer Res* (2017) 77(21):e104–7. doi: 10.1158/0008-5472.CAN-17-0339
26. Edalat-Javid M, Shiri I, Hajianfar G, Abdollahi H, Arabi H, Oveisi N, et al. Cardiac SPECT radiomic features repeatability and reproducibility: A multi-scanner phantom study. *J Nucl Cardiol Off Publ Am Soc Nucl Cardiol* (2020). doi: 10.1007/s12350-020-02109-0
27. Ekert K, Hinterleitner C, Baumgartner K, Fritz J, Horger M. Extended Texture Analysis of Non-Enhanced Whole-Body MRI Image Data for Response Assessment in Multiple Myeloma Patients Undergoing Systemic Therapy. *Cancers* (2020) 12(3):761. doi: 10.3390/cancers12030761
28. Haralick RM, Shanmugam K, Dinstein I. Textural Features for Image Classification. *IEEE Trans Syst Man Cybern* (1973) SMC-3(6):610–21. doi: 10.1109/TSMC.1973.4309314
29. Cuocolo R, Stanzione A, Ponsiglione A, Romeo V, Verde F, Creta M, et al. Clinically significant prostate cancer detection on MRI: A radiomic shape features study. *Eur J Radiol* (2019) 116:144–9. doi: 10.1016/j.ejrad.2019.05.006
30. Kim J, Choi S, Lee S, Lee H, Park H. Predicting Survival Using Pretreatment CT for Patients With Hepatocellular Carcinoma Treated With Transarterial Chemoembolization: Comparison of Models Using Radiomics. *AJR Am J Roentgenol* (2018) 211(5):1026–34. doi: 10.2214/AJR.18.19507
31. Baidya Kayal E, Kandasamy D, Khare K, Bakhshi S, Sharma R, Mehndiratta A. Texture analysis for chemotherapy response evaluation in osteosarcoma using MR imaging. *NMR Biomed* (2020) 34(2):e4426. doi: 10.1002/nbm.4426
32. Chekouo T, Mohammed S, Rao A. A Bayesian 2D functional linear model for gray-level co-occurrence matrices in texture analysis of lower grade gliomas. *NeuroImage Clin* (2020) 28:102437. doi: 10.1016/j.nicl.2020.102437
33. Coroller T, Agrawal V, Narayan V, Hou Y, Grossmann P, Lee S, et al. Radiomic phenotype features predict pathological response in non-small cell lung cancer. *Radiother Oncol J Eur Soc Ther Radiol Oncol* (2016) 119(3):480–6. doi: 10.1016/j.radonc.2016.04.004
34. Pyka T, Bundschuh R, Andratschke N, Mayer B, Specht H, Papp L, et al. Textural features in pre-treatment [F18]-FDG-PET/CT are correlated with risk of local recurrence and disease-specific survival in early stage NSCLC patients receiving primary stereotactic radiation therapy. *Radiat Oncol (London England)* (2015) 10:100. doi: 10.1186/s13014-015-0407-7
35. Tsarouchi M, Vlachopoulos G, Karahaliou A, Vassiou K, Costaridou L. Multi-parametric MRI lesion heterogeneity biomarkers for breast cancer diagnosis. *Phys Med PM Int J Devoted Appl Phys Med Biol Off J Ital Assoc Biomed Phys (AIFB)* (2020) 80:101–10. doi: 10.1016/j.ejmp.2020.10.007
36. Xu F, Zhu W, Shen Y, Wang J, Xu R, Qutesh C, et al. Radiomic-Based Quantitative CT Analysis of Pure Ground-Glass Nodules to Predict the Invasiveness of Lung Adenocarcinoma. *Front Oncol* (2020) 10:872. doi: 10.3389/fonc.2020.00872
37. Weis SM, Cheresh DA. Tumor angiogenesis: molecular pathways and therapeutic targets. *Nat Med* (2011) 17(11):1359–70. doi: 10.1038/nm.2537
38. Huang J, Yao X, Zhang J, Dong B, Chen Q, Xue W, et al. Hypoxia-induced downregulation of miR-30c promotes epithelial-mesenchymal transition in human renal cell carcinoma. *Cancer Sci* (2013) 104(12):1609–17. doi: 10.1111/cas.12291
39. Xie C, Schwarz EM, Sampson ER, Dhillon RS, Li D, O'Keefe RJ, et al. Unique angiogenic and vasculogenic properties of renal cell carcinoma in a xenograft model of bone metastasis are associated with high levels of vegf-a and decreased ang-1 expression. *J Orthop Res* (2012) 30(2):325–33. doi: 10.1002/jor.21500
40. Gigli F, Zattoni F, Zamboni G, Valotto C, Bernardin L, Mucelli RP, et al. [Correlation between pathologic features and perfusion CT of renal cancer: a feasibility study]. *Urologia* (2010) 77(4):223–31. doi: 10.1177/039156031007700401
41. Langley R, Fidler I. Tumor cell-organ microenvironment interactions in the pathogenesis of cancer metastasis. *Endocr Rev* (2007) 28(3):297–321. doi: 10.1210/er.2006-0027
42. Ling B, Liao X, Huang Y, Liang L, Jiang Y, Pang Y, et al. Identification of prognostic markers of lung cancer through bioinformatics analysis and in vitro experiments. *Int J Oncol* (2020) 56(1):193–205. doi: 10.3892/ijo.2019.4926
43. Qiu X, Feng J, Qiu J, Liu L, Xie Y, Zhang Y, et al. ITGBL1 promotes migration, invasion and predicts a poor prognosis in colorectal cancer. *Biomed Pharmacother = Biomed Pharmacother* (2018) 104:172–80. doi: 10.1016/j.biopha.2018.05.033
44. Tampakis A, Tampaki E, Nonni A, Tsourouflis G, Posabella A, Patsouris E, et al. L1CAM expression in colorectal cancer identifies a high-risk group of patients with dismal prognosis already in early-stage disease. *Acta Oncol (Stockholm Sweden)* (2020) 59(1):55–9. doi: 10.1080/0284186X.2019.1667022

45. Wang Y, Li L, Zhao Z, Wang Y, Ye Z, Tao H. L1 and epithelial cell adhesion molecules associated with gastric cancer progression and prognosis in examination of specimens from 601 patients. *J Exp Clin Cancer Res CR* (2013) 32:66. doi: 10.1186/1756-9966-32-66
46. Ho T, Serie D, Parasramka M, Cheville J, Bot B, Tan W, et al. Differential gene expression profiling of matched primary renal cell carcinoma and metastases reveals upregulation of extracellular matrix genes. *Ann Oncol Off J Eur Soc Med Oncol* (2017) 28(3):604–10. doi: 10.1093/annonc/mdw652
47. Park J, Scherer P. Adipocyte-derived endotrophin promotes malignant tumor progression. *J Clin Invest* (2012) 122(11):4243–56. doi: 10.1172/JCI63930
48. Majo S, Courtois S, Souleyreau W, Bikfalvi A, Auguste P. Impact of Extracellular Matrix Components to Renal Cell Carcinoma Behavior. *Front Oncol* (2020) 10:625. doi: 10.3389/fonc.2020.00625
49. Chen J, Chen J, He F, Huang Y, Lu S, Fan H, et al. Design of a Targeted Sequencing Assay to Detect Rare Mutations in Circulating Tumor DNA. *Genet Test Mol Biomarkers* (2019) 23(4):264–9. doi: 10.1089/gtmb.2018.0173
50. Han Y, Wang L, Wang Y. Integrated Analysis of Three Publicly Available Gene Expression Profiles Identified Genes and Pathways Associated with Clear Cell Renal Cell Carcinoma. *Med Sci Monit Int Med J Exp Clin Res* (2020) 26:e919965. doi: 10.12659/MSM.919965
51. Milosevic N, Kühnemuth B, Mühlberg L, Ripka S, Griesmann H, Lölkes C, et al. Synthetic lethality screen identifies RPS6KA2 as modifier of epidermal growth factor receptor activity in pancreatic cancer. *Neoplasia (New York NY)* (2013) 15(12):1354–62. doi: 10.1593/neo.131660
52. Pancholi S, Lykkesfeldt A, Hilmi C, Banerjee S, Leary A, Drury S, et al. ERBB2 influences the subcellular localization of the estrogen receptor in tamoxifen-resistant MCF-7 cells leading to the activation of AKT and RPS6KA2. *Endocr Relat Cancer* (2008) 15(4):985–1002. doi: 10.1677/ERC-07-0240

Conflict of Interest: The authors declare that the research was conducted in the absence of any commercial or financial relationships that could be construed as a potential conflict of interest.

frontiers in Oncology

ORIGINAL RESEARCH
published: 23 April 2021
doi: 10.3389/fonc.2021.633034

A Non-Invasive Scoring System to Differential Diagnosis of Clear Cell Renal Cell Carcinoma (ccRCC) From Renal Angiomyolipoma Without Visible Fat (RAML-wvf) Based on CT Features

Xiao-Jie Wang[1†], Bai-Qiang Qu[2†], Jia-Ping Zhou[1], Qiao-Mei Zhou[1], Yuan-Fei Lu[1], Yao Pan[1], Jian-Xia Xu[3], You-You Miu[4], Hong-Qing Wang[5] and Ri-Sheng Yu[1]*

[1] Department of Radiology, Second Affiliated Hospital, Zhejiang University School of Medicine, Hangzhou, China, [2] Department of Radiology, Wenling Hospital of Traditional Chinese Medicine, Taizhou, China, [3] Department of Radiology, The Second Affiliated Hospital of Zhejiang Chinese Medical University, Hangzhou, China, [4] Department of Ultrasonic, Wenzhou Central Hospital, Wenzhou, China, [5] Department of Radiology, First Affiliated Hospital of Wenzhou Medical University, Wenzhou, China

Background: Renal angiomyolipoma without visible fat (RAML-wvf) and clear cell renal cell carcinoma (ccRCC) have many overlapping features on imaging, which poses a challenge to radiologists. This study aimed to create a scoring system to distinguish ccRCC from RAML-wvf using computed tomography imaging.

Methods: A total of 202 patients from 2011 to 2019 that were confirmed by pathology with ccRCC (n=123) or RAML (n=79) were retrospectively analyzed by dividing them randomly into a training cohort (n=142) and a validation cohort (n=60). A model was established using logistic regression and weighted to be a scoring system. ROC, AUC, cut-off point, and calibration analyses were performed. The scoring system was divided into three ranges for convenience in clinical evaluations, and the diagnostic probability of ccRCC was calculated.

Results: Four independent risk factors are included in the system: 1) presence of a pseudocapsule, 2) a heterogeneous tumor parenchyma in pre-enhancement scanning, 3) a non-high CT attenuation in pre-enhancement scanning, and 4) a heterogeneous enhancement in CMP. The prediction accuracy had an ROC of 0.978 (95% CI, 0.956–0.999; P=0.011), similar to the primary model (ROC, 0.977; 95% CI, 0.954–1.000; P=0.012). A sensitivity of 91.4% and a specificity of 93.9% were achieved using 4.5 points as the cutoff value. Validation showed a good result (ROC, 0.922; 95% CI,

OPEN ACCESS

Edited by:
Abhishek Mahajan, Tata Memorial Hospital, India

Reviewed by:
Smita Manchanda, All India Institute of Medical Sciences, India
Mohamed Nazih Mohamed Ibrahim Shehata, University of Louisville, United States
Mohamed Abou El-Ghar, Mansoura University, Egypt
Giuseppe Simone, Regina Elena National Cancer Institute (IRCCS), Italy

***Correspondence:**
Ri-Sheng Yu
risheng-yu@zju.edu.cn

†These authors have contributed equally to this work and share first authorship

Specialty section:
This article was submitted to Cancer Imaging and Image-directed Interventions, a section of the journal Frontiers in Oncology

Received: *24 November 2020*
Accepted: *31 March 2021*
Published: *23 April 2021*

Citation:
Wang X-J, Qu B-Q, Zhou J-P, Zhou Q-M, Lu Y-F, Pan Y, Xu J-X, Miu Y-Y, Wang H-Q and Yu R-S (2021) A Non-Invasive Scoring System to Differential Diagnosis of Clear Cell Renal Cell Carcinoma (ccRCC) From Renal Angiomyolipoma Without Visible Fat (RAML-wvf) Based on CT Features. Front. Oncol. 11:633034. doi: 10.3389/fonc.2021.633034

0.854–0.991, P=0.035). The number of patients with ccRCC in the three ranges (0 to <2 points; 2–4 points; >4 to ≤11 points) significantly increased with increasing scores.

Conclusion: This scoring system is convenient for distinguishing between ccRCC and RAML-wvf using four computed tomography features.

Keywords: clear cell renal cell carcinoma, renal angiomyolipoma without visible fat, computed tomography, scoring system, differential diagnoses

INTRODUCTION

Approximately 75% of renal cell carcinomas are clear cell renal carcinomas (ccRCC) (1), the most common presentation of which is a renal mass. However, no malignant tumor among the renal masses accounts for more than 20%, and renal angiomyolipoma (RAML) is one of the most common benign cell types (2). RAML can often be diagnosed easily, due to macroscopic fat tissue within the tumor that can be detected by imaging. However, about 5% of RAML has insufficient fat for identification using conventional imaging modalities; these are regarded as RAML without visible fat (RAML-wvf) (3, 4). RAML-wvf mimics ccRCC on imaging due to the absence of fat, and is often diagnosed incorrectly (5). This presents a difficult challenge to radiologists and clinicians; since misdiagnosis might cause harm for patients, diagnosis is typically confirmed through biopsy or surgery. For distinguishing between RCC and RAML-wvf, the tumor texture, unenhanced computed tomography (CT) density, enhancement pattern, chemical shift parameter, sonographic features, and other imaging indexes were useful in previous reports (6–10). Most reports were based on qualitative analysis of imaging features because of the low incidence of RAML-wvf

CT is the preferred imaging method for evaluating renal mass in clinical settings (11). Previous studies have attempted to identify useful strategies based on CT imaging to differentiate ccRCC from RAML-wvf A hyperattenuating mass on unenhanced CT with homogeneous enhancement pattern on enhanced CT is highly suggestive of RAML-wvf (12–15). Investigators also tried detecting hidden fat tissue within the renal masses by counting negative-attenuation pixels using CT scans, thin-section (2–5 mm) scanning, and histogram analysis (16–18). However, these strategies are either too subjective or too time-consuming. Therefore, some quantitative methods have been reported recently, such as CT texture analysis (19, 20), machine learning-based texture analysis (11), and a CT-based radiomics nomogram (21). However, these methods might not be sufficiently convenient for clinical application.

Therefore, we aimed to identify characteristic CT features that could be used to distinguish patients with ccRCC from those with RAML-wvf weighted scores were assigned to the resulting model to make it more concise and convenient for use in clinical practice.

Abbreviations: ccRCC, clear cell renal cell carcinoma; RAML-wvf, renal angiomyolipoma without visible fat; ROC, receiver operating characteristic; CMP, corticomedullary phase; NP, nephrographic phase; EP, excretory phase.

MATERIALS AND METHODS

Study Population

A total of 202 patients from 2011 to 2019 that were confirmed with ccRCC (n = 123) or RAML (n = 79) by pathology were retrospectively analyzed. The inclusion criteria were: 1) patients who had a definitive pathologic diagnosis of either RAML or ccRCC, 2) patients underwent CT and the image quality was satisfactory for analysis, 3) there was no visible fat on unenhanced CT images, and 4) patients did not receive chemotherapy or radiotherapy before the images were taken. There were five patients excluded because of limited data. The 202 patients were divided randomly into a training cohort (n = 142) and a validation cohort (n = 60) (**Figure 1**).

Acquisition of Images

CT examinations were performed with multidetector CT (SOMATOM Definition Flash; Siemens Healthcare and LightSpeed 16; GE Healthcare). The scanning parameters were 120 kVp tube voltage, 220 mA tube current, slice thickness, and a 5-mm slice interval. Enhanced scanning was performed in three phases, including the post-contrast corticomedullary phase (CMP) (delay 30 s), post-contrast nephrographic phase (NP) (delay 90 s), and post-contrast excretory phase (EP) (delay 180 s).

Analysis of Images

CT images were evaluated independently by two abdominal radiologists who were blinded to the pathology results. The observed variables of CT features included the tumor number (single or multiple), location, contour (regular or irregular), and edge (clear or blurred), the existence of special findings (calcification, necrotic or cystic, pseudocapsule, wedge-shape sign, round tumor-kidney interface), features of the tumor parenchyma in pre-enhancement scanning, features of the total tumor in different scanning phases, and the enhancement pattern.

The tumor locations were classified into four patterns: A) the whole mass located in the renal parenchyma, B) the proportion of the mass that highlights the outline of the kidney <50%, C) the proportion of the mass that highlights the outline of the kidney >50%, and D) the mass grew into the renal medulla. A pseudocapsule was defined as an unenhanced arc area between the lesion and renal parenchyma. A wedge-shaped sign indicated that the tumor was triangular and pointing to the renal hilum.

The tumor CT attenuation in pre-enhancement scanning was categorized as high or not-high density compared with that of renal parenchyma (a difference > 5 HU). Heterogeneity was

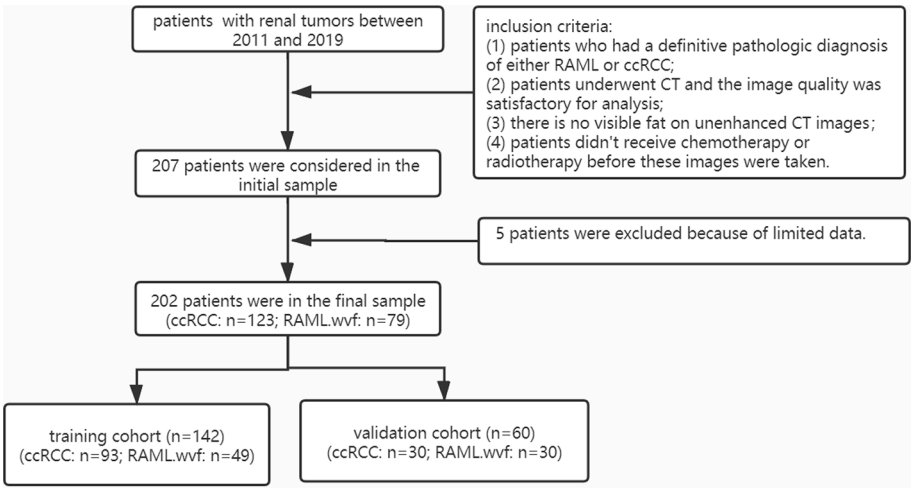

FIGURE 1 | Patient flow diagram.

defined as the difference between the highest and lowest attenuations being more than 30% of the highest value. Heterogeneous parenchyma in pre-enhancement scanning was considered when the parenchyma mass that could be enhanced was mixed. The enhanced scanning ratio 1 (ESR 1) was defined as the CT attenuation of the lesion minus the renal parenchyma in the CMP; ESR 2 was minus the aorta in the NP. The lesions significantly enhanced in CMP were classified as either "fast-in, fast-out" (the lesion quickly cleared in NP), "fast-in, slow-out" (the lesion was cleared in EP), or "persistent enhancement" (the lesion was still enhanced in EP).

Radiologists carefully outlined a 20-mm^2 region of interest (ROI) to include as much tissue mass as possible, avoiding necrotic or cystic areas when the CT attenuation of the tumor parenchyma was obtained. The ROI was determined at least twice, and the average was taken before obtaining the final CT attenuation. In addition, other clinical data (e.g., age, sex) were collected for all cases.

Statistical Analysis

Continuous variables were calculated as median with range (M-R), and categorical variables as the frequency with percentage. Data of the training cohort were used to establish the scoring system. The same variables between patients with RAML-wvf and with ccRCC were compared using the Student t-test for continuous variables and the chi-square or Fisher's exact test for categorical variables. Variables that were significant in univariate analysis were obtained to a logistic regression model after confirming there was no multicollinearity. For the training of an integer-based distinguishing scoring system, we decided to use the method described by Ben Ayed et al. (22). We first used the following formula to get the initial value: β/β_{min} (β, regression coefficient of each variable; β_{min}, minimum value of regression coefficient), which was rounded to the nearest integer to get the final score of each CT feature. The total score was calculated by summing the individual score corresponding to the related variables. The performance of the predicting model was evaluated by discrimination and calibration metrics. The receiver operating characteristic (ROC) was used to assess the discriminatory power of the model, and the Hosmer-Lemeshow goodness-of-fit test evaluated the calibration (23). A comparison among ROC of different models has been performed using the Delong nonparametric method (24). Further validation was performed using data from another 60 independent patients.

All the data were analyzed by SPSS version 25.0 software (IBM Crop, Aromonk, NY), except ROC comparison performed by MedCale statistical software, version 19.0 (MedCale Software bvba), $P < 0.05$ was defined as statistically significant.

RESULTS

Characteristics of the Study Patients

Differences in clinical and CT characteristics between patients with RAML-wvf and ccRCC are presented in **Table 1**. Sex, necrosis or cystic, heterogeneous parenchyma in pre-enhancement scanning, pseudocapsule, wedge shape sign, degree of CT attenuation in pre-enhancement scanning, enhancement in three scanning phases, enhancement pattern, ESR 1, and ESR 2 showed a statistically significant difference between the two groups ($P < 0.05$).

Establishment of the Primary Model

In the univariate analysis, necrosis or cystic, heterogeneous parenchyma in pre-enhancement scanning, pseudocapsule, absence of wedge shape sign, non-high CT attenuation in pre-enhancement scanning, enhancement in three scanning phases (heterogeneous), enhancement pattern, ESR 1, and ESR 2 were significantly associated with ccRCC compared with RAML-wvf

TABLE 1 | Comparison of Characteristics Between Patients with ccRCC and RAML-wvf.

	Patients with ccRCC (n = 93)	Patients with RAML-wvf (n = 49)	P
Age	57 (33–84)	54 (26–90)	0.267
Gender			<0.001
Male	67 (72.0)	18 (36.7)	
Female	26 (28.0)	31 (63.3)	
Amount			1
Single	88 (94.6)	46 (93.9)	
Multiple	5 (5.4)	3 (6.1)	
Growth pattern			0.163
Pattern A	20 (21.5)	13 (26.5)	
Pattern B	71 (76.3)	32 (65.3)	
Pattern C	2 (2.2)	4 (8.2)	
Pattern D	0 (0)	0 (0)	
Contour			0.175
Regular	69 (74.2)	31 (63.3)	
Irregular	24 (25.8)	18 (36.7)	
Edge			0.184
Blurred	35 (37.6)	13 (26.5)	
Clear	58 (62.4)	36 (73.5)	
Wedge shape sign			<0.001
No	82 (88.2)	29 (59.2)	
Yes	11 (11.8)	20 (40.8)	
Round tumor-kidney interface			0.353
No	76 (81.7)	43 (87.8)	
Yes	17 (18.3)	6 (12.2)	
Pseudocapsule			<0.001
No	25 (26.9)	45 (91.8)	
Yes	68 (73.1)	4 (8.2)	
Necrosis or cystic			<0.001
No	30 (32.3)	40 (81.6)	
Yes	63 (67.7)	9 (18.4)	
Calcification			1
No	90 (96.8)	46 (95.8)	
Yes	3 (3.2)	2 (3.2)	
Heterogeneous tumor parenchyma in pre-enhancement scanning			0.002
No	74 (79.6)	48 (98.0)	
Yes	19 (20.4)	1 (2.0)	
Degree of CT attenuation in pre-enhancement scanning			<0.001
Not-high	63 (67.7)	3 (6.1)	
High	30 (32.3)	46 (93.9)	
Enhancement in pre-enhancement scanning			<0.001
Homogeneous	26 (28.0)	34 (69.4)	
Heterogeneous	67 (72.0)	15 (30.6)	
Enhancement in CMP			<0.001
Homogeneous	7 (7.5)	35 (71.4)	
Heterogeneous	86 (92.5)	14 (28.6)	
Enhancement in NP			<0.001
Homogeneous	18 (19.4)	41 (83.7)	
Heterogeneous	75 (80.6)	8 (16.3)	
ESR 1			<0.001
<1–1	44 (47.3)	43 (87.8)	
≥1	49 (52.7)	6(12.2)	
ESR 2			0.011
<1	78 (83.9)	48 (98.0)	
≥1	15 (16.1)	1(2.0)	
Enhancement pattern			<0.001
Fast-in-fast-out	76 (81.7)	20 (40.8)	
Fast-in-slow-out	10 (10.8)	21 (42.9)	
Persistent enhancement	7 (7.5)	8 (16.3)	

It was confirmed that there was no multicollinearity among these factors by checking tolerance (>0.1) and variance inflation factor (VIF <10) before they were obtained in multivariate analysis. Multivariate analysis demonstrated four independent risk factors for distinguishing ccRCC: pseudocapsule, heterogeneous parenchyma in pre-enhancement scanning, non-high attenuation in pre-enhancement scanning, and heterogeneous enhancement in CMP (**Table 2**), which would be adopted to develop the distinguishing scoring system. The Hosmer-Lemeshow goodness-of-fit test indicates good calibration of this primary predictive model (P = 0.365, >0.05). The ROC (0.977; 95% CI, 0.954–1.000; P = 0.012) shows a good result.

Establishment of the Scoring System

We assigned risk scores relative to the regression coefficient of each variable that showed statistical significance in the multivariate analysis (**Table 2**): 2 points for tumors having a pseudocapsule (**Figure 2**); 2 points for heterogeneous tumor parenchyma in pre-enhancement scanning (**Figure 3**); 4 points for non-high attenuation in pre-enhancement scanning (**Figure 3**); and 3 points for heterogeneous enhancement in CMP (**Figure 3**). In the distinguishing scoring system, the total score was calculated by summing the individual scores corresponding to the related variables, which produced scores ranging from 0 to 11 points. The Hosmer-Lemeshow goodness-of-fit test indicated good calibration of this scoring model (P = 0.918). The prediction accuracy of this distinguishing scoring system, measured by ROC, was 0.978 (95% CI, 0.956–0.999; P = 0.011). This is similar to the primary model, presenting good distinguishing power for ccRCC, with a sensitivity of 91.4% and a specificity of 93.9% that can be achieved when using 4.5 points as the cutoff value. A comparison of ROC showed no statistical difference between the two models (P = 0.651) (**Figure 4**), which indicates that the distinguishing scoring system has made full use of the primary predictive model.

To provide further convenience for radiologists, we divided the final scores into three ranges: 0 to <2 points; 2–4 points; and >4 to ≤11 points. Patients with ccRCC among the three ranges significantly increased with increasing scores (**Table 3**).

Internal validation of the distinguishing scoring system showed good results. The validation cohort included 30 patients with ccRCC and 30 patients with RAML-wvf. Among the scoring ranges, ccRCC patients were 0/18 (0%) of the first (0 to <2 points) range; 4/10 (40%) of second range (2–4 points); and 26/32 (81.25%) of the last range (>4 to ≤11 points) (**Table 3**). The prediction accuracy measured by ROC was 0.922 (95% CI, 0.854–0.991, P = 0.035).

DISCUSSION

CT is the first-line imaging method used to evaluate renal masses in clinical practice. Patients with RAML-wvf can avoid unnecessary surgery for suspected RCC when an accurate diagnosis is determined preoperatively by CT. Previous studies

TABLE 2 | Predictors of Distinguishing scoring system of ccRCC.

	Univariate analysis P	P	HR	Multivariate analysis 95% CI	β	Score
Wedge shape sign (no)	<0.001	0.069				
Pseudocapsule (yes)	<0.001	0.04	10.824	2.133–54.922	2.382	2
Necrosis or cystic (yes)	<0.001	0.216				
Heterogeneous tumor parenchyma in pre-enhancement scanning (yes)	0.016	0.049	17.513	1.276–240.377	2.863	2
Degree of CT attenuation in pre-enhancement scanning	<0.001	<0.001				
Not-high			232.451	15.118–3574.181	5.449	4
High						
Density pattern in pre-enhancement scanning (heterogeneous)	<0.001	0.71				
Density pattern in CMP (heterogeneous)	<0.001	0.01	60.25	4.722–768.737	4.099	3
Density pattern in NP (heterogeneous)	<0.001	0.348				
ESR 1 (<1)	<0.001	0.957				
ESR 2 (≥1)	0.034	0.059				
Enhancement pattern	<0.001					
Fast-in-fast-out		0.295				
Fast-in-slow-out		0.137				
Persistent enhancement		0.295				

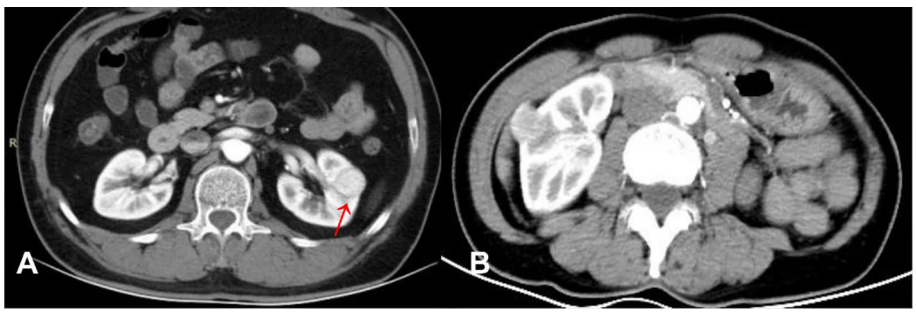

FIGURE 2 | **(A)** ccRCC in a 46-year-old male, post-contrast image depicted an unenhanced arc area between the lesion and renal parenchyma (arrow). **(B)** RAML-wvf in a 55-year-old male, there is no pseudocapsule sign that could be seen.

have proposed specific CT imaging characteristics for differentiating between RAML-wvf and ccRCC. Yang et al. (25) reported that being female, an angular interface, a hypodense rim, homogeneity, and high, unenhanced attenuation were useful characteristics that suggest RAML-wvf However, as described above, using these characteristics or searching for hidden fat tissue is not clinically convenient. Quantitative methods have been reported recently, Hodgdon et al. and Yan et al. (19, 20) proposed that CT texture analysis can quantitatively distinguish between RAML-wvf and ccRCC at three phases with nonlinear discriminant analysis. Lee et al. (26) proposed a texture-based classification system using a three-feature selection method and four-feature classifiers. Nie et al. (21) developed a radiomics nomogram that incorporates a radiomics signature and clinical factors for preoperative differentiation between RAML-wvf and RCC. However, for general radiologists, these technologies may need to be verified and perfected by big data before they can be mature and widely used in clinical practice. We have developed a reliable, convenient-to-use, scoring system consisting of four evaluable factors for discriminating between ccRCC and RAML-wvf based using CT. The simple score system and high accuracy are important strengths of our model, it is simple to use and can be verified by the users including clinicians and radiologists, which make it easier to be widely used.

Among the three ranges in the scoring system, there were no patients with ccRCC in either the training cohort or validation cohort for the first range (0 to <2 points). This indicates that RAML-wvf is more likely to be diagnosed when none of the factors is observed. In the third range (>4 to ≤11 points), 96.6% of patients had ccRCC (81.25% in the validation cohort), indicating that ccRCC is more likely to be diagnosed when more than two critical factors are observed.

Four independent risk factors are included in the system: 1) presence of a pseudocapsule, 2) a heterogeneous tumor parenchyma in pre-enhancement scanning, 3) a non-high CT attenuation in pre-enhancement scanning, and 4) a heterogeneous enhancement in CMP. In addition, women were found to be more likely to have RAML-wvf compared to ccRCC, which is consistent with previous results (11). However, since the desired scoring system is based on CT findings, the patient's sex was not incorporated into the model. A round tumor-kidney interface and calcification are reported as

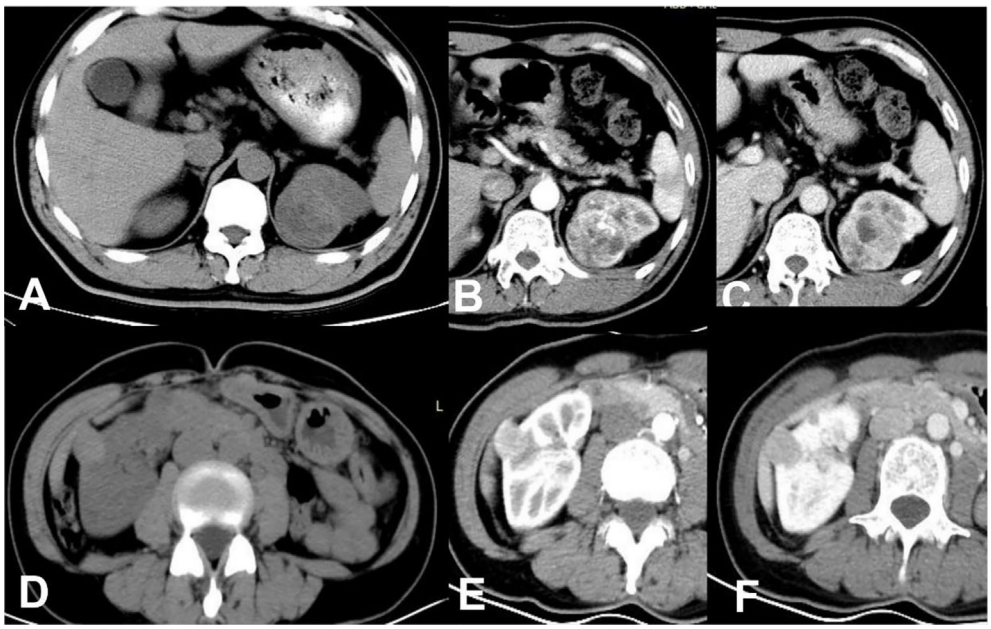

FIGURE 3 | ccRCC in a 48-year-old male, which presented not-high attenuation in plain scanning **(A)**, the attenuation of the mass parenchyma that could be enhanced was mixed. Besides, it was heterogeneous enhanced in CMP **(B)** or NP **(C)**, thus a score of 9 was assigned in this patient. RAML-wvf in a 61-year-old female showed homogeneous high attenuation in plain scanning **(D)** and homogeneous enhancement pattern in CMP **(E)** or NP **(F)**, thus a score of 0 was assigned in this patient and presented one of the minimum values in this model.

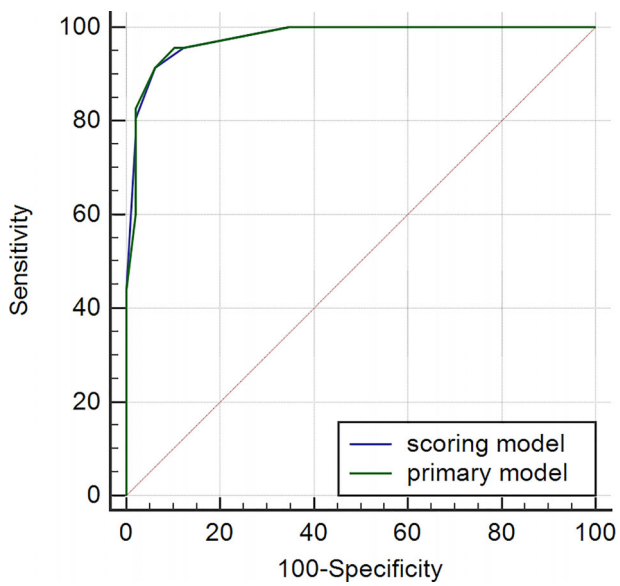

FIGURE 4 | ROC of primary and scoring model.

meaningful phenomena previously (27), but showed no statistical significance in this study. Wedge-shaped signs and necrotic or cystic lesions showed a significant difference between RAML-wvf and ccRCC, according to Ma et al. (28), but they did not show statistical significance in multivariate analysis in this study.

Among the independent risk factors, a non-high CT attenuation of the tumor in pre-enhancement scanning is the predominant factor, which means the tumor attenuation is lower than the attenuation of renal parenchyma. This indicates that RAML-wvf more often presents with high-CT attenuation in pre-enhancement scanning, according to previous reports that found hyperattenuating presentation was a useful method for discriminating between RAML-wvf and ccRCC (12–14). RAML-wvf tends to present homogeneous enhancement after contrast agent administration compared to RCC (12, 13, 15), which is consistent with our research findings (69.4%, 71.4%, 83.7%, respectively, in three enhancement phases). The heterogeneous enhancement pattern is more suggestive of RCC in terms of HR (HR, 60.25; 95% CI, 4.722–768.737), and heterogeneity in this study was defined as the difference between the highest and lowest attenuations being more than 30% of the highest value. Heterogeneous tumor parenchyma in pre-enhancement scanning is also a meaningful factor in terms of HR (17.513; 95% CI, 1.276–240.377), which defined as the parenchyma mass that could be enhanced was mixed. This heterogeneous appearance in unenhanced and enhanced scanning may be due to the fact that ccRCC is an adenocarcinoma derived from renal tubular epithelial cells, often with hemorrhage, necrosis, and cystic, growing rapidly, and presenting a high degree of malignancy. The pseudocapsule is one of the indications of malignancy (29), composed mainly of a fibrous pseudocapsule

TABLE 3 | Patients with ccRCC among three groups in Training cohort and validation cohort.

Score groups	Number of patients with ccRCC		Total Number		Diagnostic probability of ccRCC	
	Training cohort	Validation cohort	Training cohort	Validation cohort	Training cohort	Validation cohort
0 to <2 points	0	0	31	18	0%	0%
2–4 points	8	4	23	10	34.8%	40%
>4 to ≤11 points	85	26	88	32	96.6%	81.25%

and compressed renal parenchyma, which presents as an unenhanced arc area between the lesion and renal parenchyma. Yamashita et al. and Sung et al. reported, respectively, that the pseudocapsule sign was found in 66% and 90% of small RCCs, and was also observed in 0% to 10% of RAML-wvf (28, 30, 31). In this study, 73.1% of patients with ccRCC presented with the pseudocapsule sign (8.2% in RAML-wvf), and the HR of this sign was 10.824 (95% CI, 2.133–54.922). RAML-wvf, presenting the biological behavior of benign tumors in most cases, grows as a non-invasive pattern and exerts less pressure on the adjacent renal tissues, which may result in a low probability of pseudocapsule formation.

This study has several limitations. First, there may be an inherent selection bias due to the retrospective study design. Second, although we have collected more cases than previous reports, the total sample size was small, mainly because of the low clinical incidence of RAML-wvf, which may increase the risk of overfitting. In addition, the prediction accuracy of this scoring system in the validation cohort was somewhat lower, compared to that in the training cohort, which might be related to biases caused by the relatively small sample size of the validation cohort. A further prospective cohort with a larger sample size is strongly warranted to validate our diagnostic scoring system.

In conclusion, this study investigated risk characteristics of CT features and built a convenient-to-use scoring system incorporating the four most meaningful factors: pseudocapsule, a heterogeneous tumor parenchyma in pre-enhancement scanning, non-high CT attenuation in pre-enhancement scanning, and heterogeneous enhancement in CMP. This scoring system could be valuable for discriminating ccRCC from RAML-wvf in clinical practice, although a further prospective cohort with a larger sample size will be required to confirm these results.

DATA AVAILABILITY STATEMENT

The original contributions presented in the study are included in the article/supplementary material. Further inquiries can be directed to the corresponding author.

ETHICS STATEMENT

This study was approved by the local institutional review board from The Second Affiliated Hospital of Zhejiang University and informed consent was waived according to the retrospective design.

AUTHOR CONTRIBUTIONS

The work reported in the above for publications has been done by all authors. X-JW contributed to data analysis and manuscript editing. B-QQ collected the data of patients and J-XX supported. J-PZ, Y-FL, Y-YM, and H-QW helped in images analysis. Q-MZ helped in manuscript preparation. And R-SY contributed to the supervision of the whole process. All authors contributed to the article and approved the submitted version.

REFERENCES

1. Li ZC, Zhai G, Zhang J, Wang Z, Liu G, Wu GY, et al. Differentiation of Clear Cell and non-Clear Cell Renal Cell Carcinomas by All-Relevant Radiomics Features From Multiphase CT: A VHL Mutation Perspective. *Eur Radiol* (2019) 29(8):3996–4007. doi: 10.1007/s00330-018-5872-6
2. Fujii Y, Komai Y, Saito K, Iimura Y, Yonese J, Kawakami S, et al. Incidence of Benign Pathologic Lesions At Partial Nephrectomy for Presumed RCC Renal Masses: Japanese Dual-Center Experience With 176 Consecutive Patients. *Urology* (2008) 72(3):598–602. doi: 10.1016/j.urology.2008.04.054
3. Thiravit S, Teerasamit W, Thiravit P. The Different Faces of Renal Angiomyolipomas on Radiologic Imaging: A Pictorial Review. *Br J Radiol* (2018) 91(1084):20170533. doi: 10.1259/bjr.20170533
4. Hakim SW, Schieda N, Hodgdon T, McInnes MD, Dilauro M, Flood TA. Angiomyolipoma (AML) Without Visible Fat: Ultrasound, CT and MR Imaging Features With Pathological Correlation. *Eur Radiol* (2016) 26 (2):592–600. doi: 10.1007/s00330-015-3851-8
5. Mete O, van der Kwast TH. Epithelioid Angiomyolipoma: A Morphologically Distinct Variant That Mimics a Variety of Intra-Abdominal Neoplasms. *Arch Pathol Lab Med* (2011) 135(5):665–70. doi: 10.1043/2009-0637-rsr.1
6. Lim RS, Flood TA, McInnes MDF, Lavallee LT, Schieda N. Renal Angiomyolipoma Without Visible Fat: Can We Make the Diagnosis Using CT and MRI? *Eur Radiol* (2018) 28(2):542–53. doi: 10.1007/s00330-017-4988-4
7. You MW, Kim N, Choi HJ. The Value of Quantitative CT Texture Analysis in Differentiation of Angiomyolipoma Without Visible Fat From Clear Cell Renal Cell Carcinoma on Four-Phase Contrast-Enhanced CT Images. *Clin Radiol* (2019) 74(7):547–54. doi: 10.1016/j.crad.2019.02.018
8. Park KJ, Kim MH, Kim JK, Cho KS. Sonographic Features of Small (< 4 Cm) Renal Tumors With Low Signal Intensity on T2-Weighted Mr Images: Differentiating Minimal-Fat Angiomyolipoma From Renal Cell Carcinoma. *AJR Am J Roentgenol* (2018) 211(3):605–13. doi: 10.2214/ajr.17.18909
9. Woo S, Kim SY, Cho JY, Kim SH. Differentiation Between Papillary Renal Cell Carcinoma and Fat-Poor Angiomyolipoma: A Preliminary Study Assessing Detection of Intratumoral Hemorrhage With Chemical Shift MRI and T2*-weighted Gradient Echo. *Acta Radiol* (2018) 59(5):627–34. doi: 10.1177/0284185117723371
10. Kim YH, Han K, Oh YT, Jung DC, Cho NH, Park SY. Morphologic Analysis With Computed Tomography may Help Differentiate Fat-Poor Angiomyolipoma From Renal Cell Carcinoma: A Retrospective Study With

602 Patients. *Abdom Radiol (NY)* (2018) 43(3):647–54. doi: 10.1007/s00261-017-1244-y
11. Feng Z, Rong P, Cao P, Zhou Q, Zhu W, Yan Z, et al. Machine Learning-Based Quantitative Texture Analysis of CT Images of Small Renal Masses: Differentiation of Angiomyolipoma Without Visible Fat From Renal Cell Carcinoma. *Eur Radiol* (2018) 28(4):1625–33. doi: 10.1007/s00330-017-5118-z
12. Jinzaki M, Tanimoto A, Narimatsu Y, Ohkuma K, Kurata T, Shinmoto H, et al. Angiomyolipoma: Imaging Findings in Lesions With Minimal Fat. *Radiology* (1997) 205(2):497–502. doi: 10.1148/radiology.205.2.9356635
13. Hafron J, Fogarty JD, Hoenig DM, Li M, Berkenblit R, Ghavamian R. Imaging Characteristics of Minimal Fat Renal Angiomyolipoma With Histologic Correlations. *Urology* (2005) 66(6):1155–9. doi: 10.1016/j.urology.2005.06.119
14. Woo S, Cho JY, Kim SH, Kim SY. Angiomyolipoma With Minimal Fat and non-Clear Cell Renal Cell Carcinoma: Differentiation on MDCT Using Classification and Regression Tree Analysis-Based Algorithm. *Acta Radiol* (2014) 55(10):1258–69. doi: 10.1177/0284185113513887
15. Kim JK, Park SY, Shon JH, Cho KS. Angiomyolipoma With Minimal Fat: Differentiation From Renal Cell Carcinoma At Biphasic Helical CT. *Radiology* (2004) 230(3):677–84. doi: 10.1148/radiol.2303030003
16. Kim JY, Kim JK, Kim N, Cho KS. CT Histogram Analysis: Differentiation of Angiomyolipoma Without Visible Fat From Renal Cell Carcinoma At CT Imaging. *Radiology* (2008) 246(2):472–9. doi: 10.1148/radiol.2462061312
17. Catalano OA, Samir AE, Sahani DV, Hahn PF. Pixel Distribution Analysis: can it be Used to Distinguish Clear Cell Carcinomas From Angiomyolipomas With Minimal Fat? *Radiology* (2008) 247(3):738–46. doi: 10.1148/radiol.2473070785
18. Silverman SG, Israel GM, Herts BR, Richie JP. Management of the Incidental Renal Mass. *Radiology* (2008) 249(1):16–31. doi: 10.1148/radiol.2491070783
19. Hodgdon T, McInnes MD, Schieda N, Flood TA, Lamb L, Thornhill RE. Can Quantitative Ct Texture Analysis be Used to Differentiate Fat-Poor Renal Angiomyolipoma From Renal Cell Carcinoma on Unenhanced Ct Images? *Radiology* (2015) 276(3):787–96. doi: 10.1148/radiol.2015142215
20. Yan L, Liu Z, Wang G, Huang Y, Liu Y, Yu Y, et al. Angiomyolipoma With Minimal Fat: Differentiation From Clear Cell Renal Cell Carcinoma and Papillary Renal Cell Carcinoma by Texture Analysis on CT Images. *Acad Radiol* (2015) 22(9):1115–21. doi: 10.1016/j.acra.2015.04.004
21. Nie P, Yang G, Wang Z, Yan L, Miao W, Hao D, et al. A CT-based Radiomics Nomogram for Differentiation of Renal Angiomyolipoma Without Visible Fat From Homogeneous Clear Cell Renal Cell Carcinoma. *Eur Radiol* (2020) 30 (2):1274–84. doi: 10.1007/s00330-019-06427-x
22. Ben Ayed H, Koubaa M, Hammami F, Marrakchi C, Rekik K, Ben Jemaa T, et al. Performance of an Easy and Simple New Scoring Model in Predicting Multidrug-Resistant Enterobacteriaceae in Community-Acquired Urinary Tract Infections. *Open Forum Infect Dis* (2019) 6(4):ofz103. doi: 10.1093/ofid/ofz103
23. Seo N, Han K, Hyung WJ, Chung YE, Park CH, Kim JH, et al. Stratification of Postsurgical Computed Tomography Surveillance Based on the Extragastric Recurrence of Early Gastric Cancer. *Ann Surg* (2020) 272(2):319–25. doi: 10.1097/sla.0000000000003238
24. DeLong ER, DeLong DM, Clarke-Pearson DL. Comparing the Areas Under Two or More Correlated Receiver Operating Characteristic Curves: A Nonparametric Approach. *Biometrics* (1988) 44(3):837–45. doi: 10.2307/2531595
25. Yang CW, Shen SH, Chang YH, Chung HJ, Wang JH, Lin AT, et al. Are There Useful CT Features to Differentiate Renal Cell Carcinoma From Lipid-Poor Renal Angiomyolipoma? *AJR Am J Roentgenol* (2013) 201(5):1017–28. doi: 10.2214/ajr.12.10204
26. Lee HS, Hong H, Jung DC, Park S, Kim J. Differentiation of Fat-Poor Angiomyolipoma From Clear Cell Renal Cell Carcinoma in Contrast-Enhanced MDCT Images Using Quantitative Feature Classification. *Med Phys* (2017) 44(7):3604–14. doi: 10.1002/mp.12258
27. Cong X, Zhang J, Xu X, Zhang M, Chen Y. Renal Epithelioid Angiomyolipoma: Magnetic Resonance Imaging Characteristics. *Abdom Radiol (NY)* (2018) 43(10):2756–63. doi: 10.1007/s00261-018-1548-6
28. Ma Y, Cao F, Xu X, Ma W. Can Whole-Tumor Radiomics-Based CT Analysis Better Differentiate Fat-Poor Angiomyolipoma From Clear Cell Renal Cell Caricinoma: Compared With Conventional CT Analysis? *Abdom Radiol (NY)* (2020) 45(8):2500–7. doi: 10.1007/s00261-020-02414-9
29. Roy C, El Ghali S, Buy X, Lindner V, Lang H, Saussine C, et al. Significance of the Pseudocapsule on MRI of Renal Neoplasms and its Potential Application for Local Staging: A Retrospective Study. *AJR Am J Roentgenol* (2005) 184 (1):113–20. doi: 10.2214/ajr.184.1.01840113
30. Yamashita Y, Honda S, Nishiharu T, Urata J, Takahashi M. Detection of Pseudocapsule of Renal Cell Carcinoma With MR Imaging and CT. *AJR Am J Roentgenol* (1996) 166(5):1151–5. doi: 10.2214/ajr.166.5.8615260
31. Sung CK, Kim SH, Woo S, Moon MH, Kim SY, Kim SH, et al. Angiomyolipoma With Minimal Fat: Differentiation of Morphological and Enhancement Features From Renal Cell Carcinoma At CT Imaging. *Acta Radiol* (2016) 57(9):1114–22. doi: 10.1177/0284185115618547

Conflict of Interest: The authors declare that the research was conducted in the absence of any commercial or financial relationships that could be construed as a potential conflict of interest.

frontiers | Frontiers in Oncology

TYPE Original Research
PUBLISHED 27 October 2022
DOI 10.3389/fonc.2022.979613

OPEN ACCESS

EDITED BY
Abhishek Mahajan,
The Clatterbridge Cancer Centre,
United Kingdom

REVIEWED BY
Alessandro Stefano,
Institute of Bioimaging and Molecular Physiology (CNR), Italy
Rakesh Shiradkar,
Emory University, United States

*CORRESPONDENCE
Weixin Xie
wxxie@szu.edu.cn
Ge Wen
m13360022166@163.com

†These authors have contributed equally to this work and share first authorship

SPECIALTY SECTION
This article was submitted to Cancer Imaging and Image-directed Interventions, a section of the journal Frontiers in Oncology

RECEIVED 27 June 2022
ACCEPTED 11 October 2022
PUBLISHED 27 October 2022

CITATION
Yin F, Zhang H, Qi A, Zhu Z, Yang L, Wen G and Xie W (2022) An exploratory study of CT radiomics using differential network feature selection for WHO/ISUP grading and progression-free survival prediction of clear cell renal cell carcinoma. *Front. Oncol.* 12:979613. doi: 10.3389/fonc.2022.979613

An exploratory study of CT radiomics using differential network feature selection for WHO/ISUP grading and progression-free survival prediction of clear cell renal cell carcinoma

Fu Yin[1†], Haijie Zhang[2,3†], Anqi Qi[2], Zexuan Zhu[4], Liyang Yang[2], Ge Wen[2*] and Weixin Xie[1*]

[1]College of Electronics and Information Engineering, Shenzhen University, Shenzhen, China, [2]Medical Imaging Department, Nanfang Hospital, Southern Medical University, Guangzhou, China, [3]Center of Positron Emission Tomography-Computed Tomography (PET/CT), Shenzhen Second People's Hospital, Shenzhen, China, [4]College of Computer Science and Software Engineering, Shenzhen University, Shenzhen, China

Objectives: To explore the feasibility of predicting the World Health Organization/International Society of Urological Pathology (WHO/ISUP) grade and progression-free survival (PFS) of clear cell renal cell cancer (ccRCC) using the radiomics features (RFs) based on the differential network feature selection (FS) method using the maximum-entropy probability model (MEPM).

Methods: 175 ccRCC patients were divided into a training set (125) and a test set (50). The non-contrast phase (NCP), cortico-medullary phase, nephrographic phase, excretory phase phases, and all-phase WHO/ISUP grade prediction models were constructed based on a new differential network FS method using the MEPM. The diagnostic performance of the best phase model was compared with the other state-of-the-art machine learning models and the clinical models. The RFs of the best phase model were used for survival analysis and visualized using risk scores and nomograms. The performance of the above models was tested in both cross-validated and independent validation and checked by the Hosmer-Lemeshow test.

Results: The NCP RFs model was the best phase model, with an AUC of 0.89 in the test set, and performed superior to other machine learning models and the clinical models (all p <0.05). Kaplan-Meier survival analysis, univariate and multivariate cox regression results, and risk score analyses showed the NCP

RFs could predict PFS well (almost all $p < 0.05$). The nomogram model incorporated the best two RFs and showed good discrimination, a C-index of 0.71 and 0.69 in the training and test set, and good calibration.

Conclusion: The NCP CT-based RFs selected by differential network FS could predict the WHO/ISUP grade and PFS of RCC.

KEYWORDS

clear cell renal carcinoma, radiomics features, differential network feature selection, WHO/ISUP grade, progression-free survival

Introduction

The nuclear grade of clear cell renal cell carcinoma (ccRCC) is strongly related to 5-year survival time, with higher grades associated with shorter survival (1, 2) and higher risk for recurrence after partial nephrectomy (3). The World Health Organization/International Society of Urological Pathology (WHO/ISUP) (4) grading system is a new four-level system commonly used in clinical which has improved the interobserver reproducibility, and is easier to apply and more clinically relevant, as well as a better independent prognostic factor (5), compared to the former Fuhrman grading system. However, earlier studies have shown no significant difference in the survival rate between grade 1 and grade 2 RCC (6, 7) and between grade 3 and grade 4 RCC (1, 2). Therefore, some scholars tend to simplify it into low-grade and high-grade lesions. In terms of clinical decision-making, patients with low-grade RCC may be treated relatively conservatively, such as through nephron-saving surgery, radiofrequency ablation, or active surveillance. In contrast, patients with high-grade RCC may receive more radical interventions and closer follow-up (8). Therefore, preoperative WHO/ISUP grading is very helpful in guiding clinical decision-making (8, 9).

Histopathological examination is the standard method to determine the WHO/ISUP grade of ccRCC. However, needle biopsy accuracy remains controversial (10, 11), and tumor grade is often underestimated (12–14). At the same time, the biopsy is invasive, associated with complications, and may be limited by tumor location and timely status. Therefore, a new noninvasive method to preoperatively predict the pathological grade of ccRCC would be of clinical merit. Studies have shown that radiomics can be used noninvasively to predict the presence of oncogenes, prognosis, and the effectiveness of different treatments (15, 16). Accumulating evidence has shown that radiomics features (RFs) are useful for predicting the pathological grade of RCC (17).

In radiomics, the number of features is usually larger than the experiment samples, which is easy to overfit and hinders the model's prediction. Therefore, feature selection (FS) methods are necessary. Traditional FS methods pick up a subset of features based on specific criteria, removing redundant, irrelevant, and noisy data. Based on a reasonable assumption, the RFs used to predict grade very well could also perform well on progression free survival (PFS) prediction, as the grade is strongly related to the prognosis. However, unfortunately, we are unsure about that, as most studies only focus on a single experiment objective: predicting the grade or the PFS, which causes the support for the assumption not enough and the interpretability of RFs poor. Therefore, designing a suitable FS method should make the selected RFs that can not only make accurate grade predictions but may also decipher the survival mechanisms associated with prognosis remains a significant challenging problem (18).

Several machine learning FS methods have been used in earlier studies to analyze image data, including Lasso regression (LR), decision tree (DT), support vector machine (SVM), convolution neural network (CNN), and random forest. Although the above methods have been successfully used to select RFs and build prediction models, they have a few limitations. For example, some methods select at most n variables before it saturates (19). However, the most number 'n' is not easy to decide. For example, the sparsity ratio λ in LR and penalty coefficient C in SVM should be chosen based on the prior empirical knowledge of the researchers or complicated cross-validation, which is not easy and very time-consuming.

Moreover, suppose there is a group of features among which the pairwise correlations are very high. In that case, they tend to arbitrarily select only one feature from the group, which means some important RFs will be lost. It could work to improve the model prediction performance. However, the interpretability of the RFs should be selected was not good enough, as choosing only one from the redundant features and removing the rest could lose much helpful information about the RFs. At last, most machine learning FS methods were wrapped-based; improving the model's performance in the training sets was their priority. Thus, the generalization performance of the models was easy to overfit. In the meantime, the performance of the existing machine learning FS methods is not stable when dealing with small and unbalanced sample size problems. Therefore, a more reliable FS method is urgently needed. The ideal RFs should not only have an accurate WHO/ISUP grade classification but also have some interpretable biological characteristics, such as PFS.

Differential network analysis based on network theory and related methodologies has shown outstanding robustness in analyzing various forms of large-scale data, which is evident in its ability to identify biomarkers (20). Most of the existing machine learning FS methods are a feature-centric analytic approach that assesses changes in individual features to a target. In contrast, differential network FS is a network-centric analytical approach that focuses on detecting the changes in a feature's associations with other features—comparing the difference between two different populations or groups' networks to select features. It is especially effective in detecting essential features that have less dramatic changes for specific experiments and show outstanding performance in dealing with small and unbalanced sample problems.

The correlation networks are widely used in constructing the networks, such as Pearson correlation, Euclidean distance, Spearman rank correlation, and so on. It should be noted that this correlation is between features, unlike in some filter FS methods between features and target labels. However, the biggest problem of such network constructing methods is that they could be misleading in reflecting the correlation of two features as it ignores the influence of the rest ones. The maximum-entropy probability model (MEPM) (21) is proposed to solve such a problem. It finds that inverting the matrix of covariances of features (Pearson correlation) could describe the correlations that remain once the indirect effects are removed, thereby providing a more robust description of the interactions between features.

However, there was no literature report on its application in the search for imaging RFs. For these reasons, this study aimed to investigate the feasibility of predicting the WHO/ISUP grade and PFS of ccRCC from the RFs based on the differential network FS using the MEPM. Furthermore, this paper expected to find evidence that the selected RFs of the WHO/ISUP grade prediction model were related to PFS of ccRCC to make the radiomics prediction models with more interpretable biological information through our new FS method.

Material and methods

Patients

This retrospective study was approved by the Ethics Committee of Southern Medical University, and because of the retrospective nature of the analysis, the requirement of informed patient consent was waived.

Medical records and picture archiving and communication systems were searched for patients with RCC treated at our hospital from March 2011 to March 2016. The age, gender, maximum tumor size, clinical stage, symptom, growth pattern, histological subtype, WHO/ISUP nuclear grade, and PFS were collected.

There were 434 patients with ccRCC confirmed by two pathologists were preliminarily enrolled. Exclusion criteria: 1) Patients lacking histopathological material for WHO/ISUP re-grading (98 cases); 2) Patients who were treated for RCC before CT examination (29 cases); 3) Patients without compete non-contrast phase (NCP), cortico-medullary phase (CMP), nephrographic phase (NP), and excretory phase (EP) phases CT scan (74 cases) and patients with inadequate quality images (38 cases); 4) Patients with 2 or more lesions in unilateral (2 cases) or bilateral (3 cases) kidneys; 5) Patients with tumors with mixed features (8 cases) and cystic RCC (75% or more cystic components) (7 cases). Finally, 175 Patients were enrolled and randomly divided into a training set (125 cases) and a test set (50 cases). Patient enrollment and experimental flow charts are shown in Figures 1A, E.

In performing survival analysis, the follow-up information is selected based on the criteria as follows: 1) survival information was obtained by telephone follow-up visits for all patients for at least 5 years after surgery; 2) tumor recurrence included *in situ* recurrence and distant metastasis; 3) diagnosis was mainly based on imaging examination comparison, and the follow-up deadline was June 2021;4) PFS was selected as the clinical endpoint.

CT parameters

A 64 multiprobe spiral CT scanner (Siemens, Somatom Definition CT scanner, 121 patients) and a 256 multiprobe spiral CT scanner (Philips, Brilliance ICT, 54 patients) were performed with patients. The range included both kidneys and masses in the supine position and a breath-holding scan. The scanning parameters were: tube voltage = 120 kV; tube current = 150-320 mA; slice thickness = 5 mm; layer spacing = 5 mm; field

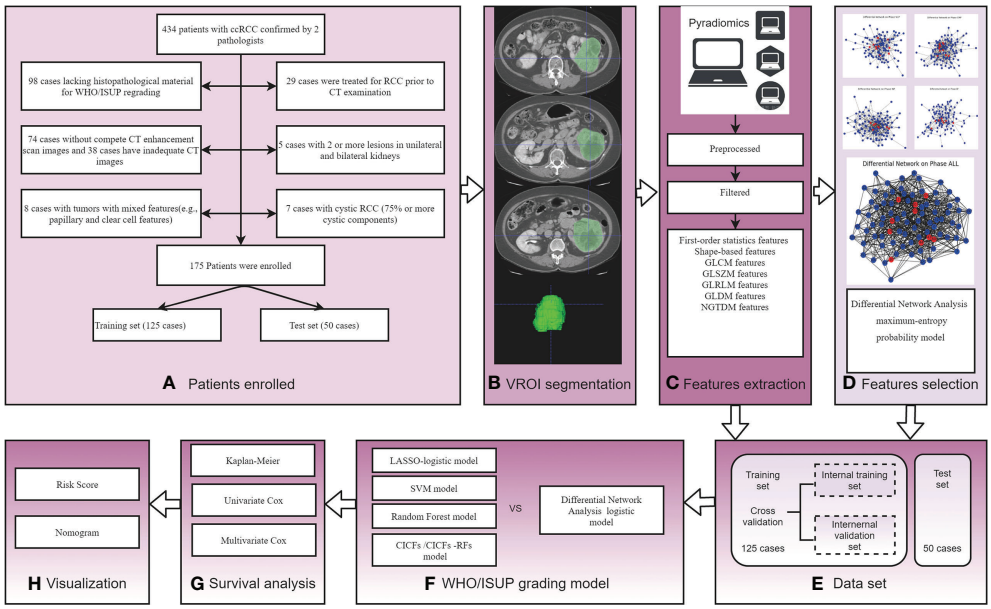

FIGURE 1
The experimental process of this study. **(A)** Patient enrollment flow charts; **(B)** Schematic diagram of image segmentation; **(C)** Schematic diagram of feature extraction; **(D)** Schematic diagram of differential networks features selection method; **(E)** Experimental Data set. **(F)** WHO/ISUP grading model construction and comparison; **(G)** Survival analysis by Kaplan-Meier survival, univariate, and multivariate Cox analysis; **(H)** Visualization risk score and nomogram.

of view (FOV) = 360 mm; matrix = 512×512. Spiral scanning and thin-layer reconstructions were performed for all 4 stages. After the NCP scan, the contrast agent was injected into the anterior cubital vein with a high-pressure syringe at a dose of 2 ml/kg and an injection rate of 2.5 ml/s. CMP, NP, and EP scanning were started at 30-35 s, 60-70 s, and 190-200 s, respectively.

Images segmentation and radiomics feature extraction

The tumor volume region of interest (VOI) was segmented by 2 radiologists with 10-year and 15-year experience using ITK-snap software (www.itk-snap.org). Four phases (NCP, CMP, NP, and EP) VOI segmented images were obtained for each patient, and its boundary was kept about 2 mm away from the tumor edge to reduce interference from adjacent tissues (22). When the boundary of the tumor was not clear, the boundary of the CMP image was compared for segmentation. Images segmentation examples are shown in Figure 1B.

The segmented images were first preprocessed, including resampling, normalization, and filtering to remove noise. Then the RFs were extracted from segmented images using the PyRadiomics computing platform. Features extraction is shown in Figure 1C. The initial setting of the Pyradiomics are as follows: binWidth = 25, label= 1, interpolato r= 'sitkBSpline', resampledPixelSpacing = 'None', weightingNorm = 'None'.

To assess feature robustness, we conducted a test-retest study. Two physicians (Doctor A 10 years, and Doctor B 9 years experience) individually contoured the ROIs in the random 30 images. Intraclass correlation coefficient (ICC) was used to test the stability between Doctor A and Doctor B groups, and the results showed that ICC was> 0.75 between groups. One week later, Doctor A repeated the same procedure to assess the reproducibility, and the results showed that ICC > 0.75 within the group (Doctor A). The results between groups and within the group suggest the segmentation was consistent, and the remaining image segmentation was performed by Doctor A.

Features selection

A differential network FS using MEPM was proposed in this study. The flow chart is shown in Figure 2. At first, five control groups were constructed based on different phases of RFs (NCP, CMP, EP, MP, ALL). i.e., the NCP group consists of all the samples with only NCP RFs, and the ALL group consists of all the samples with all 4 phase RFs. All samples in each group were marked based on their WHO/ISUP grade (high-grade or low-grade). Then, high-grade and low-grade networks of each group were constructed using MEPM based on the corresponding

10.3389/fonc.2022.979613

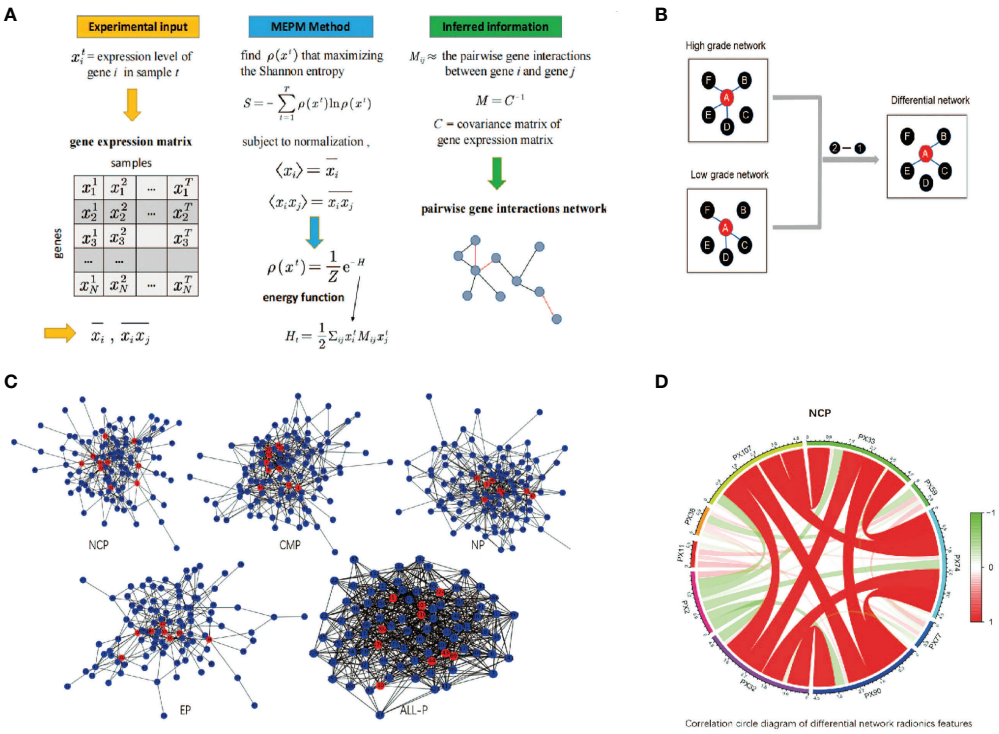

FIGURE 2
The schematic diagram of differential network feature selection. **(A)** An example of GRN inference using maximum-entropy probability model (MEPM); **(B)** An example of using differential networks analysis; **(C)** The differential networks using MEPM of the non-contrast phase (NCP), cortico-medullary phase (CMP), nephrographic phase (NP), excretory phase (EP), and all phase (ALL-P), where the red nodes were the selected RFs; **(D)** Correlation circle diagram of the RFs of the NCP model.

samples (Figure 2A). i.e., NCP high-grade network was constructed only using the samples in the NCP group marked high grade. After that, each phase's differential network of the high-low grade was constructed after comparing the differential topology structure between their high-grade network and low-grade network, i.e., network2 - network1 (Figure 2B). To be more specific, For example, features A and F were linked in both high-grade and low-grade networks, which means the structure of feature A to feature in these two networks was no different. So there was no link between feature A and feature F in its high-low differential network. At last, the RFs for each control group were selected based on the node degree histogram in their high-low differential network (Figure 2C), i.e., the nodes (RFs) which had the highest degree in the network were considered the critical RFs (marked in red in Figure 1D and Figure 2C); in this case, the number of selected features was set to less than 15.

MEPM networks construction

Let the state vector $x = (x_1, \ldots, x_N)$ denote the expression levels of the N features in an experiment, and a series of T measurements then has associated with its T distinct state vectors. Let $\rho(x)$ denote the probability that the genome is in the arbitrary state x. We determine $\rho(x)$ by maximizing the Shannon entropy

$$S = -\rho(\overrightarrow{x}) \ln (\overrightarrow{x}) \tag{1}$$

subject to the $\rho(x)$ is normalized

$$\sum_{\vec{x}} \rho(\overrightarrow{x}) = 1 \tag{2}$$

first moment, $<x_i>$, and second moment, $<x_i, x_j>$

$$< x_i >= \sum_{\vec{x}} \rho(\overrightarrow{x_i}) x_i = \frac{1}{T} \sum_{k=1}^{T} x_i^k \tag{3}$$

$$< x_i, x_j >= \sum_{\vec{x}} \rho(\overrightarrow{x}) x_i x_j = \frac{1}{T} \sum_{k=1}^{T} x_i^k x_j^k \tag{4}$$

Eq. (2) provides the normalization condition that the probabilities of all observable states sum to 1. Eqs. (3) and (4) ensure that the distribution $\rho(x)$ preserves the mean expression level of each gene and the correlations between genes. This procedure leads to a Boltzmann-like distribution:

$$\rho(x) \sim e^{-H}$$

where

$$H = \frac{1}{2}\sum_{ij} x_i M_{ij} x_j$$

The elements of the matrix M are the effective pairwise gene interactions that reproduce the gene profile covariances exactly while maximizing the entropy of the system. The matrix of M can be obtained by inverting the matrix of their covariances C. This makes a substantial difference. The covariance matrix C reflects the unconditional correlation between features and, therefore, contains indirect effects. On the other hand, its inverse, i.e., M, describes the correlations that remain once the indirect effects are removed and thereby provides a more robust description of the interactions between features.

However, in the high dimensional setting where the number of features p is larger than the number of observations n, the empirical covariance matrix C is singular and so can't be inverted to yield an estimate of M. Many MEPM-based methods have been proposed for inferring networks, including partial-correlation-based, likelihood-based, and mutual-information-based approaches.

In our case, we chose a multi-objective memetic algorithm to infer the MEPM networks (23, 24) and some other method like Glasso could get the similar results (25).

Prediction model construction and performance comparison

The performance of all experiment models was explored and verified by 5 times hierarchical 5-fold cross-validation in the training set and independently valid in the test set. To be more specific, the training set was divided into an internal training set and validation set (4:1) in each 5-fold cross-validation. The data split is using the python package sklearn: 'train_test_split' and set the 'stratify' = result, which makes the classification ratio of data in the training set and the test set will be the same.

In this study, the NCP, CMP, NP, EP, and ALL models were constructed using Logistic regression based on the corresponding RFs. At first, each experiment model was constructed based on the corresponding selected RFs using the proposed differential network FS in the internal training set. For example, the selected RFs of the NCP model was taken in the internal training set and then constructed using Logistic regression. Then, the average performance of the experiment model in 5 times cross-validation in the internal training and validation sets was considered the final performance in the training and validation sets. At last, the best selected RFs of each model in cross-validation were tested in the test set.

According to the performance results in all data sets, the best of the above five models was selected as our WHO/ISUP grade prediction model. After that, the LASSO, SVM, and Random Forest models were constructed based on all four phase RFs as control models and compared with our model on the same dataset. More specifically, model training and performance testing follow the same processing mentioned above (Figure 1F). Lasso is implemented using the python package sklearn: 'lassocv', which could select penalty parameter adaptively; SVM is using the python package sklearn: 'RFE' and 'SVM'; Random Forest is using the python package sklearn: 'RandomForestClassifier'. We keep the default parameter values for all these methods. Then, the conventional image and clinical features mode (CICFs) is constructed using Logistic regression based on the clinic features. The CICFs-RFs model combined clinic features, and RFs were constructed as control models and compared with our model following the performance mentioned above test processing. Finally, the receiver operating characteristic (ROC), the area under curve ROC curve (AUC), precision, sensitivity, and accuracy were determined to estimate the performance of the above models. At last, the best prediction model was refit on the complete training set as the final WHO/ISUP grade prediction model.

Survival analysis and performance comparison

Survival analysis was performed to explore more biological information about the selected RFs in the final WHO/ISUP grade prediction model and find whether they were related to PFS. At first, Kaplan-Meier analysis by converting the RFs into a dichotomous variable (high and low group) was used to estimate the selected RFs. Then, the univariate and multivariate Cox proportional hazard regression models were used to investigate the factors of RFs associated with PFS (Figure 1G). Independent variables with $p < 0.05$ in univariate results and multivariate were selected. After that, risk score analyses of ccRCC patients were used to describe the selected RFs. Finally, the selected RFs were used to build the final multivariate Cox regression model and visualized using nomograms (Figure 1H). The C-index of the final model was determined. The Hosmer-Lemeshow test was used to check the calibration.

Statistical analysis

Continuous data were presented as mean ± standard deviation, and categorical data were presented as numbers and percentages (%). For comparisons of means between groups, Student's independent t-test or Mann-Whitney U test was used, depending on the normality assumption. Categorical data were tested using the chi-square test or Fisher's exact test (if an expected value ≤ 5 was found). In all analyses, a 2-tailed value of $p < 0.05$ was considered to

TABLE 1 Patient's clinical characteristics between the training set and test set.

	Levels	Training set (N=125)	Test set (N=50)	*p*
Age (year, mean ± SD)		52.31 ± 14.51	52.06 ± 13.19%	0.915
Gender	Male	84 (67.2%)	31 (62.0%)	0.632
	Female	41 (32.8%)	19 (38.0%)	
Diameter (mm, median)		43.98	43.9	0.589*
WHO/ISUP	low	91 (72.8%)	31 (62.0%)	0.221
	high	34 (27.2%)	19 (38.0%)	
T	T1	97 (77.6%)	38 (76.0%)	0.541
	T2	16 (12.8%)	9 (18.0%)	
	T3	12 (9.6%)	3 (6.0%)	
N	N0	115 (92.0%)	47 (94.0%)	0.891
	N1	10 (8.0%)	3 (6.0%)	
TNM	Stage I	90 (72.0%)	37 (74.0%)	0.439
	Stage II	17 (13.6%)	9 (18.0%)	
	Stage III	18 (14.4%)	4 (8.0%))	
Symptom	no	65 (52.0%)	25 (50.0%)	0.943
	yes	60 (48.0%)	25 (50.0%)	
Grow pattern	Exophytic	40 (32.0%)	20 (40.0%)	0.241
	Mixed	60 (48.0%)	17 (34.0%)	
	Endophytic	25 (20.0%)	13 (26.0%)	
PFS (month, median)		56	66.5	0.122*

*p values were calculated by the Kruskal-Wallis test.

indicate statistical significance. The surv_cutpoint function in the surviminer package finds the best cutoff value for a continuous variable and is used to predict PFS. Statistical analyses and mapping were performed by R software (version 4.2) with the 'rms', 'proc', 'survival', 'rmda', and 'ggplot' package.

Result

Patient and tumor characteristics

175 patients were included in the analysis, including 125 cases in the training set and 50 cases in the test set. Table 1 summarizes the characteristics of the patients. 122 cases were diagnosed with low-grade ccRCC (WHO/ISUP grades 1 and 2) and 53 cases with high-grade ccRCC (WHO/ISUP grades 3 and 4). All characteristics of patients in the training set and the test set were no statistical difference ($p > 0.05$).

Features extraction and selection

A total of 107 RFs were extracted from the 3D multiphase CT images of each phase of each patient: 18 first-order statistics features, 14 shape-based features, 24 gray level co-occurrence matrix (GLCM) features, 16 gray level size zone matrix (GLSZM) features, 16 gray level run length matrix (GLRLM) features, 14 gray level dependence matrix (GLDM) features, and 5 neighboring gray-tone difference matrix (NGTDM) features. A total of 428 (4×107) RFs were extracted from the 4-phase CT images.

Differences in scanner models should be verified as the dataset collected comes from two scanners. Thus, principal component analysis (PCA) was performed on the extracted features to plot data in the space of reduced dimensions (26). Visual inspection of Supplement Figure 1 suggests the absence of batch effects. Furthermore the Kruskal–Wallis test, carried out on both the first and second main component scores, also confirmed the absence of clusters (PC 1 scores: p-value = 0.526 > 0.05 and PC 2 scores: p-value = 0.174 > 0.05).

Through the differential network FS, there were 10, 10, 8, 8, and 10 RFs were selected from NCP, CMP, NP, EP, and ALL-P in the complete training set, respectively. The differential networks of different phases are shown in Figure 2C where the red nodes represent the selected RFs. The designation, phase, abbreviation, classification, and description of RFs are shown in Table 2.

WHO/ISUP grade prediction model construction and performance comparison

The ROC analysis of different phase models in the training set, validation set, and test set are shown in Figures 3A–C, respectively. DeLong test was used to compare the AUCs of the

TABLE 2 The name and the abbreviation of the RFs of different phases using the differential network feature selection.

NCP (P)	CMP (A)	NP (V)	EP (D)	ALL-P
X107-Strength	X7-Maximum2D_DiameterSlice	X1-Elongation	X11-Sphericity	VX11-Sphericity
X77-Long Run Low Gray Level Emphasis	X8-Maximum3D_Diameter	X107-Strength	X1-Elongation	AX11- Sphericity
X59-Dependence Non-Uniformity Normalized	X11-Sphericity	X11-Sphericity	X45-Idn	VX70- Small Dependence Low Gray Level Emphasis
X74-High Gray Level Run Emphasis	X34-Cluster Shade	X21-Maximum	X35-Cluster Shade	AX70- Small Dependence Low Gray Level Emphasis
X2-Flatness	X35-Cluster Shade	X2-Flatness	X54-Sum Average	PX11-Sphericity
X11-Sphericity	X2-Flatness	X94-Low Gray Level Zone Emphasis	X90-High Gray Level Zone Emphasis	AX44- Idmn
X90-High Gray Level Zone Emphasis	X21-Maximum	X99-Small Area Low Gray Level Emphasis	X95-Size Zone Non-Uniformity	AX45- Idn
PX38-Correlation	X45-Idn	X48-Inverse Variance	X103-Busyness	DX104- Coarseness
X33-Autocorrelation	X26-Range			VX1- Elongation
PX32-Variance	AX29-Skewness			VX96- Size Zone Non-Uniformity Normalized

different models. The best two models were the NP and the NCP models in the training set (AUC = 0.75 and 0.74, respectively). They were significantly better than the rest models ($p < 0.05$), and there was no subtle difference between them ($p = 0.087$). The NCP model was still the best in the validation set (AUC = 0.71), significantly better than the other models (all $p < 0.05$). Finally, the NCP model (AUC = 0.84) remained one of the best two models in the test set; the other one was the ALL-P model

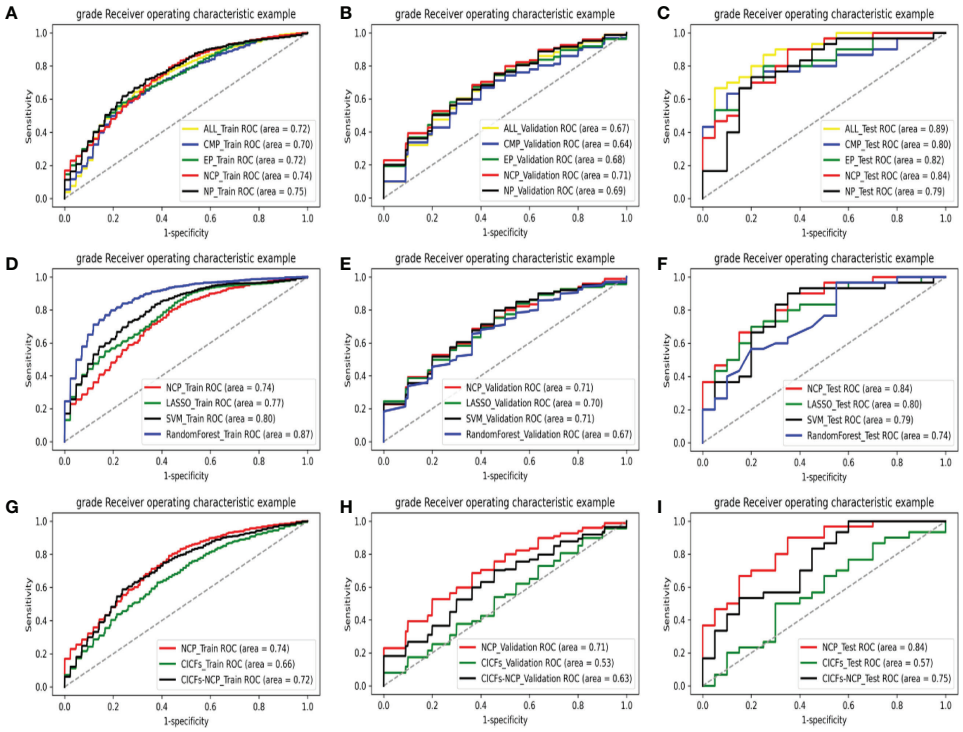

FIGURE 3
The ROC curves of various models on all data sets: comparing with different phases models in the training set **(A)**, validation set **(B)**, and test set **(C)**; comparing with the machine learning control models in the training set **(D)**, validation set **(E)**, and test set **(F)**; comparing with the clinic control models in the training set **(G)**, validation set **(H)**, and test set **(I)**.

(AUC = 0.89). Their performance was significantly better than the rest models (all $p < 0.05$), and no significant difference ($p = 0.062$) was found between them. Taking all the results together, the NCP model performed robustly and showed a good capability of predicting WHO/ISUP grade.

This result indicated that the NCP features selected by our method contain more helpful information than the enhanced scan features in terms of ccRCC grading prediction. This could provide a new basis for reducing the use of contrast media and reducing patients' radiation in the future. The model formula constructed in the training set (125 cases) is NCP_Y = 0.56×PX107+0.40×PX77-0.35×PX59+ 0.11×PX74 +0.25×PX2+0.84×PX11+0.11×PX90- 0.33×PX32 +0.11×PX33-0.37×PX38. The performance of the NCP model is shown in Table 3.

After that, the NCP model was compared with the machine learning control models (LASSO, SVM, and the Random Forest model). The ROC analysis of the above models in the training set, validation set, and test set are shown in Figures 3D–F, respectively. The control models performed significantly better (all $p < 0.05$) than the NCP model (AUC = 0.74) in the training set. However, their performance sharply deteriorated in the validation set, which made the NCP model become the best (AUC = 0.71), and no significant difference was found among them (all $p > 0.05$). What's more, the NCP model (AUC = 0.84) significantly outperformed other models (all $p < 0.05$) in the test set. Compared with the traditional FS methods, experimental results show that our FS method was more effective. Moreover, unlike the other methods, i.e., the validation and test set performance sharply deteriorated from the training set, our approach performed stably in all data sets with good prediction capability and outstanding robustness.

Finally, the NCP model was compared with the clinic control models (CICFs and CICFs-NCP model), The ROC analysis of the above models in the training set, validation set, and test set are shown in Figures 3G–I, respectively. The performance of the NCP-model (AUC = 0.74, 0.71, and 0.84) was significantly better than the CICFs ($p < 0.001$) and the CICFs-NCP model ($p < 0.001$) in all data sets.

Kaplan-Meier survival analysis

The Kaplan-Meier survival analysis results of the RFs of the NCP model in the training set are shown in Figure 4. All RFs were significant differences between their high and low groups (all $p < 0.05$), except PX32 ($p = 0.091$). The correlation circle diagram of the RFs of the NCP model is shown in Figure 2D.

Univariate and multivariate Cox regression analyses

The univariate and multivariate Cox regression analyses results of the relations of independent variables of the RFs to PFS in the training set are shown in Table 4. Univariate results showed that PX2, PX11, PX38, and PX107 were significant ($p < 0.05$), and were entered into the multivariate model. Similarly, RFs were substantial in the multivariate model: PX2 and PX11 ($p < 0.05$) were established as the final NCP model for PFS.

Risk score analyses

Risk score analyses of ccRCC patients in the training set based on the NCP model are shown in Figure 5. The risk scores of the NCP model where the rank of patients was set into the high-low risk group are shown in Figure 5.

Risk scores ranked the relationships between survival status and survival times of RCC patients are shown in Figure 5B. In addition, the heatmap of the two RFs of the final NCP model is shown in Figure 5C. The PX2 was a risk factor as its expression distribution was like to the risk scores; conversely, PX11 was a protective factor. Thus, these two NCP RFs could accurately predict patient prognosis and potentially impact the occurrence and development of tumors.

Nomogram

The nomogram of the final NCP model for clinical visualization was established in Figure 6A. The final NCP model for PFS was established using the PX2 and PX11, including risk estimations of PFS and 1-, 3-, and 5-year survival. It was found that the C-index of the final NCP model was 0.71 ($p = 0.038$) and 0.69 ($p = 0.066$) in 3the training set and test set. The calibration curve of the nomogram of 60 months is shown in Figure 6B, indicating that the final model fits the real predicted value.

TABLE 3 The performance of the NCP model of predicting WHO/ISUP grading in the training set, validation set, and test set.

NCP - Model	AUC	Precision	Sensitivity	Accuracy
Training set	0.74	0.71	0.66	0.67
Validation set	0.71	0.70	0.64	0.66
Test set	0.89	0.79	0.76	0.76

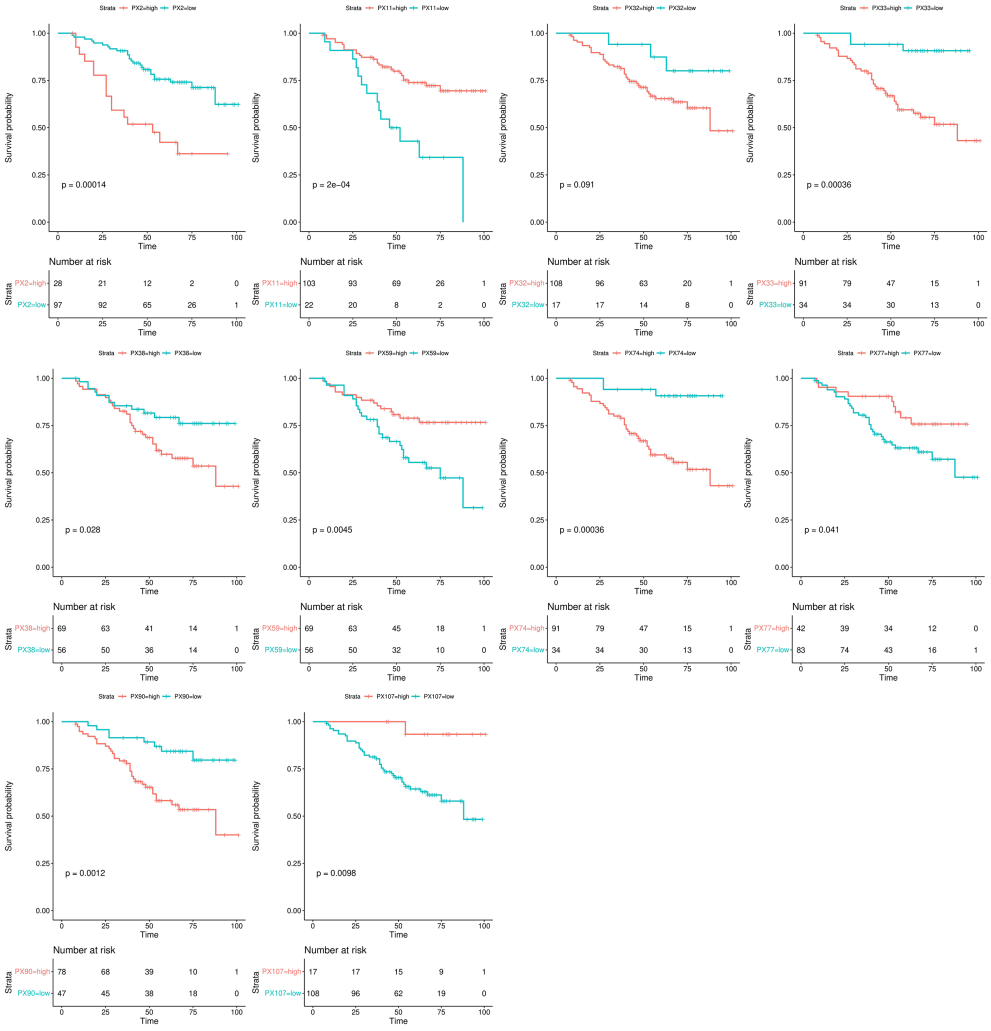

FIGURE 4
Kaplan-Meier analysis of the RFs of the NCP model.

TABLE 4 The univariate and multivariate Cox regression analysis of the independent RFS of the NCP model to PFS in the training set.

RFS	Levels	HR (univariable)	HR (multivariable)
PX2	0.7 ± 0.1	299.26 (6.08-14724.37, p = .004)	3828.42 (39.13.00-37458.02, p <.001)
PX11	0.7 ± 0.0	0.00 (0.00-0.06, p = .006)	0.00 (0.00-0.00, p <.001)
PX32	41.0 ± 160.1	1.00 (1.00-1.00, p = .687)	
PX33	287.0 ± 618.4	1.00 (1.00-1.00, p = .598)	
PX38	0.3 ± 0.1	19.94.00 (1.02-389.01, p =. 046)	13.32 (0.65-272.58, p = .093)
PX59	0.1 ± 0.0	0.00 (0.00-5764.93, p = .097)	
PX74	40.2 ± 158.8	1.00 (1.00-1.00, p = .687)	
PX77	0.7 ± 0.7	0.68 (0.36-1.28, p =. 228)	
PX90	38.6 ± 156.5	1.00 (1.00-1.00, p = .695)	
PX107	0.0 ± 0.2	0.00 (1.00-0.18, p = .027)	0.00 (0.00-1202.86, p = .402)

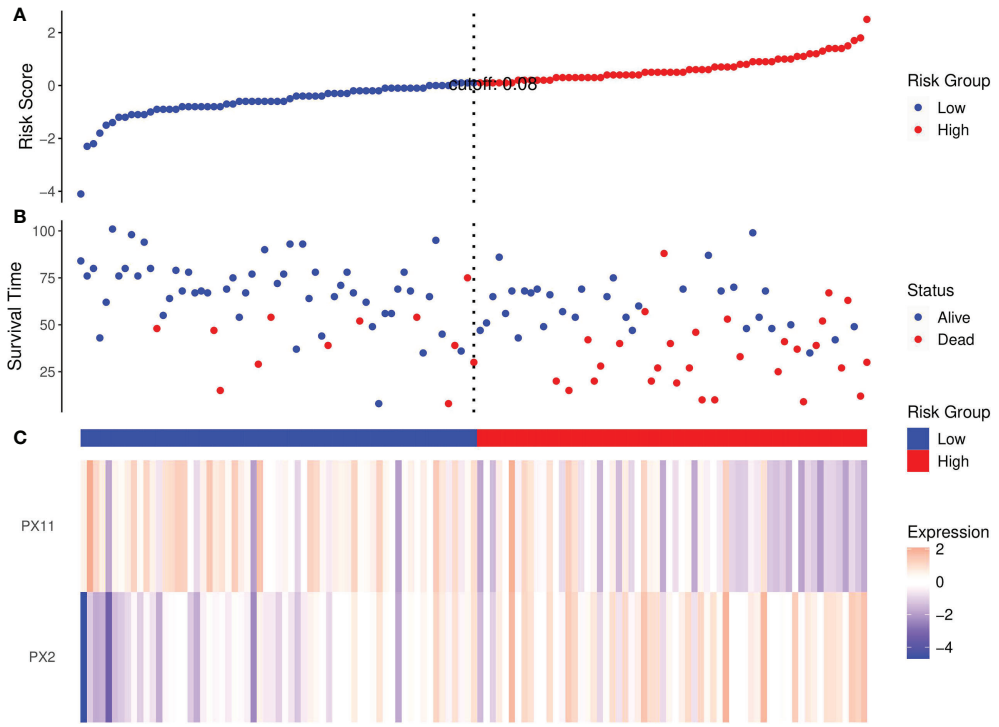

FIGURE 5
Risk score analysis of RCC patients in the training set based on the RFs of the NCP model. **(A)** Distribution of risk scores per patient; **(B)** Relationships between survival status and survival times of ccRCC patients ranked by risk score; **(C)** Heatmap of the RFS. Colors from blue to red indicate decreasing levels from high to low.

Discussion

In this retrospective analysis, we developed a new RFs FS method based on differential network analysis using MEPM. According to the Radiomics Quality Score (RQS) (27), this paper received 22 points for self-evaluation, with a total score of 36 points, indicating the high quality of this paper. Five WHO/ISUP grade prediction models with different phase RFs were constructed based on this method. According to their performance in all data sets, the NCP model was set as the final WHO/ISUP grade prediction model. This model was very competitive with three classical machine learning models and the clinical models in terms of good prediction capability and outstanding robustness. Survival analysis was performed to further explore the biology of the selected RFs. The results showed that almost all selected RFs could effectively

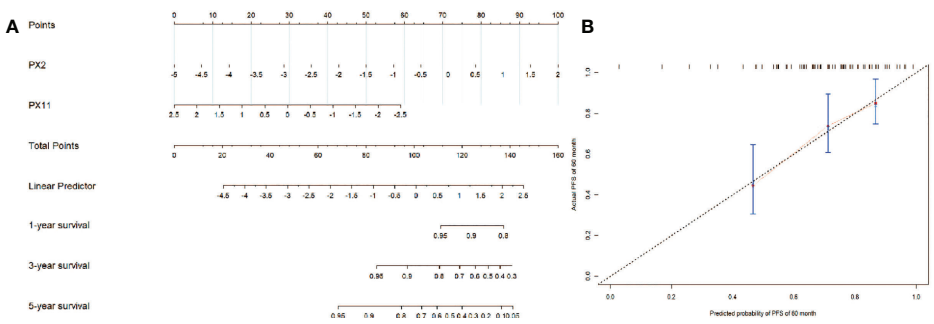

FIGURE 6
(A) The nomogram of the final NCP model; **(B)** The calibration curve of the nomogram of the final NCP model.

distinguish PFS. In the meantime, PX2 (NCP-Flatness) was a risk factor, and PX11 (NCP-Sphericity) was a protective factor for PFS. The results showed that the newly selected NCP RFs were significant for WHO/ISUP classification and survival prediction. Thus, the competitiveness and the interpretability of our new FS method were verified.

The one main difference between this study and prior similar studies is that we first used a new FS method based on differential network analysis using MEPM to select RFs. It focused on the inherent topology of the network of RFs that could reflect the high-low WHO/ISUP grades of RCC very well. It should be noticed that different network inference methods could lead to vastly different results in differential network analysis. The most common association measure was the well-known Pearson correlation coefficient. However, the Pearson correlation could be misleading in reflecting the correlation of two features as it ignores the influence of the rest ones (28). The MEPMs were proposed to solve this problem which relied on Boltzmann's concept of entropy maximization to support statistical inference with minimal reliance on the form of missing information (21). An example of applications of MEPM to infer gene networks is shown in Figure 2A. The elements of the matrix $M_{i\ j}$reflect the pairwise gene interactions between gene *i* and gene *j*. The matrix M can be obtained by inverting the matrix of their covariances C by using Pearson correlation (21). The covariance matrix C reflects the unconditional correlation between features and contains indirect effects. On the other hand, its inverse, i.e., M, describes the correlations that remain once the indirect effects are removed, thereby providing a more robust description of the interactions between genes. For the above reasons, MEPM was used to construct the high-low WHO/ISUP grade networks.

In our study, the NCP model performed better than the other phase model based on our FS method. It is a promising noninvasive rediomics model even without a tri-phase enhancement scan for predicting the grade of ccRCC. It can preoperatively predict the tumor's aggressiveness and provide a reference for predicting the prognosis. What's more, it can also provide a reference for selecting surgical plans and follow-up plans and can help guide to make more accurate treatment decisions for ccRCC. Our conclusion is consistent with the study of Kocak et al. (29) who reported that using an artificial neural network is a promising noninvasive method for predicting the grade of ccRCC. Using the traditional machine learning methods, most other research groups suggested that RFs from the CMP or NP, or combined phases, produced more accurate results. For example, Shu et al. (30) found that a combined CMP and NP model provided a diagnostic accuracy. Our method is different from the traditional machine learning method, and it could have advantages in exploring more potential significant information of NCP RFs in predicting WHO/ISUP grade.

The existing machine learning FS methods can generally be classified into two categories: 1) filter-based and 2) wrapper-based methods. Filter-based FS methods use feature relevance criteria, such as mutual information or the Pearson correlation coefficient, to select the feature subset. Wrapper-based methods utilize a classification algorithm to estimate the importance of the selected features. Although the filter-based methods are computationally less expensive than the wrapper ones, they ignore the performance of the selected features on the prediction performancethus, the selected features by the filter methods are often worse than those achieved by the wrapper-based FS methods (31). Therefore, this study mainly focuses on comparing wrapper-based FS methods. However, it should be noted that it does not mean the filter-based FS method does not work for the radiomics study. Parmar C et al. (32) mRMR showed the highest prognostic performance in head and neck cancer. Stefano Barone et al. (33) showed promising results on prostate cancer radiomics.

In the meantime, unlike the other FS methods, i.e., the validation and test set performance sharply deteriorated from the training set, our approach performed stably in all data sets with good prediction capability and outstanding robustness. One reason for that could be our FS method paid more attention to the differences topological of high-low grade network of the RFs, rather than the prediction performance in the training set, avoiding the overfitting of the model. On the other hand, our method used MEPM to construct the GRN, which could remove the variational effect due to the influence of the remaining RFs to ensure the selected RFs were more robust with good generalization performance. Finally, the differential network analyses have proved to have strong and stable performance in finding biomarkers in bioinformatics studies nowadays when the dataset is small and unbalanced (34), and the results in our study confirm these advantages.

Another contribution of this paper is that we first explore the relationship between the RFs of the WHO/ISUP grade prediction model and the PFS of the ccRCC. According to survival analysis, the biological association of the selected RFs with the PFS of ccRCC was proved. The results showed that almost all the selected NCP RFs of the WHO/ISUP grade prediction model could effectively distinguish PFS. This could suggest that the RFs may be related to some intrinsic biologic behavior. Most previous studies had either explored the grading or survival prediction abilities of RFs alone rather than combining them. Feng et al. (35) reported that entropy was the most critical imaging marker for predicting the Fuhrman grade of ccRCC. Bektas et al. (36) reported that the SVM method provided the best model for predicting Fuhrman low-grade or high-grade ccRCCs using ML-based portal-phase contrast-enhanced CT texture data. In another study, Shu et al. (37)

reported that a model combined k-nearest neighbor, logistic regression, multilayer perceptron, random forest, and SVM methods exhibited better performance than a CMP or NP model. Beyond an accurate classification, learning an interpretable model with features biologically relevant to the target could be more meaningful in understanding the mechanism of a radiomics model. This study further explored the underlying molecular basis of the identified RFs of the WHO/ISUP grade prediction model by assessing the possible biological association with the PFS. The results showed that our differential network FS method is applicable.

In this experiment, the image segmentation method is manual, unlike the other semi-automatic or automatic segmentation methods, which are most widely used in the lung and brain. However, the existing general semi-automatic segmentation method seems to have low accuracy in renal tumors. For example, separating tumors from normal tissues during the NCP is impossible because most tumors are of equal or slightly low density. In the EP, due to the highly enhanced tumor, which may infiltrate the renal pelvis and encroach renal veins, it is difficult to exclude these non-tumor normal tissues using semi-automatic segmentation of regional growth. Though it could cause problems with repetition and consistency (38, 39), manual segmentation is still used in most renal radiomics studies (40, 41). In response to the lack of automated segmentation, the Medical Imaging Computing and Computer Assisted Intervention (MICCAI) society developed the KiTS19 (Kidney Tumor Segmentation) Grand Challenge, where scientists compete using algorithms to automate the segmentation of kidney tumors. Although the effect is good in the arterial phase, there is still a lack of studies on the effectiveness of the NCP. To make the experiment more rigorous, we selected senior doctors for image segmentation and trained two doctors to standardize the segmentation process. In addition, our experiments aim to propose a new FS method, and we prefer to let the feature selection part mainly decide which RFs should be retained to test the performance of FS methods. Thereby we are relatively relaxed in RFs estimation before the feature selection, choosing ICC >0.75 instead of ICC >0.8 or 0.9 to ensure more features could be involved in the feature selection while avoiding eliminating potentially valuable features to improve the repeatability (30). Fortunately, all features were retained.

There are still some limitations to this study. First, as our work was a single-center and retrospective study, the dataset was relatively small. In the meantime, comparing with the other network construction methods and filter-based FS methods are necessary to verify the effectiveness of the model developed in this study. Furthermore, we know that only using the protective or risk factor for PFS to prove the biological meaning of the RFs is not enough. Therefore, future research will study the relationship between the RFs and the genomic or pathology information in the RCC pattern (42).

Data availability statement

The original contributions presented in the study are included in the article/Supplementary Material. Further inquiries can be directed to the corresponding authors.

Ethics statement

The studies involving human participants were reviewed and approved by Ethics Committee of Southern Medical University. Written informed consent for participation was not required for this study in accordance with the national legislation and the institutional requirements.

Author contributions

FY: Conceptualization, Writing - Original Draft, Software, Validation. HZ: Conceptualization, Writing - Original Draft, Methodology, Statistics. AQ: Investigation, Formal analysis. ZZ: Investigation, Formal analysis. LY:Investigation. WX: Conceptualization. GW: Conceptualization, Writing - Review and Editing. All authors contributed to the article and approved the submitted version.

Conflict of interest

The authors declare that the research was conducted in the absence of any commercial or financial relationships that could be construed as a potential conflict of interest.

Publisher's note

Supplementary material

The Supplementary Material for this article can be found online at: https://www.frontiersin.org/articles/10.3389/fonc.2022.979613/full#supplementary-material

SUPPLEMENTARY FIGURE 1
PCA results, PC 1: First Principal Component, PC 2: Second Principal Component.

References

1. Delahunt B, Mckenney JK, Lohse CM, Leibovich BC, Thompson RH, Boorjian SA, et al. A novel grading system for clear cell renal cell carcinoma incorporating tumor necrosis. *Am J Surg Pathol* (2013) 37(3):311–22. doi: 10.1097/PAS.0b013e318270f71c

2. Kuthi L, Jenei A, Hajdu A, Németh I, Varga Z, Bajory Z, et al. Prognostic factors for renal cell carcinoma subtypes diagnosed according to the 2016 WHO renal tumor classification: a study involving 928 patients. *Pathol Oncol Res* (2017) 23(3):689–98. doi: 10.1007/s12253-016-0179-x

3. Mouracade P, Kara O, Maurice MJ, Dagenais J, Malkoc E, Nelson RJ, et al. Patterns and predictors of recurrence after partial nephrectomy for kidney tumors. *J Urol* (2017) 197(6):1403–9. doi: 10.1016/j.juro.2016.12.046

4. Perrino CM, Cramer HM, Chen S, Idrees MT, Wu HH. World health organization (WHO)/International society of urological pathology (ISUP) grading in fine-needle aspiration biopsies of renal masses. *Diagn Cytopathol* (2018) 46(11):895–900. doi: 10.1002/dc.23979

5. Dagher J, Delahunt B, Rioux-Leclercq N, Egevad L, Srigley JR, Coughlin G, et al. Clear cell renal cell carcinoma: validation of world health Organization/International society of urological pathology grading. *Histopathology* (2017) 71(6):918–25. doi: 10.1111/his.13311

6. Robila V, Kraft AO, Smith SC. New entities, new technologies, new findings: A review of the cytologic features of recently established subtypes of renal cell carcinoma. *Cancer Cytopathol* (2019) 127(2):79–97. doi: 10.1002/cncy.22093

7. Siegel RL, Miller KD, Jemal A. Cancer statistics 2018. *CA Cancer J Clin* (2018) 68(1):7–30. doi: 10.3322/caac.21442

8. Chen W, Zheng R, Baade PD, Zhang S, Zeng H, Bray F, et al. Cancer statistics in China 2015. *CA Cancer J Clin* (2016) 66(2):115–32. doi: 10.3322/caac.21338

9. Yan Y, Liu L, Zhou J, Li L, Li Y, Chen M, et al. Clinicopathologic characteristics and prognostic factors of sarcomatoid renal cell carcinoma. *J Cancer Res Clin Oncol* (2015) 141(2):345–52. doi: 10.1007/s00432-014-1740-1

10. Kutikov A, Smaldone MC, Uzzo RG, Haifler M, Bratslavsky G, Leibovich BC. Renal mass biopsy: Always, sometimes, or never? *Eur Urol* (2016) 70(3):403–6. doi: 10.1016/j.eururo.2016.04.001

11. Millet I, Curros F, Serre I, Taourel P, Thuret R. Can renal biopsy accurately predict histological subtype and fuhrman grade of renal cell carcinoma? *J Urol* (2012) 188(5):1690–4. doi: 10.1016/j.juro.2012.07.038

12. Blumenfeld AJ, Guru K, Fuchs GJ, Kim HL. Percutaneous biopsy of renal cell carcinoma underestimates nuclear grade. *Urology* (2010) 76(3):610–3. doi: 10.1016/j.urology.2009.09.095

13. Ficarra V, Brunelli M, Novara G, D'elia C, Segala D, Gardiman M, et al. Accuracy of on-bench biopsies in the evaluation of the histological subtype, grade, and necrosis of renal tumours. *Pathology* (2011) 43(2):149–55. doi: 10.1097/PAT.0b013e32834317a4

14. Jeldres C, Sun M, Liberman D, Lughezzani G, De La Taille A, Tostain J, et al. Can renal mass biopsy assessment of tumor grade be safely substituted for by a predictive model? *J Urol* (2009) 182(6):2585–9. doi: 10.1016/j.juro.2009.08.053

15. Lambin P, Rios-Velazquez E, Leijenaar R. Radiomics: extracting more information from medical images using advanced feature analysis. *Eur J Cancer* (2012) 48:441. doi: 10.1016/j.ejca.2011.11.036

16. Pinker K, Shitano F, Sala E, Do RK, Young RJ, Wibmer AG, et al. Background, current role, and potential applications of radiogenomics. *J Magn Reson Imaging* (2017) 7:604–20. doi: 10.1002/jmri.25870

17. Zhou H, Mao H, Dong D, Fang M, Gu D, Liu X, et al. Development and external validation of radiomics approach for nuclear grading in clear cell renal cell carcinoma. *Ann Surg Oncol* (2020) 27(10):4057–65. doi: 10.1245/s10434-020-08255-6

18. Li ZC, Zhai G, Zhang J, Wang Z, Liu G, Wu GY, et al. Differentiation of clear cell and non-clear cell renal cell carcinomas by all-relevant radiomics features from multiphase CT: a VHL mutation perspective. *Eur Radiol* (2019) 29(8):3996–4007. doi: 10.1007/s00330-018-5872-6

19. Al-Kasassbeh M, Mohammed S, Alauthman M, Almomani A. Feature selection using a machine learning to classify a malware. In: Gupta BB, Perez GM, Agrawal DP, Gupta D, editors. *Handbook of computer networks and cyber security: Principles and paradigms*. Cham: Springer International Publishing (2020). p. 889–904.

20. Grimes T, Potter SS, Datta S. Integrating gene regulatory pathways into differential network analysis of gene expression data. *Sci Rep* (2019) 9(1):5479. doi: 10.1038/s41598-019-41918-3

21. De Martino A, De Martino D. An introduction to the maximum entropy approach and its application to inference problems in biology. *Heliyon* (2018) 4(4):e00596. doi: 10.1016/j.heliyon.2018.e00596

22. Kocak B, Ates E, Durmaz ES, Ulusan MB, Kilickesmez O. Influence of segmentation margin on machine learning-based high-dimensional quantitative CT texture analysis: a reproducibility study on renal clear cell carcinomas. *Eur Radiol* (2019) 29(9):4765–75. doi: 10.1007/s00330-019-6003-8

23. Tian Y, Lu C, Zhang X, Cheng F, Jin Y. A pattern mining-based evolutionary algorithm for Large-scale sparse multiobjective optimization problems. *IEEE Trans Cybern* (2021) 52(7):6784–97. doi: 10.1109/TCYB.2020.3041325

24. Yin F, Zhou J, Zhu Z, Ma X, Xie W. *Inferring small-scale maximum-entropy genetic regulatory networks by using DE algorithm*. Springer International PublishingCham (2021) 347–57.

25. Friedman J, Hastie T, Tibshirani R. Sparse inverse covariance estimation with the graphical lasso. *Biostatistics* (2008) 9(3):432–41. doi: 10.1093/biostatistics/kxm045

26. Pasini G, Bini F, Russo G, Comelli A, Marinozzi F, Stefano A. matRadiomics: A novel and complete radiomics framework, from image visualization to predictive model. *J Imaging* (2022) 8(8):221. doi: 10.3390/jimaging8080221

27. Lambin P, Leijenaar RTH, Deist TM, Peerlings J, De Jong EEC, Van Timmeren J, et al. Radiomics: the bridge between medical imaging and personalized medicine. *Nat Rev Clin Oncol* (2017) 14(12):749–62. doi: 10.1038/nrclinonc.2017.141

28. Chanda P, Costa E, Hu J, Sukumar S, Van Hemert J, Walia R. Information theory in computational biology: Where we stand today. *Entropy (Basel)* (2020) 22(6):627. doi: 10.3390/e22060627

29. Kocak B, Durmaz ES, Ates E, Kaya OK, Kilickesmez O. Unenhanced CT texture analysis of clear cell renal cell carcinomas: A machine learning-based study for predicting histopathologic nuclear grade. *AJR Am J Roentgenol* (2019) 11:W1–8. doi: 10.2214/AJR.18.20742

30. Shu J, Tang Y, Cui J, Yang R, Meng X, Cai Z, et al. Clear cell renal cell carcinoma: CT-based radiomics features for the prediction of fuhrman grade. *Eur J Radiol* (2018) 109:8–12. doi: 10.1016/j.ejrad.2018.10.005

31. Chandrashekar G, Sahin F. A survey on feature selection methods. *Comput Electrical Eng* (2014) 40(1):16–28. doi: 10.1016/j.compeleceng.2013.11.024

32. Parmar C, Grossmann P, Rietveld D, Rietbergen MM, Aerts H. Radiomic machine learning classifiers for prognostic biomarkers of head & neck cancer. *Front Oncol* (2015) 5(4). doi: 10.3389/fonc.2015.00272

33. Barone S, Cannella R, Comelli A, Pellegrino A, Salvaggio G, Stefano A, et al. Hybrid descriptive-inferential method for key feature selection in prostate cancer radiomics. *Appl Stochastic Models Business Industry* (2021) 37(5):961–72. doi: 10.1002/asmb.2642

34. Wu N, Huang J, Zhang XF, Ou-Yang L, He S, Zhu Z, et al. Weighted fused pathway graphical lasso for joint estimation of multiple gene networks. *Front Genet* (2019) 10:623. doi: 10.3389/fgene.2019.00623

35. Feng Z, Shen Q, Li Y, Hu Z. CT texture analysis: a potential tool for predicting the fuhrman grade of clear-cell renal carcinoma. *Cancer Imaging* (2019) 19(1):6. doi: 10.1186/s40644-019-0195-7

36. Bektas CT, Kocak B, Yardimci AH, Turkcanoglu MH, Yucetas U, Koca SB, et al. Clear cell renal cell carcinoma: Machine learning-based quantitative computed tomography texture analysis for prediction of fuhrman nuclear grade. *Eur Radiol* (2019) 29(3):1153–63. doi: 10.1007/s00330-018-5698-2

37. Shu J, Wen D, Xi Y, Xia Y, Cai Z, Xu W, et al. Clear cell renal cell carcinoma: Machine learning-based computed tomography radiomics analysis for the prediction of WHO/ISUP grade. *Eur J Radiol* (2019) 121:108738. doi: 10.1016/j.ejrad.2019.108738

38. Timmeren J, Cester D, Tanadini-Lang S, Alkadhi H, Baessler B. Radiomics in medical imaging—"how-to" guide and critical reflection. *Insights into Imaging* (2020) 11(1):91–107. doi: 10.1186/s13244-020-00887-2

39. Sharma N, Aggarwal LM Automated medical image segmentation techniques. *Journal of Medical Physics* (2010) 35(1):3–14. doi: 10.4103/0971-6203.58777

40. Suarez-Ibarrola R, Basulto-Martinez M, Heinze A, Gratzke C, Miernik A Radiomics Applications in Renal Tumor Assessment: A Comprehensive Review of the Literature. *Cancers (Basel)* (2020) 12(6):1387. doi: 10.3390/cancers12061387

41. Bhandari A, Ibrahim M, Sharma C, Liong R, Gustafson S Prior M.CT-based radiomics for differentiating renal tumours: a systematic review. *Abdom Radiol* (2020) 46(5):2052–63. doi: 10.1007/s00261-020-02832-9

42. Algohary A, Shiradkar R, Pahwa S, Purysko A, Verma S, Moses D, et al. Combination of peri-tumoral and intra-tumoral radiomic features on bi-parametric MRI accurately stratifies prostate cancer risk: A multi-site study. *Cancers (Basel)* (2020) 12(8):2200. doi: 10.3390/cancers12082200

frontiers | Frontiers in Oncology

TYPE Original Research
PUBLISHED 28 April 2023
DOI 10.3389/fonc.2023.1036734

OPEN ACCESS

EDITED BY
Haibin Shi,
Soochow University, China

REVIEWED BY
Stephan Ursprung,
University Hospital Tuebingen, Germany
Mohamed Shehata,
University of Louisville, United States

*CORRESPONDENCE
Sipeng Shen
sshen@njmu.edu.cn
Shifeng Su
shifengsu@163.com
Zengjun Wang
zengjunwang@njmu.edu.cn

†These authors have contributed equally to this work and share first authorship

RECEIVED 05 September 2022
ACCEPTED 18 April 2023
PUBLISHED 28 April 2023

CITATION
Xing J, Liu Y, Wang Z, Xu A, Su S, Shen S and Wang Z (2023) Incremental value of radiomics with machine learning to the existing prognostic models for predicting outcome in renal cell carcinoma. *Front. Oncol.* 13:1036734. doi: 10.3389/fonc.2023.1036734

Incremental value of radiomics with machine learning to the existing prognostic models for predicting outcome in renal cell carcinoma

Jiajun Xing[1†], Yiyang Liu[1], Zhongyuan Wang[1†], Aiming Xu[1], Shifeng Su[1*], Sipeng Shen[2*] and Zengjun Wang[1*]

[1]Department of Urology, The First Affiliated Hospital of Nanjing Medical University, Nanjing, China, [2]Department of Biostatistics, School of Public Health, Nanjing Medical University, Nanjing, Jiangsu, China

Purpose: To systematically evaluate the potential of radiomics coupled with machine-learning algorithms to improve the predictive power for overall survival (OS) of renal cell carcinoma (RCC).

Methods: A total of 689 RCC patients (281 in the training cohort, 225 in the validation cohort 1 and 183 in the validation cohort 2) who underwent preoperative contrast-enhanced CT and surgical treatment were recruited from three independent databases and one institution. 851 radiomics features were screened using machine-learning algorithm, including Random Forest and Lasso-COX Regression, to establish radiomics signature. The clinical and radiomics nomogram were built by multivariate COX regression. The models were further assessed by Time-dependent receiver operator characteristic, concordance index, calibration curve, clinical impact curve and decision curve analysis.

Result: The radiomics signature comprised 11 prognosis-related features and was significantly correlated with OS in the training and two validation cohorts (Hazard Ratios: 2.718 (2.246,3.291)). Based on radiomics signature, WHOISUP, SSIGN, TNM Stage and clinical score, the radiomics nomogram has been developed. Compared with the existing prognostic models, the AUCs of 5 years OS prediction of the radiomics nomogram were superior to the TNM, WHOISUP and SSIGN model in the training cohort (0.841 vs 0.734, 0.707, 0.644) and validation cohort2 (0.917 vs 0.707, 0.773, 0.771). Stratification analysis suggested that the sensitivity of some drugs and pathways in cancer were observed different for RCC patients with high-and low-radiomics scores.

Conclusion: This study showed the application of contrast-enhanced CT-based radiomics in RCC patients, creating novel radiomics nomogram that could be used to predict OS. Radiomics provided incremental prognostic value to the existing models and significantly improved the predictive power. The radiomics nomogram might be helpful for clinicians to evaluate the benefit of surgery or

adjuvant therapy and make individualized therapeutic regimens for patients with renal cell carcinoma.

KEYWORDS

renal cell carcinoma, radiomics, prognostic model, machine learning, computed tomography running title, incremental value estimation

1 Introduction

The most common malignant tumor in the kidney is renal cell carcinoma (RCC), which originates from the proximal tubular epithelial system of the renal parenchyma, and more than 60,000 people worldwide suffer from it every year (1–3). According to European Association of Urology Guidelines, surgical treatment is the first choice for patients with RCC, of whom the overall 5-year survival rate was in the range of 50–60% (4, 5).

RCC is recognized as having a highly variable natural history, according to the previous reports (6). RCC patients have different responses to surgical treatment and prognosis (7). Many prognostic models for RCC have previously been developed to provide prognostic assessment for patients and to inform clinical management strategies and improve risk stratification for clinical trials, including prognostic scores based on TNM stage, tumor size, nuclear grade and necrosis (SSIGN), tumor-node-metastasis (TNM) stage and WHOISUP (8). According to a report from a retrospective study evaluating 358 patients with RCC, the predictive efficiency of the SSIGN model was slightly better than that of the TNM stage system (9).

According to the European Association of Urology guidelines, among patients with stage I-II localized RCC, neoadjuvant therapy is still experimental, and chemotherapy and targeted therapy are not standard treatments for most patients (10). Especially for resectable tumors, it should not be routinely presented outside of clinical trials. However, despite following postoperative surveillance guidelines, approximately 20% to 30% of patients with TNM stage I and II RCC who were considered to have a better prognosis would develop recurrence or metastasis after surgery (11, 12). Therefore, existing prognostic models showed certain limitations in current clinical practice, and the ability to accurately predict individual patient outcomes remained limited. An accurate and simple RCC prognostic tool is still urgently needed.

Tumor heterogeneity is defined as tumor cell with distinct molecular and phenotypic characteristics. Recent evidence suggested that the level of tumor heterogeneity could serve as a prognostic biomarker (13). Tumor heterogeneity manifests at multiple spatial dimensions, mainly including genetic, cellular, histological, and radiological levels. The TNM stage and SSIGN score system are mainly based on the anatomical and histological features of tumors, which cannot reflect the heterogeneity of tumors and may not be sufficient to provide accurate prognostic information for RCC patients (14, 15). In current clinical practice, the phenotypic heterogeneity of RCC was mainly assessed by biopsy-based microscopy and gene expression analysis. However, the capabilities of genomics, proteomics or histology were limited. It was difficult to assess intratumor heterogeneity well with a random sample alone.

Radiomics is a promising approach to automatically mine a lot of quantitative image features that are difficult to identify with the naked eye and reveal aspects of intratumor heterogeneity with potential prognostic relevance (16, 17). The application of machine learning in radiomics has emerged as a non-invasive and low-cost method for accurate prognosis assessment.

The aim of this study was to identify radiomics features associated with overall survival in RCC, to evaluate its incremental value to clinical characteristics and other existing prognostic models, to establish a visual nomogram for patients with RCC and to provide reference for neoadjuvant therapy and surgical plan.

2 Related work

Radiomics refers to the extraction of high-throughput quantitative features from radiographic images, the in-depth non-invasive analysis of tumor heterogeneity across the tumor volume, and the establishment of predictive models that correlate imaging features with genomic patterns and clinical outcomes. Recently, radiomics has been widely applied in tumor imaging-based diagnosis, prognosis prediction, and efficacy monitoring. Some of the studies were presented below:

According to previous reports, among patients with stage I lung adenocarcinoma, the radiomics signature was associated with overall survival. The clinical-radiomics nomogram could accurately predict Axillary lymph node metastasis (ALNM) (AUC: 0.92) (18). The model, integrating clinical variables and radiomics features, had good performance for predicting Microvascular invasion (MVI) and clinical outcomes (19). Meanwhile, Ruizhi Gao et al. provided a predictive nomogram that integrates radiomic and clinicopathological characteristics for predicting the progression-free interval (PFI) of kidney renal clear cell carcinoma patients (20). Mostafa Nazari et al. developed a robust radiomics-based classifier that was capable of accurately predicting overall survival of RCC patients for prognosis of ccRCC patients (21).

In addition, Multiparametric MRI (mpMRI) allows assessment of the anatomical and functional characteristics of the renal mass. Using diffusion MRI, parenchymal wash index, and ADC ratio were correlated with clear-cell RCC Fuhrman grade, with a pooled

sensitivity and specificity of DWI to differentiate between high and low grades of 78% and 86%, respectively (22, 23).

Most of the above studies have used texture analysis, meanwhile, other studies have also used convolutional neural network (CNN). An ensemble model based on residual convolutional neural network (ResNet) was built combining clinical variables and T1C and T2WI MR images using a bagging classifier to predict renal tumor pathology. Stavropoulos et al. found that compared with all experts averaged, the ensemble deep learning model had higher test accuracy (0.70 vs. 0.60, P = 0.053), sensitivity (0.92 vs. 0.80, P = 0.017), and specificity (0.41 vs. 0.35, P = 0.450) (24).

3 Materials and methods

3.1 Study design and patients

A total of 689 patients with renal cell carcinoma confirmed by histology were recruited in this study. 281 RCC patients came from the First Affiliated Hospital of Nanjing Medical University (NJMU) from 2010 to 2019. In addition, 408 patients were collected from three external database (Clinical Proteomic Tumor Analysis Consortium (CPTAC), Kidney Tumor Segmentation Challenge (KITS) and The Cancer Imaging Archive (TCIA)). The criteria for inclusion and exclusion are as follows: i) patients with complete baseline and follow-up information; ii) patients with contrast-enhanced CT imaging including arterial phase before surgical resection; iii) patients histologically confirmed RCC; iv) no imaging artifacts. The detailed flowchart summarizing patient inclusion and exclusion in this study was presented in Figure S1.

In the phase of model development, we used the NJMU as the training cohort (N=281) and the remaining datasets (CPTAC, TCIA, and KITS) as the two independent validation cohorts (N1 = 225, N2 = 183). The validation cohort1 contained the patients in TCIA and CPTAC (NCI) datasets while the validation cohort2 contained the patients in KITS dataset. All relevant data was collected in July 2020, and for patients who could not visit the hospital, a follow-up phone call was conducted. The overall survival was calculated from the date of pathological diagnosis to the time of death or the last follow-up. Baseline data consisted of Age, Gender, Body Mass Index (BMI), TNM stage, WHOISUP, Tumor size, Laterality, Location, Tumor margin, SSIGN. The TNM stage is based on The Union for International Cancer Control tumor node metastasis staging system (8). In SSIGN, risk points are accumulated and added up to provide a risk score (25).

The primary tool to assess frailty was the modified frailty index of the Canadian Study of Health and Aging (11-CSHA), which is a validated tool based on clinical data and consisting of eleven elements. The sum score is divided by 11 and a cut-off of ≥ 0.27 has been defined to mirror frailty (26).

3.2 Radiomics feature extraction

In the training set, a total of two types of CT scanners are involved, including Philips iCT 256 (Koninklijke Philips, Nevada, USA) and Somatom force CT A50A (Siemens Healthcare GmbH, Erlangen, Germany). The detail CT scanning parameters are shown in Table S1.

The workflow of the study was shown in Figure 1. The regions of interest (ROIs) in the RCC were separately manually slice-by-slice contoured and segmented using 3D Slicer (version 4.11.2) by two urologists (Yiyang Liu and Shifeng Su), who were not informed of the patients' personal information. Each of them with at least 10 years of clinical experience in kidney CT, took full responsibility for the ROI delineation. The ROIs were evaluated by experts following the medical imaging standards. After the ROIs of the SRMs were delineated, the CT images were transferred to a radiomics plugin for 3D Slicer (PyRadiomics). Then, the extraction of in-house radiomics features was performed using PyRadiomics package. Each ROI in contrast-enhanced CT imaging (arterial phase) had eight sets of radiomics features. The voxel-based features included shape 2D, shape 3D, first-order, gray-level cooccurrence matrix (GLCM), gray-level size zone matrix (GLSZM), gray-level dependence matrix (GLDM), gray level run length matrix (GLRLM) and neighbouring gray tone difference matrix (NGTDM), containing a total of 851 quantitative features. The Bland-Altman test was used for assessment of interobserver variability.

The extracted radiomics features in each dataset were further normalized with mean value=0 and standard deviation=1 to make all the variables comparable across different dataset and applicable easily in the future.

3.3 Unsupervised clustering and subgroup discovery

Unsupervised hierarchical clustering, based on the raw radiomics data scaled by mean and centered, was performed using cutree package in R. Kaplan-Meier overall survival curves were plotted using survival package in R. The statistical difference in survival between the two patient subgroups was calculated with the coxph function. The heatmap was plotted using the pheatmap package in R.

3.4 Development of the radiomics signature

Random Forest was performed using the ranger package. The random forest feature importance was obtained from ranger-package's variable-importance-parameter on a trained random forest model. In the training cohort, the radiomics features associated with overall survival were screened by the least absolute shrinkage and selection operator (LASSO) Cox regression. The Radiomics signature was calculated with a linear combination of the selected radiomics features multiplied by their corresponding LASSO-Cox coefficients. Based on median radiomics score, patients were classified as high-risk or low-risk group. Kaplan-Meier overall survival analysis was performed between the stratified subgroups.

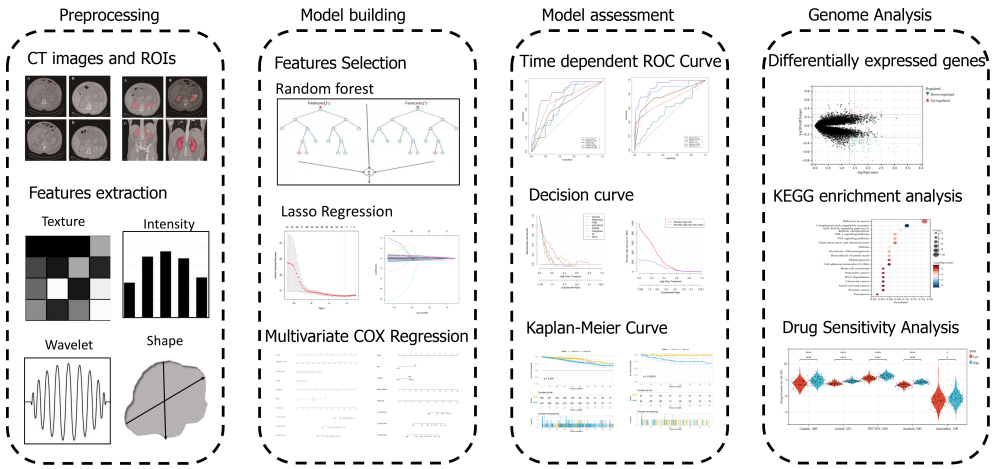

FIGURE 1
Graphical abstract of radiomics analysis and model building.

3.5 Development of the radiomics nomogram

The association between clinical characteristics and overall survival was separately evaluated by the univariable and multivariable Cox regression analysis. The hazard ratio (HR) of each predictor was obtained simultaneously. The clinical nomogram and radiomics nomogram, which predicted 1-, 3- and 5-year overall survival, were separately constructed using the rms and survival package in R. Based on TMN Stage, WHOISUP and SSIGN, the prognosis model for OS Prediction has been developed by survival package in R.

3.6 Identification of DEGs and functional enrichment analysis

The differentially expressed genes (DEGs) were identified between the high- and low-risk subgroups using the limma package with criteria of |log2-fold change (FC)| ≥ 1 and p-value < 0.05.

The KEGG enrichment analysis was performed using the clusterProfiler package to obtain the results of gene set enrichment. For Gene set enrichment analysis (GSEA), the GSEA software was obtained from the GSEA website (http://software.broadinstitute.org/gsea/index.jsp) to evaluate related pathways and molecular mechanisms.

3.7 Mutation and drug sensitivity analysis

The mutational profiles of RCC patients between high and low risk subgroups were identified using the maftools package. To explore the sensitivity of antineoplastic drugs in RCC patients, the semi-inhibitory concentration (IC50) values of common drugs was calculated using the oncoPredict package.

3.8 Statistical analysis

Statistical tests were performed with R statistical software. To evaluate the performance of the prognosis model, we used calibration curves constructed by rms package. The performance of the models was evaluated by the time-dependent area under the curve (AUC) of receiver operator characteristic (ROC). The decision curve analysis (DCA) was performed with the rmda package. For all analyses, $P < 0.05$ was considered statistically significant.

4 Result

4.1 Basic characteristics

Table S2 showed the clinical characteristics of the entire cohort (689 participants, median 58.8 years), training cohort (NJMU, 281 participants, median 57 years), validation cohort 1 (NCI, 225 participants, median 61 years) and validation cohort 2 (183 participants, median 58 years). The mean follow-up for patients in the entire cohort was 41 months; and the 5-year OS rates were 86.9%, which was slightly higher than 71% reported in localized RCC in the literature, which might well be attributable to loss of some patients without surgery.

4.2 Overview of radiomics profile in RCC

To understand the radiomics features of RCC, the unsupervised hierarchical clustering analysis was conducted in the entire cohort. Based purely on the radiomics data, two distinct subgroups within RCC patients were identified (Figure 2A). Subgroup 2 was significantly associated with poor OS (p =0.004, log-rank test; Figure 2B). Furthermore, in the forest plot of the entire cohort, the significant Hazard Ratios were found for the subgroup, more specifically, in each age level (<60 and >=60), each BMI level (<=24 and >24), and

regardless of TMN Stage, SSIGN level and WHOISUP (Figure 2C). In aggregate, unsupervised analysis suggested an intrinsic association between radiomics features and clinical characteristics, warranting further research.

4.3 Radiomics Signature for OS prediction with machine learning

To construct the radiomics signature, we extracted the 851 radiomics features of contrast-enhanced CT images. These features were screened in the random forest model to obtain the robust predictive factors. Based on the importance scores of features from the random forest model, the top five percent of the variables, 43 radiomics features were selected (Figure 3A; Table S3). Then, by LASSO-Cox regression analysis, 11 potential predictors from the 43 candidate variables were selected in the training cohort (Figures 3B, C). The calculation formula of radiomics signature was shown in the Table S4. Accordingly, the patients with RCC were divided into low-risk and high-risk groups. The high-risk group was significantly associated with poor OS in the three cohorts ($p < 0.001$, log-rank test; Figures 3D–F).

The prognostic power of the radiomics signature was assessed using time-dependent ROC analysis in the training cohort and two validation cohorts (Figures 4A–C). The radiomics model resulted in AUCs of 5-year OS prediction, 0.7409, 0.7947 and 0.830, respectively.

4.4 TNM stage, WHOISUP and SSIGN for OS prediction

The TNM Stage, WHOISUP and SSIGN are relatively common prognostic predictors. We put the three prognostic factors separately into the COX regression to establish overall survival prediction model. The above three prognostic predictors were negatively correlated to OS (HR for TNM Stage: 2.563, 95% CI: 1.246-5.271; HR for WHOISUP: 5.096, 95% CI: 2.435-10.670; HR for SSIGN: 1.2, 95% CI: 1.058-1.360).

The TNM Stage, WHOISUP and SSIGN models resulted in AUCs of 5 years OS prediction, 0.7409,0.7947 and 0.830, respectively, in the training cohort (Figure 4A) and 0.771,0.707 and 0.773 in validation cohort 2 (Figure 4C).

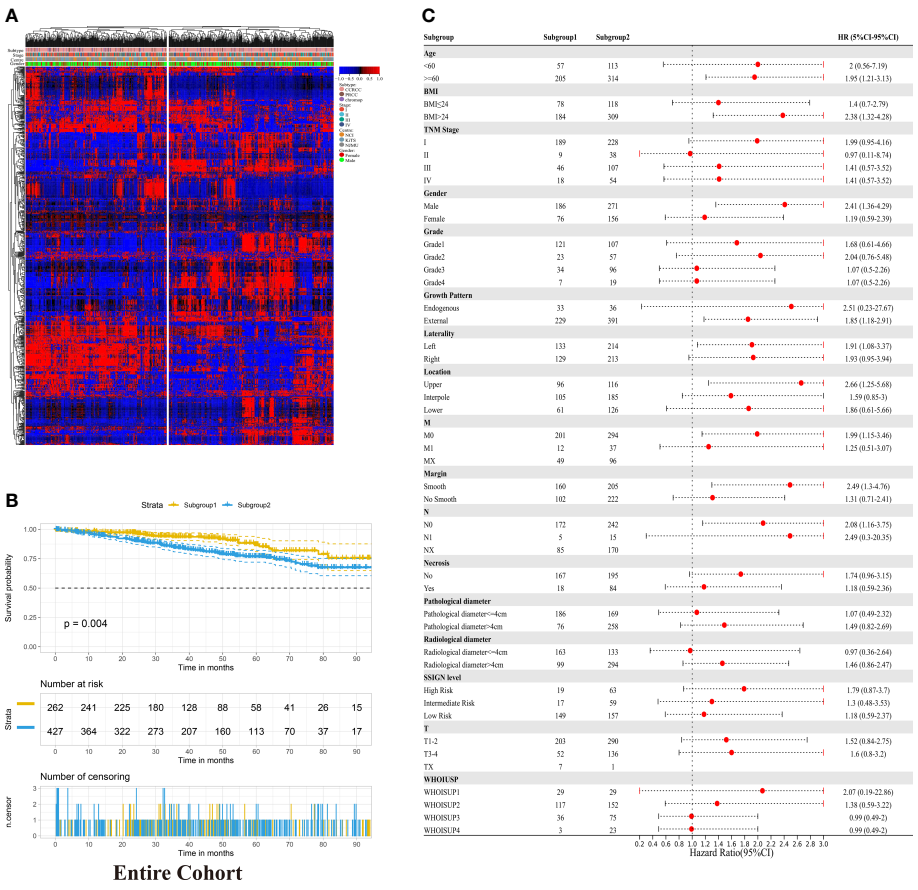

FIGURE 2
Unsupervised clustering analysis of radiomic data in RCC. **(A)** Unsupervised hierarchical clustering of radiomic profile from RCC identified two distinct subgroups. The associations between radiomic subgroups with gender, subtype and TNM stage are indicated on the right. **(B)** Kaplan-Meier analysis of the radiomic subgroups with OS in the entire cohort. **(C)** Hazard Ratios for radiomics grouping in each clinicopathological subgroup in the entire cohort.

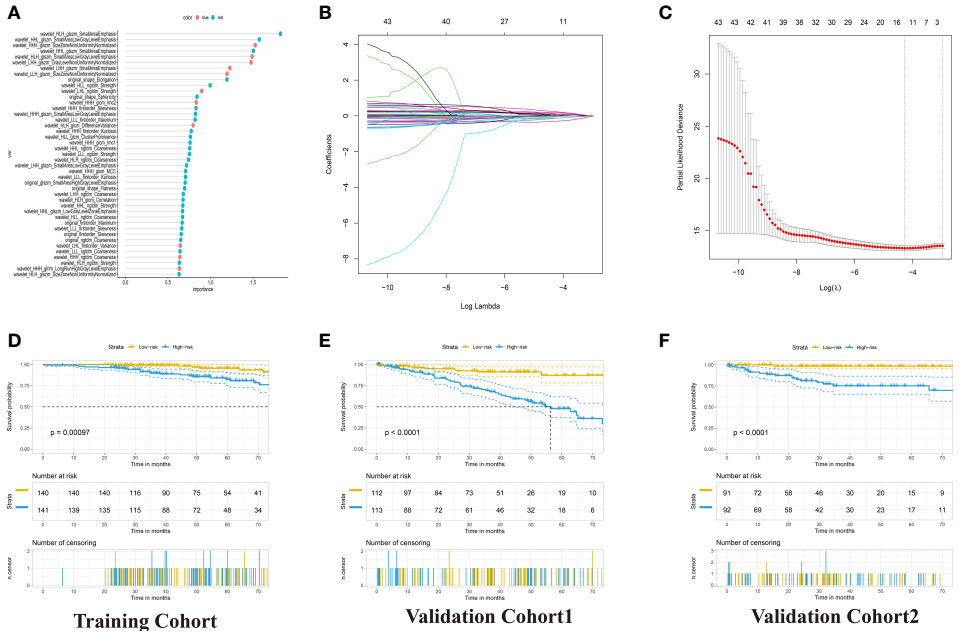

FIGURE 3
Development of the Radiomics Signature for OS Prediction with Machine Learning. **(A)** 43 radiomics feature importance from random-forest models. **(B)** The 5-fold cross-validation for tuning parameter screening in the LASSO regression model. **(C)** LASSO coefficient profiles of the features at different lambda values. **(D–F)** Kaplan–Meier curves for patients with High- and Low-Radiomics Score in the training and two validation cohorts.

4.5 Clinical nomogram and radiomics nomogram for OS prediction

The results of univariate and multivariable COX regression analyses in the training cohort were shown in Table S5. The age-level, location and radio-diameter were significantly associated with OS, and these factors as independent prognostic factors were used to develop the clinical nomogram (Table S6). The clinical nomogram could distinguish high-risk from low-risk patients in the training cohort (p =0.0015, log-rank test) and the validation cohorts (Figures 5A, C; S2D, S2I).

The radiomics nomogram was built with Radiomics signature, TNM Stage, WHOISUP, SSIGN and Clinical score by the multivariate Cox regression analysis (Figure 5B, Table S7). The radiomics nomogram could distinguish high-risk from low-risk patients in the training cohort (p<0.0001, log-rank test, Figure 5D) and the validation cohort1 (p<0.001, Figure S2H). The clinical nomogram and radiomics nomogram resulted in AUCs of 5 years OS prediction, 0.676 and 0.841 in the training cohort, respectively, and 0.567 and 0.917 in validation cohort 2 (Figures 4A, C).

4.6 Prediction performance of the models

The prediction performances of the six models (clinical nomogram, radiomics nomogram, TNM Stage model, WHOISUP model, SSIGN model and radiomics signature) were presented in Table 1.

Compared with the existing prognostic models, the AUC of 5 years OS prediction of the radiomics nomogram was superior to the TNM, WHOISUP and SSIGN model in the training cohort (0.841 vs 0.734, 0.707, 0.644) and validation cohort 2 (0.917 vs 0.707, 0.773, 0.771). Radiomics provided incremental value to traditional models and improved the power to predict prognosis. The risk plot of radiomics nomogram suggested as risk score increased, overall survival time decreased and mortality rose (Figures 4G, H). Moreover, the heatmap of selected prognostic predictors was shown in Figure 4I.

The calibration curves of the radiomics nomogram for the probability of 5 years OS were presented in Figure 6F. The estimations with the radiomics nomogram were consistent with actual observations in the training, and 2 validation cohorts. And, the corresponding calibration curves of other models at 5 years were shown in Figures 6; S3.

To evaluate clinical applicability of these prognostic models, Clinical impact curve (CIC) analysis was conducted in Figures 6G–L and Figure S3. CIC visually indicated that the radiomics nomogram had a greater overall net benefit across a range of threshold probabilities, suggesting that the radiomics nomogram possessed significant prognostic value.

In the DCA analysis for the 6 prognostic models, the radiomics signature and radiomics nomogram showed superior overall net benefit over the existing prognostic models in predicting OS in the training and validation cohorts (Figures 4D–F). If the threshold probability of the traditional existing models was greater than 10% for predicting OS, radiomics nomogram had more benefit than either the SSISN, TNM Stage WHOISUP, or radiomics signature alone.

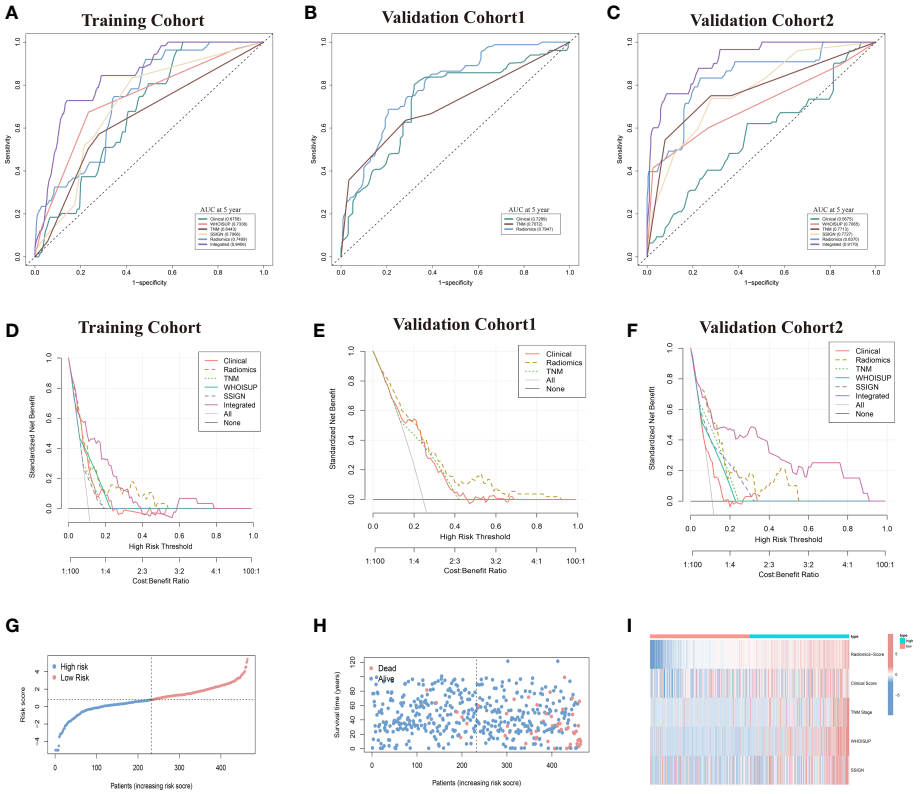

FIGURE 4
Prediction performance of the six models in the training and validation cohorts. **(A–C)** Time-independent ROC curves comparing the predictive accuracy of six models in the training and two validation cohorts. **(D–F)** Decision curves comparing six models among a series of risk thresholds in the training and two validation cohorts. **(G, H)** Ranked dot and scatter plots showing the radiomics-nomogram score distribution and patient survival status. **(I)** Component patterns of 5 selected prognostic factors in high- and low-risk groups for radiomics nomogram.

4.7 Biological interpretation and drug sensitivity of the radiomics signature

To explore the radiomics-related biological characteristics of renal cell carcinoma, based on their radiomics signatures, we divided the NCI validation cohort1 into high- and low-risk groups. We compared the transcriptome data of the two groups to find out the DEGs (Figures 7A, C; S4A, S4C). Then, we evaluated enrichments of KEGG pathways (Figures 7D and S4B); We found that HIF-1 signaling pathways and TNF signaling pathways were significantly enriched in the DEGs. Similarly, we identified that in gene set enrichment analysis (GSEA), for RCC patient samples in high-risk group, three signaling pathways were significantly enriched: P53-Signaling Pathway, G2 Phase and Composition of Lipid Particles (Figures 7E–G).

Additionally, the distribution differences of the somatic mutations were investigated between high-risk and low-risk groups in the TCGA-RCC dataset. As shown in Figure 7B, the VHL mutation incidence of were higher than 20% in RCC patients in two groups. Interestingly, compared with RCC in low-risk group, these tumor-related genes were more likely to be mutated in the high-risk group.

Further, to determine the power of radiomics signature to predict drug therapeutic response among RCC patients, the IC50 values of 198 drugs were evaluated in TCGA-RCC patients. We found that RCC patients in low-risk group might positively respond to Axitinib, Cisplatin, Gemcitabine, PD173074 and Sorafenib (Figure 7H). In summary, these findings suggested that radiomics signature was correlated with drug sensitivity.

4.8 Sensitivity analysis for the consistency of radiomics features

To evaluate the consistency and robustness of the extracted radiomics features, we further reanalyzed the CT images of our study using 3D Slicer by two urologists. The repeated radiomic features showed a high consistency (Pearson r, median (IQR): 0.71 (0.43-0.85)). 532 of 851 features (62.5%) had Pearson r > 0.6 (Figure S5A). Additionally, we estimated the mean difference between 11 duplicate radiomics features, and compared Bland-Altman plots of agreement between two observers (Bland and Altman, 1986) (Figures S5B–L; Table S8). There was high measurement agreement between two observers using the Bland-Altman test.

5 Discussion

In this study, we evaluated the predictive performance of the existing prognostic models for OS in RCC patients, and established a radiomics signature by machine learning algorithms and a

10.3389/fonc.2023.1036734

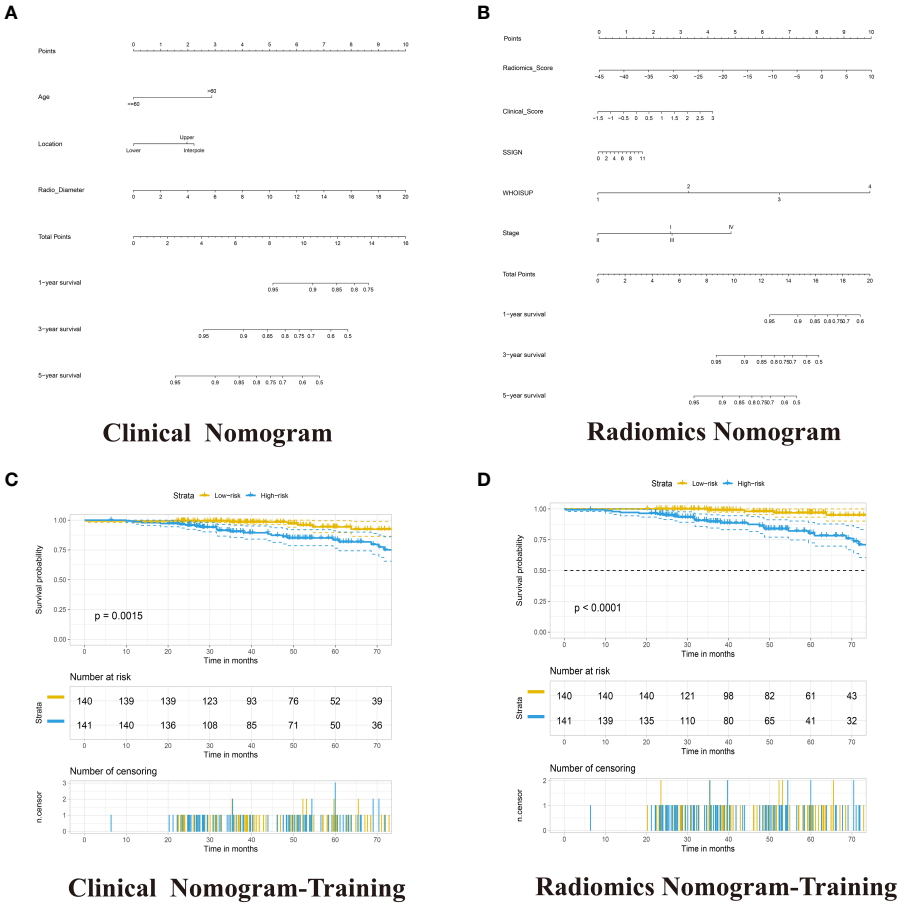

FIGURE 5
Development of the Clinical Nomogram and Radiomics Nomogram. **(A)** Nomogram for predicting the ratio of RCC patients with a certain survival time incorporating Age-level, Location and Radio-diameter in the training cohort. **(B)** Nomogram for predicting the ratio of RCC patients with a certain survival time incorporating Clinical score, SSIGN, TNM Stage, WHOISUP and radiomics signature in the training cohort. **(C, D)** Kaplan–Meier analysis of overall survival curves of High- and Low- Clinical or Radiomics nomogram in training group.

radiomics nomogram by multivariate COX regression. We demonstrated that the addition of the radiomics signature significantly improved the predictive power of traditional prognostic models, the model's ability to significantly classify patients into low- and high-risk groups, and its stability across both training and validation cohorts. Finally, our preliminary studies about genomics revealed a correlation between radiomics signature and the enrichment of certain pathways in tumors, as well as drug sensitivity.

The Tumor, Node and Metastasis (TNM) staging system is a method for stratifying cancer patients based on data from a large multicenter study involving a large number of patients and has a good level of evidence (15). TNM staging is also the most commonly used prognostic system for renal cell carcinoma.

TABLE 1 Performance of six prognostic models in training and validation cohorts.

Cohort	Training Cohort		Validation Cohort1		Validation Cohort2		Threshold
	AUC at 5 years	C index	AUC at 5 years	C index	AUC at 5 years		
Radiomics Signature	0.741	0.614(0.498,0.73)	0.795	0.707(0.625,0.789)	0.837	0.828(0.748,0.908)	0.275
Clinical Nomogram	0.676	0.709(0.627,0.791)	0.729	0.691(0.622,0.76)	0.567	0.719(0.617,0.821)	-0.193
WHOISUP Model	0.734	0.73(0.63,0.83)	–	–	0.707	0.791(0.681,0.901)	1.87
SSIGN Model	0.707	0.675(0.575,0.775)	–	–	0.773	0.74(0.617,0.863)	-0.183
TNM Stage Model	0.644	0.62(0.52,0.72)	0.707	0.741(0.665,0.817)	0.771	0.761(0.632,0.89)	0.9
Radiomics Nomogram	0.841	0.834(0.779,0.889)	–	–	0.917	0.923(0.878,0.968)	0.78

10.3389/fonc.2023.1036734

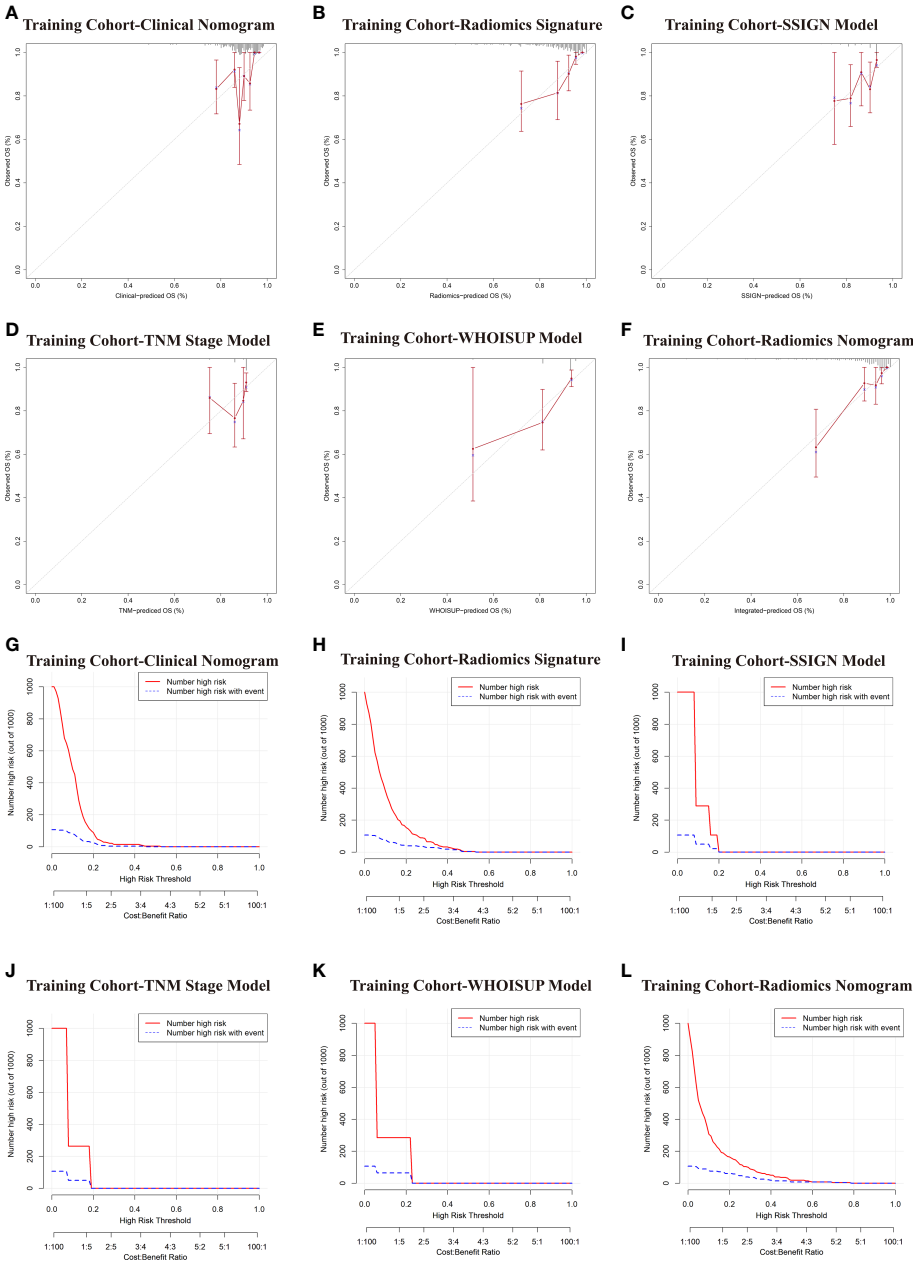

FIGURE 6
Comparative evaluation of various models in the training and validation cohorts. **(A–F)** Calibration plots describing the calibration of six models based on the consistency between predicted and observed 5-year OS results. **(G–L)** Clinical Impact Curve (CIC) of six models in the training cohort. The red curve (Number high Risk) represents the number of people classified as positive (high risk) by the model at each threshold probability; The blue curve (Number high risk with outcome) is the Number of true positives at each threshold probability.

However, patients with the same TNM stage often could have various genetic and clinicopathological features and inconsistent survival rates. WHOISUP is also an important standard for the commonly used microscopic classification of renal cell carcinoma (27). According to the World Health Organization/International Society of Urological Pathology (WHO/ISUP) 4th edition grading system, RCC is classified into grades I to IV. Among RCC patients after surgery, including those with Partial nephrectomy (PN) and Radical nephrectomy (RN), the SSIGN score is a valuable prognostic tool (14). The existing prognostic models are widely recognized and used for post-operative management and clinical trial design. For patients with good or moderate prognosis, especially for patients with limited tumor burden and few symptoms, regular follow-up observation is generally recommended after surgery (28). Follow-up schedule for localized renal cell carcinoma after surgery should depend on the possibility of recurrence. CT scans of the chest and abdomen are routinely performed at intervals depending on the prognostic risk rating. For patients with poor prognosis, pembrolizumab combined with axitinib, lenvatinib and other drugs can be considered after

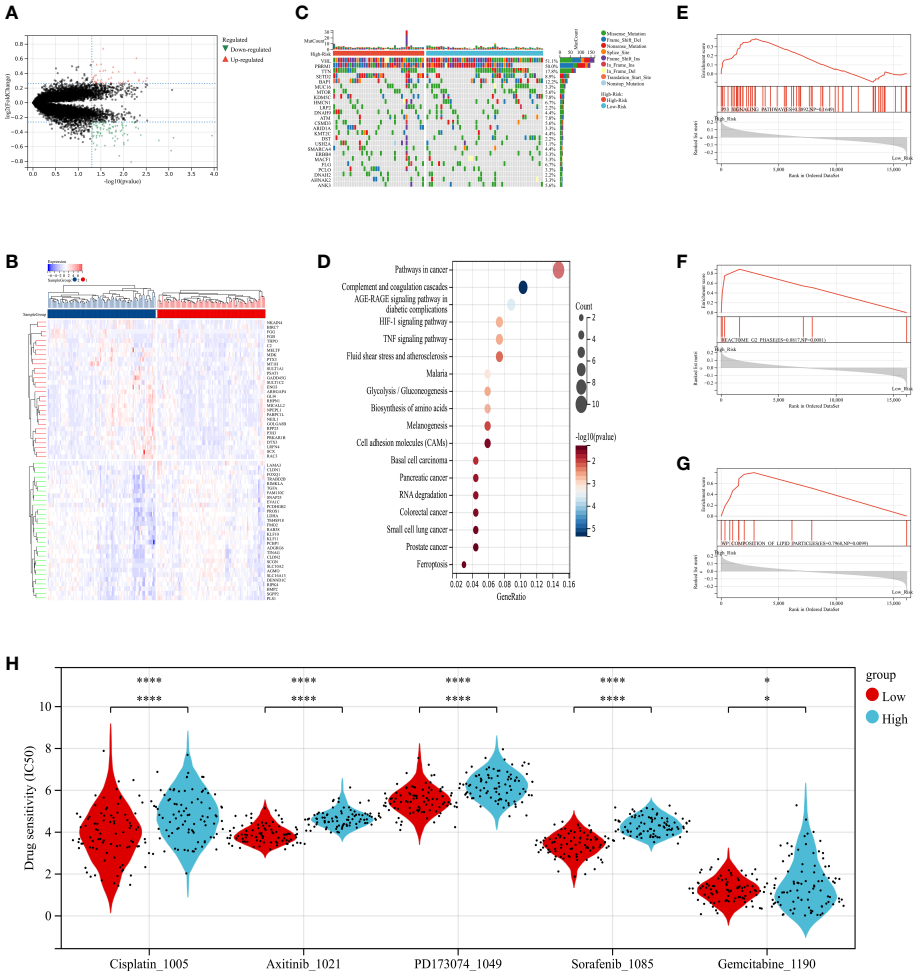

FIGURE 7
The relationship between radiomics and genomics in TCGA. **(A)** A volcano plot generated using the data of DEGs between high-risk and low-risk groups from TCGA. **(B)** The waterfall plot of somatic genetic alteration features established with high- and low- radiomics score. **(C)** Hierarchical clustering of 30 DEGs of RCC. **(D)** KEGG pathways analysis of DEGs associated with radiomics signature. **(E–G)** Gene Set Enrichment Analyses showed three representative pathways enriched in the high-radiomics score group. **(H)** Relationships between radiomics signature and drug sensitivity.

surgery (29, 30). Therefore, accurate prediction of patient prognosis and risk stratification of RCC patients is an urgent problem.

It has been reported that frailty put patients undergoing surgery at a higher risk for developing poor healthcare outcomes (31). Besides tumor characteristics, patient characteristics, such as frailty, seemed to be the main aspects determining the postoperative outcome (32). However, the mean frailty score based on 11-CSHA score for patients was 0.18 ± 0.08 and 0.12 ± 0.06, respectively, in the training cohort and in validation cohort 2. There were only 16 patients (frailty score≥ 0.27) in the validation cohort2. This could be because frailty has been an important factor for the therapeutic strategy patients and clinicians choose as treatment for RCCs.

Although the above models took into account clinicopathological variables, tumor heterogeneity, which was thought to be associated with poorer patient outcomes, was not taken into account. It has been reported that the predictive power of these existing prognostic models might be significantly overestimated (33, 34). Although, tumor heterogeneity reduced the value of histopathology based on cell morphology and gene expression, it provided an opportunity for medical imaging to characterize whole tumors in a non-invasive and reproducible manner. In traditional radiology practice, images were typically evaluated visually or qualitatively, with the exception of a few measurements such as dimensions and volumes. This approach not only involved intra- and interobserver variability, but also left a large amount of deep hidden data in medical images that were not used, which limited the potential of precision medicine. In contrast, radiomics provides important complementary data on imaging phenotypes that may be informative (35).

Combining radiomic features, traditional staging systems, and other clinicopathological risk factors can improve the predictive power of tumor prognosis (36). In this study, a radiomics nomogram, combining radiomics signature with Clinical score, TNM stage, WHOISUP, and SSIGN prognostic factors, was established. The nomogram outperformed models using either radiomics or prognostic model alone (C index: 0.834 vs 0.62, 0.675, 0.73, 0.709). The radiomics nomogram combined multiple

prognostic factors to accurately predict OS and stratify high and low-risk groups in RCC patients. This result was not surprising, as radiomics reflected higher-order imaging features that captured more tumor heterogeneity than macroscopic-level histopathological and clinical information. In this study, we included more patients with combined clinical characteristics and radiomics features to predict individualized survival with superior performance. Our discovery would take a critical step in which predictive models based on radiomics features could benefit physicians, patients and caregivers in managing RCC and facilitating personalized treatment.

Meanwhile, some studies have demonstrated different results due to the instability and low reproducibility of the radiomics model. A meta-analysis has indicated that image biomarkers based on the adjacent grey tone difference matrix and the size zone matrix should not be used in multi-center study, because these radiomics features were extremely sensitive to variations (37). Furthermore, CT images obtained from different hospitals may vary widely, thus leading to potential bias in multicenter studies. Multicenter normalization of medical images is the key to improve the predictive performance of radiomics-based applications. The robustness of reliability and repeatability is a major issue for clinical implementation of diagnosis and treatment prediction. In this study, the performance on both the training cohort and two independent validation cohorts was good (C index: 0.834 and 0.923), indicating that our prediction model was stable. Compared with previous studies that lacked interpretation of prognostic features, we comprehensively described biological and clinical characteristics associated with radiomics features that would help guide future clinical decision-making processes in a reliable and reproducible manner. Among the 11 selected radiomics features, GLCM, GLSZM and NGTDM measured the ROI array heterogeneity, with greater values of these features representing greater heterogeneity or a larger range of radiomics signature.

Additionally, in several previous studies, the prognostic models based on genomic and transcriptomic information of tumor tissues, such as gene expression, DNA methylation, CNAs, and non-coding RNAs were developed. It has been reported that a nomogram which was combined with six genes was able to accurately distinguish patients with higher risk of cancer-specific death (38). Meanwhile, Patrick et al. has established 13-gene signature whose expression levels could predict distinct outcomes of patients with RCC (39). But these molecular prediction models were difficult to translate into routine clinical applications because of the timeliness of tumor specimens and the large intratumor heterogeneity, resulting in insufficient prognostic power and high detection costs. The radiomics signature we proposed was simple and based solely on information from routine preoperative CECT scans at the time of patient onset. By observing the entire tumor area and extracting high-dimensional features such as wavelets and features, radiomics avoided tumor tissue features limited to a single site, and could mine more prognostic information than genomics. Therefore, it might serve as a surrogate biomarker for prognostic stratification of RCC patients.

And even more interesting, according to the radiomics hypothesis, intra-tumoral imaging heterogeneity might be an expression of underlying genetic heterogeneity that might lead to treatment resistance and thus suggested poorer prognosis. Based on DEGs between low-high radiomics score groups, some pathways in cancer, such as HIF-1 signaling pathways and TNF signaling pathways, were significantly enriched. The VHL regulated the drug sensitivity of renal cell carcinoma *via* HIF-1 pathway (40). The RNF26/CBX7 axis modulated the TNF pathway to promote Renal cell carcinoma proliferation (41). The RCC patients in low radiomics score group appeared to respond better to Axitinib, Cisplatin, Gemcitabine, PD173074 and Sorafenib, which have been approved for treatment of advanced renal cell carcinoma, than patients in high radiomics score group. Image data is a high-throughput macroscopic data. Based on macroscopic imaging data, we have found connections to the microscopic world, which may be a powerful tool for tumor prognosis and treatment prediction in the future.

Nevertheless, there were several limitations to the present study. First, in a retrospective study, bias was inevitable. Due to the retrospective nature of the study, the heterogeneity of abdominal enhanced CT versions and lack of algorithmic standardization existed across and within centers. Second, we did not assess the proportion of the patients died because of competing risks instead of progressive RCC. Third, the TCGA data alone could not prove that there was a difference between high- and low-radiomics score groups in tumor microenvironment and drug sensitivity. Fourth, RCC patients who did not undergo surgery for various reasons were not included in the study cohort. The absence of this group of patients might have caused selection bias in the study. Another limitation was the lack of information on the WHOISUP and SSIGN in validation cohort 1(NCI). Thus, to further validate these findings, a prospective multi-center study is needed.

In conclusion, we developed multiple prognostic models for RCC and evaluated their predictive performance, based on clinical characteristics and radiomics features from CECT. Radiomics signature provided statistically significant incremental value to the existing prognosis models in predicting OS and have broad clinical applications.

Data availability statement

The raw data supporting the conclusions of this article will be made available by the authors, without undue reservation.

Ethics statement

This study was approved by the Ethics Committee of the First Affiliated Hospital of Nanjing Medical University. The requirement for written informed consent was waived in view of the retrospective nature of the study (ethics approval number, 2021-SR-430).

Author contributions

JJX, YYL and ZYW designed the research. JJX, YYL and SPS performed the data analysis and drafted the manuscript. ZYW and

AMX collected clinical data. JJX, ZJW and SFS critically revised the manuscript. All authors contributed to the article and approved the submitted version.

Funding

This study was supported by by National Natural Science Foundation of China (No. 81771640 to ZJW, NO.82103946 to SS) and Natural Science Foundation of the Jiangsu Higher Education Institutions of China (NO.21KJB330004 to SS).

Acknowledgments

We are grateful to all of the patients and cooperators for participating in this retrospective study, especially for the data from TCGA, CPTAC and KITS.

Conflict of interest

The authors declare that the research was conducted in the absence of any commercial or financial relationships that could be construed as a potential conflict of interest.

Publisher's note

Supplementary material

The Supplementary Material for this article can be found online at: https://www.frontiersin.org/articles/10.3389/fonc.2023.1036734/full#supplementary-material

SUPPLEMENTARY FIGURE 1
Flow chart of the study population enrolment with inclusion and exclusion criteria.

SUPPLEMENTARY FIGURE 2
Kaplan–Meier curves for overall survival in the training and validation cohorts.

SUPPLEMENTARY FIGURE 3
Comparative evaluation of various models in the validation cohorts. **(A-J)** Calibration plots describing the calibration of six models based on the consistency between predicted and observed 5-year OS results. **(K-S)** Clinical Impact Curve (CIC) of six models in the validation cohort. The red curve (Number high Risk) represents the number of people classified as positive (high risk) by the model at each threshold probability; The blue curve (Number high risk with outcome) is the Number of true positives at each threshold probability.

SUPPLEMENTARY FIGURE 4
The relationship between radiomics and genomics in CPTAC. **(A)** Hierarchical clustering of 30 DEGs of RCC. **(B)** KEGG pathways analysis of DEGs associated with radiomics signature. **(C)** A volcano plot generated using the data of differentially expressed genes (DEGs) between high-risk and low-risk groups from CPTAC.

SUPPLEMENTARY FIGURE 5
Sensitivity analysis for the consistency of radiomics features. (A) Histogram of Pearson r values calculated from the radiomic features between the initial dataset and repeated dataset. (B-L) Bland-Altman plots were used to test the potential agreement between two observers. Mean difference (dashed line) is close to zero, showing no bias; solid black lines delimit limits of agreement (95% CI).

References

1. Siegel R, Naishadham D, Jemal A. Cancer statistics, 2012. *CA Cancer J Clin* (2012) 62:10–29. doi: 10.3322/caac.20138

2. Espana-Agusti J, Warren A, Chew SK, Adams DJ, Matakidou A. Loss of PBRM1 rescues VHL dependent replication stress to promote renal carcinogenesis. *Nat Commun* (2017) 8:2026. doi: 10.1038/s41467-017-02245-1

3. Ricketts CJ, Linehan WM. Multi-regional sequencing elucidates the evolution of clear cell renal cell carcinoma. *Cell* (2018) 173:540–2. doi: 10.1016/j.cell.2018.03.077

4. Andrade HS, Zargar H, Caputo PA, Akca O, Kara O, Ramirez D, et al. Five-year oncologic outcomes after transperitoneal robotic partial nephrectomy for renal cell carcinoma. *Eur Urol* (2016) 69:1149–54. doi: 10.1016/j.eururo.2015.12.004

5. Lam JS, Klatte T, Kim HL, Patard J-J, Breda A, Zisman A, et al. Prognostic factors and selection for clinical studies of patients with kidney cancer. *Crit Rev Oncol Hematol* (2008) 65:235–62. doi: 10.1016/j.critrevonc.2007.08.003

6. Gordon MS, Hussey M, Nagle RB, Lara PNJr., Mack PC, Dutcher J, et al. Phase II study of erlotinib in patients with locally advanced or metastatic papillary histology renal cell cancer: SWOG S0317. *J Clin Oncol* (2009) 27:5788–93. doi: 10.1200/JCO.2008.18.8821

7. Gulati S, Martinez P, Joshi T, Birkbak NJ, Santos CR, Rowan AJ, et al. Systematic evaluation of the prognostic impact and intratumour heterogeneity of clear cell renal cell carcinoma biomarkers. *Eur Urol* (2014) 66:936–48. doi: 10.1016/j.eururo.2014.06.053

8. Escudier B, Porta C, Schmidinger M, Algaba F, Patard JJ, Khoo V, et al. Renal cell carcinoma: ESMO clinical practice guidelines for diagnosis, treatment and follow-up. *Ann Oncol* (2014) 125 Suppl 3:iii49–56. doi: 10.1093/annonc/mdu259

9. Palumbo C, Perri D, Zacchero M, Bondonno G, Martino JD, D'Agate D, et al. Risk of recurrence after nephrectomy: comparison of predictive ability of validated risk models. *Urol Oncol* (2022) 40:167.e1–7. doi: 10.1016/j.urolonc.2021.11.025

10. Escudier B, Porta C, Schmidinger M, Rioux-Leclercq N, Bex A, Khoo V, et al. Renal cell carcinoma: ESMO clinical practice guidelines for diagnosis, treatment and follow-up†. *Ann Oncol: Off J Eur Soc Med Oncol* (2019) 30:706–20. doi: 10.1093/annonc/mdz056

11. Choueiri TK, Motzer RJ. Systemic therapy for metastatic renal-cell carcinoma. *N Engl J Med* (2017) 376:354–66. doi: 10.1056/NEJMra1601333

12. Lotan Y, Margulis V. Predicting recurrence in patients with localised renal cell carcinoma after nephrectomy. *Lancet Oncol* (2019) 20:473–5. doi: 10.1016/S1470-2045(19)30024-5

13. Park SY, Lee HE, Li H, Shipitsin M, Gelman R, Polyak K. Heterogeneity for stem cell-related markers according to tumor subtype and histologic stage in breast cancer. *Clin Cancer Res* (2010) 16:876–87. doi: 10.1158/1078-0432.CCR-09-1532

14. Parker WP, Cheville JC, Frank I, Zaid HB, Lohse CM, Boorjian SA, et al. Application of the stage, size, grade, and necrosis (SSIGN) score for clear cell renal cell carcinoma in contemporary patients. *Eur Urol* (2017) 71:665–73. doi: 10.1016/j.eururo.2016.05.034

15. Ficarra V, Galfano A, Mancini M, Martignoni G, Artibani W. TNM staging system for renal-cell carcinoma: current status and future perspectives. *Lancet Oncol* (2007) 8:554–8. doi: 10.1016/S1470-2045(07)70173-0

16. Lambin P, Rios-Velazquez E, Leijenaar R, Carvalho S, van Stiphout RGPM, Granton P, et al. Radiomics: extracting more information from medical images using

advanced feature analysis. *Eur J Cancer* (2012) 48:441–6. doi: 10.1016/j.ejca.2011.11.036

17. Gillies RJ, Kinahan PE, Hricak H. Radiomics: images are more than pictures, they are data. *Radiology* (2016) 278:563–77. doi: 10.1148/radiol.2015151169

18. Yu Y, Tan Y, Xie C, Hu Q, Ouyang J, Chen Y, et al. Development and validation of a preoperative magnetic resonance imaging radiomics-based signature to predict axillary lymph node metastasis and disease-free survival in patients with early-stage breast cancer. *JAMA Netw Open* (2020) 3:e2028086. doi: 10.1001/jamanetworkopen.2020.28086

19. Xu X, Zhang HL, Liu QP, Sun SW, Zhang J, Zhu FP, et al. Radiomic analysis of contrast-enhanced CT predicts microvascular invasion and outcome in hepatocellular carcinoma. *J Hepatol* (2019) 70:1133–44. doi: 10.1016/j.jhep.2019.02.023

20. Gao R, Qin H, Lin P, Ma C, Li C, Wen R, et al. Development and validation of a radiomic nomogram for predicting the prognosis of kidney renal clear cell carcinoma. *Front Oncol* (2021) 11:613668. doi: 10.3389/fonc.2021.613668

21. Nazari M, Shiri I, Zaidi H. Radiomics-based machine learning model to predict risk of death within 5-years in clear cell renal cell carcinoma patients. *Comput In Biol Med* (2021) 129:104135. doi: 10.1016/j.compbiomed.2020.104135

22. Cornelis F, Tricaud E, Lasserre AS, Petitpierre F, Bernhard JC, Le Bras Y, et al. Multiparametric magnetic resonance imaging for the differentiation of low and high grade clear cell renal carcinoma. *Eur Radiol* (2015) 25:24–31. doi: 10.1007/s00330-014-3380-x

23. Posada Calderon L, Eismann L, Reese SW, Reznik E, Hakimi AA. Advances in imaging-based biomarkers in renal cell carcinoma: a critical analysis of the current literature. *Cancers (Basel)* (2023) 15. doi: 10.3390/cancers15020354

24. Xi IL, Zhao Y, Wang R, Chang M, Purkayastha S, Chang K, et al. Deep learning to distinguish benign from malignant renal lesions based on routine MR imaging. *Clin Cancer Res* (2020) 26:1944–52. doi: 10.1158/1078-0432.CCR-19-0374

25. Leibovich BC, Blute ML, Cheville JC, Lohse CM, Frank I, Kwon ED, et al. Prediction of progression after radical nephrectomy for patients with clear cell renal cell carcinoma: a stratification tool for prospective clinical trials. *Cancer* (2003) 97:1663–71. doi: 10.1002/cncr.11234

26. Tsiouris A, Hammoud ZT, Velanovich V, Hodari A, Borgi J, Rubinfeld I. A modified frailty index to assess morbidity and mortality after lobectomy. *J Surg Res* (2013) 183:40–6. doi: 10.1016/j.jss.2012.11.059

27. Delahunt B, Cheville JC, Martignoni G, Humphrey PA, Magi-Galluzzi C, McKenney J, et al. The international society of urological pathology (ISUP) grading system for renal cell carcinoma and other prognostic parameters. *Am J Surg Pathol* (2013) 37:1490–504. doi: 10.1097/PAS.0b013e318299f0fb

28. Chen DY, Uzzo RG. Optimal management of localized renal cell carcinoma: surgery, ablation, or active surveillance. *J Natl Compr Canc Netw* (2009) 7:635–42. doi: 10.6004/jnccn.2009.0044

29. Bedke J, Rini BI, Plimack ER, Stus V, Gafanov R, Waddell T, et al. Health-related quality of life analysis from KEYNOTE-426: pembrolizumab plus axitinib versus sunitinib for advanced renal cell carcinoma. *Eur Urol* (2022) 82:427–39. doi: 10.1016/j.eururo.2022.06.009

30. Motzer R, Porta C, Alekseev B, Rha SY, Choueiri TK, Mendez-Vidal MJ, et al. Health-related quality-of-life outcomes in patients with advanced renal cell carcinoma treated with lenvatinib plus pembrolizumab or everolimus versus sunitinib (CLEAR): a randomised, phase 3 study. *Lancet Oncol* (2022) 23:768–80. doi: 10.1016/S1470-2045(22)00212-1

31. Walach MT, Wunderle MF, Haertel N, Mühlbauer JK, Kowalewski KF, Wagener N, et al. Frailty predicts outcome of partial nephrectomy and guides treatment decision towards active surveillance and tumor ablation. *World J Urol* (2021) 39:2843–51.

32. Campi R, Berni A, Amparore D, Bertolo R, Capitanio U, Carbonara U, et al. Impact of frailty on perioperative and oncologic outcomes in patients undergoing surgery or ablation for renal cancer: a systematic review. *Minerva Urol Nephrol* (2022) 74:146–60.

33. Stewart GD, O'Mahony FC, Powles T, Riddick AC, Harrison DJ, Faratian D. What can molecular pathology contribute to the management of renal cell carcinoma? *Nat Rev Urol* (2011) 8:255–65.

34. Karakiewicz PI, Trinh Q-D, Bhojani N, Bensalah K, Salomon L, de la Taille A, et al. Renal cell carcinoma with nodal metastases in the absence of distant metastatic disease: prognostic indicators of disease-specific survival. *Eur Urol* (2007) 51:1616–24.

35. Aerts HJWL, Velazquez ER, Leijenaar RTH, Parmar C, Grossmann P, Carvalho S, et al. Decoding tumour phenotype by noninvasive imaging using a quantitative radiomics approach. *Nat Commun* (2014) 5:4006.

36. Coroller TP, Agrawal V, Huynh E, Narayan V, Lee SW, Mak RH, et al. Radiomic-based pathological response prediction from primary tumors and lymph nodes in NSCLC. *J Thorac Oncol* (2017) 12:467–76. doi: 10.1016/j.jtho.2016.11.2226

37. Zwanenburg A. Radiomics in nuclear medicine: robustness, reproducibility, standardization, and how to avoid data analysis traps and replication crisis. *Eur J Nucl Med Mol Imaging* (2019) 46:2638–55. doi: 10.1007/s00259-019-04391-8

38. Roldán FL, Izquierdo L, Ingelmo-Torres M, Lozano JJ, Carrasco R, Cuñado A, et al. Prognostic gene expression-based signature in clear-cell renal cell carcinoma. *Cancers* (2022) 14.

39. Terrematte P, Andrade DS, Justino J, Stransky B, de Araújo DSA, Dória Neto AD. A novel machine learning 13-gene signature: improving risk analysis and survival prediction for clear cell renal cell carcinoma patients. *Cancers* (2022) 14. doi: 10.3390/cancers14092111

40. Courtney KD, Infante JR, Lam ET, Figlin RA, Rini BI, Brugarolas J, et al. Phase I dose-escalation trial of PT2385, a first-in-Class hypoxia-inducible factor-2α antagonist in patients with previously treated advanced clear cell renal cell carcinoma. *J Clin Oncol* (2018) 36:867–74. doi: 10.1200/JCO.2017.74.2627

41. Liu W, Wang H, Jian C, Li W, Ye K, Ren J, et al. The RNF26/CBX7 axis modulates the TNF pathway to promote cell proliferation and regulate sensitivity to TKIs in ccRCC. *Int J Biol Sci* (2022) 18:2132–45. doi: 10.7150/ijbs.69325

frontiers | Frontiers in Oncology

TYPE Original Research
PUBLISHED 26 October 2023
DOI 10.3389/fonc.2023.1203922

OPEN ACCESS

EDITED BY
Abhishek Mahajan,
The Clatterbridge Cancer Centre,
United Kingdom

REVIEWED BY
Albert Guvenis,
Boğaziçi University, Türkiye
Giuseppe Simone,
Hospital Physiotherapy Institutes (IRCCS),
Italy

*CORRESPONDENCE
DeXin Yu
yudexin0330@sina.com

†These authors have contributed equally to this work and share first authorship

RECEIVED 11 April 2023
ACCEPTED 09 October 2023
PUBLISHED 26 October 2023

CITATION
Cheng Q, Ren A, Xu X, Meng Z, Feng X, Pylypenko D, Dou W and Yu D (2023) Application of DKI and IVIM imaging in evaluating histologic grades and clinical stages of clear cell renal cell carcinoma. *Front. Oncol.* 13:1203922. doi: 10.3389/fonc.2023.1203922

Application of DKI and IVIM imaging in evaluating histologic grades and clinical stages of clear cell renal cell carcinoma

QiChao Cheng[1†], AnLi Ren[2†], XingHua Xu[1†], Zhao Meng[1], Xue Feng[1], Dmytro Pylypenko[3], WeiQiang Dou[3] and DeXin Yu[1*]

[1]Department of Radiology, Qilu Hospital of Shandong University, Jinan, China, [2]Department of Radiology, Affiliated Hospital of Shandong University of Traditional Chinese Medicine, Jinan, China, [3]MR Research, GE Healthcare, Beijing, China

Purpose: To evaluate the value of quantitative parameters derived from diffusion kurtosis imaging (DKI) and intravoxel incoherent motion (IVIM) in differentiating histologic grades and clinical stages of clear cell renal cell carcinoma (ccRCC).

Materials and methods: A total of 65 patients who were surgically and pathologically diagnosed as ccRCC were recruited in this study. In addition to routine renal magnetic resonance imaging examination, all patients underwent preoperative IVIM and DKI. The corresponding diffusion coefficient (D), pseudo-diffusion coefficient (D*), perfusion fraction (f), mean diffusivity (MD), kurtosis anisotropy (KA), and mean kurtosis (MK) values were obtained. Independent-samples t-test or Mann–Whitney U test was used for comparing the differences in IVIM and DKI parameters among different histologic grades and clinical stages. The diagnostic efficacy of IVIM and DKI parameters was evaluated using the receiver operating characteristic (ROC) curve. Spearman's correlation analysis was used to separately analyze the correlation of each parameter with histologic grades and stages of ccRCC.

Results: The D and MD values were significantly higher in low-grade ccRCC than high-grade ccRCC (all $p < 0.001$) and in low-stage than high-stage ccRCC (all $p < 0.05$), and the f value of high-stage ccRCC was lower than that of low-stage ccRCC ($p = 0.007$). The KA and MK values were significantly higher in low-grade than high-grade ccRCC ($p = 0.000$ and 0.000, respectively) and in low-stage than high-stage ccRCC ($p = 0.000$ and 0.000, respectively). The area under the curve (AUC) values of D, D*, f, MD, KA, MK, DKI, and IVIM+DKI values were 0.825, 0.598, 0.626, 0.792, 0.750, 0.754, 0.803, and 0.857, respectively, in grading ccRCC and 0.837, 0.719, 0.710, 0.787, 0.796, 0.784, 0.864, 0.823, and 0.916, respectively, in staging ccRCC. The AUC of IVIM was 0.913 in staging ccRCC. The D, D*, and MD values were negatively correlated with the histologic grades and clinical stages (all $p < 0.05$), and the KA and MK values showed a positive correlation with histologic grades and clinical stages (all $p < 0.05$). The f value was also negatively correlated with the ccRCC clinical stage ($p = 0.008$).

Conclusion: Both the IVIM and DKI values can be used preoperatively to predict the degree of histologic grades and stages in ccRCC, and the D and MD values

have better diagnostic performance in the grading and staging. Also, further slightly enhanced diagnostic efficacy was observed in the model with combined IVIM and DKI parameters.

KEYWORDS

diffusion kurtosis imaging, intravoxel incoherent motion, histologic grades, clinical stages, clear cell renal cell carcinoma

Introduction

Renal cell carcinoma (RCC) is a common malignancy in the urologic system, with a 2%–3% annual increase worldwide (1). Clear cell RCC (ccRCC) is the most common type of RCC. With the advancement of imaging techniques, such as ultrasound (US), computed tomography (CT), magnetic resonance imaging (MRI), and PET-CT/MRI, small and low-stage kidney tumors can now be easily detected (2). While radical nephrectomy was once considered the standard curative therapy, partial nephrectomy is now preferred due to its better preservation of renal function (3). Relevant studies have confirmed that partial nephrectomy is widely employed for localized renal tumors. The study, as evidenced by the references you provided, demonstrates that the glomerular filtration rate, chronic kidney disease prevalence, and operative time in the off-clamp partial nephrectomy group were superior to those in the on-clamp group (4, 5). Studies have shown that the histologic differentiation of RCC is an important prognostic factor for patients undergoing partial nephrectomy. High-grade RCC is more aggressive and is associated with a higher risk of relapse or metastasis after surgery (3, 6). Therefore, preoperative prediction of the histologic grade and clinical stage of ccRCC is essential for the development of effective therapeutic strategies.

Compared with US and CT examination, MRI has good spatial and contrast resolution without ionizing radiation burden. Therefore, it was considered a proper method for preoperative assessment for the prognosis of ccRCC (7). MRI should be carried out by contrast injection in detecting malignant lesions; although gadolinium contrast is safer, patients with chronic renal were also affected by the use of gadolinium contrast material (8, 9). Diffusion-weighted imaging (DWI) was mainly applied to quantify the diffusion of water molecules and provided information on cellular density, membrane integrity, and tissue perfusion, which can distinguish viable from necrotic tumors in a non-invasive manner (10). Several previous studies on DWI have demonstrated good value in the grades and stages of renal tumors and differential diagnosis between renal benign and malignant tumors (11–13). However, due to the complexity and restriction of microstructures and water molecule diffusion, DWI is primarily used to quantify the diffusion of water molecules with a Gaussian distribution and cannot accurately reflect the information of the lesion. Moreover, the original apparent diffusion coefficient (ADC) values do not distinguish between the pure diffusive motion of water molecules and the effects of microcapillary perfusion (14, 15). In recent years, with the development of MRI, more advanced intravoxel incoherent motion (IVIM) and diffusion kurtosis imaging (DKI) models have been developed on the basis of DWI. By using multiple b values, IVIM may help to evaluate tissue microcapillary perfusion and provide an accurate characterization of tissue diffusivity motion (16). A previous study has shown that IVIM is helpful for distinguishing RCC from fat-poor angiomyolipoma (17). In addition, IVIM-derived parameters showed important value in the assessment of different renal tumor subtypes (18). DKI is an advanced DWI model that reflects tissue complexity by using higher b values and quantifies the non-Gaussian behavior of diffusion and the excess kurtosis of tissue (16, 19). Compared with the DWI model, the DKI model is mainly applied to detect non-Gaussian water molecule motion to reflect the lesion microstructure and identify tumor and necrotic tissue (20). Previous studies have shown that DKI is able to distinguish different types of RCCs (21, 22). Meanwhile, related studies have revealed that different DKI parameters have certain values in ccRCC grade (23, 24). Based on the different advantages of IVIM and DKI, the different models could show different features of ccRCC tissue, and it may be valuable to explore grading and staging of the ccRCC. Yang L et al. (14) showed that IVIM and DKI were helpful in the assessment of tumor staging and grading after neoadjuvant chemoradiotherapy in patients with locally advanced rectal cancer. However, in ccRCC-related results, previous studies were limited to IVIM or DKI for ccRCC grading or staging; no studies may have applied both IVIM and DKI techniques in ccRCC systematic histologic grades and clinical stages diagnosis.

Therefore, the purpose of our study was to investigate the value of IVIM and DKI parameters in differentiating ccRCC histologic grades and clinical stages, which was further helpful for the management of therapeutic strategies.

Materials and methods

Patients

This retrospective study was approved by the Qilu Hospital of Shandong University ethics committee, and written informed consent was provided by all the patients. A total of 71 patients with RCC based on clinical history from September 2022 to January

2023 were recruited. Postoperative pathologies of five patients showed other renal tumors (angiomyolipoma = 1, chromophobe = 1, oncocytoma = 2, and MiT family transcription = 1), and one patient with obvious image artifact was excluded. Finally, 65 ccRCC patients were enrolled in this study, including 43 men and 22 women. The age range was between 27 and 76 years, and the average age was 54 years. The tumor types were classified into four grades regarding the tumor nuclear size, shape, and chromatin pattern as described by the World Health Organization/International Society of Urological Pathology (WHO/ISUP) grading system. After the cytological assessment, the tumors were merged into two groups: low-grade (WHO/ISUP grades 1 and 2, n = 39) and high-grade (WHO/ISUP grades 3 and 4, n = 26) RCCs. The tumor node metastasis (TNM) classification of ccRCC was in four stages and then merged into two groups: low-stage (stages 1 and 2, n = 45) and high-stage (stages 3 and 4, n = 20) RCC. Figure 1 shows the flowchart of ccRCC.

MRI acquisition

All subjects underwent a 3.0T MRI scan (Discovery 750w, GE Healthcare, Chicago, IL, USA), with a 24-channel abdominal phased array coil, in a supine and foot-first position. Pre-inspection preparation was performed including fasting over 4 hours and breath-holding practice. MRI scan sequences included axial T1-weighted imaging (T1WI), fat-saturated T2-weighted imaging (T2WI), and dynamic contrast-enhanced MRI (DCE-MRI). IVIM and DKI imaging were performed on the kidney after acquiring the corresponding T2-weighted anatomical images. For IVIM, a single-shot spin-echo echo-planar imaging sequence was applied in axial view with 10 b values (25, 50, 75, 100, 150, 200, 400, 600, 800, and 1,000 s/mm^2) and respiratory triggered: repetition time/echo time (TR/TE) = 4,000/80.4 ms; field of view (FOV) = 36 × 36 cm^2; matrix = 128 × 128; slice thickness = 5 mm; scan time = 276 s. For DKI, a separate respiratory-triggered single-shot spin-echo echo-planar imaging sequence with 3 b values (0, 500, and 1,000 s/mm^2) and 15 diffusion directions per b value was applied. Other scan parameters were as follows: TR/TE = 6,000/126 ms; FOV = 36 × 36 cm^2; matrix = 128 × 128; slice thickness = 4 mm; scan time = 128 s.

Data post-processing

All IVIM and DKI data were post-processed with vendor-provided analytic software embedded in the GE ADW4.6 workstation. The resulting IVIM- and DKI-derived parametric maps were generated. The IVIM model was Sb/S0 = (1 − f).exp (−bD) + f.exp (−b [D* + D]) (25), where D is the pure molecular diffusion coefficient, D* is the pseudo-diffusion coefficient representing incoherent microcirculation of the capillary networks, and f is the perfusion fraction. The DKI model was Sb/S0 = exp (−b MD + b2·MD2·MK/6), where MK is the mean kurtosis (MK), and mean diffusion (MD) value is similar to the corrected average ADC value (26). Meanwhile, the kurtosis anisotropy (KA) value was calculated with the DKI model.

The region of interest (ROI) was selected and drawn separately by two abdominal radiologists with over 10 years of experience in MRI protocols. The size and location of the ROI were consistent on the IVIM and DKI parameter maps. The reviewers were blinded to the provided clinical data and pathological diagnosis. The criteria for ROI selection included combining conventional T2WI images, setting the large lesion dimension as the ROI on the b0 image and

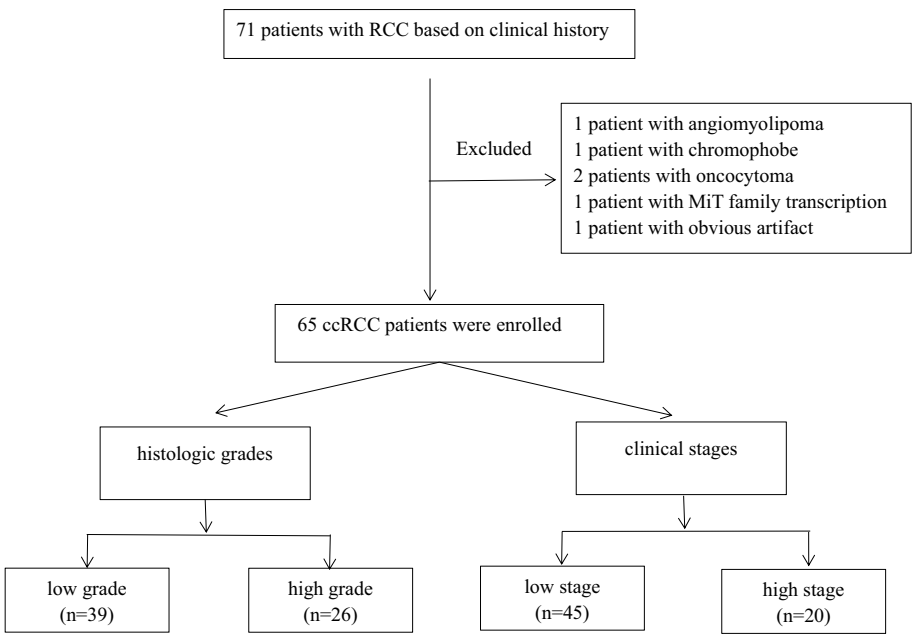

FIGURE 1
The flowchart of ccRCC. ccRCC, clear cell renal cell carcinoma.

co-registering other b values of IVIM and DKI images to the b0 image. The scope of the lesion was made as large as possible, and internal areas with necrosis, calcification, and bleeding were excluded. Clear cell RCCs are classically T2 hyperintense, and hemorrhage can be variable on T2WI alone (21).

Histologic grades

The surgically resected kidney specimens were used for the pathological evaluation and assessed by a urological pathologist who has 12 years of experience and was blinded to clinical data. Histologic grade was classified according to the criteria of the WHO/ISUP grade: grade 1, the nucleolus was absent or not obvious at ×400 magnification; grade 2, under the microscope at ×400 magnification, the tumor cells showed clear nucleoli, but at ×100, the nucleoli were not obvious or unclear; grade 3, the nucleoli were clear at ×100 magnification; grade 4, tumor giant cells, sarcomatoid differentiation, and/or rhabdoid morphology (27). The tumors were merged into two groups: low-grade (WHO/ISUP grades 1 and 2) and high-grade (WHO/ISUP grades 3 and 4) ccRCC (28).

Clinical stages

Clinical stages were classified according to the criteria of the TNM classification based on the American Joint Committee on Cancer (29): stage 1, the ccRCC tumor was confined to the renal parenchyma, and the maximum diameter of the mass was less than 7 cm; stage 2, the tumor was confined to the renal parenchyma, and the maximum diameter of the tumor was >7 cm; stage 3 refers to tumor thrombus in the renal vein or its branches, upper and lower vena cava, or tumor invasion of the renal pelvis and calyces, perirenal or sinus fat but not beyond the renal fascia; stage 4, the tumor broke through the renal fascia. The tumors were merged into two groups: low-stage (stages 1 and 2) and high-stage (stages 3 and 4) RCC.

Statistical analysis

Statistical analyses were performed using the SPSS 22 software package (IBM, Armonk, NY, USA). According to the characteristics of data distribution, quantitative data were expressed as the mean ± standard deviation. Inter-class correlation coefficient (ICC) analysis was used to evaluate the interobserver agreement of IVIM and DKI parameter measurements (ICC 0.61–0.80 indicates good, and >0.8 indicates excellent). Independent-samples t-test and Mann–Whitney U test were used to evaluate the differences in IVIM and DKI parameters between high-grade and low-grade as well as between high-stage and low-stage ccRCC. Parameters with $p < 0.05$ were selected for further multivariate logistic regression (30, 31). Receiver operating characteristic (ROC) analysis was performed using MedCalc software (version 11.4.2.0, Ostend, Belgium) to obtain the area under the curve (AUC), sensitivity, and specificity of low and high grades and stages of ccRCC for different parameters and their combinations; optimal cutoff points of different parameters were also determined. Spearman's correlation analysis was used to analyze the correlation between each IVIM and DKI parameter and the histologic grade and clinical stage of ccRCC. The differences were considered statistically significant at $p < 0.05$.

Results

Clinical data

Among the 65 cases of HCC, 39 were low-grade and 26 high-grade patients, and 45 were low clinical stage and 20 were high clinical stage patients. Detailed patient pathological grades and clinical stages are summarized in Table 1. Figures 2 and 3 show the features of low-grade and low-stage ccRCC and high-grade and high-stage on T2-weighted images: D, D*, f, MD, KA, and MK maps. The agreements of IVIM and DKI parameters between two observers were perfect by high ICC for D(0.873), D*(0.838), f (0.786), MD(0.861), KA(0.860), and MK(0.885).

Comparison of IVIM and DKI parameters between low- and high-grade ccRCC

The D and MD values were higher in low-grade than high-grade ccRCC ($p = 0.000$ and 0.000, respectively), and KA and MK values were lower in low-grade than high-grade ccRCC ($p = 0.000$ and 0.000, respectively). However, the D* and f values had no significant difference in low- and high-grade ccRCC ($p = 0.185$ and 0.088).

TABLE 1 Pathological grades and clinical stages.

Grade	Stage	Clinical stages			
		Stage 1	Stage 2	Stage 3	Stage 4
WHO/ISUP	G1	13	/	/	/
	G2	21	4	1	/
	G3	7	/	17	1
	G4	/	/	1	/

WHO/ISUP, World Health Organization/International Society of Urological Pathology.

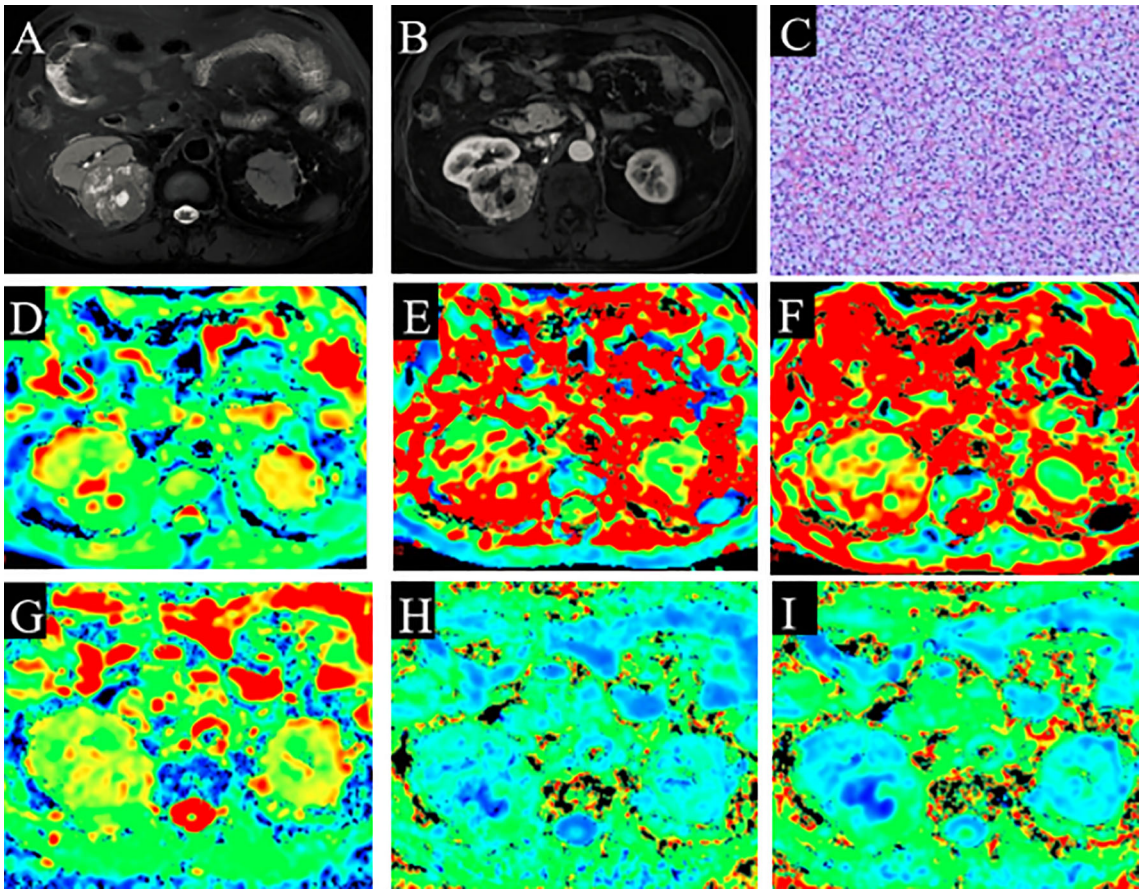

FIGURE 2
A 60-year-old man with ccRCC (grade 1 and stage 1). **(A)** Slightly high signal intensity on fat-saturated T2WI. **(B)** The lesion shows enhancement on solid part of ccRCC. **(C)** Pathological analysis confirmed ccRCC (grade 1). **(D)** D map. **(E)** D* map. **(F)** f map. **(G)** MD map. **(H)** KA map. **(I)** MK map. The necrotic areas in the center of the ccRCC. ccRCC, clear cell renal cell carcinoma; T2WI, T2-weighted imaging; MD, mean diffusivity; KA, kurtosis anisotropy; MK, mean kurtosis.

Table 2 shows the differences in IVIM and DKI parameters between the low- and high-grade ccRCCs.

Comparison of IVIM and DKI parameters between low- and high-stage ccRCC

The D, D*, f, and MD values were higher in low-stage than high-stage ccRCC (p = 0.000, 0.005, 0.007, and 0.000, respectively), and the KA and MK values were lower in low-stage than high-stage ccRCC (p = 0.000 and 0.000, respectively). Table 3 shows the differences in the IVIM and DKI parameters between the low- and high-stage ccRCC.

Correlation analyses of IVIM and DKI parameters with histologic grade and clinical stage of ccRCC

The D, D*, and MD values were negatively correlated with the histologic grades (r = −0.524, −0.258, and −0.561, p = 0.000, 0.038, and 0.000, respectively) and clinical stages (r = −0.470, −0.413, and −0.516, p = 0.000, 0.001, and 0.000, respectively). In contrast, the KA and MK values were positively correlated with the histologic grades (r = 0.504 and 0.542, p = 0.000 and 0.000, respectively) and clinical stages (r = 0.478 and 0.421, p = 0.000 and 0.000, respectively). The f value was also negatively correlated with the ccRCC clinical stage (r = −0.326, p = 0.008). Tables 4 and 5 show the correlations of IVIM and DKI parameters with the grade and stage of ccRCC, respectively.

ROC curve analysis in differentiating histologic grade and clinical stage of ccRCC

The AUC values of D, D*, f, MD, KA, and MK values were 0.825, 0.598, 0.626, 0.792, 0.750, and 0.754, respectively, in grading ccRCC and 0.837, 0.719, 0.710, 0.787, 0.796, and 0.784, respectively, in staging ccRCC. The D, MD, KA, and MK values were significant predictors in differentiating low from high grade and stage of ccRCC. Marginally, the model incorporating IVIM and DKI

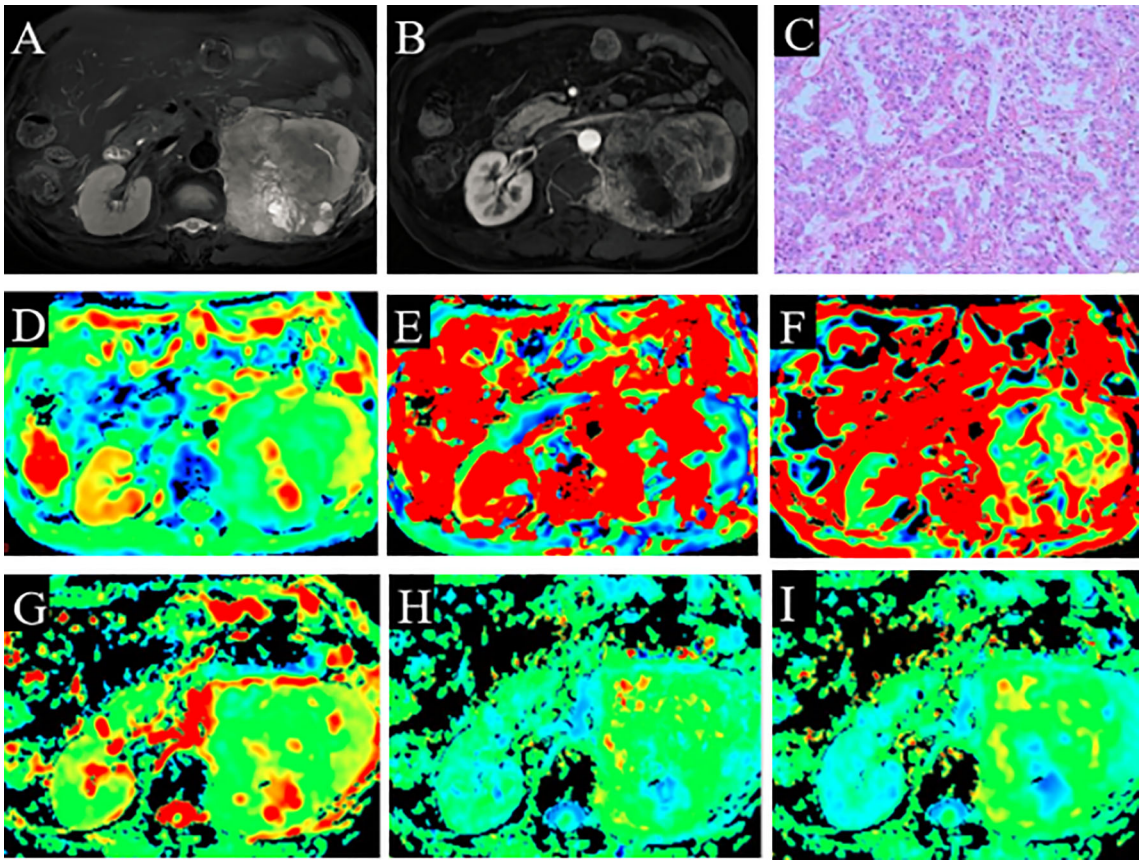

FIGURE 3
A 66-year-old man with ccRCC (grade 3 and stage 3). **(A)** High signal intensity on fat-saturated T2WI. **(B)** Solid part shows enhancement. **(C)** Pathological analysis confirmed ccRCC (grade 3). **(D)** D map. **(E)** D* map. **(F)** f map. **(G)** MD map. **(H)** KA map. **(I)** MK map. ccRCC, clear cell renal cell carcinoma; T2WI, T2-weighted imaging; MD, mean diffusivity; KA, kurtosis anisotropy; MK, mean kurtosis.

parameters exhibited improved diagnostic capabilities. The AUC values of DKI and IVIM+DKI values were 0.803 and 0.857, respectively, in grading ccRCC and 0.823 and 0.916, respectively, in staging ccRCC, and the AUC of IVIM was 0.913 in staging ccRCC. The AUC values, cutoff values, sensitivity, and specificity in differentiating tumor stage and histologic grade of ccRCC are shown in Tables 6 and 7 and Figures 4–7.

Discussion

This study explored the value of IVIM and DKI in evaluating tumor grades and T stages in ccRCC patients. The results showed that IVIM and DKI parameters are of great value in differentiating low and high grades and stages, and the D, MD, KA, and MK values have better diagnostic values in grades and stages. In addition, the f values also helped to assess clinical stages. Meanwhile, the diagnostic performance saw a minor enhancement when IVIM and DKI parameters were combined.

IVIM provides a unique view of tissue perfusion without using exogenous contrast agents. The D values of low-grade ccRCC were higher those of than high-grade ccRCC. The degree of tumor differentiation is closely related to its aggressiveness. The IVIM parameters of low-stage ccRCC were higher than those of high-stage ccRCC. The D values represent the water molecule diffusion, which indicates the change in the microenvironment (32). The solid tumor components of RCC have greater cellular density and collagenous interstitial stroma, close arrangement, and small extracellular space, which reduce water diffusion velocity. The D values of low-grade ccRCC were significantly higher than those of high-grade ccRCC (13, 33, 34). Histologic grade and clinical stage were significantly negatively correlated with the D values, and poorer differentiation in histologic grade and clinical stage resulted in lower D values. The reduction in D values can be attributed to the hindrance of water motion due to the increased viscosity of the tumor tissue. Poorer tumor differentiation led to faster proliferation, resulting in increases in the number of tumor cells and the tumor density and a decrease in intercellular substance. The diffusion of water molecules within the tumor tissue was more constrained, which was reflected by significant decreases in D values (35). Yang L et al. (14) explored the value of IVIM in evaluating tumor T stages in locally advanced rectal cancer patients; the D value was significantly distinguished in the diagnosis of staging, and these findings are consistent with ours. Moreover, previous studies

TABLE 2 The differences in the IVIM and DKI parameters between the low- and high-grade ccRCC.

	Low-grade	High-grade	t	*p*
D ($\times 10^{-3}$)	1.538 ± 0.429	1.080 ± 0.300	5.068	0.000
D*	0.077 ± 0.063	0.057 ± 0.030	/	0.185
F	0.286 ± 0.112	0.240 ± 0.121	/	0.088
MD	2.422 ± 0.530	1.834 ± 0.598	4.544	0.000
KA	0.773 ± 0.294	1.067 ± 0.315	−3.795	0.000
MK	0.589 ± 0.258	0.854 ± 0.288	3.791	0.000

IVIM, intravoxel incoherent motion; DKI, diffusion kurtosis imaging; ccRCC, clear cell renal cell carcinoma; MD, mean diffusivity; KA, kurtosis anisotropy; MK, mean kurtosis. D, corresponding diffusion coefficient; D*, pseudo-diffusion coefficient; f, perfusion fraction.

TABLE 3 The differences in the IVIM and DKI parameters between the low- and high-stage ccRCC.

	Low-stage	High-stage	t	*p*
D ($\times 10^{-3}$)	1.503 ± 0.427	1.021 ± 0.262	4.667	0.000
D*	0.082 ± 0.060	0.040 ± 0.031	/	0.005
f	0.294 ± 0.112	0.213 ± 0.112	/	0.007
MD	2.383 ± 0.515	1.789 ± 0.507	4.334	0.000
KA	0.779 ± 0.292	1.116 ± 0.294	−4.270	0.000
MK	0.603 ± 0.264	0.895 ± 0.268	−4.077	0.000

IVIM, intravoxel incoherent motion; DKI, diffusion kurtosis imaging; ccRCC, clear cell renal cell carcinoma; MD, mean diffusivity; KA, kurtosis anisotropy; MK, mean kurtosis. D, corresponding diffusion coefficient; D*, pseudo-diffusion coefficient; f, perfusion fraction.

TABLE 4 The correlations between IVIM, DKI parameters, and grade of ccRCC.

	IVIM			DKI		
	D	D*	f	MD	KA	MK
r	−0.524	−0.258	−0.211	−0.561	0.504	0.542
p	0.000	0.038	0.092	0.000	0.000	0.000

IVIM, intravoxel incoherent motion; DKI, diffusion kurtosis imaging; ccRCC, clear cell renal cell carcinoma; MD, mean diffusivity; KA, kurtosis anisotropy; MK, mean kurtosis. D, corresponding diffusion coefficient; D*, pseudo-diffusion coefficient; f, perfusion fraction.

have proven negative correlations of D values with the histologic grade in RCC and that D values can be used for histologic grading of RCC (36–39).

The D* and f values are the perfusion parameters, which could be used to analyze the vascularity of the tissue. The D* value is defined as the average blood flow and mainly reflects the capillary blood velocity, and the f value measures the microvascular volume fraction (32). Zhou Y et al. investigated the IVIM of 40 HCC patients and found that the D* and f values did not significantly correlate with the histologic grade (40), being consistent with our study. Huang YC et al. (41) showed that IVIM parameters are negatively correlated with stages of esophageal squamous cell carcinoma, and microvascular volume fraction helps detect and stage esophageal squamous cell carcinoma. As the tumor stage progresses, the central microvessel density decreases while its volume expands. This results in an insufficient central blood supply to the ccRCC, leading to increased micronecrosis (42). The D* and f values of low-grade ccRCC were not statistically significant. The main reasons include 1) the relatively small sample size of ccRCC in the high-grade group; 2) the f value correlated well with the enhancement degree of renal lesions, and partial low-stage ccRCC displays as cystic mass showing slight enhancement, leading the f value of low- and high-grade ccRCC to have no statistical significance (17). In our study, the diagnostic efficiency of the D* and f values was lower than that of the D value, and the AUC of the D value was higher than that of the D* and f values. The limited importance of the D* and f values in this study was explained previously by its high uncertainty and poor reproducibility (43). Additionally, the relatively small sample size might affect the results.

DKI reflects tissue complexity by using higher b values. The signal intensity largely depends on the b values applied, which could

TABLE 5 The correlations between IVIM, DKI parameters, and stage of ccRCC.

	IVIM			DKI		
	D	D*	f	MD	KA	MK
r	−0.470	−0.413	−0.326	−0.516	0.478	0.421
p	0.000	0.001	0.008	0.000	0.000	0.000

IVIM, intravoxel incoherent motion; DKI, diffusion kurtosis imaging; ccRCC, clear cell renal cell carcinoma; MD, mean diffusivity; KA, kurtosis anisotropy; MK, mean kurtosis. D, corresponding diffusion coefficient; D*, pseudo-diffusion coefficient; f, perfusion fraction.

identify tumor and necrotic tissue (44). However, a higher b value reduces the signal-to-noise ratio. In our research, the b values used in DKI were 500 and 1,000 s/mm^2 with 15 diffusion directions per b value. Previous studies have shown that b values of 500 and 1,000 s/mm^2 are acceptable for kidney tumors, and DKI could provide additional information for revealing the renal microstructure and function (21, 45). Some previous works have confirmed that DKI can effectively distinguish high- from low-grade RCC; this is consistent with the results of this study (22–24). Compared with the results of previous studies, we systematically analyzed the value of DKI in the differentiation and grading of ccRCC, and histologic grade was classified according to the criteria of the WHO/ISUP grade; related research shows that the WHO/ISUP grade system has been considered to be easier to apply to clinical management and superior to the Fuhrman grading system (46). The MD value is corrected by non-Gaussian bias and could give insights into the structural connectivity of tissues, potentially providing useful information on the pathophysiology of diseases. Yang L (14) et al. explored the DKI parameters of the high stage and found that they were lower than those of the low stage in locally advanced rectal

TABLE 6 Diagnostic value of IVIM and DKI parameters in differentiating low- and high-grade of ccRCC.

	AUC (area = 0.5)	Cutoff	Sensitivity	Specificity
D	0.825 ($p < 0.0001$)	≤0.0014	88.5	74.4
D*	0.598 ($p = 0.1798$)	≤0.061	61.5	64.1
f	0.626 ($p = 0.1082$)	≤0.173	46.2	89.7
MD	0.792 ($p < 0.0001$)	≤2.28	88.5	71.8
KA	0.750 ($p < 0.0001$)	>0.895	73.1	71.8
MK	0.754 ($p < 0.0001$)	>0.584	84.6	61.5
DKI(MD+KA+MK)	0.803 ($p < 0.0001$)	/	88.5	61.5
IVIM(D)+DKI	0.857 ($p < 0.0001$)	/	92.3	71.8

IVIM, intravoxel incoherent motion; DKI, diffusion kurtosis imaging; ccRCC, clear cell renal cell carcinoma; AUC, area under the curve; MD, mean diffusivity; KA, kurtosis anisotropy; MK, mean kurtosis. D, corresponding diffusion coefficient; D*, pseudo-diffusion coefficient; f, perfusion fraction.

TABLE 7 Diagnostic value of IVIM and DKI parameters in differentiating low- and high-stage ccRCC.

	AUC (area = 0.5)	Cutoff	Sensitivity	Specificity
D	0.837 ($p < 0.0001$)	≤0.0013	95.0	71.1
D*	0.719 ($p = 0.0020$)	≤0.0325	65.0	82.2
f	0.710 ($p = 0.0086$)	≤0.166	55.0	91.1
MD	0.787 ($p < 0.0001$)	≤2.28	90.0	64.4
KA	0.796 ($p < 0.0001$)	>0.791	90.0	64.4
MK	0.784 ($p < 0.0001$)	>0.841	65.0	84.4
IVIM(D+D*+f)	0.913 ($p < 0.0001$)	/	90.0	80.0
DKI(MD+KA+MK)	0.823 ($p < 0.0001$)	/	70.0	86.7
IVIM+DKI	0.916 ($p < 0.0001$)	/	95.0	73.3

IVIM, intravoxel incoherent motion; DKI, diffusion kurtosis imaging; ccRCC, clear cell renal cell carcinoma; MD, mean diffusivity; KA, kurtosis anisotropy; MK, mean kurtosis. D, corresponding diffusion coefficient; D*, pseudo-diffusion coefficient; f, perfusion fraction.

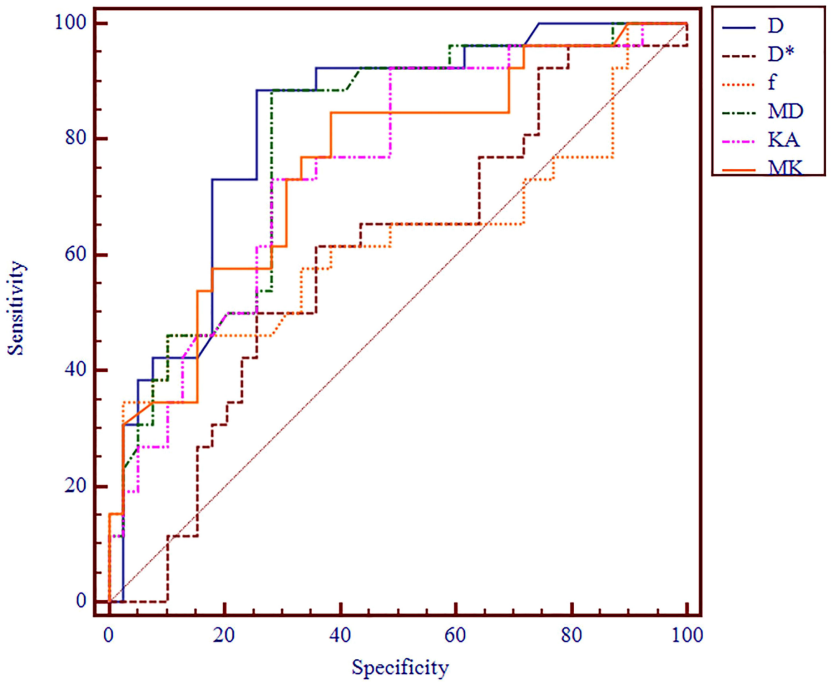

FIGURE 4
ROC analysis of IVIM and DKI parameters in differentiating histologic grade. ROC, receiver operating characteristic; IVIM, intravoxel incoherent motion; DKI, diffusion kurtosis imaging.

cancer patients; in particular, the MD values also yielded comparable overall diagnostic abilities in differentiating the low-stage from high-stage patients. These findings are consistent with ours. Moreover, the MK value identifies deviations of diffusion from Gaussian motions. The changes in organizational structure can affect both MK and KA values (47). Thus, MK and KA are not completely independent, although both indicators can be used to test for different aspects of diffusion. Zhu Q et al. (21) found that

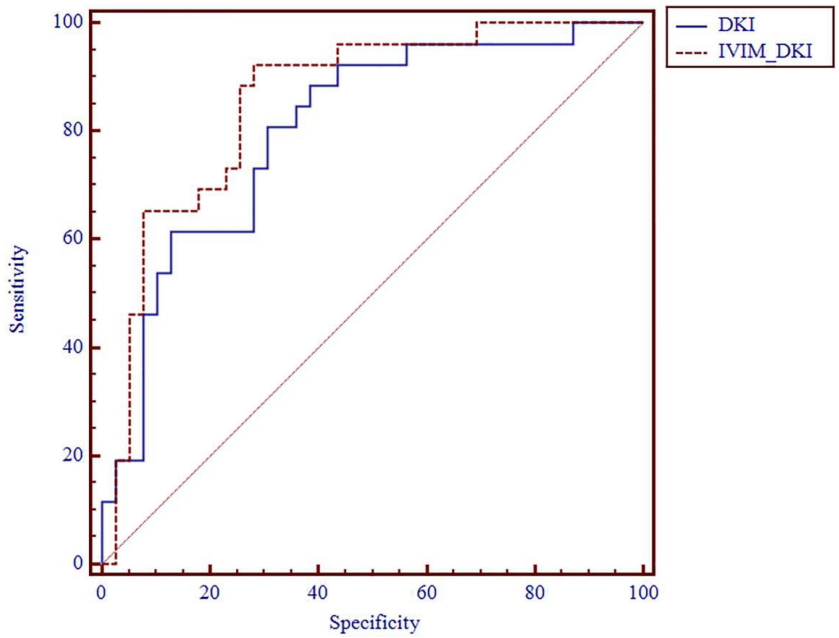

FIGURE 5
ROC analysis of DKI and IVIM+DKI in differentiating histologic grade. ROC, receiver operating characteristic; DKI, diffusion kurtosis imaging; IVIM, intravoxel incoherent motion.

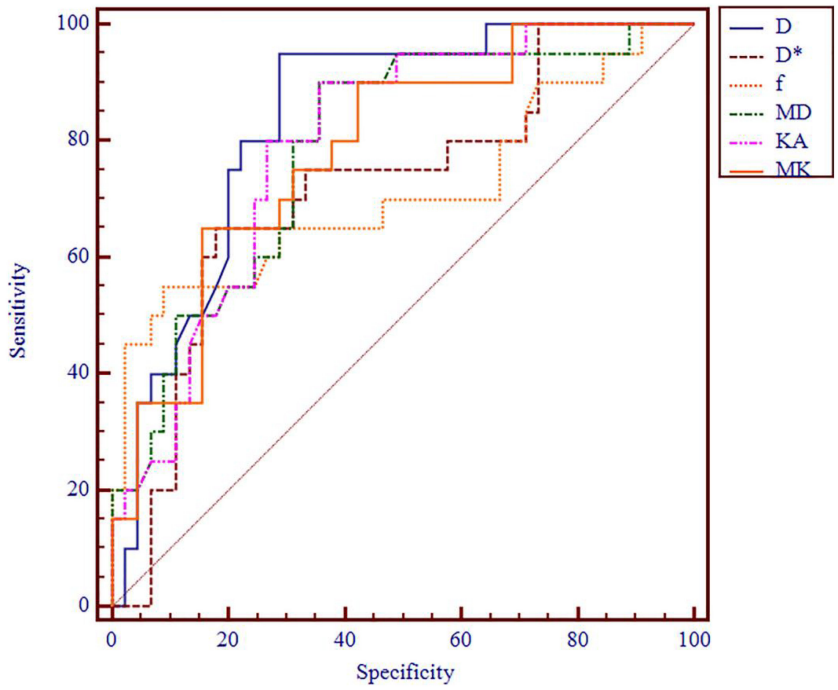

FIGURE 6
ROC analysis of IVIM and DKI parameters in differentiating clinical stage. ROC, receiver operating characteristic; IVIM, intravoxel incoherent motion; DKI, diffusion kurtosis imaging.

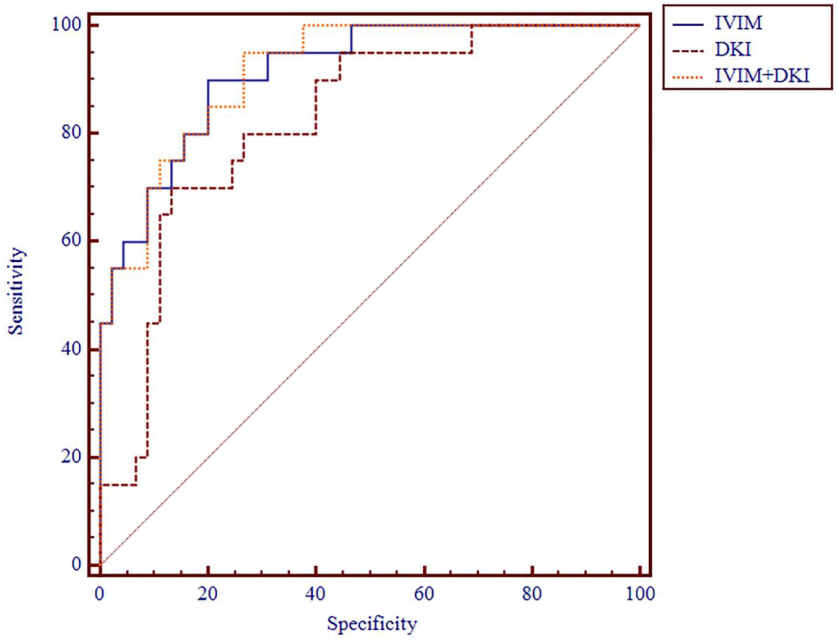

FIGURE 7
ROC analysis of IVIM, DKI, and IVIM+DKI in differentiating clinical stage. ROC, receiver operating characteristic; IVIM, intravoxel incoherent motion; DKI, diffusion kurtosis imaging.

papillary RCC has higher MK and KA values as compared with ccRCC due to its aggressiveness and histological heterogeneity. High-grade and stage ccRCC are more aggressive and histologically heterogeneous as compared to low-grade and stage ccRCC and increased the MK and KA values. Moreover, the KA value itself is important in predicting histologic grades and clinical stages of ccRCC.

In our study, we found that the D, MD, KA, and MK values were significantly different in evaluating the histologic grades and clinical stages of ccRCC, whereas the D* and f values were useful only in staging diagnosis Therefore, in the IVIM model, we recommend to combine only the valuable D, D*, and f values for clinical stages. In the DKI model, we recommend combining the valuable MD, KA, and MK values for both histologic grades and clinical stages. Previous research demonstrated that the combined parameters with a $p < 0.05$ from the statistical analysis had the best diagnostic ability (30, 31). Subsequently, we integrated the valuable parameters from both IVIM and DKI models for a more comprehensive evaluation of the histologic grades and clinical stages of ccRCC. This primarily includes the D value from the IVIM model and MD, KA, and MK values from the DKI model for evaluating histologic grades. For clinical staging, we recommend a combination of D, D*, and f parameters from the IVIM model and MD, KA, and MK parameters from the DKI model. Previous research has demonstrated that combining DKI with chemical exchange saturation transfer sequences is more effective than using a single sequence for grading and staging ccRCC (21). In our study, by combining the IVIM and DKI parameters, the resultant model showed a higher AUC than that obtained with a single sequence or parameter.

The limitations of our study include the relatively small sample, which might result in bias in the comparative evaluations. All ccRCC patients received radical or partial nephrectomy treatment. Since all the ccRCC patients in our study underwent either radical or partial nephrectomy, the number of patients with high-grade and advanced-stage ccRCC was relatively low. Further analyses with a larger cohort of ccRCC patients are necessary to study the correlations among different stages and grades.

In conclusion, compared to other relevant research, our study highlights the potential of both IVIM and DKI techniques in systematically characterizing and distinguishing between ccRCC grades and stages, presenting a more effective tool for accurate diagnosis. The combined utilization of the IVIM and DKI models offers enhanced diagnostic accuracy and efficiency. This combination provides valuable insights for clinical decision-making concerning surgical plans, including the choice between partial and radical nephrectomy, and informs patient management during follow-up. Moving forward, we will focus on expanding the sample size, with particular emphasis on including a greater number of cases with high-grade and advanced-stage ccRCC, in order to further validate the correlations with histologic grades and clinical stages.

Data availability statement

The original contributions presented in the study are included in the article/supplementary material. Further inquiries can be directed to the corresponding author.

Ethics statement

The studies involving humans were approved by Qilu Hospital of Shandong University ethics committee. The studies were conducted in accordance with the local legislation and institutional requirements. The participants provided their written informed consent to participate in this study. Written informed consent was obtained from the individual(s) for the publication of any potentially identifiable images or data included in this article.

Author contributions

DY guaranteed the study conception and design. QC carried out the analysis and interpretation of data. AR and XX carried out acquisition of data. QC, ZM, and XF prepared the drafting of manuscript. DY, WD, and DP: critical revision the manuscript. DP for the English revision. All authors contributed to the article and approved the submitted version.

Acknowledgments

The authors thank DY for his assistance with research and DP for the English revision of this article.

Conflict of interest

Authors DP, and WD were employed by the company GE Healthcare.

The remaining authors declare that the research was conducted in the absence of any commercial or financial relationships that could be construed as a potential conflict of interest.

Publisher's note

References

1. Laguna MP, Algaba F, Cadeddu J, Clayman R, Gill I, Gueglio G, et al. Current patterns of presentation and treatment of renal masses: a clinical research office of the endourological society prospective study. *J Endourol* (2014) 28:861–70. doi: 10.1089/end.2013.0724

2. Brace CL. Radiofrequency and microwave ablation of the liver, lung, kidney, and bone: what are the differences? *Curr Probl Diagn Radiol* (2009) 38:135–43. doi: 10.1067/j.cpradiol.2007.10.001

3. Shah PH, Leibovich BC, Van Houten H, Lyon TD, Yao X, Knoedler M, et al. Association of partial versus radical nephrectomy with subsequent hypertension risk following renal tumor resection. *J Urol* (2019) 202:69–75. doi: 10.1097/JU.0000000000000171

4. Tuderti G, Mastroianni R, Anceschi U, Bove AM, Brassetti A, Ferriero M, et al. Assessing the trade-off between the safety and effectiveness of off-clamp robotic partial nephrectomy for renal masses with a high RENAL score: A propensity score-matched comparison of perioperative and functional outcomes in a multicenter analysis. *Eur Urol Focus* (2023) 23:00120–7. doi: 10.1016/j.euf.2023.05.009

5. Simone G, Capitanio U, Tuderti G, Presicce F, Leonardo C, Ferriero M, et al. On-clamp versus off-clamp partial nephrectomy: Propensity score-matched comparison of long-term functional outcomes. *Int J Urol* (2019) 26:985–91. doi: 10.1111/iju.14079

6. Jamil ML, Keeley J, Sood A, Dalela D, Arora S, Peabody JO, et al. Long-term risk of recurrence in surgically treated renal cell carcinoma: A *post hoc* analysis of the eastern cooperative oncology group-american college of radiology imaging network E2805 trial cohort. *Eur Urol* (2020) 77:277–81. doi: 10.1016/j.eururo.2019.10.028

7. Venkatesan AM, Wood BJ, Gervais DA. Percutaneous ablation in the kidney. *Radiology* (2011) 261:375–91. doi: 10.1148/radiol.11091207

8. Johnson PT, Horton KM, Fishman EK. Adrenal imaging with MDCT: Nonneoplastic disease. *AJR Am J Roentgenol* (2010) 194:1001–12. doi: 10.2214/AJR.09.2551

9. Thomsen HS, Morcos SK, Dawson P. Is there a causal relation between the administration of gadolinium based contrast media and the development of nephrogenic systemic fibrosis (NSF)? *Clin Radiol* (2006) 61:905–6. doi: 10.1016/j.crad.2006.09.003

10. Koh DM, Collins DJ, Orton MR. Intravoxel incoherent motion in body diffusion-weighted MRI: reality and challenges. *AJR Am J Roentgenol* (2011) 196:1351–61. doi: 10.2214/AJR.10.5515

11. Göya C, Hamidi C, Bozkurt Y, Yavuz A, Kuday S, Gümüş H, et al. The role of apparent diffusion coefficient quantification in differentiating benign and Malignant renal masses by 3 tesla magnetic resonance imaging. *Balkan Med J* (2015) 32:273–8. doi: 10.5152/balkanmedj.2015.15475

12. Maruyama M, Yoshizako T, Uchida K, Araki H, Tamaki Y, Ishikawa N, et al. Comparison of utility of tumor size and apparent diffusion coefficient for differentiation of low-and high-grade clear-cell renal cell carcinoma. *Acta Radiol* (2015) 56:250–6. doi: 10.1177/0284185114523268

13. Yu X, Lin M, Ouyang H, Zhou C, Zhang H. Application of ADC measurement in characterization of renal cell carcinomas with different pathological types and grades by 3.0 T diffusion-weighted MRI. *Eur J Radiol* (2012) 81:3061–6. doi: 10.1016/j.ejrad.2012.04.028

14. Yang L, Xia C, Zhao J, Zhou X, Wu B. The value of intravoxel incoherent motion and diffusion kurtosis imaging in the assessment of tumor regression grade and T stages after neoadjuvant chemoradiotherapy in patients with locally advanced rectal cancer. *Eur J Radiol* (2021) 136:109504. doi: 10.1016/j.ejrad.2020.109504

15. Farley DR, Weaver AL, Nagorney DM. "Natural history" of unresected cholangiocarcinoma: patient outcome after noncurative intervention. *Mayo Clin Proc* (1995) 70(5):425–9. doi: 10.4065/70.5.425

16. Li X, Yang L, Wang Q, Tao J, Pan Z, Wang S. Soft tissue sarcomas: IVIM and DKI correlate with the expression of HIF-1α on direct comparison of MRI and pathological slices. *Eur Radiol* (2021) 31:4669–79. doi: 10.1007/s00330-020-07526-w

17. Ding Y, Zeng M, Rao S, Chen C, Fu C, Zhou J. Comparison of biexponential and monoexponential model of diffusion-weighted imaging for distinguishing between common renal cell carcinoma and fat poor angiomyolipoma. *Korean J Radiol* (2016) 17:853–63. doi: 10.3348/kjr.2016.17.6.853

18. Chandarana H, Kang SK, Wong S, Rusinek H, Zhang JL, Arizono S, et al. Diffusion-weighted intravoxel incoherent motion imaging of renal tumors with histopathologic correlation. *Invest Radiol* (2012) 47:688–96. doi: 10.1097/RLI.0b013e31826a0a49

19. Jensen JH, HelPern JA. MRI quantification of non-Gaussian water diffusion by kurtosis analysis. *NMR BioMed* (2010) 23:698–710. doi: 10.1002/nbm.1518

20. Yuan ZG, Wang ZY, Xia MY, Li FZ, Li Y, Shen Z, et al. Diffusion kurtosis imaging for assessing the therapeutic response of transcatheter arterial chemoembolization in hepatocellular carcinoma. *J Cancer* (2020) 11:2339–47. doi: 10.7150/jca.32491

21. Zhu Q, Xu Q, Dou W, Zhu W, Wu J, Chen W, et al. Diffusion kurtosis imaging features of renal cell carcinoma: a preliminary study. *Br J Radiol* (2021) 94:20201374. doi: 10.1259/bjr.20201374

22. Wang K, Cheng J, Wang Y, Wu G. Renal cell carcinoma: preoperative evaluate the grade of histological Malignancy using volumetric histogram analysis derived from magnetic resonance diffusion kurtosis imaging. *Quant Imaging Med Surg* (2019) 9:671–80. doi: 10.21037/qims.2019.04.14

23. Cao J, Luo X, Zhou Z, Duan Y, Xiao L, Sun X, et al. Comparison of diffusion-weighted imaging mono-exponential mode with diffusion kurtosis imaging for predicting pathological grades of clear cell renal cell carcinoma. *Eur J Radiol* (2020) 130:109195. doi: 10.1016/j.ejrad.2020.109195

24. Li S, He K, Yuan G, Yong X, Meng X, Feng C, et al. WHO/ISUP grade and pathological T stage of clear cell renal cell carcinoma: value of ZOOMit diffusion kurtosis imaging and chemical exchange saturation transfer imaging. *Eur Radiol* (2022) 33:4429–39. doi: 10.1007/s00330-022-09312-2

25. Chandarana H, Lee VS, Hecht E, Taouli B, Sigmund EE. Comparison of biexponential and monoexponential model of diffusion weighted imaging in evaluation of renal lesions: preliminary experience, Invest. *Radiol* (2011) 46:285–91. doi: 10.1097/RLI.0b013e3181ffc485

26. Guo R, Yang SH, Lu F, Han ZH, Yan X, Fu CX, et al. Evaluation of intratumoral heterogeneity by using diffusion kurtosis imaging and stretched exponential diffusion-weighted imaging in an orthotopic hepatocellular carcinoma xenograft model, Quant. *Imaging Med Surg* (2019) 9:1566–78. doi: 10.21037/qims.2019.08.18

27. Humphrey PA, Moch H, Cubilla AL, Ulbright TM, Reuter VE. The 2016 WHO classification of tumours of the urinary system and male genital organs-part B: prostate and bladder tumours. *Eur Urol* (2016) 70:106–19. doi: 10.1016/j.eururo.2016.02.028

28. Huang X, Nie F, Zhu J, Liu L, Wang N. Diagnostic value of contrast-enhanced ultrasound features for WHO/ISUP grading in renal cell carcinoma. *J Ultrasound Med* (2023) 42:1519–25. doi: 10.1002/jum.16171

29. Delahunt B, Eble JN, Samaratunga H, Thunders M, Yaxley JW, Egevad L. Staging of renal cell carcinoma: current progress and potential advances. *Pathology* (2021) 53:120–8. doi: 10.1016/j.pathol.2020.08.007

30. Fang S, Yang Y, Tao J, Yin Z, Liu Y, Duan Z, et al. Intratumoral heterogeneity of fibrosarcoma xenograft models: whole-tumor histogram analysis of DWI and IVIM. *Acad Radiol* (2022) 22:00621–3. doi: 10.1016/j.acra.2022.11.016

31. Jia H, Jiang X, Zhang K, Shang J, Zhang Y, Fang X, et al. A nomogram of combining IVIM-DWI and MRI radiomics from the primary lesion of rectal adenocarcinoma to assess nonenlarged lymph node metastasis preoperatively. *J Magn Reson Imaging* (2022) 3:658–67. doi: 10.1002/jmri.28068

32. Granata V, Fusco R, Amato DM, Albino V, Patrone R, Izzo F, et al. Beyond the vascular profile: conventional DWI, IVIM and kurtosis in the assessment of hepatocellular carcinoma. *Eur Rev Med Pharmacol Sci* (2020) 24:7284–93. doi: 10.26355/eurrev_202007_21883

33. Manenti G, Di Roma M, Mancino S, Bartolucci DA, Palmieri G, Mastrangeli R, et al. Malignant renal neoplasms: correlation between ADC values and cellularity in diffusion weighted magnetic resonance imaging at 3 T. *Radiol Med* (2008) 113:199–213. doi: 10.1007/s11547-008-0246-9

34. Zhang JL, Sigmund EE, Chandarana H, Rusinek H, Chen Q, Vivier PH, et al. Variability of renal apparent diffusion coefficients: limitations of the monoexponential model for diffusion quantification. *Radiology* (2010) 254:783–92. doi: 10.1148/radiol.09090891

35. Le Bihan D, Breton E, Lallemand D, Grenier P, Cabanis E, Laval-Jeantet M. MR imaging of intravoxel incoherent motions: application to diffusion and perfusion in neurologic disorders. *Radiology* (1986) 161:401–7. doi: 10.1148/radiology.161.2.3763909

36. Woo S, Suh CH, Kim SY, Cho JY, Kim SH. Diagnostic performance of DWI for differentiating high- from low-grade clear cell renal cell carcinoma: A systematic review and meta-analysis. *AJR Am J Roentgenol* (2017) 209:W374–W381. doi: 10.2214/AJR.17.18056

37. Zhang YD, Wu CJ, Wang Q, Zhang J, Wang XN, Liu XS, et al. Comparison of utility of histogram apparent diffusion coefficient and R2* for differentiation of low-grade from high-grade clear cell renal cell carcinoma. *AJR Am J Roentgenol* (2015) 205:W193–201. doi: 10.2214/AJR.14.13802

38. Dagher J, Delahunt B, Rioux-Leclercq N, Egevad L, Coughlin G, Dunglison N, et al. Assessment of tumour-associated necrosis provides prognostic information additional to World Health Organization/International Society of Urological Pathology grading for clear cell renal cell carcinoma. *Histopathology* (2019) 74:284–90. doi: 10.1111/his.13737

39. Zhu Q, Ye J, Zhu W, Wu J, Chen W. Value of intravoxel incoherent motion in assessment of pathological grade of clear cell renal cell carcinoma. *Acta Radiol* (2018) 59:121–7. doi: 10.1177/0284185117716702

40. Zhou Y, Yang G, Gong XQ, Tao YY, Wang R, Zheng J, et al. A study of the correlations between IVIM-DWI parameters and the histologic differentiation of

hepatocellular carcinoma. *Sci Rep* (2018) 11:10392. doi: 10.1038/s41598-021-89784-2

41. Huang YC, Chen TW, Zhang XM, Zeng NL, Li R, Tang YL, et al. Intravoxel incoherent motion diffusion-weighted imaging of resectable oesophageal squamous cell carcinoma: association with tumour stage. *Br J Radiol* (2018) 91:20170421. doi: 10.1259/bjr.20170421

42. Godley PA, Stinchcombe TE. Renal cell carcinoma. *Curr Opin Oncol* (1999) 11:213–7. doi: 10.1097/00001622-199905000-00014

43. Zhu HB, Zhang XY, Zhou XH, Li XT, Liu YL, Wang S, et al. Assessment of pathological complete response to preoperative chemoradiotherapy by means of multiple mathematical models of diffusion-weighted MRI in locally advanced rectal cancer: A prospective single-center study. *J Magn Reson Imaging* (2017) 46:175–83. doi: 10.1002/jmri.25567

44. Taron J, Johannink J, Bitzer M, Nikolaou K, Notohamiprodjo M, Hoffmann R. Added value of diffusion-weighted imaging in hepatic tumors and its impact on patient management. *Cancer Imaging* (2018) 18:10. doi: 10.1186/s40644-018-0140-1

45. Huang Y, Chen X, Zhang Z, Yan L, Pan D, Liang C, et al. MRI quantification of non-Gaussian water diffusion in normal human kidney: a diffusional kurtosis imaging study. *NMR BioMed* (2015) 28:154–61. doi: 10.1002/nbm.3235

46. Zhao Y, Wu C, Li W, Chen X, Li Z, Liao X, et al. 2-[18F]FDG PET/CT parameters associated with WHO/ISUP grade in clear cell renal cell carcinoma. *Eur J Nucl Med Mol Imaging* (2021) 48:570–9. doi: 10.1007/s00259-020-04996-4

47. Inoue T, Ogasawara K, Beppu T, Ogawa A, Kabasawa H. Diffusion tensor imaging for preoperative evaluation of tumor grade in gliomas. *Clin Neurol Neurosurg* (2005) 107:174–80. doi: 10.1016/j.clineuro.2004.06.011

Frontiers in Oncology

Advances knowledge of carcinogenesis and tumor progression for better treatment and management

The third most-cited oncology journal, which highlights research in carcinogenesis and tumor progression, bridging the gap between basic research and applications to imrpove diagnosis, therapeutics and management strategies.

Discover the latest Research Topics

See more →

Frontiers

Avenue du Tribunal-Fédéral 34
1005 Lausanne, Switzerland
frontiersin.org

Contact us

+41 (0)21 510 17 00
frontiersin.org/about/contact